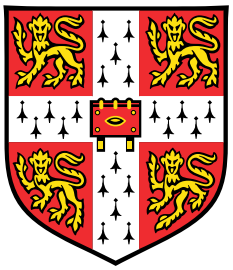

On convective penetration of a buoyant plume into a stably stratified layer

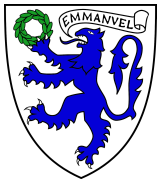

Charles William Powell

Supervisors: Prof. Peter H. Haynes & Prof. John R. Taylor

Department of Applied Mathematics & Theoretical Physics
University of Cambridge

This dissertation is submitted for the degree of
Doctor of Philosophy

Emmanuel College February 2025

They don't think it be like it is, but it do.

Oscar Gamble

Declaration

This thesis is the result of my own work and includes nothing which is the outcome of work done in collaboration except as declared in the preface and specified in the text. It is not substantially the same as any work that has already been submitted, or, is being concurrently submitted, for any degree, diploma or other qualification at the University of Cambridge or any other University or similar institution except as declared in the preface and specified in the text. It does not exceed the prescribed word limit for the relevant Degree Committee.

The discussion on convective hydration of the Tropical Tropopause Layer in section 1.1.1 and section 5.2.1 is modified from a review article written with Dr. Alison D. Ming and my PhD supervisors Prof. Peter H. Haynes and Prof. John R. Taylor:

Powell, C. W., Haynes, P. H., Taylor, J. R., and Ming, A. D. (2025). Moisture transport by convective overshoots in the Tropical Tropopause Layer. *Weather*, 80:6.

The study presented in chapter 3 has been published with advising from my PhD supervisors:

Powell, C. W., Haynes, P. H., and Taylor, J. R. (2024). Diagnosing tracer transport in convective penetration of a stably stratified layer. *Journal of Fluid Mechanics*, 997:A48.

The study presented in chapter 4 (with the exception of section 4.5) has been published with advising from Prof. Bruce R. Sutherland and my PhD supervisors:

Powell, C. W., Sutherland, B. R., Haynes, P. H., and Taylor, J. R. (2025). Internal waves generated by a plume impinging on a stratified fluid. *Journal of Fluid Mechanics (Rapids)*, 1006:R2.

Charles William Powell
February 2025

Acknowledgements

First and foremost I am incredibly grateful for the collaboration and insightful guidance of my supervisors, Peter and John. I have benefited enormously from their wealth of knowledge and intuition and above all I appreciate their treatment of me as a peer, which has allowed me the freedom to develop as a researcher and to find my way in the world of academia. Their patience has been immense and their support unwavering.

I am also fortunate to have worked in the vibrant community that is DAMTP and to have spent my time with friends and colleagues in the Atmosphere-Ocean Dynamics group who, like me, find delight in exploring the world around us. I am particularly indebted to Alison and Aaron who have provided friendship, sanity checks, and debugging tips. I may never have run a simulation without Aaron's neatly drawn cheat sheets and my scientific horizons would be foggier without Alison's support. My thanks also go to Stephen Cowley who first nurtured my interest in fluid dynamics and still offers wise advice over coffee many years later. I have also had the privilege of working with Bruce Sutherland whose collaboration has greatly enriched my experience of research.

Outside of academia, my spiritual home has been Emmanuel Boat Club. Embedding myself in the community at EBC is one of the best decisions I have ever made and has led me to who I am today. Thank you to all those I have rowed with: "there is nothing half so much worth doing as simply messing about in boats." Thank you also to the coaches who have spent many hours on the bank attempting to fix my rowing, many of whom have become close friends. I owe a debt of thanks to many others, home and abroad, who I am fortunate to call my friends.

Most of all, thank you to my family for their care and resolute support of my endeavours, and to my partner Chloe for her loving companionship.

Abstract

The convective penetration of a buoyant plume from a uniform layer into an overlying stably stratified layer is relevant to a wide variety of geophysical and industrial flows. An example we focus on is the hydration of the tropical lower stratosphere (TLS) by overshooting deep convection in the tropics. In these flows, turbulent mixing between the plume and environment results in significant diapycnal transport of tracers carried by the plume. Internal gravity waves are also generated within the stratified region which can transport horizontal momentum in the vertical, thereby influencing atmospheric winds. Despite its relevance, convective penetration of an individual buoyant plume remains an understudied problem. This thesis serves to address the turbulent mixing, wave generation, and tracer transport occurring in this fluid dynamical problem using large-eddy simulations (LES) of the flow at laboratory scale.

We first examine the turbulent mixing between the plume and environment, using a representation of the plume in buoyancy-tracer phase space to consider the mixing in more detail than has previously been achieved. We develop a new method for objectively partitioning plume fluid in buoyancy-tracer space into three regions, each of which corresponds to a coherent region in physical space. This enables quantification of different measures of turbulence and mixing within each of the three regions. Using simulations in which the stratification strength ranges over two orders of magnitude, we then examine the structure and source of internal waves that appear to emanate from the top of the plume. Internal waves are generated with frequencies in a relatively narrow band that is moderately smaller than the buoyancy frequency, despite the broad-banded frequency spectrum of turbulence in the plume and oscillations of the plume top. We provide evidence that the waves originate from within the turbulent flow rather than at the turbulent/non-turbulent interface between the plume top and the surrounding stratified fluid, and explain the frequency selection using a linear viscous decay model. Finally, we formulate a parameterisation of moisture which retains the essential processes involved in convective hydration of the TLS:

condensation/sublimation of vapour/ice and sedimentation of ice. Using this model, we explore the interaction between transport, microphysical processes and mixing in convective hydration of a stratified layer and examine the influence of large-scale vertical shear. We find that hydration is controlled by mixing which is modulated by sedimentation and directly influenced by convective intensity. Vertical shear enhances hydration by promoting small-scale mixing via internal wave breaking and shear instabilities.

In summary, this thesis presents three results: a novel understanding of the stages of mixing in convective penetration of a stably stratified layer, the first evidence that internal waves are generated within the turbulent plume rather than at the interface between the plume and environment, and a more fundamental understanding of the role of microphysics, mixing, transport and large-scale shear in controlling convective hydration of a stratified layer. The latter study offers insight on the physical processes which are most important in convective hydration of the TLS and may aid in the interpretation of more comprehensive studies and development of convective parameterisations in climate models.

Table of contents

1 Introduction **1**

1.1 Geophysical relevance 2

1.1.1 Convective hydration of the tropical lower stratosphere 4

1.1.2 Other geophysical examples 11

1.2 Plumes & fountains 15

1.3 Transport, mixing and wave generation in stratified turbulence 18

1.3.1 Stratified turbulence 18

1.3.2 Turbulent transport and mixing 20

1.3.3 Internal waves 21

1.4 Numerical methods 23

1.5 Overview of results chapters 25

2 Large-eddy simulations of a buoyant plume **29**

2.1 Integral plume theory 29

2.2 Numerical scheme 32

2.2.1 Governing equations and SGS model 32

2.2.2 Simulation setup 35

2.2.3 Plume generation method 37

2.3 Verifying the numerical method 40

2.3.1 Plume in a uniform environment 41

2.3.2 Plume in a stratified environment 50

2.3.3 Gibbs ringing 55

3 Diagnosing tracer transport in convective penetration **57**

3.1 Introduction 57

3.2 Flow & tracer structure 59

3.3 Buoyancy-tracer volume distribution 64

3.3.1 Definition & properties . . . 64
3.3.2 Idealised example . . . 68
3.3.3 Numerical implementation . . . 69
3.3.4 Results . . . 72
3.3.5 Quasi-steady state . . . 75
3.3.6 Source, transport and accumulation regions . . . 77
3.3.7 Entrainment . . . 81
3.3.8 Three-stage mixing process . . . 84
3.4 Mixing diagnostics . . . 87
3.4.1 Characterising mixing . . . 87
3.4.2 Results & discussion . . . 89
3.5 Conclusions . . . 93
Appendix 3.A Buoyancy-tracer volume distribution evolution equation . . . 96
Appendix 3.B Potential energy budget . . . 98

4 Internal waves generated by convective penetration 101
4.1 Introduction . . . 101
4.2 Numerical setup . . . 102
4.3 Comparison of plume and wavefield evolution . . . 104
4.4 Analyses . . . 107
4.4.1 Spectral analysis . . . 107
4.4.2 Viscous internal wave model . . . 108
4.4.3 Dynamic mode decomposition and ray tracing . . . 111
4.5 Comparison with a two-layer flow . . . 114
4.5.1 Two-layer flow structure . . . 114
4.5.2 Spectral analysis . . . 115
4.6 Discussion and conclusions . . . 118

5 Minimal model of convective hydration of a stratified layer 121
5.1 Introduction . . . 121
5.2 Literature review . . . 122
5.2.1 Convective hydration of the TTL . . . 122
5.2.2 Minimal moisture models . . . 125
5.3 Idealised model of moist convection . . . 130
5.3.1 Model formulation . . . 130
5.3.2 Simulation setup & numerical implementation . . . 133

5.3.3 Quantifying model regimes . . . 136
5.4 Exploring model behaviour . . . 138
5.5 Moist buoyancy-tracer volume distributions . . . 143

6 Influence of processes in a minimal model of convective hydration 151
6.1 Introduction . . . 151
6.2 Experimental design . . . 156
6.3 Convective hydration of a stably stratified layer . . . 160
6.3.1 Evolution of moist tracers and temperature . . . 160
6.3.2 Quantifying hydration of the stratified layer . . . 163
6.3.3 Evolution of mixing statistics . . . 164
6.4 Competing effects of sedimentation and mixing . . . 166
6.4.1 Evolution of moist tracers . . . 168
6.4.2 Semi-quantitative hydration models . . . 169
6.5 Influence of convective intensity on hydration . . . 173
6.5.1 Evolution of moist tracers . . . 174
6.5.2 Turbulent mixing . . . 176
6.5.3 Consequences for semi-quantitative models . . . 178
6.6 Convective penetration in the presence of large-scale vertical shear . . . 179
6.6.1 Evolution of flow and moist tracers . . . 179
6.6.2 Influence on mixing . . . 183
6.6.3 Influence on internal gravity wave response . . . 188
6.7 Discussion and conclusions . . . 198

7 Conclusions 203
7.1 Thesis summary . . . 203
7.2 Future directions & outlook . . . 209

References 215

Chapter 1

Introduction

Plumes arise from a continuous release of buoyant fluid from a localised source. This thesis is concerned with the flow in which a plume rises through a region with constant density ρ_0 and penetrates into a *stratified* region where the initial density profile $\rho(z)$ is horizontally uniform. In stratified flows it is convenient to introduce the *buoyancy* $b = -g\rho'/\rho_0$ in place of the density, where $\rho' = \rho - \rho_0$ is the perturbation from the reference density ρ_0 and g is the gravitational acceleration. Fluid parcels accelerate upwards when $b > 0$ and downwards when $b < 0$, unless balanced by other forces. We consider in particular penetration of plume into a *stably* stratified layer where $\partial\rho/\partial z < 0$ or equivalently $\partial b/\partial z > 0$. In a stably stratified region, fluid parcels vertically perturbed from their equilibrium height will oscillate up and down with a natural frequency N, defined by

$$N^2 = -\frac{g}{\rho_0}\frac{\partial\rho}{\partial z} = \frac{\partial b}{\partial z}. \tag{1.1}$$

We refer to N as the buoyancy (or Brunt-Väisälä) frequency. We refer to the flow with a buoyant plume penetrating into an overlying stratified region as *convective penetration*. We focus in particular on penetration of linearly stably stratified layers with constant buoyancy frequency N_0.

The interaction between active convection and neighbouring stably stratified regions is relevant to many geophysical flows. This work is primarily motivated by the need to understand and quantify turbulent transport, mixing and wave generation by strong atmospheric convection that penetrates from the bottom layer of the atmosphere into the overlying stably stratified layer, irreversibly transporting water vapour and other trace gases which influence the wider atmosphere. This problem can be studied by

considering the idealised flow of convective penetration of a stably stratified layer. In this introductory chapter we discuss this problem in detail and survey a variety of other relevant geophysical problems. We also summarise the study of plumes and convective penetration in fluid dynamics and introduce the physical background needed to understand turbulent transport, mixing, and wave generation in stratified turbulent flows. We then introduce the numerical methods that we use to study the flow and conclude the introductory chapter with an overview of the thesis.

1.1 Geophysical relevance

Earth's atmosphere is separated into layers, broadly determined by the vertical rate of change of temperature. In this thesis we focus on the bottom two layers. The lowest layer, the 'troposphere', is where our weather occurs. The temperature decreases from the surface up to the 'tropopause' which separates the troposphere from the 'stratosphere' where temperatures increase with height. The troposphere is weakly stratified, meaning the vertical density gradient is weak so vertical motions are not inhibited by the stratification, and well mixed by convective overturning. Deep convection, characterised by strong updrafts and rising most of the way through the troposphere, carries fluid from the near-surface boundary layer to the upper troposphere, with main convective outflow around 12.5 km in the tropics (Fueglistaler et al., 2009). Transport and mixing between the upper troposphere and the overlying stably stratified stratosphere is typically limited by the sharp increase in stratification strength at the tropopause. On large spatial and temporal scales, the tropopause acts as a 'rigid lid' on the troposphere that prevents direct exchange with the stratosphere, though upward-propagating waves generated in the troposphere can indirectly influence the stratosphere. On short timescales and in localised regions, direct troposphere-stratosphere exchange can occur as a result of strong convective motions that overshoot the tropopause and penetrate into the stably stratified stratosphere as shown in figure 1.1. This exchange plays an important role in setting lower stratospheric composition both in the tropics and extratropics. Owing to the weaker vertical motions in the stratosphere, its dynamics are primarily governed by chemical and radiative processes which strongly depend on the concentration of trace gases. It is therefore essential to understand the contribution of overshooting convection to the control of lower stratospheric composition.

Internal gravity waves are disturbances that propagate horizontally and vertically through a stratified fluid, driven by buoyancy forces. Deep convection impinging on the

Fig. 1.1 Deep convection with overshooting tops over North America, 12th May 2012, photographed from an aircraft. Photograph courtesy of NASA Earth Observatory.

base of the stratosphere can generate gravity waves that propagate horizontally as well as vertically into the stratosphere, though the generation mechanism is debated (Fritts and Alexander, 2003). Figure 1.2 shows an example of convectively-generated gravity waves propagating outward from deep convection – perturbation of the vertical velocity and temperature results in the formation of banded clouds which visualise the waves. As internal waves propagate in the vertical direction they transport horizontal momentum, which can significantly influence background atmospheric winds via wave–mean-flow interaction (Eliassen and Palm, 1961). For example, convectively-generated gravity waves contribute to the wave forcing of the stratospheric Quasi-biennial Oscillation (QBO; Dunkerton (1997)). The QBO is the primary mode of variability in the stratosphere, characterised by an oscillating band of strong zonal winds between $20 - 50\,\mathrm{km}$ in altitude confined to the tropics with a period of around 28 months (Baldwin et al., 2001). Until recent disruptions (Osprey et al., 2016), these oscillating winds were remarkably consistent. The QBO has been shown to exert control on numerous other climate drivers such as the El-Niño Southern oscillation (García-Franco et al., 2022), Madden-Julian oscillation (Son et al., 2017), and the stratospheric polar vortex (Holton and Tan, 1980). These atmospheric processes themselves influence

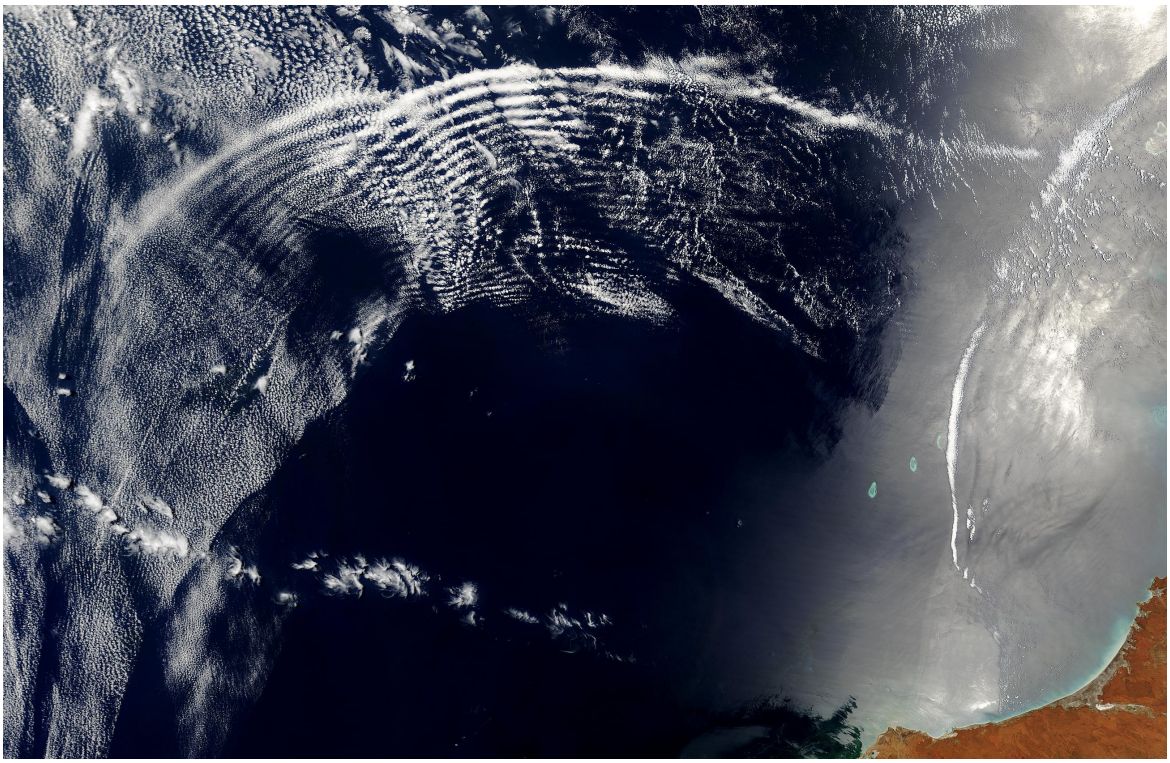

Fig. 1.2 Convectively-generated atmospheric gravity waves propagating away from the Australian coastline, 11th November 2003, photographed by the Terra satellite. Photograph courtesy of NASA Earth Observatory.

surface weather around the globe. Internal waves generated by convection are therefore an important pathway for small-scales to influence large-scale atmospheric dynamics.

1.1.1 Convective hydration of the tropical lower stratosphere

An important influence of tropopause-penetrating convection on the lower stratosphere is the mixing of tropospheric and stratospheric air that results in the irreversible vertical transport of moisture and trace gases. This process occurs in both the tropics and extratropics. The tropopause is lower in the extratropics (around 8 to 10 km, compared with 14 to 18 km in the tropics), which allows deep convection to more frequently reach the tropopause. However, convective penetration of the tropical lower stratosphere is more influential because the transition from the weakly stratified troposphere to the strongly stratified stratosphere is more gradual, which allows convection to penetrate further above the tropopause, and also because composition of the tropical lower stratosphere directly influences composition of the stratosphere as a whole.

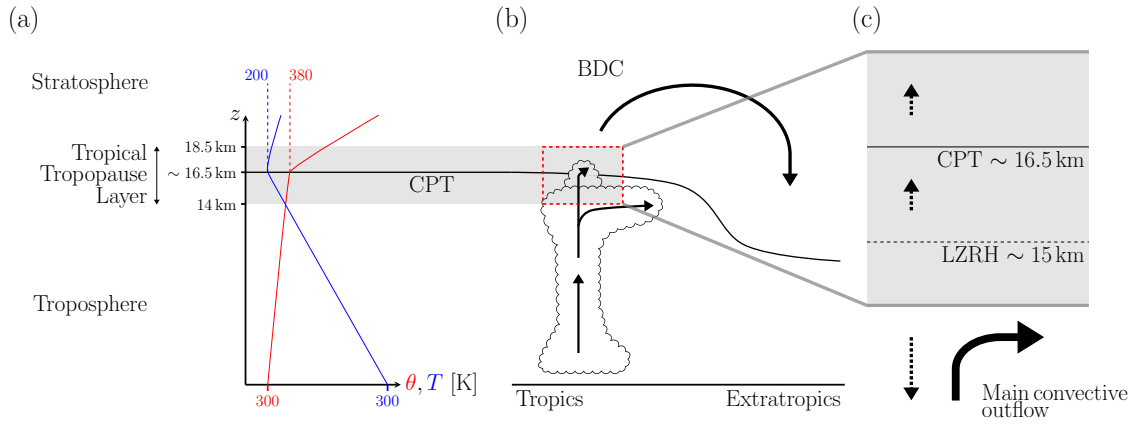

Fig. 1.3 Schematic diagram of convective overshooting and the tropical tropopause layer (TTL). (a) Layers of the atmospheric structure and approximate upper and lower bounds of the TTL and cold-point tropopause (CPT) height, alongside illustrative vertical profile of potential temperature θ and temperature T with approximate values (in K) at the surface and CPT. (b) Dashed line indicates latitudinal variation of the CPT height. Grey shading indicates the TTL. Arrows indicate motion in deep convection. Main convective outflow is in the upper troposphere. Convective overshoots penetrate into the TTL and occasionally cross the CPT (red dashed box, indicating the region considered in figure 5.1). Thick arrow illustrates transport of air from the TTL into the extratropical stratosphere by the Brewer-Dobson circulation (BDC). (c) TTL structure and vertical flow outside convection. Slow upwelling (radiative heating) above the level of zero radiative heating (LZRH) and subsidence (radiative cooling) below the LZRH. Main convective outflow below the TTL (solid arrow). The CPT lies above the LZRH and constrains the water vapour concentration of air parcels that slowly rise through the TTL.

The transitional layer between the tropical troposphere and stratosphere is called the tropical tropopause layer (TTL). The TTL is important as a gateway to the wider stratosphere, since the Brewer-Dobson circulation (BDC) carries air from the upper part of the TTL into the tropical stratosphere and then the extratropical stratosphere on timescales of a few years (Butchart, 2014), thereby to a large extent setting global stratospheric composition. The TTL is also interesting as a transition region between two distinct dynamical regimes; it can be identified as the region where the significant longitudinal variations in tropospheric dynamics manifest themselves in the more zonally uniform equatorial stratosphere (Fueglistaler et al., 2009).

Definitions of the TTL structure vary. We adopt the Fueglistaler et al. (2009) definition as shown in figure 1.3, with the lower boundary of the TTL at 14.5 km, above the height of the major convective outflow, and the upper boundary at 18.5 km. There is a temperature minimum at the cold-point tropopause (CPT), around 16.5 km. We refer to the region above the CPT as the upper TTL. Within the TTL, above the level of zero

radiative heating (LZRH) around 15 km, there is net radiative heating and corresponding large-scale slow upwelling which forms the start of the BDC. Below the LZRH in the air outside of convective clouds there is radiative cooling and correspondingly large-scale subsidence. Outside of convective regions, motion in the upper TTL is quasi-horizontal with air parcels travelling significant horizontal distances during their slow ascent, on the timescale of several weeks. Note that we refer to the region above the TTL as the tropical lower stratosphere (TLS); many studies instead refer to the region above the CPT, including the upper TTL, as part of the lower stratosphere.

TTL processes play an important role in determining water vapour concentrations in the stratosphere. The concentration of water vapour in a parcel of air is limited by the saturation vapour concentration which, according to the Clausius-Clapeyron relation, decreases rapidly with temperature. The very low temperatures at the tropical CPT reduce water vapour concentrations to the order of a few parts per million by volume (ppmv). The fact that the CPT is above the LZRH is an important aspect of vertical water vapour transport and dehydration in the TTL; the majority of the air that penetrates above the LZRH is likely to ascend into the stratosphere and the same is true of air passing through the CPT, therefore temperatures at the CPT exert significant control on stratospheric water vapour concentrations. Methane oxidation also contributes to water vapour concentrations in the stratosphere and plays an increasingly important role with height (Noël et al., 2018). It has been shown that the radiative balance of the troposphere is particularly sensitive to the concentration of water vapour in the lower stratosphere (Forster and Shine, 2002), even though these concentrations are very small relative to those in the troposphere itself. In addition, these concentrations are important for aspects of the chemistry of stratospheric ozone (Brasseur and Jacob, 2017). The potential climate sensitivity to lower stratospheric water vapour and its role in stratospheric chemistry and radiative balance highlights the importance of understanding the vertical transport of water vapour and the accompanying dehydration processes in the TTL.

The important role of the tropical CPT in setting stratospheric water vapour concentrations was identified in a classic paper by Brewer (1949). Since then, there has been much debate about the detail of the processes, in what we now recognise as the TTL, which determine the precise concentrations. A summary of the state of understanding about 10 years ago is given by Randel and Jensen (2013). Observations have shown clearly how variations in the CPT, leading to variations in the 'entry-value' of stratospheric water vapour concentrations, are propagated into the stratosphere

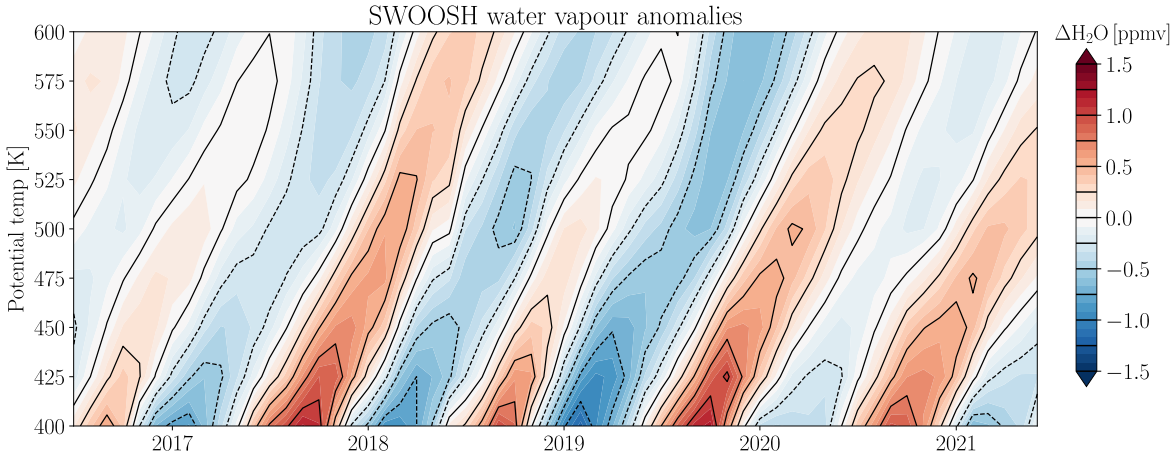

Fig. 1.4 Atmospheric tape recorder. Zonal mean water vapour anomaly in the TLS from the SWOOSH dataset (Davis et al., 2016) plotted on isentropic levels from 400 K (around 80 hPa, 18 km) to 600 K (around 30 hPa, 24 km), averaged over 15° N–S and with respect to the time mean from Jan 2006 to Jul 2024.

by transport and mixing effects of the BDC. This is illustrated in figure 1.4 which shows the time-height variation of water vapour anomalies in the tropical stratosphere; seasonal variation in CPT temperatures imprints on water vapour concentration and slow upwelling by the BDC lifts the anomalies through the stratosphere over time resulting in an 'atmospheric tape recorder' (Mote et al., 1996). One viewpoint (e.g. Fueglistaler and Haynes (2005)), apparently consistent with observations such as the 'tape recorder' signal, is that at first order concentrations are determined by temperatures on a relatively large scale, provided it is taken into account that as air parcels undergo slow ascent through the region of the CPT, they sample significant geographical and temporal variability in temperatures. This variability is important in reducing water vapour concentrations below what would be expected from time-mean, e.g. monthly mean, CPT temperatures (Dessler, 1998). To improve on this first-order picture further processes must be invoked, some operating at relatively small scales. One is the microphysics of dehydration, e.g. particle formation and sedimentation. Another is vertical transport through the TTL via convective overshooting, when particularly strong thunderstorm complexes penetrate deep into the TTL on the time scale of a few hours. This provides a secondary pathway into and through the TTL, alongside slow radiative ascent. Rapid transport of air from the lower troposphere deep into the TTL and, more rarely, directly into the TLS, via convective penetration allows for injection of very short-lived species, such as bromine, which influence stratospheric ozone concentration (Keeble et al., 2021). Without rapid convective transport these

species would otherwise play little role in stratospheric chemistry owing to their short lifetimes (Hosking et al., 2010; Robinson and Sherwood, 2006). Convective transport also potentially allows the cold point constraint on water vapour concentrations to be avoided. This can result in increases in water vapour concentrations in the main body of the stratosphere (Jensen et al., 2007) as the additional moisture above the tropical CPT can be transported vertically by the BDC, as illustrated by the 'tape recorder' effect seen in figure 1.4, and quasi-horizontally into the extratropics as illustrated in figure 1.5.

The influence of convective hydration on moisture in the TTL and TLS remains an active area of research. Convective overshoots penetrate into the TTL on timescales on the order of tens of minutes and have horizontal lengthscales on the order of kilometres. The combination of these small-scale flows with the large-scale quasi-horizontal motions of the TTL, and the complex microphysics of moisture transport, makes modelling of convective overshoots a significant challenge. Overshoots are too small to be resolved by global climate models which instead represent their effects with convective parameterisations. There is poor agreement between stratospheric water vapour content predicted by current global climate models and observations (Keeble et al., 2021), with a general tendency for models to underpredict relative to observations, but large variation across models. The extent to which the lack of agreement is caused by poor representation of, or indeed neglect of, convective penetration is not clear.

It is understood that water vapour content in the TLS is primarily governed by temperatures at the CPT, as is evident from the tape recorder where the seasonal cycle imprints on observations. On shorter timescales and in localised regions, convection can exert an influence on moisture which is regarded as second order (Schiller, 2009; Wright et al., 2011). There have been very different approaches to estimating the quantitative contribution of convective hydration to TTL and TLS water vapor. Estimates of the convective contribution to water vapour mass input into the TLS generally lie in the $10 - 20\%$ range, although some estimates are significantly lower than this; table 1.1 summarises recent estimates. The methodology can broadly be categorised into those using Lagrangian trajectory models and those using global storm-resolving models. There are differences in the way that convective 'contribution' is quantified which makes comparison difficult; for example, Schoeberl et al. (2018), Ueyama et al. (2015) and Ueyama et al. (2018) compare predicted water vapour concentrations entering the stratosphere that would be estimated with and without convection, whilst Dauhut and Hohenegger (2022) consider the TLS water vapour budget directly from a

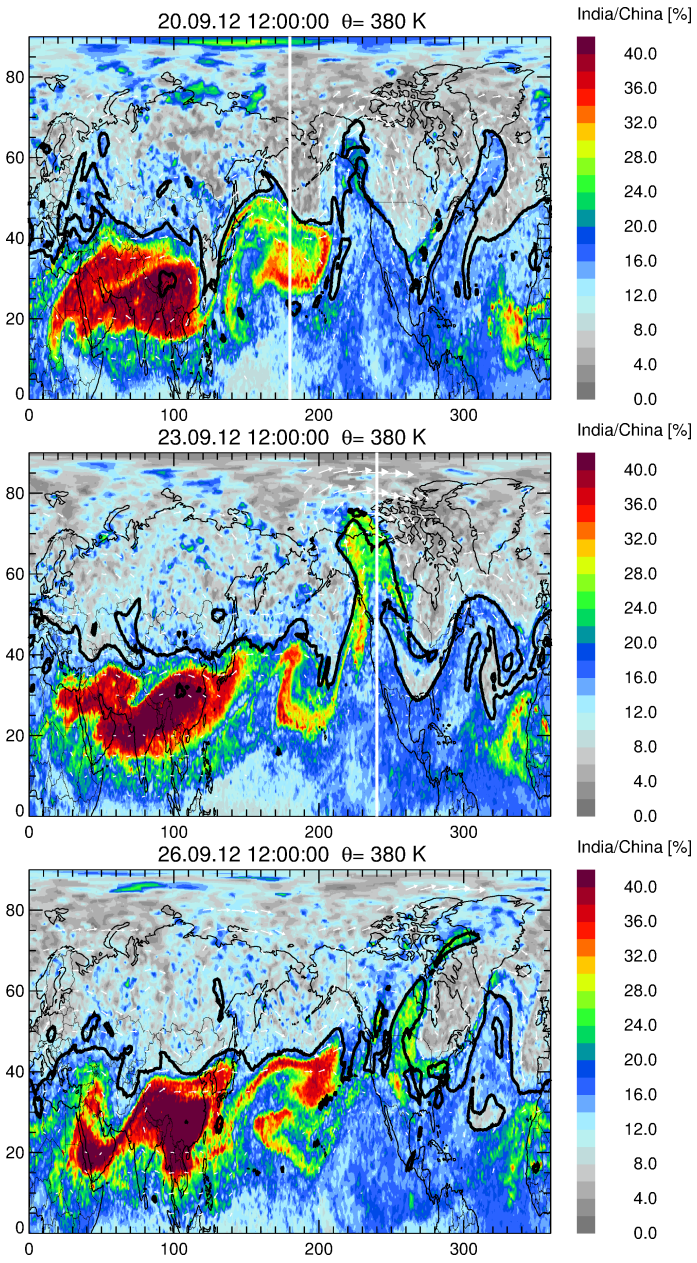

Fig. 1.5 Adapted from Vogel et al. (2016). Horizontal distribution on the 380 K surface of a modelled artificial tracer originating at the surface in the India/China region. This tracer is transported vertically by convection to give an effective localised source in the TTL in the Asian Summer Monsoon, and then horizontally both within the tropics and into the extratropical lower stratosphere. A moisture anomaly arising in the same region, through variation in CPT temperatures, or through convective hydration, would be correspondingly transport and therefore affect overall water vapour concentrations in the stratosphere. Snapshots are shown on 20, 23, and 26 September 2012. The horizontal winds are indicated by white arrows. The 7.2 PVU surface is shown as a thick black line indicating a climatological isentropic transport barrier at 380 K identified by Kunz et al. (2015).

Methodology	Study	Period & domain	Contribution definition	Estimated contribution
Lagrangian trajectory model with simple cloud model	Schoeberl et al. (2014)	boreal winter 2008/09, 60° S to 60° N	Water vapour mass input at 19 km	13%
	Schoeberl et al. (2018)	boreal winter 2008/09, 30° S to 30° N	Net change in water vapour at last convective encounter, with & without convective transport	2%
Lagrangian trajectory model with expensive microphysics scheme	Ueyama et al. (2015)	7-day period in boreal summer 2007, 20°S to 20°N	Net change in water vapour at 100 hPa with & without convection	14%
	Ueyama et al. (2018)	7-day period in boreal winter 2006/07, 10°S to 50°N		15%
Simulation of a single convective system upscaled to tropics	Dauhut et al. (2015)	Full year extrapolated from event in boreal winter 2005, 20°S to 20°N	Water vapour mass input across 100 hPa	18%
Global storm-resolving model	Dauhut and Hohenegger (2022)	40-day period in boreal summer 2016, 10°S to 30°N	Water vapour mass input to 17-20 km altitude	11%

Table 1.1 Estimates of the contribution of convective hydration to the TTL water vapour budget. Note the different methodologies and definitions of convective contribution, which makes comparison between studies difficult. Other than Schoeberl et al. (2018), these estimates support the conclusion that convective overshooting makes a non-negligible but modest contribution.

global storm-resolving model. Estimates are also calculated with varying spatial and temporal domains which might not be expected to agree given the seasonal variation in convective activity and TTL temperatures. Estimates are also sensitive to the choice of cloud microphysics scheme, since the potential for an overshoot to hydrate the TTL relies on sublimation of convectively lofted ice. Similarly, dehydration (by overshooting and also in subsequent quasi-horizontal transit through the TTL) relies on an appropriate representation of the growth of ice particles in a supersaturated and very cold environment (Jensen and Pfister, 2004; Randel and Jensen, 2013).

Lagrangian models calculate trajectories using reanalysis datasets and estimate water vapour transport using a microphysical scheme, some of which are simplified, e.g. Schoeberl et al. (2014, 2018), and some which are more sophisticated and computationally expensive, e.g. Ueyama et al. (2018, 2015). Estimates are limited by the accuracy and resolution of temperature and wind fields used to calculate trajectories, as well as the need to model convective encounters which relies on the resolution and accuracy of cloud models and datasets. It should also be noted that estimates by Ueyama et al. (2018, 2015) are calculated slightly below the CPT rather than deep in the TTL and are therefore difficult to compare with other studies; the contribution may be underestimated since the lower part of the TTL tends to be close to saturation, or overestimated since the number of convective systems that actually penetrate the CPT is much smaller. Global storm-resolving models are capable of resolving individual convective systems and therefore do not rely on parameterisations of convection. Other uncertainties remain, since individual convective overshoots are not fully resolved. Dauhut and Hohenegger (2022) present the first estimate of the vertical water vapour mass flux into the TLS using a global storm-resolving model, with results that are broadly in agreement with many of the trajectory-based estimates.

1.1.2 Other geophysical examples

Further examples of naturally occurring flows involving convective penetration of stable layers arise in the atmosphere. Under certain atmospheric conditions, a layer forms in which the usual decrease of temperature with height in the troposphere reverses, with warm air sitting over cold air. This is called an atmospheric ‘inversion’ and acts to trap air below the warm layer. Inversions can form on small scales, such as in valleys, or on larger scales in the lower troposphere (such as during periods of high atmospheric pressure) or in the mid-troposphere. Figure 1.6 shows an example

Fig. 1.6 An atmospheric inversion visualised by a smoke plume in Lochcarron, Scotland, 30th January 2006. Photograph courtesy of Wikimedia Commons.

of the former case, where the presence of an inversion close to the surface is clearly visualised by the trapping of a smoke plume. This figure also illustrates one of the fundamental aspects of convective penetration: overshooting of the plume as it initially penetrates into the inversion, mixing with its surroundings, followed by subsidence to its neutral buoyancy height. Crucially, the neutral buoyancy height is increased relative to that inferred from properties of the plume at penetration because mixing with the warmer environment increases the buoyancy of mixed fluid parcels in the plume. Over time, shallow convection rising into the inversion gradually mixes cold air from below the inversion with warm air in it, eroding the inversion. Internal waves are generated in the stably stratified layer and transport energy from the convective motions into the inversion (Stull, 1976). Atmospheric inversions that form in the mid-troposphere can act as a 'cap' that prevents deep convective towers from reaching higher altitudes. When the cap is broken, thunderstorms can form. This is a key process in the formation of severe thunderstorm outbreaks and critically depends on turbulent transport and mixing of heat and momentum that occurs during convective penetration of the inversion (Kurbatskii, 2001).

An atmospheric example with particular relevance in recent years is the injection of large quantities of gas and particulates into the stratosphere by volcanic eruptions (Carazzo et al., 2008; Textor et al., 2003) – figure 1.7 shows an example of a volcanic plume penetrating into the stratosphere where strong horizontal winds perturb the plume sideways. Highly explosive events such as Hunga Tonga-Hunga Ha'apai in 2022 can affect the climate on long timescales owing to the significant transport of potent

Fig. 1.7 Plume rising from an eruption of Mount Etna in Sicily, 30th October 2002, photographed from the International Space Station. Photograph courtesy of NASA Earth Observatory.

greenhouses gases like water vapour (Millán et al., 2022). These short, intense eruptions are more faithfully modelled by 'jets', where the vertical velocity dominates buoyancy, and latent heat release from phase changes during ascent plays a more important role than in convective hydration of the TTL. Nonetheless, the flow itself is closely related to convective penetration of a stably stratified layer as the volcanic plume is limited by the strongly stratified stratosphere. In this case, mixing plays a weak role in setting the penetration height (which is more strongly influenced by the initial explosive forcing) but the mixing of tracers into the environment is an important aspect of the transport; understanding the 'detrainment' profile, i.e. the heights at which tracer is mixed into the environment, is an important first step in quantifying the climate impact of these events.

Finally, convective penetration of stably stratified layers is relevant in the open ocean, where mixing between the deep ocean and near-surface water is hindered by the strong vertical density gradients of the thermocline. In some regions, including several locations in high latitude oceans and the Mediterranean Sea, intense buoyancy loss from the ocean surface to the atmosphere results in strong, deep-reaching convection (Herrmann et al., 2008; Marshall and Schott, 1999). The transport of surface water into

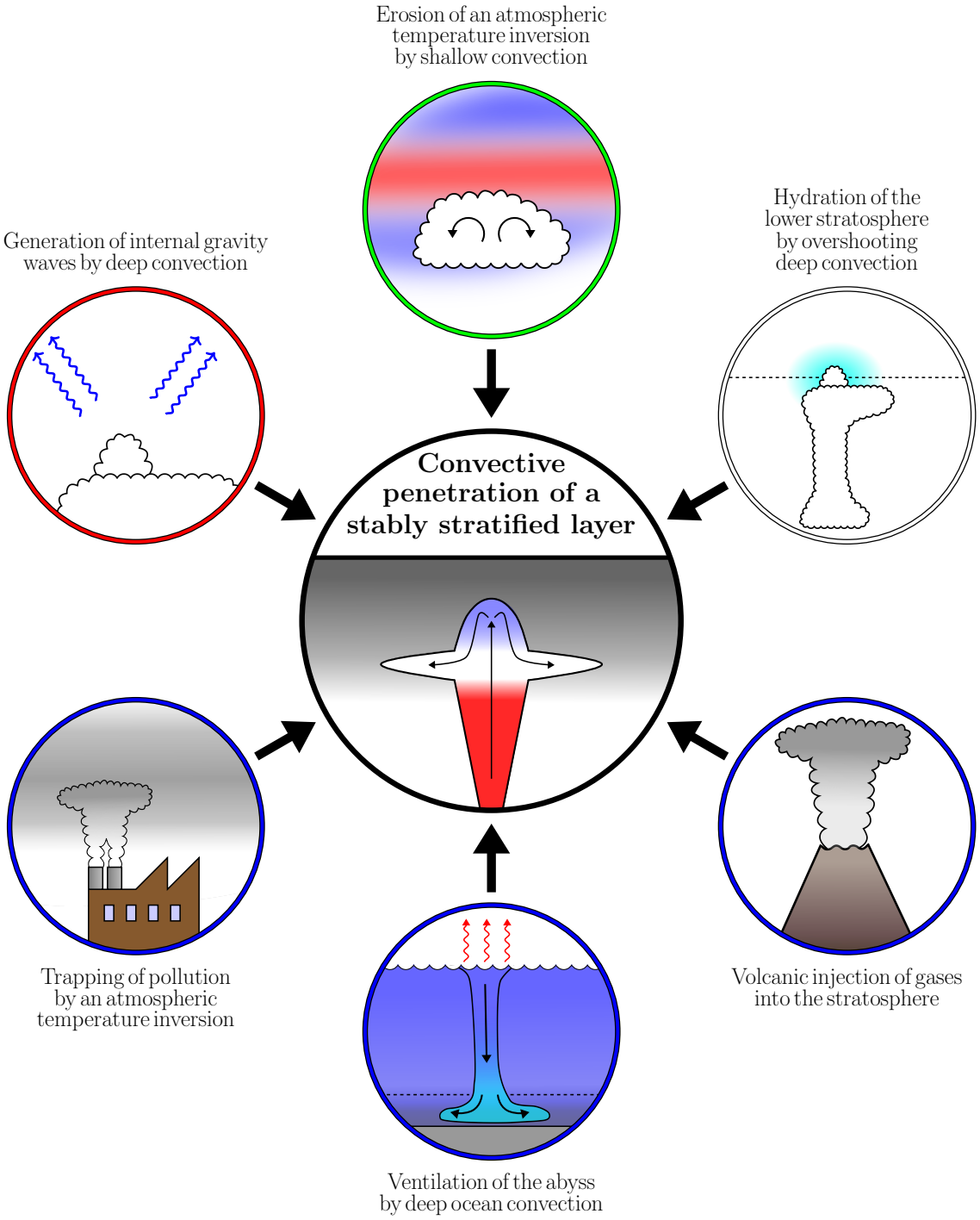

Fig. 1.8 Overview of geophysical problems which can be idealised as convective penetration of a stably stratified layer by a buoyant plume. The colour of each circle indicates the relevant fluid dynamical aspect. Blue: turbulent transport & mixing of passive tracers, considered in chapter 3. Green: turbulent mixing, considered in chapter 3. Red: internal gravity wave generation & propagation, considered in chapter 4. White: a combination of all three aspects – transport and mixing of moist tracers, including the effect of gravity waves, considered in chapters 5 & 6.

the deep ocean sets and maintains the properties of the abyss (Marshall and Schott, 1999), both in terms of the general circulation and also biogeochemical cycles (Ulses et al., 2021). In this flow, tracer transport via turbulent mixing is again a key aspect.

Note that in the examples discussed here there are a wide variety of processes which drive convection, ranging from latent heating in the case of atmospheric convection to buoyancy loss at the surface driving convective plumes in the ocean. The processes which drive convection are not considered relevant to this thesis; these processes determine the conditions of the flow as it penetrates into the stably stratified layer. We focus solely on the flow within the stratified layer given these conditions at penetration. It is therefore unimportant how these conditions are attained. We choose to drive convection by imposing a buoyancy flux, which results in the formation of an approximately axisymmetric plume that transforms into a 'fountain' within the stratified layer – see the following section for a discussion of these terms in detail. Figure 1.8 illustrates the geophysical flows discussed in this introductory chapter which can be understood in part by studying the convective penetration of a buoyant plume into a stably stratified layer. Each example is coloured to indicate the fluid dynamical aspects which are most relevant to the flow in that case: blue indicates turbulent transport & mixing of tracers, green indicates turbulent mixing alone, red indicates the relevance of internal gravity waves, and white indicates the combined relevance of turbulent mixing, tracer transport, and gravity wave generation.

1.2 Plumes & fountains

Here we discuss the structure and behaviour of plumes, i.e. continuous releases of buoyant fluid, and fountains which arise when buoyant plumes rise into stratified environments. We also summarise experimental and theoretical studies of plumes and fountains and examine why relatively few studies address convective penetration experimentally.

The dynamics of a turbulent plume are driven by differences in buoyancy, which determine the acceleration felt by the plume. Entrainment, i.e. mixing of environmental fluid surrounding the plume into the plume itself, modifies the buoyancy difference. In a uniform environment, a buoyant plume entrains denser (less buoyant) fluid from its surroundings, reducing its upward acceleration. The plume eventually ceases to rise once the buoyancy difference tends towards zero. In the presence of a stably stratified environment, where buoyancy increases with height, a plume first rises

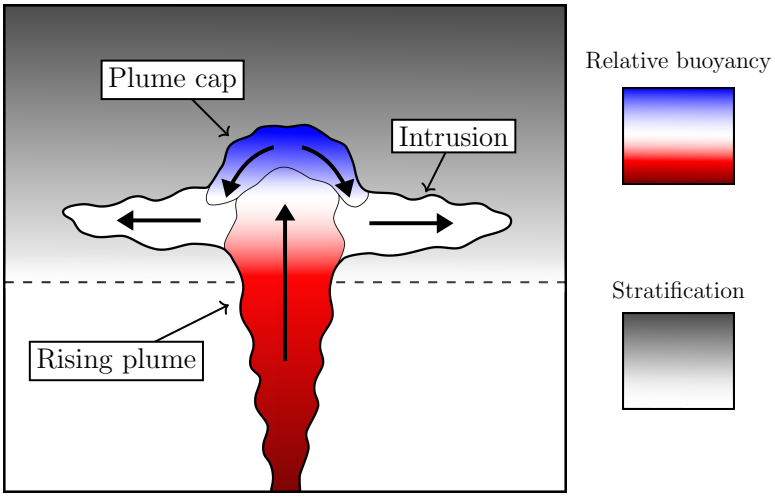

Fig. 1.9 Schematic diagram of the structures of a buoyant plume penetrating into a stably stratified environment. The stratification is represented by grey shading. Colour within the plume represents the buoyancy relative to the environment. The rising plume is more buoyant than its surroundings and rises above its level of neutral buoyancy in the stratified layer. Fluid becomes negatively buoyant in the plume cap and eventually overturns. Fluid subsides towards its level of neutral buoyancy and spreads radially in the intrusion.

through less buoyant surroundings and eventually becomes negatively buoyant relative to the environment. Excess upward momentum causes the plume to overshoot its level of neutral buoyancy and rise to its maximum penetration height where it overturns, producing an additional downward flow component that shrouds the upward flow. The overturning and downward flow can be described as a *fountain*. Mixing between the plume and environment as it rises and overturns reduces the buoyancy difference towards zero at some height below the maximum penetration depth. Here, the flow spreads outwards, forming an *intrusion*. In this thesis, we refer to the upward flow as the *rising plume* and the overturning region as the *plume cap*. For convenience, we will refer to the entire structure as a plume on the understanding that literature referring to a 'fountain' is relevant to the plume dynamics in the stratified layer only. Figure 1.9 illustrates the structures in the plume, with colours indicating the buoyancy of the plume relative to the surrounding stratified environment.

As a canonical example of a turbulent flow, significant attention has been paid to the study of plumes in uniform environments. Plume theory is built upon the *entrainment hypothesis* (Batchelor, 1954; Taylor, 1945) which states that the upward flow in a plume is proportional to the inward radial flow from the environment. The proportionality constant acts a simple measure of turbulent entrainment, quantifying

in dimensionless terms the amount of environmental fluid that is mixed into the plume as it rises. In modern studies, entrainment remains a focus of research and debate since it characterises fundamental aspects of plume behaviour. Modern studies often build on early experimental and theoretical work by Morton et al. (1956) (henceforth MTT) and Priestley and Ball (1955) who developed theoretical models for plumes based on volume and energy conservation, respectively. The canonical MTT plume equations describe the evolution of volume, momentum and buoyancy. The self-similar solutions that arise have been shown to accurately describe experimental observations of plumes in numerous studies and have recently been extended to account for turbulent modifications to self-similar profiles (Craske and van Reeuwijk, 2015). Other modern developments have focussed on understanding the entrainment properties of plumes and fountains in terms of bulk quantities (Hunt and Burridge, 2015; Van Reeuwijk et al., 2016) across a wide range of regimes (Carazzo et al., 2008, 2010; Kaye and Hunt, 2006). Most of these studies focus on a fountain in a uniform environment, where progress has been made in understanding and modelling entrainment at the fountain top (Hunt and Debugne, 2016; Shrinivas and Hunt, 2014) using analytic techniques beyond the MTT plume equations (Debugne and Hunt, 2016) and experimental studies (Talluru et al., 2022). A review of the canonical MTT plume model and current understanding of turbulent transport and entrainment in plumes is given in chapter 2.

The MTT equations are derived under the Boussinesq approximation that density perturbations away from the mean are small. Whilst a definite criterion on the maximum admissible density difference to consider the Boussinesq approximation valid is not clear, studies considering plumes which are significantly more buoyant than their surroundings have been performed using releases of various gases into air. These studies showed that entrainment is smaller in the non-Boussinesq regime (Ricou and Spalding, 1961). However, the majority of experimental and numerical studies consider Boussinesq flows owing to practical constraints. Study also tends to be limited to plumes for which inertia dominates viscosity (high Reynolds number) and advection dominates diffusion (high Péclet number). To our knowledge, the experiments of Ansong and Sutherland (2010) are the only published studies which consider a buoyant plume penetrating from a uniform region into a stably stratified layer. Their results provide a useful benchmark for validating the numerical simulations presented in this thesis. The introduction of a linear stratification does not (significantly) alter the fundamental entrainment properties of a plume but does introduce a dependence on

where the entrainment takes place; plume fluid reaching deeper into the stratified layer can access significantly more buoyant environmental fluid.

Convective penetration of a stably stratified layer appears to be a relatively understudied problem experimentally because of the complexity of maintaining a linearly stratified layer above a uniform layer. Moreover, for practical reasons, most experimental and numerical studies of plumes consider closed domains with two layers of constant buoyancy or a completely stratified environment. This setup permits more straightforward calculation of bulk entrainment properties by considering the time evolution of the interface between the two layers or the stratification profile, respectively. A fundamental limitation in experimental studies of plumes is the difficulty in recording three-dimensional data without disturbing the flow. This is necessary to understand mixing in convective penetration given the spatial inhomogeneity of turbulence in the flow. Numerical simulations – if properly validated – are a powerful solution to this, allowing access to full dynamical fields and straightforward modification of the simulation setup.

1.3 Transport, mixing and wave generation in stratified turbulence

1.3.1 Stratified turbulence

In this thesis we consider the buoyancy-driven flow of a fluid satisfying the non-rotating Navier-Stokes equations. We make the Boussinesq approximation so that changes in the density are small compared to the mean density. In terms of buoyancy, the equivalent assumption is that the magnitude of the acceleration due to buoyancy is much smaller than the gravitational acceleration g. In the atmosphere, this assumption is not appropriate in deep flows where the density can vary over several orders of magnitude. However, when focusing on shallow regions of a flow (as in this thesis, where we focus on the bottom of the stratified layer), the assumption remains valid. The equations of motion for the velocity $\boldsymbol{u}$, pressure p, buoyancy b and passive tracer

ϕ are

$$\frac{\partial \boldsymbol{u}}{\partial t} + \boldsymbol{u} \cdot \nabla \boldsymbol{u} = -\frac{1}{\rho_0} \nabla p + b\hat{\boldsymbol{k}} + \nu \nabla^2 \boldsymbol{u} + \boldsymbol{F}, \tag{1.2}$$

$$\nabla \cdot \boldsymbol{u} = 0, \tag{1.3}$$

$$\frac{\partial b}{\partial t} + \boldsymbol{u} \cdot \nabla b = \kappa_b \nabla^2 b, \tag{1.4}$$

$$\frac{\partial \phi}{\partial t} + \boldsymbol{u} \cdot \nabla \phi = \kappa_\phi \nabla^2 \phi, \tag{1.5}$$

where ν is the molecular viscosity, ρ_0 is a reference density, $\hat{\boldsymbol{k}}$ is the unit vector in the vertical direction z, κ_b is the diffusivity of buoyancy, κ_ϕ is the diffusivity of the passive tracer, and $\boldsymbol{F}$ represents other forcing. Note that in this formulation the pressure p excludes the hydrostatic component $p_h = \rho_0 g z$. We include a passive tracer as it is an important part of our diagnostic approach; mixing of both the buoyancy and passive tracer field is crucial to understanding tracer transport via turbulent mixing.

In a region with background stratification N_0, perturbed fluid parcels are driven back towards their equilibrium height by buoyancy. The competition between inertia and buoyancy is quantified by the bulk Richardson number

$$\mathrm{Ri}_0 = \frac{N_0^2 L^2}{U^2}, \tag{1.6}$$

where U and L are the characteristic velocity and length scales of the mean/large-scale flow. Equivalently, the Froude number,

$$\mathrm{Fr}_0 = \frac{U}{L N_0} = \mathrm{Ri}_0^{-1/2}, \tag{1.7}$$

is the ratio of the buoyancy timescale N_0^{-1} and the advective timescale L/U. The competition between inertial and viscous forces is quantified by the Reynolds number

$$\mathrm{Re} = \frac{UL}{\nu}. \tag{1.8}$$

When Re is large, inertia overcomes viscosity and the flow can become turbulent. Locally, vertical shear generated by turbulence can overcome the stabilising effect of

stratification. This is characterised by the local gradient Richardson number

$$\mathrm{Ri}_g = \frac{\partial_z b}{\left(\frac{\partial u}{\partial z}\right)^2 + \left(\frac{\partial v}{\partial z}\right)^2}, \tag{1.9}$$

where u and v are the horizontal components of velocity and $\partial_z b$ is the vertical buoyancy gradient. Note that Ri_g is an equivalent formulation to Ri_0 except using local measures of the buoyancy and velocity.

In summary, in flows with $\mathrm{Ri}_0 \gtrsim 1$ and sufficiently large Re, buoyancy has a leading order influence and the stratification acts to stabilise the flow on large scales. Locally, turbulence overcomes this stabilising effect when $\mathrm{Ri}_g \lesssim 1/4$. In these regions, turbulent transport and mixing can be significantly enhanced. We refer to this regime as *stratified turbulence*.

1.3.2 Turbulent transport and mixing

In stably stratified flows, motion tends to follow surfaces of constant density (equivalently, constant buoyancy) called isopycnals, since it is energetically preferable to avoid doing work against buoyant forces. Horizontal and vertical motions are distinguished by introducing a vertical lengthscale $L_v = U/N_0$ and corresponding velocity scale U_v defined in terms of L_v and the timescale of horizontal motion L/U, giving $U_v = U^2/(N_0 L)$ (Billant and Chomaz, 2001). The relevant Reynolds number is then $L_v U_v/\nu = U^3/(L N_0^2 \nu)$ which scales with the buoyancy Reynolds number

$$\mathrm{Re}_b = \frac{\varepsilon}{\nu N^2}, \tag{1.10}$$

since the viscous dissipation rate of turbulent kinetic energy (TKE; Kolmogorov (1941)), ε, scales as $\varepsilon \sim U^3/L$. In this 'strongly stratified' regime where $L_v \ll L$, the turbulent transport of density and tracers is predominantly determined by *diapycnal* transport perpendicular to isopycnals which tend to be horizontal. The diapycnal flux of a quantity ψ is then approximately $\overline{w'\psi'}$ where $w' = w - \overline{w}$ is the turbulent component of the vertical velocity (similarly for ψ') and the overbar represents an appropriate large-scale temporal and spatial average. The diapycnal flux is a useful measure of mixing on large temporal and spatial scales. However, the assumption that isopycnals are flat is often invalid on shorter timescales, especially where convective instability (or otherwise) significantly perturbs isopycnals. Moreover, a complete picture of tracer

transport in stratified flows depends not only on mixing of the tracer itself, but also mixing of the buoyancy of fluid parcels since this determines the height at which tracers will settle once the flow is 'resorted' as isopycnals relax following transient perturbations. For these reasons we will consider the joint effect of mixing on both buoyancy and tracer concentration further in chapter 3.

An alternative view of turbulent mixing follows from an energetic perspective; the two-step process of stirring and diffusion involves dissipation of kinetic energy to stir the fluid, which sharpens density and scalar gradients, and dissipation of potential energy as density gradients are eroded by diffusion. Of the energy feeding a turbulent mixing 'event', some goes toward irreversible mixing and the remainder is dissipated viscously. The fraction of energy actually resulting in mixing is quantified by the *mixing efficiency* (Davies Wykes et al., 2015; Peltier and Caulfield, 2003). This quantity is calculated by utilising the partitioning of potential energy in a stratified flow into background potential energy, which is not available to do work, and available potential energy which is stored in the buoyancy field and can be irreversibly converted into background potential energy by turbulent mixing (Lorenz, 1955). See chapter 3 for further discussion of mixing efficiency.

1.3.3 Internal waves

The presence of turbulence in a stably stratified fluid has been noted to generate internal gravity waves in a wide variety of flows, including turbulent boundary layers (Taylor and Sarkar, 2007), shear layers (Sutherland and Linden, 1998), gravity currents (Flynn and Sutherland, 2004) and grid-generated turbulence (Linden, 1975). In the (stratified) atmosphere and ocean, internal gravity waves are studied in part because of their influence on the global circulation. In the ocean interior, the mixing from breaking internal gravity waves is needed to balance upwelling in the ocean interior and close the global ocean circulation. In the atmosphere, internal waves can affect the circulation by transporting momentum from the region in which they are generated to a distant region where waves can influence the flow via several mechanisms, e.g. wave breaking or critical-layer absorption.

The detailed mechanism for wave generation by convection is not well understood. Three main mechanisms have been identified: the mechanical oscillator effect (Pierce and Coroniti, 1966), the obstacle effect (Clark et al., 1986) and the deep heating effect (Pandya and Alexander, 1999). Some studies have concluded that a single mechanism

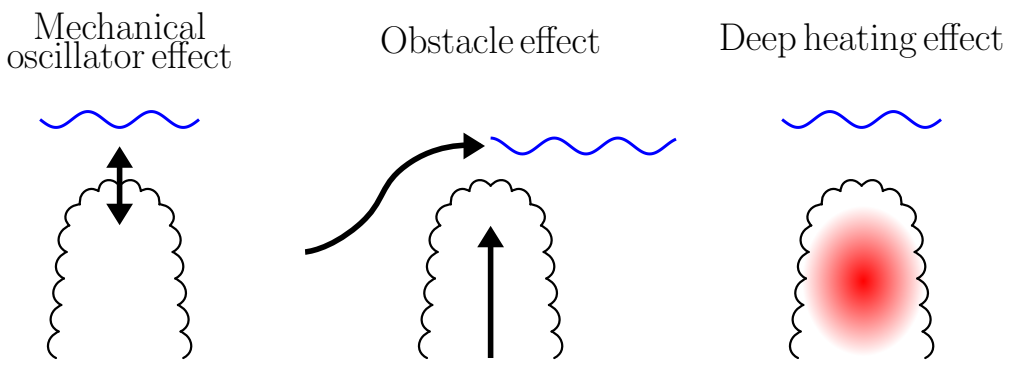

Fig. 1.10 Schematic diagram of the three main mechanisms proposed for convective generation of gravity waves.

is primarily responsible for generating the gravity waves (Clark et al., 1986) but more recent reviews (e.g. Fritts and Alexander (2003)) conclude that all mechanisms are important and each one can explain observations in certain contexts. The mechanisms are illustrated in figure 1.10. In the mechanical oscillator effect, vertical oscillations of the central updraft of a convective cell around its level of neutral buoyancy (in the upper troposphere) excites gravity waves in the overlying stratosphere. This is analogous to the generation of internal gravity waves by an oscillating rigid body (e.g. Kataoka et al. (2017)). In the obstacle effect, the central updraft acts as an obstacle to a surrounding large-scale horizontal flow across the cloud tops, generating waves in an analogous way to flow over topography. Finally, the deep heating effect suggests that internal waves can be understood as the linear response to a time- and space-dependent thermal forcing (e.g. from latent heat release).

As introduced in § 1.2, Ansong and Sutherland (2010) present an experimental study of a plume penetrating into a stably stratified layer. In the absence of a large-scale horizontal flow, and with no latent heating in the experiment (which used salt water to generate the buoyant plume), the mechanical oscillator effect is the remaining mechanism that could explain the generation of internal waves by the plume. However, their results suggest that the motion of the top of a convective plume penetrating a stably stratified layer cannot be the source of internal waves since there is a mismatch between the oscillation frequency of the plume top and the frequency of the waves themselves. The mechanisms introduced above do not rely on the presence of turbulence to explain the generation of internal waves. Recent numerical simulations of convective plumes penetrating into a very strongly stratified layer have shown that turbulent

Reynolds stresses within the convective region better explain the excitation of internal waves compared with perturbation of the stratified layer interface (Lecoanet et al., 2015). However, application of this theory to a less strongly stratified regime is difficult since there is no scale separation between the waves and turbulence. Further discussion of internal waves and their generation mechanism can be found in chapter 4.

1.4 Numerical methods

Turbulence is characterised by a separation between the large scales on which energy enters the flow and the small scales at which energy is dissipated by viscosity, with a cascade of energy through the statistically isotropic intermediate scales. The smallest features in a turbulent flow appear close to the Kolmogorov length scale,

$$\eta_k \sim \left(\frac{\nu^3}{\varepsilon}\right)^{1/4}, \tag{1.11}$$

whilst the fastest evolving features arise on a timescale

$$t_{\eta_k} \sim \left(\frac{\nu}{\varepsilon}\right)^{1/2}. \tag{1.12}$$

In order to fully represent turbulence with minimal numerical artefacts, simulations must resolve these scales. A simulation with sufficient temporal and spatial resolution to achieve this is called a direct numerical simulation (DNS). In flows with a wide range of scales, DNS is computationally expensive and has only recently become feasible (Alfonsi, 2011). Consequently, there are relatively few direct numerical simulations of plumes (Craske, 2016) and, to our knowledge, none which consider convective penetration into a stably stratified layer.

Large-eddy simulation (LES) avoids the computationally prohibitive resolution requirement by only resolving scales larger than some prescribed lengthscale, termed the 'filter width'. The effect of sub-filter scales on the resolved flow are modelled using a *parameterisation scheme*. In contrast to DNS, there are many examples of plumes simulated using LES (e.g. Devenish et al. (2010); Pham et al. (2007)). The optimal choice of filter width is debated (Verstappen, 2018) but typically chosen to match the numerical grid spacing, in which case we refer to the parameterisation scheme as a *sub-grid-scale* (SGS) model. Large-eddy simulations represent three-dimensional turbulence with a good level of accuracy, yet can be performed with a practical level

of computational cost. However, the turbulence characteristics can be sensitive to the choice of SGS model. Consequently, it is important to carefully consider the intended regime for which an SGS model has been developed. For example, the earliest 'eddy-viscosity' models (Smagorinsky, 1963) were designed for fully turbulent flows and therefore perform poorly when the flow transitions between laminar and turbulent states. Similarly, many SGS models make crude assumptions on the SGS diffusivity κ_{SGS} for scalar fields including buoyancy. The SGS diffusivity represents turbulent transport on the smallest scales. The simplest models invoke Reynolds' analogy – that SGS Prandtl number $\mathrm{Pr}_{\mathrm{SGS}} = \nu_{\mathrm{SGS}}/\kappa_{\mathrm{SGS}} = 1$ – thus prescribing the SGS diffusivity as equal to the SGS viscosity, which represents transport of momentum on the smallest scales. The assumption is that both momentum and scalar transport largely depend on the same turbulent eddies. In flows where the turbulent transport of tracers is of central importance, such as in this thesis, the assumption of Reynolds' analogy is insufficient for a complete description of the flow.

Numerical simulations of convective penetration events have been performed using realistic and complex meteorological models (Dauhut et al., 2015, 2018) containing many physical processes but these are computationally expensive and challenging to interpret. Our approach is to use numerical models of an idealised flow first to understand the underlying processes that influence turbulent mixing and wave generation. Later, we introduce a moist parameterisation that represents only the essential microphysical processes involved in convective hydration of the TTL. Unlike in comprehensive models of moisture, we neglect latent heating and represent only the vapour and solid (ice) phases of water. In the TTL, the extremely cold temperatures mean vapour concentrations are small so latent heating is negligible and condensed water vapour rapidly freezes into ice that sediments downwards. Our approach sacrifices realism in favour of computational simplicity, allowing exploration of a broader parameter space. We choose to neglect complicating factors such as complex environmental profiles of moisture and temperature, faithful representation of the processes driving atmospheric convection, and detailed representations of microphysical processes such as sedimentation. An underlying assumption is that processes below the TTL simply act to set conditions at penetration into the TTL and need not be modelled exactly. The use of an idealised representation of the problem means that our results are more easily interpreted and we gain clarity on the interaction between different processes.

1.5 Overview of results chapters

The study of a buoyant plume generated in a uniform region rising into a stably stratified layer is linked to a multitude of geophysical, industrial and fluid dynamical problems. However, the literature has focused on characterising bulk entrainment properties of similar fountain-like flows and identifying the spectral properties of internal waves generated by convective penetration. With respect to turbulent transport of tracers, mixing characteristics, and wave generation, it is a relatively understudied problem. In this thesis, we address the gap in the literature using large-eddy simulations. In chapter 2 we validate the capability for the chosen numerical method to faithfully represent a plume. Following a detailed description of the numerical method, we extensively compare an LES of a plume in a uniform environment with recent DNS results (Craske, 2016; Van Reeuwijk et al., 2016) to show that the plume dynamics and turbulent statistics are consistent with theoretical expectations. We then validate simulations with a stratified layer by comparing characteristic plume quantities with experimental results from Ansong and Sutherland (2010).

In chapter 3 we introduce a method of examining turbulent transport and mixing in convective penetration by forming a joint distribution of tracer concentration and buoyancy with units of volume. Whilst this does not determine the diapycnal flux explicitly, our diagnostic approach offers a more complete picture of the way in which a plume mixes with a surrounding stratified environment compared to estimates of diapycnal transport or detrainment profiles alone. Using the buoyancy-tracer volume distribution, we develop a method for objectively partitioning plume fluid in buoyancy-tracer space into three regions, each of which corresponds to a coherent region in physical space. Specifically, we identify a 'source' region where undiluted plume fluid enters the stratified layer, a 'transport' region where much of the transition from undiluted to mixed fluid occurs in the plume cap, and an 'accumulation' region corresponding to a radially spreading intrusion. This method enables quantification of different measures of turbulence and mixing within each of the three regions, including potential energy and turbulent kinetic energy dissipation rates, an activity parameter, and the instantaneous mixing efficiency. We find that the most intense buoyancy gradients lie in a thin layer at the cap of the penetrating plume. This provides the primary stage of mixing between plume and environment and exhibits a mixing efficiency around 50%. Newly generated mixtures of environmental and plume fluid join the intrusion and experience relatively weak turbulence and buoyancy gradients. As the intrusion spreads

radially, environmental fluid surrounding the intrusion is mixed into the intrusion with moderate mixing efficiency. This dominates the volume of environmental fluid entrained into the region containing plume fluid. However, the 'strongest' entrainment, as measured by the specific entrainment rate, is largest in the plume cap where the most buoyant environmental fluid is entrained.

In chapter 4 we address the generation of internal waves by convective penetration of a stably stratified layer. First, we establish the spectral properties of the flow at a range of heights with the squared buoyancy frequency varied over two orders of magnitude. Consistent with laboratory studies (Ansong and Sutherland, 2010), we identify a broad-banded frequency spectrum inside the plume which becomes narrow-banded, close to the buoyancy frequency, above the plume. Motivated by the success of a viscous dissipation model in explaining the spectrum of internal waves generated by a turbulent boundary layer (Taylor and Sarkar, 2007), we apply the model to our axisymmetric wave geometry. We find that the model captures the decay in spectral power and selection of high frequencies when initialised from a turbulent spectrum within the plume. We then use the Dynamic Mode Decomposition (DMD, Schmid (2010)) to extract flow structures associated with internal wave frequencies and use ray tracing to show that the internal wave beams apparent above the plume can be traced to a source inside the plume. Our results are compared with the strongly stratified regime where convective plumes do not penetrate into the stratified layer (Couston et al., 2018); we identify a transition between this 'scouring' regime, which does not exhibit frequency selection, with the 'penetrative' regime we consider.

In chapters 5 and 6 we focus attention on convective hydration of the TTL. In chapter 5, we review the essential processes involved in hydration of the TTL via convective overshoots and formulate a minimal moisture model which captures these processes. We then explore the regimes that arise in the model of moist convection and use a modified version of the buoyancy-tracer volume distribution in chapter 3 to understand the combined effect of the hydration mechanism on buoyancy, vapour concentration, and ice concentration. In chapter 6 we consider a set of experiments designed to explore the interaction between sedimentation, mixing, convective forcing, and large-scale vertical shear in the stratified layer. For a given convective forcing, the total hydration is determined by the competition between sedimentation, which settles ice out of the plume, and mixing which acts to convert ice into vapour once cold plume fluid and warm environmental fluid mix. Convective forcing increases the total hydration by raising the maximum penetration height and carrying more vapour.

Vertical shear also increases total hydration, by promoting small-scale turbulent mixing via shear instabilities and internal wave breaking. Whilst the mixing efficiency is unaffected by convective forcing, vertical shear increases the efficiency in a critical range of shear rates and otherwise decreases efficiency since mixing becomes primarily shear-driven rather than buoyancy-driven. Finally, we show that vertical shear plays a weak role in driving vertical displacement of fluid parcels, questioning its role in generating above-anvil cirrus plumes in the TTL.

Chapter 2

Large-eddy simulations of a buoyant plume

2.1 Integral plume theory

The rise of a buoyant plume into a uniform environment is a canonical example of a 'self-similar' flow, meaning that far from the plume source and ignoring molecular effects, radial profiles of the flow variables collapse onto a single curve when the radial coordinate r (measured from the plume centreline), vertical velocity w and buoyancy b are normalised by characteristic scales r_m, w_m and b_m respectively. The scale r_m represents the plume radius whilst the scales w_m and b_m represent half of the vertical velocity and buoyancy on the plume centreline, respectively. These scales can be defined in several ways, often exploiting the experimental observation that the mean velocity and buoyancy profiles are well represented by a Gaussian curve (List, 1982; Papanicolaou and List, 1988; Shabbir and George, 1994). An approach independent of this observation is to define the scales in terms of integral quantities of the flow, namely the integral volume flux Q, specific momentum flux M and buoyancy flux F_b defined as

$$Q = 2\int_0^\infty \overline{w} r \,\mathrm{d}r, \quad M = 2\int_0^\infty \overline{w}^2 r \,\mathrm{d}r, \quad F_b = 2\int_0^\infty \overline{w}\overline{b} r \,\mathrm{d}r, \tag{2.1}$$

where $\bar{\cdot}$ represents an appropriate temporal and spatial average. Owing to the approximate axisymmetry of a plume, the spatial component is chosen to be an azimuthal average. The temporal average is taken over a sufficiently long period to smooth turbulent fluctuations. For a plume carrying a passive tracer with concentration ϕ we

can also define the tracer flux F_ϕ as

$$F_\phi = 2\int_0^\infty \overline{w}\overline{\phi} r \,\mathrm{d}r. \tag{2.2}$$

These integral quantities fully determine the plume dynamics and depend on the vertical coordinate z only. In terms of these quantities the characteristic scales are

$$r_m \equiv \frac{Q}{M^{1/2}}, \quad w_m \equiv \frac{M}{Q}, \quad b_m \equiv \frac{F_b}{\theta_m Q}, \quad \phi_m \equiv \frac{F_\phi}{\theta_m Q}, \tag{2.3}$$

where θ_m is a dimensionless profile coefficient that alters the shape of the buoyancy (and tracer) radial profiles relative to the velocity profile. In turbulent 'pure' plumes, $\theta_m \sim 1$, meaning the buoyancy, tracer and vertical velocity profiles have the same radial width. Here, we have introduced the characteristic scale ϕ_m for the passive tracer concentration. As with w_m and b_m, this represents half of the tracer concentration on the plume centreline. Note that the fluxes Q, M, F_b and F_ϕ are the scaled rather than actual integral fluxes; a factor of π is neglected for convenience (Van Reeuwijk et al., 2016). The fluxes are governed by equations which we refer to as the MTT plume equations henceforth. These are derived by radially integrating the axisymmetric Boussinesq equations (e.g. Craske (2016)) for conservation of mass, momentum, buoyancy and energy, giving

$$\frac{\mathrm{d}Q}{\mathrm{d}z} = 2\alpha M^{1/2}, \tag{2.4}$$

$$\frac{\mathrm{d}}{\mathrm{d}z}\left(\beta_g M\right) = \frac{F_b Q}{\theta_m M}, \tag{2.5}$$

$$\frac{\mathrm{d}}{\mathrm{d}z}\left(\frac{\theta_g}{\theta_m}F_b\right) = -N^2 Q, \tag{2.6}$$

$$\frac{\mathrm{d}}{\mathrm{d}z}\left(\gamma_g \frac{M^2}{Q}\right) = 2F_b + \delta_g \frac{M^{5/2}}{Q^2}. \tag{2.7}$$

The (passive) tracer flux F_ϕ evolves identically to F_b. Here, N^2 is the buoyancy frequency associated with the ambient fluid, which may be constant or depend on z, and α is the entrainment coefficient. As discussed in §1.2, this coefficient arises from the entrainment hypothesis of Taylor (1945) which relates the radial inflow to the upward flux. In particular, α is defined by

$$-\left[ru\right]_{r=\infty} = \alpha r_m w_m, \tag{2.8}$$

at any given height z. In a fully developed plume, α is approximately constant with height. An equivalent definition of the entrainment coefficient α in terms of fluxes follows from using the definitions of r_m and w_m with (2.4), giving

$$\alpha = \frac{1}{2M^{1/2}}\frac{\mathrm{d}Q}{\mathrm{d}z} = \frac{1}{2r_m w_m}\frac{\mathrm{d}Q}{\mathrm{d}z}, \tag{2.9}$$

which suggests that α can be interpreted as half of the normalised increase in volume flux per unit r_m. This supports the interpretation of α as measuring dilution of the plume.

The remaining parameters $\beta, \theta, \delta, \gamma$ in the MTT plume equations are 'profile coefficients' describing the relative shape of the self-similar profiles (Van Reeuwijk and Craske, 2015) and are associated with the dimensionless momentum flux, buoyancy flux, turbulence and energy flux respectively. These parameters account for, in a radially averaged sense, the (non-dimensionalised) eddy terms neglected in deriving the MTT plume equations. The subscripts m, f and p refer to contributions from the mean flow, turbulence and pressure respectively. Full details on their definition are given in Van Reeuwijk and Craske (2015). For our purposes, we simply note that in a fully developed self-similar plume these coefficients are constant.

The MTT plume equations form an initial value problem which, given source conditions, fully specifies the evolution of the integral quantities of a plume. Notionally, this requires specifying source values of the fluxes Q, M and F_b. However, to simplify the expressions it is convenient to instead prescribe the source radius r_0 and values $w_m(0) = \frac{1}{2}w_0, b_m(0) = \frac{1}{2}b_0$ which are related to values of the vertical velocity w_0 and buoyancy b_0 on the plume centreline at the source. We then assume Gaussian profiles

$$w(z=0,r) = 2w_m(0)\exp\left[-2\frac{r^2}{r_0^2}\right], \quad b(z=0,r) = 2b_m(0)\exp\left[-2\frac{r^2}{r_0^2}\right], \tag{2.10}$$

yielding source fluxes

$$Q_0 = w_m(0)r_0^2, \quad M_0 = w_m(0)^2 r_0^2, \quad F_0 = w_m(0)b_m(0)r_0^2. \tag{2.11}$$

For the tracer concentration, we specify a source value $\phi_m(0) = \frac{1}{2}\phi_0$ such that the source tracer flux $F_0^{(\phi)} = w_m(0)\phi_m(0)r_0^2$.

The behaviour of a plume depends on the balance between buoyancy and inertia. This is quantified by the flux balance parameter Γ introduced by Morton (1959) and

defined as

$$\Gamma = \frac{5F_bQ^2}{8\alpha\beta_g\theta_m M^{5/2}} = \frac{\mathrm{Ri}}{\mathrm{Ri}_p}. \tag{2.12}$$

The parameter can be interpreted as a Richardson number $\mathrm{Ri} = b_m r_m / w_m^2$ normalised by the Richardson number for a 'pure' plume $\mathrm{Ri}_p = 8\alpha\beta_g/5$. The term 'pure' plume refers to the stable equilibrium $\Gamma = 1$ where the source momentum and buoyancy fluxes are balanced (Hunt and Kaye, 2005). A 'forced' plume has $0 < \Gamma < 1$ implying an excess of momentum at the source. A jet, which may be thought of as a zero-buoyancy plume, has $\Gamma = 0$. As shown by Hunt and Kaye (2005), given source conditions for a pure plume, there is an adjustment region above the source in which pure plume conditions are reached.

2.2 Numerical scheme

2.2.1 Governing equations and SGS model

All simulations performed as part of this thesis are carried out using the non-hydrostatic computational fluid dynamics code `DIABLO` originally developed by Taylor (2008) and Bewley (2019). `DIABLO` evolves a discrete approximation of the Boussinesq Navier-Stokes equations with coupled buoyancy and tracer evolution equations using a pseudo-spectral method in the horizontal directions with periodic boundary conditions and finite difference in the vertical direction with fixed wall boundaries. A 2/3 dealiasing rule is applied when transforming from Fourier to physical space. The wall-bounded vertical direction is treated with a central second-order finite-difference spatial discretisation. A third-order mixed implicit/explicit Runge-Kutta/Crank-Nicolson scheme is used for time-stepping. The code is parallelised using MPI which significantly increases computational efficiency.

To aid in the examination of the flow evolution and mixing, we include a passive tracer ϕ that satisfies the same evolution equation as buoyancy with the same diffusivity. The scalar field $\phi(\boldsymbol{x}, t)$ represents the (dimensionless) tracer concentration. The tracer is passive in the sense that it has no coupling with the momentum equation, so follows the flow and does not influence it. The tracer concentration is initially set to zero and forced in the plume in the same way as the buoyancy. This allows us to use the tracer to track fluid originating from the plume. In chapters 5 and 6 we introduce

additional passive tracers to model the presence of moisture; modifications to the governing equations are discussed in chapter 5.

We use the anisotropic minimum dissipation (AMD) scheme for the SGS model, developed by Rozema et al. (2015) following Abkar et al. (2016) and modified by Abkar and Moin (2017) to explicitly calculate the SGS viscosity and diffusivity (for buoyancy as well as passive & non-passive tracers) and SGS viscosity which captures the effect of unresolved scales. The AMD scheme is extensively validated in Vreugdenhil and Taylor (2018). Given a characteristic lengthscale L and timescale T, the non-dimensional governing equations for velocity $\boldsymbol{u}$, buoyancy b and tracer ϕ including sub-grid-scale (SGS) contributions are

$$\nabla \cdot \widehat{\boldsymbol{u}} = 0, \tag{2.13}$$

$$\frac{\mathrm{D}\widehat{\boldsymbol{u}}}{\mathrm{D}t} + \nabla \widehat{p} = \frac{1}{\mathrm{Re}} \nabla^2 \widehat{\boldsymbol{u}} + \widehat{b}\hat{\boldsymbol{k}} - \nabla \cdot \boldsymbol{\tau} + f_w, \tag{2.14}$$

$$\frac{\mathrm{D}\widehat{b}}{\mathrm{D}t} = \frac{1}{\mathrm{RePr}} \nabla^2 \widehat{b} - \nabla \cdot \boldsymbol{\lambda}_b + f_b, \tag{2.15}$$

$$\frac{\mathrm{D}\widehat{\phi}}{\mathrm{D}t} = \frac{1}{\mathrm{RePr}} \nabla^2 \widehat{\phi} - \nabla \cdot \boldsymbol{\lambda}_\phi + f_\phi, \tag{2.16}$$

where $\widehat{\cdot}$ indicates filtering at the resolved grid scale and $\hat{\boldsymbol{k}}$ is the unit vector in the vertical direction. The terms f_w, f_b and f_ϕ represent the forcing applied to the vertical velocity, buoyancy and passive tracer to generate the buoyant plume. The details of this forcing are discussed in §2.2.3. The SGS stress tensor $\boldsymbol{\tau}$ has components $\tau_{ij} = \widehat{u_i u_j} - \widehat{u}_i \widehat{u}_j$, the SGS buoyancy flux is $\boldsymbol{\lambda}_b = \widehat{\boldsymbol{u}b} - \widehat{\boldsymbol{u}}\widehat{b}$ and similarly the SGS tracer flux is $\boldsymbol{\lambda}_\phi = \widehat{\boldsymbol{u}\phi} - \widehat{\boldsymbol{u}}\widehat{\phi}$. The eddy-viscosity model for the deviatoric component of the SGS stress $\boldsymbol{\tau}^d$ and the SGS buoyancy and tracer flux are

$$\tau_{ij}^d = \tau_{ij} - \frac{1}{3}\delta_{ij}\tau_{kk} = -2\nu_{\mathrm{SGS}}\widehat{S}_{ij}, \tag{2.17}$$

$$\boldsymbol{\lambda}_b = -\kappa_{\mathrm{SGS}}^{(b)} \nabla \widehat{b}, \tag{2.18}$$

$$\boldsymbol{\lambda}_\phi = -\kappa_{\mathrm{SGS}}^{(\phi)} \nabla \widehat{\phi}, \tag{2.19}$$

where ν_{SGS}, $\kappa_{\mathrm{SGS}}^{(b)}$ and $\kappa_{\mathrm{SGS}}^{(\phi)}$ are the non-dimensional SGS viscosity, SGS buoyancy diffusivity and SGS tracer diffusivity respectively. The term $\widehat{S}_{ij}$ is the non-dimensional resolved shear-rate tensor

$$\hat{S}_{ij} = \frac{1}{2}\left(\partial_i \hat{u}_j + \partial_j \hat{u}_i\right). \tag{2.20}$$

The SGS viscosity and diffusivities are determined by the AMD scheme as described in Vreugdenhil and Taylor (2018). Assuming the flow is not very strongly stratified, then

$$\nu_{\mathrm{SGS}} = (C\delta)^2 \frac{\max\{-(\tilde{\partial}_k \tilde{u}_i)(\tilde{\partial}_k \tilde{u}_j)\tilde{S}_{ij}, 0\}}{(\tilde{\partial}_l \tilde{u}_m)(\tilde{\partial}_l \tilde{u}_m)}, \tag{2.21}$$

$$\kappa^{(b)}_{\mathrm{SGS}} = (C\delta)^2 \frac{\max\{-(\tilde{\partial}_k \tilde{u}_i)(\tilde{\partial}_k \hat{b})\tilde{\partial}_i \hat{b}, 0\}}{(\tilde{\partial}_l \tilde{u}_m)(\tilde{\partial}_l \tilde{u}_m)}, \tag{2.22}$$

where $C^2 = 1/12$ is a modified Poincaré constant, $\tilde{\partial}_i \tilde{u}_j = (\delta_i/\delta_j)\partial_i \hat{u}_j$, δ_i is the filter width in the x_i-direction and all variables are non-dimensional. Here, the normalised non-dimensional strain-rate tensor is

$$\tilde{S}_{ij} = \frac{1}{2}\left(\tilde{\partial}_i \tilde{u}_j + \tilde{\partial}_j \tilde{u}_i\right). \tag{2.23}$$

The SGS tracer diffusivity $\kappa^{(\phi)}_{\mathrm{SGS}}$ is calculated with $\hat{b}$ replaced by $\hat{\phi}$ in (2.22). The choice of filter widths δ_i depends on the grid discretisation; we use $\delta_i = 3\Delta x_i$ (see Vreugdenhil and Taylor (2018) for a full discussion on this choice). The SGS diffusivities and viscosity may locally exceed the molecular values by several orders of magnitude in regions with intense turbulence.

The two dimensionless parameters appearing in the non-dimensional governing equations (2.13)–(2.16) are the Reynolds number and Prandtl number,

$$\mathrm{Re} = \frac{UL}{\nu}, \quad \mathrm{Pr} = \frac{\nu}{\kappa}, \tag{2.24}$$

respectively, where ν is the molecular viscosity, κ is the molecular diffusivity for both b and ϕ and we assume that the velocity scale is $U = L/T$. The form of the Reynolds number depends on the choice of characteristic lengthscale L and timescale T. As discussed in §2.1, plumes can be characterised solely by their source radius r_0 and values of the vertical velocity and buoyancy at the source which together yield the integral source buoyancy flux $F_0 = F(z = -H)$ with units $[F_0] = L^4T^{-3}$. The choice of F_0 and r_0 for non-dimensionalising gives the plume Reynolds number $\mathrm{Re}_{\{F_0,r_0\}} = (F_0 r_0^2)^{1/3}/\nu$ with a velocity scale $U_{\{F_0,r_0\}} \sim (F_0/r_0)^{1/3}$ and timescale $T_{\{F_0,r_0\}} \sim r_0/U$. The 'turnover time' $T_{\{F_0,r_0\}}$ may be interpreted as the time for an eddy to become significantly distorted by the plume in the absence of stratification. In a linearly stratified environment, a more natural choice for non-dimensionalising is the integral source buoyancy flux F_0 and the (constant) environmental buoyancy frequency N_0. This yields a lengthscale

$L_{\{F_0,N_0\}} = F_0^{1/4} N_0^{-3/4}$ and timescale $T_{\{F_0,N_0\}} = N_0^{-1}$ which we use henceforth. The timescale is the buoyancy period, i.e. the time for a fluid parcel perturbed from the initial stratification to return to its equilibrium position. The lengthscale $L_{\{F_0,N_0\}}$ naturally arises from the MTT plume equations (2.4)–(2.7) in a stably stratified environment. Following previous experimental and numerical studies (e.g Briggs (1965); Devenish et al. (2010)), both the maximum height of the plume $z_{\max}$ and the height of the intrusion z_n above the base of the stratification (illustrated in figure 2.1) scale with $L_{\{F_0,N_0\}}$. With this choice of non-dimensionalisation, the Reynolds number takes the form

$$\mathrm{Re} = \frac{F_0^{1/2}}{\nu N_0^{1/2}}. \tag{2.25}$$

The tracer concentration ϕ is naturally non-dimensional and could be scaled to match expected values for realistic tracers, e.g. values could be interpreted as being in $\mathrm{g\,kg^{-1}}$ under an appropriate scaling. In chapter 3, we choose to normalise ϕ by its value on the plume centreline at the source so that its value clearly indicates dilution of the tracer field as the plume spreads out and mixes with the tracerless stratified environment. In chapter 5 & 6, when introducing tracers which represent water vapour and ice, we omit any normalisation.

2.2.2 Simulation setup

Here we describe the most general aspects of the simulation setup used throughout this thesis. Unless otherwise stated, the simulation setup described here is used. Minor modifications are made in chapters 4, 5 and 6 to address specific requirements for the investigation of internal waves and the introduction of a parameterisation of moist effects.

We consider the penetration of a buoyant plume with source radius r_0 and integral source buoyancy flux F_0 generated in a uniform layer of depth H into a linearly stably stratified layer with buoyancy frequency N_0. The plume carries a passive tracer with a source tracer flux $F_0^{(\phi)}$. The plume is generated near the bottom and at the horizontal centre $\boldsymbol{x}_c = (L_h/2, L_h/2, -H)$ of a domain of height L_z and horizontal extent L_h, as shown in figure 2.1. Scales are chosen to be similar to those of the laboratory experiments of Ansong and Sutherland (2010), such that $r_0 = 0.005\,\mathrm{m}$, $L_z = 0.6\,\mathrm{m}$ and $L_h = 0.6\,\mathrm{m}$. Other than chapters 5 and 6, we use a uniform grid with $N_h^2 \times N_z$ points where $N_z = N_h + 1$ and $N_h = 512$ for most simulations. The side length and

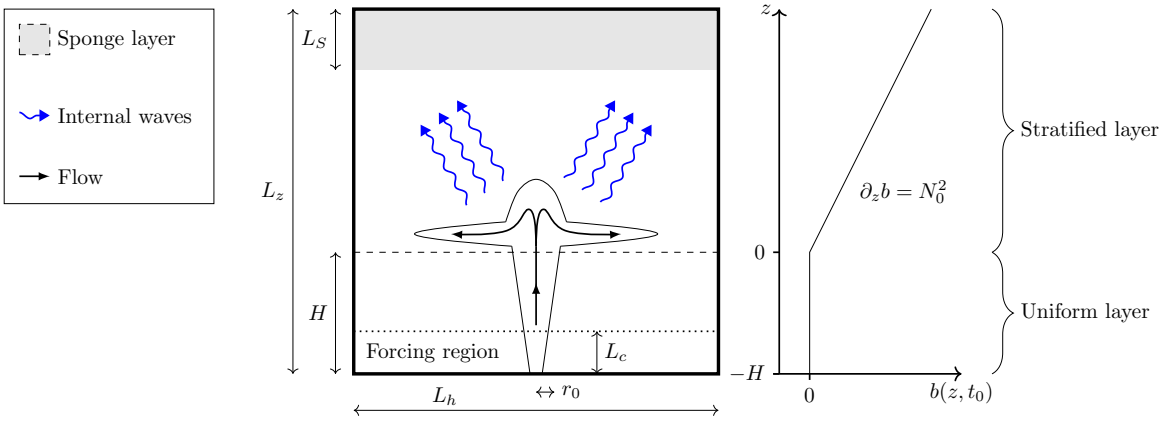

Fig. 2.1 Setup for numerical simulations of a buoyant plume with integral source buoyancy and tracer flux F_0 and source radius r_0 penetrating from a uniform layer of depth H into a linearly stably stratified layer with constant buoyancy frequency N_0. The domain has width L_h and depth L_z. The initial buoyancy profile (right) in the stratified environment is $b(\boldsymbol{x}, t_0) = N_0^2 z$ for $z \geq 0$. The dashed line marks the bottom of the stratified layer at $z = 0$. The forcing region of depth L_c at the bottom of the domain is indicated by the dotted line. Internal waves radiate outwards and upwards from the top of the plume cap (blue wavy lines) and are absorbed by the sponge layer of depth L_S at the top of the domain (light grey shading).

simulation end time $t = t_{\text{end}}$ is chosen such that edge effects are not present and the radially spreading intrusion that forms does not reach the boundary during the simulation. Other than in this chapter where we verify the numerical method, all simulations use $H = 0.2\,\text{m}$. Note that the non-dimensional depth of the uniform layer varies depending on the choice of F_0 and N_0 since lengths are normalised by $L = F_0^{1/4} N_0^{-3/4}$. Our focus is the stratified layer, so it is natural to choose the bottom of the initial stratified layer to be $z = 0$. Then, the bottom of the domain $z = -H$ and top $z = L_z - H$ vary in non-dimensional terms. We also define $t = 0$ as the time at which the plume first penetrates into the stratified layer, meaning the simulation start time $t = t_0 < 0$ varies because of the non-dimensionalisation which depends on N_0. There is also a dependence on F_0, which determines how quickly the plume will rise through the uniform layer. In cases where we consider multiple values of F_0 or N_0, it can be confusing to consider non-dimensional values because of the changing length and time scalings and we instead use dimensional units. These cases are clearly stated. We clearly state when using non-dimensional variables and, unless otherwise stated, choose to non-dimensionalise with F_0 and N_0. In the remainder of §2.2 we will use dimensional values for generality and convenience.

The initial conditions are

$$\boldsymbol{u}(\boldsymbol{x}, t_0) = \boldsymbol{0}, \quad \phi(\boldsymbol{x}, t_0) = 0, \quad b(\boldsymbol{x}, t_0) = \begin{cases} 0 & -H \leq z \leq 0, \\ N_0^2 z & 0 \leq z \leq L_z - H, \end{cases} \tag{2.26}$$

with continuous plume forcing in a thin layer $-H \leq z \lesssim -H + L_c$ at the bottom of the domain referred to as the 'forcing region'. The boundary conditions on the top and bottom boundary are no-slip $\partial_z u = \partial_z v = 0$, no-penetration $w = 0$ and no-flux $\partial_z b = \partial_z \phi = 0$. A sponge layer of depth $L_S = 0.1\,\mathrm{m}$ is added at the top of the domain (well above the top of the plume in each simulation), where the velocity is damped towards zero and the buoyancy is damped towards the initial background stratification $b(\boldsymbol{x}, t_0) = N_0^2 z$ to inhibit the reflection of internal gravity waves from the top boundary. Note that in all simulations the plume has a sufficiently small volume flux that the background stratification does not significantly vary through the simulation.

2.2.3 Plume generation method

We generate a buoyant pure plume by forcing the vertical velocity w, buoyancy b and tracer concentration ϕ in a forcing region of depth L_c at the bottom of the domain, as indicated in figure 2.1. We use a volumetric forcing method in which w, b and ϕ are relaxed towards the expected structure for a pure plume according to the MTT plume equations. As illustrated in figure 2.2, this structure is built from a Gaussian radial profile, vertical profiles derived from the MTT equations for a pure plume, and a forcing modulation function which limits forcing to the forcing region. In this chapter we use * to denote simulation parameters prescribed as part of the plume generation method.

The vertical profiles are chosen to be the far-field solutions of the MTT plume equations (2.4) – (2.7) in a uniform environment ($N_0 = 0$) for an axisymmetric pure plume with source radius r_0^* and integral source buoyancy flux

$$F_0^* = 2 \int_0^\infty \overline{w}\overline{b}\Big|_{z=-H} \, r \mathrm{d}r, \tag{2.27}$$

where $\bar{\cdot}$ denotes an azimuthal and time average. For simplicity, the source tracer flux $F_0^{(\phi)*}$ defined as

$$F_0^{(\phi)*} = 2 \int_0^\infty \overline{w}\overline{\phi}\Big|_{z=-H} \, r \mathrm{d}r, \tag{2.28}$$

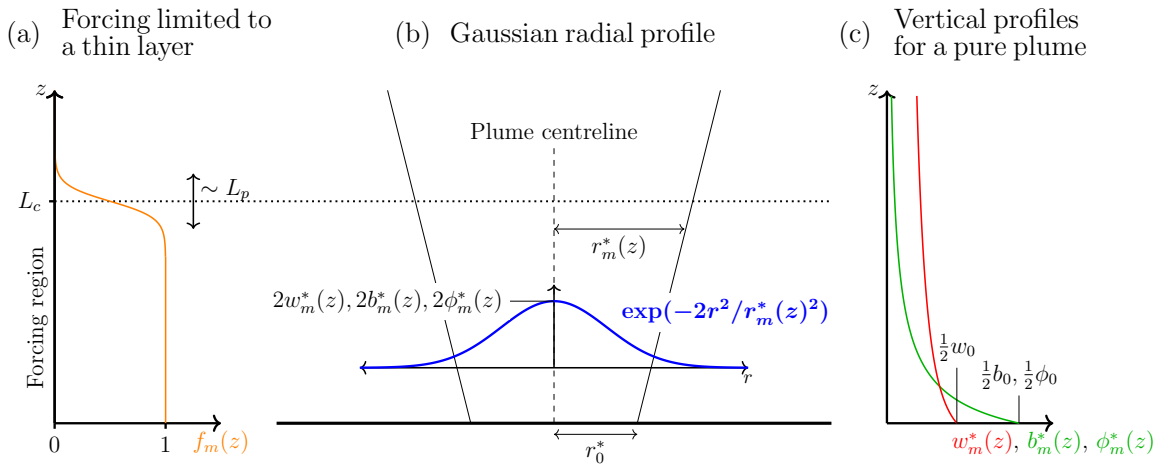

Fig. 2.2 Volumetric forcing method for generating a pure plume with source radius r_0^* and integral source buoyancy flux F_0^*. (a) The function $f_m(z)$ limits forcing to a layer of depth L_c at the bottom of the domain, with $f_m(z)$ reducing to zero over a distance $\sim L_p$ (left). (b) The forcing relaxes w, b and ϕ towards prescribed profiles which are built from a Gaussian radial profile, combined with (c) vertical profiles $r_m^*(z), w_m^*(z), b_m^*(z), \phi_m^*(z)$ derived from the MTT axisymmetric plume equations (right).

has the same dimensional value as the source buoyancy flux. Then, in non-dimensional terms, $F_0^{(\phi)*} = LT^{-2}F_0^*$, excluding the normalisation of ϕ by its source value on the plume centreline.

In a uniform environment, the MTT plume equations admit power-law solutions for Q, M, F_b and F_ϕ which, from (2.3), yield characteristic scales with vertical profiles given by

$$r_m^*(z) = \frac{6}{5}\alpha^*(z + H - z_v^*), \tag{2.29}$$

$$w_m^*(z) = \frac{5}{6\alpha^*}\left(\frac{9}{10}\alpha^* F_0^*\right)^{1/3}(z + H - z_v^*)^{-1/3}, \tag{2.30}$$

$$b_m^*(z) = \frac{5F_0^*}{6\alpha^*}\left(\frac{9}{10}\alpha^* F_0^*\right)^{-1/3}(z + H - z_v^*)^{-5/3}, \tag{2.31}$$

$$\phi_m^*(z) = \frac{5F_0^{(\phi)*}}{6\alpha^*}\left(\frac{9}{10}\alpha^* F_0^{(\phi)*}\right)^{-1/3}(z + H - z_v^*)^{-5/3}, \tag{2.32}$$

where $z_v^* = -\frac{5}{6\alpha^*}r_0^*$ is the virtual origin (which ensures a source radius r_0^*) and $\alpha^* = 0.11$ is the prescribed entrainment coefficient. Since the source tracer flux is the same as the source buoyancy flux, and b and ϕ evolve identically in the uniform layer up to a linear factor, the profile $\phi_m^*(z)$ used for the passive tracer is the same as the profile $b_m^*(z)$ used for the buoyancy except with F_0^* replaced by $F_0^{(\phi)*}$.

The full structure towards which the vertical velocity, buoyancy and tracer concentration are forced uses the vertical profiles (2.29)–(2.32) with Gaussian radial profiles of width $r_m^*(z)$. Gaussian profiles have been shown to approximate experimental data well (List, 1982; Papanicolaou and List, 1988; Shabbir and George, 1994). Tests were carried out with various other radial profiles at the source, all of which result in a Gaussian profile in w, b and ϕ far from the source where the plume is fully developed. The forcing on w, b and ϕ which is coupled to the governing equations (2.14), (2.15) and (2.16) respectively is then

$$f_w(\boldsymbol{x},t) = \frac{1}{\tau}\left[w(\boldsymbol{x},t) - 2w_m^*(z)\exp\left[-2\frac{(x-x_c)^2+(y-y_c)^2}{r_m^*(z)^2}\right]\left(1+\frac{1}{10}\xi(t)\right)\right] f_m(z), \tag{2.33}$$

$$f_b(\boldsymbol{x},t) = \frac{1}{\tau}\left[b(\boldsymbol{x},t) - 2b_m^*(z)\exp\left[-2\frac{(x-x_c)^2+(y-y_c)^2}{r_m^*(z)^2}\right]\left(1+\frac{1}{10}\xi(t)\right)\right] f_m(z), \tag{2.34}$$

$$f_\phi(\boldsymbol{x},t) = \frac{1}{\tau}\left[\phi(\boldsymbol{x},t) - 2\phi_m^*(z)\exp\left[-2\frac{(x-x_c)^2+(y-y_c)^2}{r_m^*(z)^2}\right]\left(1+\frac{1}{10}\xi(t)\right)\right] f_m(z), \tag{2.35}$$

where $\xi(t)$ is a random number between -1 and 1, used to apply uncorrelated 10% perturbations to the prescribed profiles at each step (note that a different random number is calculated for each grid cell), to initiate turbulence. The factor $1/\tau$ controls the coupling strength with the momentum equations. The size of τ must be small enough to control against dynamical variation and large enough to avoid numerical instability – the choice of τ is discussed further in §2.3. The function $f_m(z)$ constrains the forcing to a thin layer at the base of the domain. We use

$$f_m(z) = \frac{1}{2}\left[1 - \tanh\left(\frac{z+H-L_c}{L_p}\right)\right], \tag{2.36}$$

where L_c is the depth of the forcing region above $z=-H$ and L_p controls how sharply the forcing decays above $z=-H+L_c$. As illustrated in figure 2.2, $f_m(z)\approx 1$ for $z \lesssim -H+L_c$ and $f_m(z)\approx 0$ for $z \gtrsim -H+L_c$. Whilst the forcing is applied across the entire domain, $f_m(z)$ limits the depth in which the forcing is non-zero and the exponential factor in (2.33), (2.34) and (2.35) constrains the forcing to small radii $x^2+y^2 \lesssim r_m^*(z)^2$. An additional perturbation is applied to each velocity component in the two grid layers above $z=-H+L_c$ to initiate turbulence, which develops as

the plume rises through the uniform layer. We ensure that the plume has reached self-similarity (i.e. the turbulence and plume structure are fully developed) before penetrating the stratified layer – see § 2.3.2 for a demonstration of this validation step.

The forcing method detailed here is non-standard. With our numerical scheme, we found that the typical method of generating a buoyant plume by imposing a fixed buoyancy gradient on the bottom boundary (e.g. Pham et al. (2007); Van Reeuwijk et al. (2016)) results in 'necking', where the plume radius becomes very small, close to the bottom boundary where inflow dominates the diffusive boundary buoyancy flux. This method likely performs best with open boundary conditions (which are not implemented in `DIABLO`) that allow the vertical velocity through the bottom domain boundary to overcome the radial inflow. Pinching reduces control of the source radius and results in excessive numerical artefacts due to the horizontal pseudo-spectral method.

2.3 Verifying the numerical method

In this section we establish the capability for our numerical method to accurately simulate a buoyant plume. We consider a set of simulations listed in table 2.1. First, we consider simulations IC1, IC2 and U of a plume in a uniform environment (i.e. without stratification, $H = 0$, $N_0 = 0$) and compare results with the integral plume theory introduced in §2.1 and the detailed analysis of a direct numerical simulation of a pure plume presented in Van Reeuwijk et al. (2016), henceforth VR16. We verify that the simulated plume is in good agreement with theoretical expectations and ensure that the turbulence is well represented. A uniform environment is chosen so that the plume extends over a deeper vertical range. The simulation end time $t = t_{\text{end}}$ is long enough to obtain well-converged statistics, i.e. much longer than the turnover time $T_{\{F_0,r_0\}} = F_0^{-1/3} r_0^{4/3}$ which is the intrinsic timescale for a plume in a uniform environment. Note that, as opposed to the convention stated in §2.2, $t = 0$ is the simulation start time in these uniform environment simulations.

We then consider simulations with the setup detailed in § 2.2.2 with a stratified layer with buoyancy frequency $N_0 = 1.75\,\text{s}^{-1}$ above a uniform layer of depth $H = 0.15, 0.20\,\text{m}$ in simulations AS1 and AS2 respectively. These values, as well as the source radius r_0 and integral source buoyancy flux F_0, are chosen to match the laboratory experiments presented in Ansong and Sutherland (2010), henceforth AS10. In the absence of detailed results on turbulent statistics and plume dynamics, we verify that our simulations are

Simn.	N_0^2 (s^{-2})	H (m)	r_0 (m)	F_0 ($m^4 s^{-3}$)	$N_h^2 \times N_z$	t_{end} (s)	τ
IC1	0	0	0.005	5×10^{-6}	$256^2 \times 257$	100	0.1
IC2	0	0	0.005	5×10^{-6}	$256^2 \times 257$	100	1.0
U	0	0	0.005	5×10^{-6}	$512^2 \times 513$	100	1.0
AS1	3.0625	0.15	0.005	5×10^{-6}	$512^2 \times 513$	15	1.0
AS2	3.0625	0.20	0.005	5×10^{-6}	$512^2 \times 513$	15	1.0

Table 2.1 Simulation parameters for chapter 2.

consistent with the AS10 experiments by comparing characteristic heights such as the maximum penetration height and intrusion height.

In this section, we decompose a quantity χ into its mean $\overline{\chi}$ and turbulent component χ' using a combined time and azimuthal average. The time average is calculated from $t = t_{\text{end}}/5$ to $t = t_{\text{end}}$ and the azimuthal average is centred on the plume centreline, motivated by the approximately axisymmetric nature of the plume. The numerical method for calculating the azimuthal average is as described in Craske (2016). The covariance of two variables χ and ψ is defined as

$$\overline{\chi'\psi'} \equiv \overline{\chi\psi} - \overline{\chi}\,\overline{\psi}. \tag{2.37}$$

2.3.1 Plume in a uniform environment

The study by VR16 uses the integral formulation presented in §2.1 to analyse the characteristics of a buoyant pure plume in a uniform environment. Their direct numerical simulations achieve a Reynolds number $\text{Re} = 5000$ and fully resolve turbulent scales, offering a valuable benchmark to validate our large-eddy simulations which achieve $\text{Re} = 2.5 \times 10^6$. Here, we compare integral flow statistics as well as turbulent characteristics and profile coefficients which capture the effect of the mean flow, pressure and turbulence on self-similar profiles. These are calculated following the methods presented in VR16 which are detailed here where necessary. In these simulations of a uniform environment we do not include a passive tracer.

Integral plume theory describes the evolution of a buoyant pure plume entirely in terms of integral fluxes Q, M and F_b. Figure 2.3 shows the variation of these fluxes with streamwise distance z. Whilst the fluxes are defined in terms of infinite radial integrals, in the finite simulation domain we approximate the integral using the thresholding method introduced by Craske (2016); the upper limit of the integral r_ε at a given

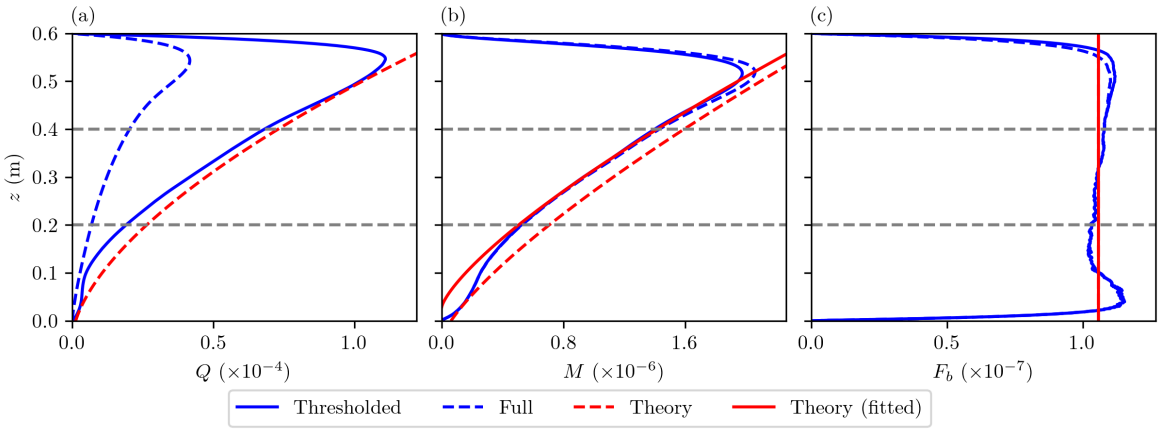

Fig. 2.3 Variation of integral fluxes (a) Q, (b) M, and (c) F with height z in simulation U. Fluxes defined in (2.1). Results with w-based thresholding shown in solid blue, representing fluxes within the plume. Fluxes across the full domain shown in dashed blue. Theoretical predictions using prescribed values α^*, z_v^* and the realised integral source buoyancy flux F_0 shown in dashed red. Theory fitted to the simulation data by varying z_v and α shown in solid red. Dashed grey lines indicate the analysis region which is used to fit the theoretical curves.

height z is defined as the radius where $\overline{w}$ is a fraction ε of its value on the centreline:

$$\overline{w}(r_\varepsilon, z) = \varepsilon \overline{w}(0, z). \tag{2.38}$$

All analyses presented henceforth use $\varepsilon = 0.02$ following VR16. The w-based thresholding method isolates the flux within the plume itself. In figure 2.3, the thresholded fluxes are shown in solid blue whilst the full fluxes (calculated across the whole domain, with the upper limit of the integral at $r = L_h/2$) are shown in dashed blue. The surrounding environment is uniform and (initially) quiescent so thresholding does not alter the momentum or buoyancy flux significantly. However, the volume flux is much larger within the plume itself. As the plume develops, a weak overturning circulation develops in the (essentially closed) domain. The thresholded flux excludes the weak downward velocity in the environment.

The power-law solutions to the MTT plume equations (2.4)–(2.7) in a uniform environment which yield characteristic scales as given in §2.2.3 scale with height z according to $Q \sim z^{5/3}, M \sim z^{4/3}$ and $F_b \sim F_0$ (constant). Theoretical curves of this form are plotted in red in figure 2.3 with coefficients derived from w_m, b_m and r_m using the prescribed values α^* and z_v^* used in the forcing functions f_w, f_b detailed in §2.2.3. The 'realised' value of the source buoyancy flux is $F_0 = 1.1 \times 10^{-7}$ m^{4}s^{-3}, calculated as the constant value attained by $F_b(z)$ over a suitable vertical range where source effects

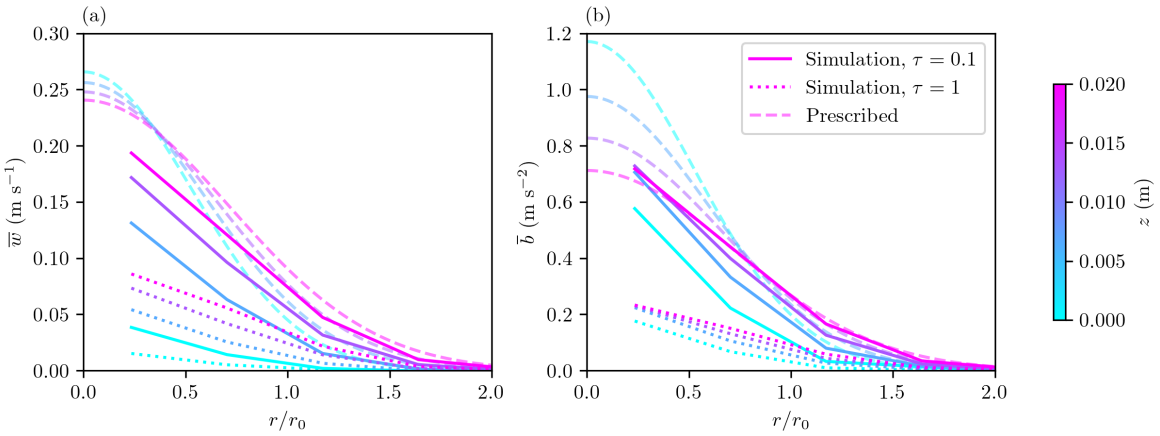

Fig. 2.4 Azimuthal and time averaged radial profiles of (a) vertical velocity $\overline{w}(r, z)$ and (b) buoyancy $\overline{b}(r, z)$ in the forcing region indicated in figure 2.1, in simulation IC1 (solid) with $\tau = 0.1$s and simulation IC2 (dotted) with $\tau = 1.0$s. Prescribed profiles derived from MTT plume theory (2.5), (2.6) shown as dashed lines. When the simulation parameter τ is smaller, the simulated profiles are closer to the prescribed profiles.

have decayed. This range is indicated by the light grey dashed lines and referred to as the 'analysis region'. The agreement between theory and simulation is reasonable but significantly improved by determining the value of z_v which achieves the best fit between the curves (red dashed lines). The optimal value of z_v tends to be negative, suggesting the plume effectively starts to evolve from a virtual source slightly above the bottom of the domain (but within the forcing region).

Note that the realised value of F_0 is around an order of magnitude smaller than the prescribed value. The parameter τ introduced in the description of the numerical method in §2.2.3 controls the coupling strength of the plume forcing with the momentum equations. Small values of τ more strongly relax the vertical velocity and buoyancy towards the prescribed analytic profiles, which ensure the generated plume has the desired source buoyancy flux. However, the more intense forcing necessitates smaller numerical time steps and can become a significant practical constraint. To illustrate this effect, figure 2.4 shows radial profiles of the time and azimuthally averaged vertical velocity and buoyancy in the forcing region in two low resolution simulations, with $\tau = 0.1$s and $\tau = 1$s, which are otherwise identical. Evidently when $\tau = 0.1$s the vertical velocity and buoyancy realised in the simulation are closer to the prescribed profiles. As a result, the realised integral source buoyancy flux is much larger with $F_0 = 2.2 \times 10^{-6}, 3.8 \times 10^{-7}$ m^4 s^{-3} when $\tau = 0.1, 1$s respectively. In the analysis

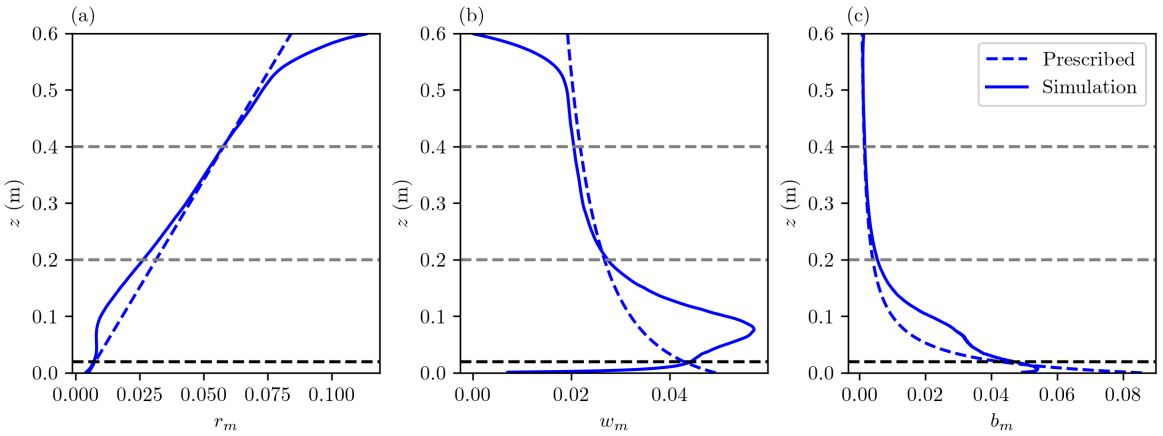

Fig. 2.5 Characteristic scales (a) r_m, (b)w_m, and (c) b_m for the plume radius, vertical velocity and buoyancy in simulation U. Curves (2.29)–(2.31) from MTT plume theory with prescribed values of α^*, z_v^* and the realised integral source buoyancy flux F_0 shown in dashed blue. Simulated curves in solid blue. The black dashed line indicates the top of the forcing region. Dashed grey lines indicate the analysis region.

that follows, and when non-dimensionalising with F_0, we use the realised rather than prescribed value of F_0.

The characteristic scales derived from the thresholded fluxes shown in figure 2.3 are compared with the prescribed scales (2.29)–(2.31) in figure 2.5. Note that we use F_0 in place of F_0^* in the prescribed scales. There is reasonable agreement between the simulated and prescribed scales above the forcing region (indicated by a black dashed line). The agreement is best for the buoyancy scale b_m. The vertical velocity scale w_m is smaller than expected. However, the volume flux within the plume shown in figure 2.3 remains close to the theoretical prediction since the characteristic plume radius r_m is wider than the theoretical radius.

Figure 2.6 shows the time and azimuthally averaged vertical velocity $\overline{w}$ and buoyancy $\overline{b}$. The buoyant plume appears as a region of strong vertical velocity and buoyancy localised to small radii. The linear increase in plume radius with height as predicted by the MTT plume equations is evident. We compare the simulated plume radius (solid black, as shown in figure 2.5) with the threshold radius r_ε (solid blue) and three theoretical predictions based on different estimates of the entrainment coefficient. The plume radius $r_m^*(z)$ defined by (2.29) is shown with the prescribed value $\alpha^* = 0.11$ (black dashed), the VR16 DNS estimate $\alpha_{\mathrm{VR16}} = 0.105$ (black dot-dashed) and the 'linear fit' estimate $\alpha_l = 0.113$ calculated by varying α^* and z_v^* in (2.29) to find the optimal fit between $r_m^*(z)$ and the simulated radius. Figure 2.6 shows that although

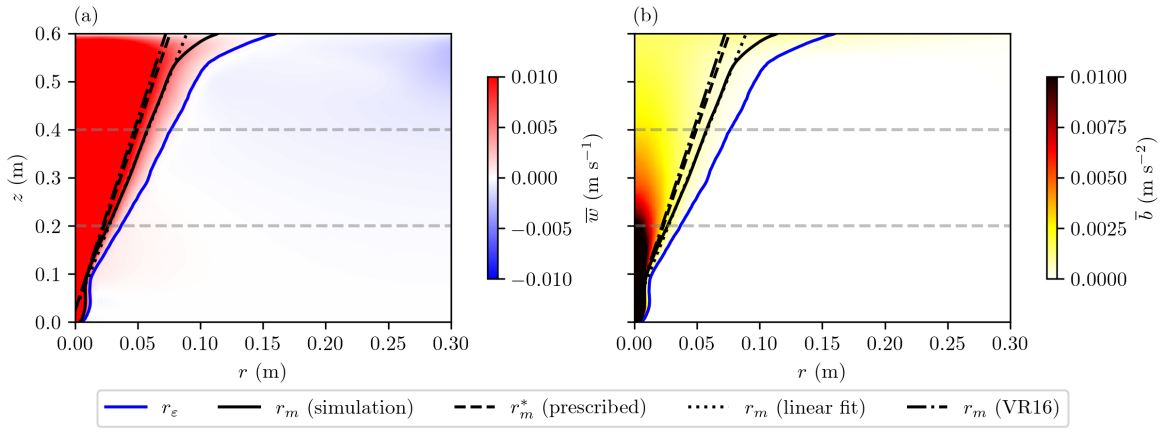

Fig. 2.6 Azimuthal and time averaged vertical velocity (a) $\overline{w}(r,z)$ and (b) buoyancy $\overline{b}(r,z)$ in simulation U. Threshold radius r_ε used to calculate integral plume fluxes shown in solid blue. In each panel, various estimates of the plume radius are overlaid in black: simulated characteristic plume radius r_m (solid), prescribed radius r_m^* defined in (2.4) (dashed), linear fit of r_m^* with r_m by varying α and z_v (dotted), prescribed radius r_m^* with VR16 estimate $\alpha = 0.105$ (dash-dotted).

r_m calculated from the simulation is larger than theoretical estimates of the plume radius, this is accounted for by the plume source effectively lying slightly above the bottom of the domain. Thus the various radii are not dissimilar in the analysis region.

The weak overturning circulation which reduces the full domain volume flux compared with the volume flux within the plume can be seen as a small downwards vertical velocity surrounding the plume in the left panel of figure 2.6. In the right panel, we find a weak stratification forming at the top of the domain, owing to the accumulation of buoyant fluid as the plume impinges on the closed top boundary and spreads laterally. This is unavoidable in a uniform environment since the plume rise is not limited by the environment. VR16 use a domain with open boundaries to avoid this issue. However, open boundaries are notoriously difficult to implement (e.g. Dhamankar et al. (2018)) so we do not use this method in our simulations. Moreover, the accumulation of fluid at the top boundary does not appear when stratification is introduced since the plume does not reach more than halfway through the domain and buoyant fluid instead accumulates in an intrusion at a lower height. This instead introduces a limitation on the maximum integration time of the stratified simulations since the intrusion can reach the side boundaries.

Perhaps the most fundamental check that the simulation is accurately described by integral plume theory is the self-similarity of the vertical velocity and buoyancy profiles. Figure 2.7 shows radial profiles of $\overline{w}, \overline{b}$ and radial momentum and buoyancy fluxes

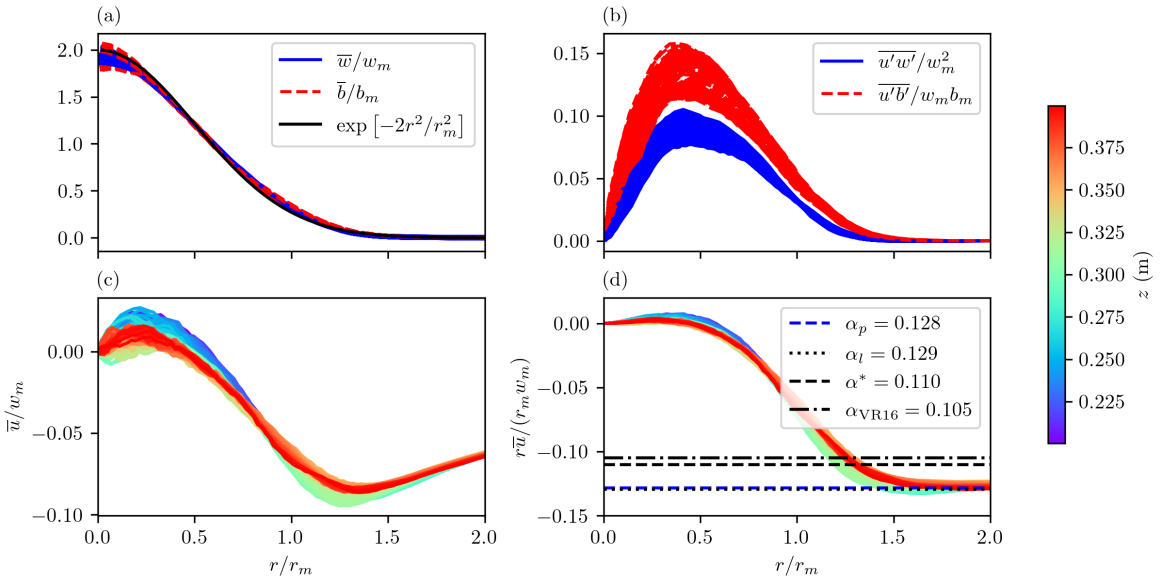

Fig. 2.7 Self-similar radial profiles of (a) $\overline{w}$ and $\overline{b}$, (b) radial momentum and buoyancy fluxes $\overline{u'w'}$ and $\overline{u'b'}$, (c) mean radial velocity $\overline{u}$, and (d) normalised mean radial specific volume flux $r\overline{u}$ in simulation U. Profiles are shown in the analysis region $0.2\,\mathrm{m} \leq z \leq 0.4\,\mathrm{m}$ indicated by dashed grey lines in figures 2.3, 2.5 and 2.6. Four estimates of the entrainment coefficient shown bottom right: linear fit of r_m^* to r_m gives α_l (dotted), VR16 estimate α_{VR16} (dot-dashed), prescribed value α^* (dashed) and value derived from fluxes (dashed blue) as shown in figure 2.8.

$\overline{u'w'}$ and $\overline{u'b'}$ over a range of streamwise heights z in the analysis region, normalised by the relevant characteristics scales. When normalised, the profiles collapse to a single curve. In the case of $\overline{w}$ and $\overline{b}$ this curve closely matches the experimentally-observed Gaussian profile with radius r_m, indicated by the black curve. Figure 2.7 also shows the normalised radial velocity and specific volume flux. Whilst they are approximately self-similar, there is more spread in $\overline{u}$ than the $\overline{w}$ and $\overline{b}$ profiles, likely due to the weak overturning circulation which disrupts the radial flow into the plume. Nonetheless, the radial specific volume flux tends towards a constant value as r/r_m increases which verifies the entrainment hypothesis and demonstrates that plume entrainment is behaving broadly as expected. According to (2.8), this constant value is $-\alpha$ where α is the entrainment coefficient. As discussed earlier, the value of α can be estimated by a linear fit of the prescribed radius r_m^* with the simulated plume radius r_m, giving $\alpha_l = 0.113$. The value can also be estimated from the identity (2.9) which gives α as a function of z. The mean α_p of this curve within the analysis region gives another estimate for the entrainment coefficient. From figure 2.7(d) we see that the large-radius behaviour of the radial specific volume flux is best represented by α_p.

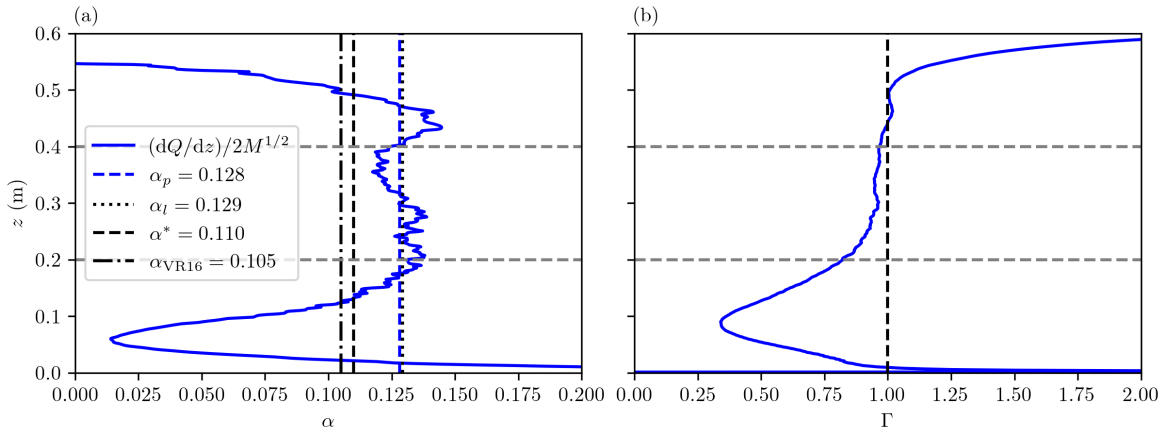

Fig. 2.8 Variation of (a) entrainment coefficient $\alpha = (2M^{1/2})^{-1}\mathrm{d}_z Q$ and (b) flux balance parameter Γ defined in (2.12) with streamwise distance z in simulation U. Four estimates of the entrainment coefficient shown as in figure 2.7.

Figure 2.8 shows the vertical variation of α with streamwise distance z and the mean α_p which is compared with the linear fit α_l, VR16 value α_{VR16}, and prescribed value α^*. Whilst there is significant variation in $\alpha(z)$, the variation is weaker in the analysis region. The mean α_p is larger than other estimates of the entrainment coefficient but remains within the range $0.1 < \alpha < 0.16$ found in the literature (Carazzo et al., 2006). Figure 2.8 also shows the streamwise variation of the flux balance parameter Γ defined in (2.12). As discussed in §2.1, Γ indicates the balance between gravitational and inertial forcing and a 'pure' plume has $\Gamma = 1$. There is some adjustment below the analysis region where $\Gamma < 1$, indicating an excess of momentum relative to buoyancy but the plume reaches a 'pure' plume state where momentum and buoyancy are balanced far above the source.

As briefly discussed in §2.1, profile coefficients are a modern addendum to the MTT plume equations which, in a radially averaged sense, account for the (non-dimensionalised) eddy terms neglected in the equations and act to modify the shape of self-similar profiles for each variable (Craske and van Reeuwijk, 2015). In a fully developed self-similar plume the coefficients are constant. The vertical variation of the profile coefficients are shown in figure 2.9. The mean flow and turbulence contributions are roughly constant in the analysis region, and match the values found in VR16 well (not shown). The pressure contribution varies with height, likely due to the weak overturning circulation discussed earlier, which reduces pressure at the bottom of the domain and increases pressure at the top.

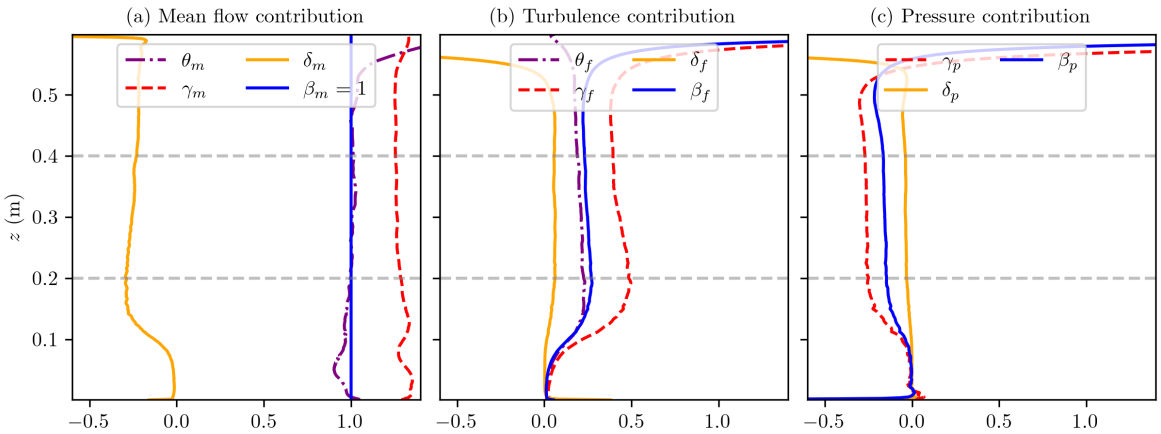

Fig. 2.9 Variation of the mean profile coefficients for (a) mean flow, (b) turbulence, and (c) pressure contributions with streamwise distance z in simulation U. Full definitions given in VR16; coefficients are constant in a pure plume.

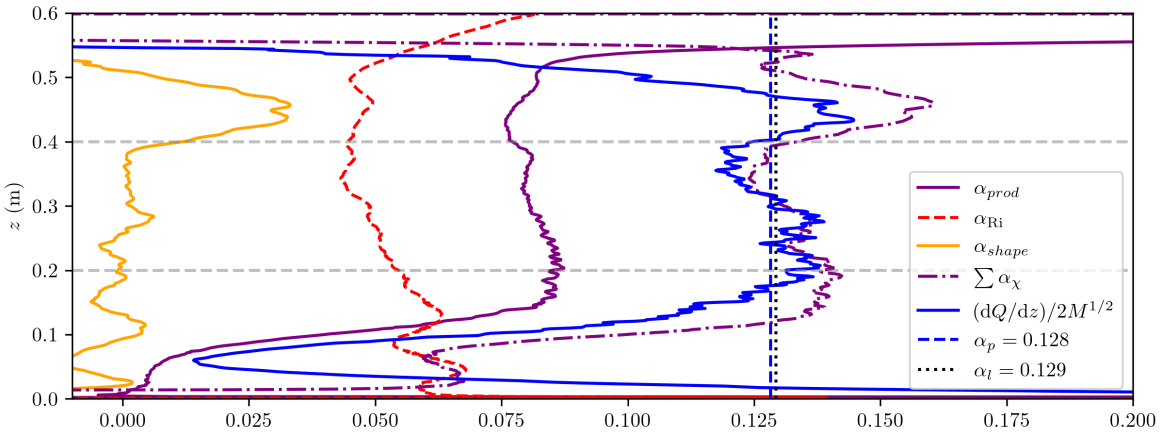

Fig. 2.10 Decomposition of the entrainment coefficient according to (2.39). Variation of contributions from (a) turbulence production α_{prod}, (b) mean buoyancy α_{Ri} and (c) changes in profile shape α_{shape} with streamwise distance z in simulation U. Sum of contributions $\sum \alpha_\chi$ shown (purple dot-dashed) along with flux-based calculation of α (solid blue), the mean α_p, and the estimate from a linear fit α_l (dotted black).

We now investigate the turbulence characteristics of the simulated plume. This can be assessed in two ways. Firstly, entrainment acts as a measure of dilution of the plume by turbulent mixing between the plume and environment. The entrainment coefficient can be decomposed as shown in Van Reeuwijk and Craske (2015), using the z-dependent definition of α given by (2.9) and the MTT plume equations (2.4)–(2.7) to give

$$\alpha = \underbrace{-\frac{\delta_g}{2\gamma_g}}_{\alpha_{\text{prod}}} + \underbrace{\left(\frac{1}{\beta_g} - \frac{\theta_m}{\gamma_g}\right)\text{Ri}}_{\alpha_{\text{Ri}}} + \underbrace{\frac{d}{d\zeta}\left[\log\frac{\gamma_g^{1/2}}{\beta_g}\right]}_{\alpha_{\text{shape}}}. \tag{2.39}$$

This decomposition quantifies the contribution to entrainment of turbulence production α_{prod}, mean buoyancy α_{Ri} and changes in profile shape α_{shape}. The streamwise variation of these contributions, the direct calculation $\alpha(z)$ shown in figure 2.8 and the estimates α_l and α_p are shown in figure 2.10. The sum of the contributions $\sum\alpha_\chi = \alpha_{\text{prod}} + \alpha_{\text{Ri}} + \alpha_{\text{shape}}$ has similar behaviour to $\alpha(z)$ and is in good agreement with the estimate α_l using r_m. This is consistent with DNS results in VR16 and demonstrates that entrainment in the simulated plume is consistent with predictions from MTT plume theory. VR16 note that the term α_{shape} is non-zero when radial profiles of first and second order plume statistics are not self-similar. This primarily occurs above the analysis region, where the plume feels the effect of the top boundary, and at the bottom of the domain where the flow transitions to turbulence and mean profiles develop their self-similar shapes. This domain is approximately 10 source radii deep or 5 cm in dimensional units. Similar transition layers are apparent for the mean buoyancy and turbulence production contributions. In particular, these contributions vary over a deeper layer up to around $z \approx 0.1\,\text{m}$. This is consistent with the buoyancy flux F_b in figure 2.3, flux balance parameter Γ and z-dependent entrainment coefficient in figure 2.8 which do not settle until above $z \approx 0.1\,\text{m}$.

The turbulent characteristics of the plume can also be assessed by considering the invariants of the deviatoric component of the Reynolds stress tensor, known as the anistropy tensor $\boldsymbol{b}$ with components defined by

$$b_{ij} = \frac{\overline{u_i'u_j'}}{\overline{u_i'u_i'}} - \frac{1}{3}\delta_{ij}. \tag{2.40}$$

The first invariant $\text{Tr}(\boldsymbol{b})$ is zero and following Lumley and Newman (1977), the second and third invariants η, ξ are defined as $6\eta^2 = b_{ij}b_{ji} = \text{Tr}(\boldsymbol{b}^2)$ and $6\xi^3 = b_{ij}b_{jk}b_{ki} = \text{Tr}(\boldsymbol{b}^3)$. These variables describe the physical state of turbulence in a 2D map known as

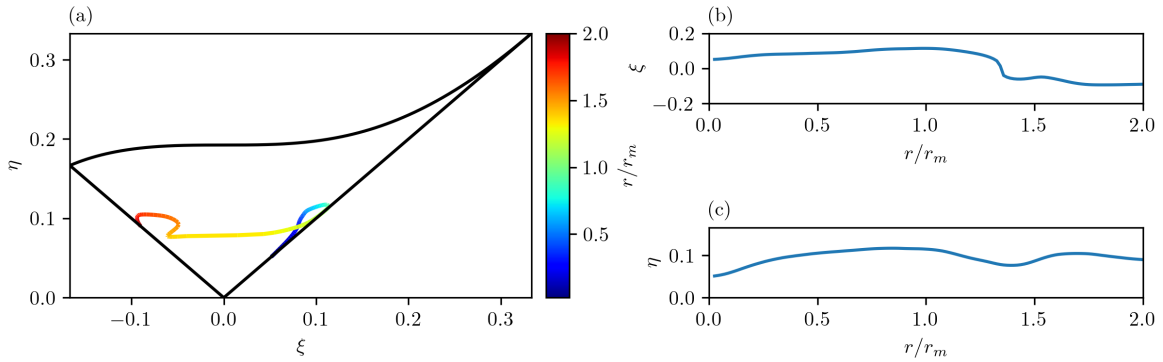

Fig. 2.11 Invariants of the anisotropy tensor (2.40) in simulation U. (a) Plotted in (ξ, η) space with the Lumley triangle shown in black with dependence of (b) ξ, (c) η on r/r_m (right).

the 'Lumley triangle'. The second invariant $\eta > 0$ identifies the degree of anistropy in the flow field, where large η indicates strong anisotropy. The third invariant ξ determines if the turbulence state is one-component, two-component, or axisymmetric. In the plume, we expect weak anistropy (small η) and axisymmetric turbulence, indicated by $\xi = \pm\eta$. This is indeed found in the results as shown in figure 2.11 and there is close agreement with the DNS results in VR16.

2.3.2 Plume in a stratified environment

We now consider simulations AS1 and AS2 which are each run four times to produce a larger set of results which are statistically independent owing to the uncorrelated perturbations applied to the forcing profiles and velocity components to initiate turbulence. The simulations use parameters matching the experiments reported by AS10. We vary the depth of the uniform layer, choosing $H = 0.15, 0.2\,\mathrm{m}$. Note that AS10 consider $H = 0, 0.05, 0.1, 0.15\,\mathrm{m}$ but we are restricted to deeper uniform layers so that the simulated plume can fully develop. Note also that whilst AS10 use a source radius $r_0 = 0.2\,\mathrm{cm}$, we instead use $r_0 = 0.5\,\mathrm{cm}$ so that the forcing profile is better resolved. Thus to attain a similar integral source buoyancy flux, the prescribed vertical velocity and buoyancy on the centreline are smaller than in the AS10 experiments. The mean simulated integral source buoyancy flux is $F_0 = 4 \times 10^{-7}\,\mathrm{m^4 s^{-3}}$ compared with the mean value $5.6 \times 10^{-7}\,\mathrm{m^4 s^{-3}}$ inferred from AS10.

In each simulation, we verify that the plume has reached a quasi-steady state before penetrating the stratified layer by repeating some of the analyses performed on the unstratified plume in the previous section. In particular, we ensure that profiles are

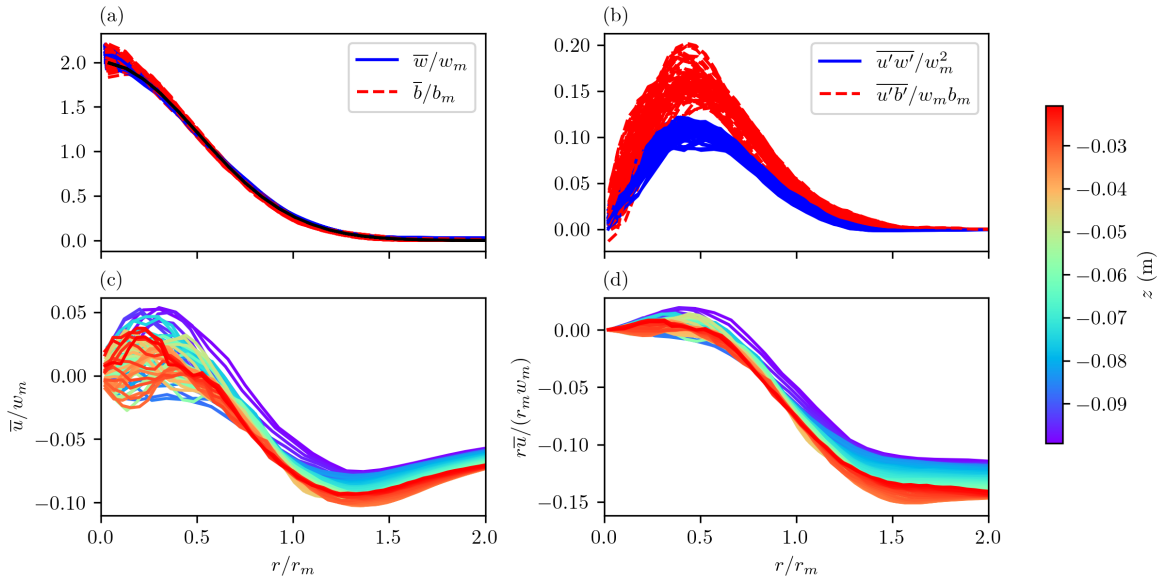

Fig. 2.12 As in figure 2.7 but calculated from simulation AS2 with analysis region $-0.1\,\mathrm{m} \leq z \leq -H/10\,\mathrm{m}$.

self-similar, profile coefficients have converged to constant values, and the integral fluxes match MTT theoretical predictions. Here we provide examples of these verification steps on a single run of simulation AS2 with $H = 0.2\,\mathrm{m}$, since this value is used in all simulations in the remainder of this thesis. The temporal average is taken over $5\,\mathrm{s} \leq t \leq 15\,\mathrm{s}$ with the plume first penetrating the stratified layer at $t = 0$. The analysis region is $-H/2 \leq z \leq -H/10$, i.e. the top half of the uniform layer, excluding a shallow region at the top of the uniform layer where the interface with the stratified layer is perturbed downwards by the intrusion. The verification process shown here is repeated in all simulations in this thesis but not reported.

Figure 2.12 shows the plume has reached a self-similar state in the analysis region, before penetrating into the stratified layer. We also see that the entrainment hypothesis holds for these profiles, with the radial specific volume flux converging to a constant value far from the plume. Figure 2.13 shows that the integral fluxes match MTT plume theory in the analysis region. There is a slightly larger discrepancy between the theoretical and simulated curves compared with the unstratified plume in the previous section, but the fitted theoretical curves closely match the simulation data, again suggesting the effective virtual source of the plume lies slightly above the bottom of the simulation domain. Note also that the integral buoyancy flux F_b is approximately constant as expected for a pure plume. Finally, figure 2.14 shows that the profile coefficients are approximately constant in the analysis region, suggesting that turbulence

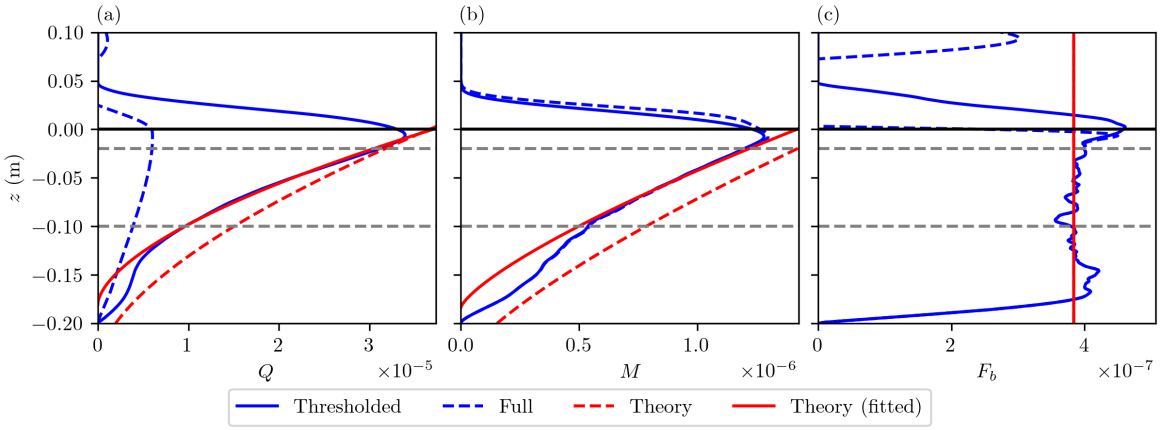

Fig. 2.13 As in figure 2.3 but calculated from simulation AS2. Grey dashed lines indicate the forcing region. The solid black line indicates the bottom of the initial stratified layer. The fluxes match theory before the plume penetrates the stratified layer.

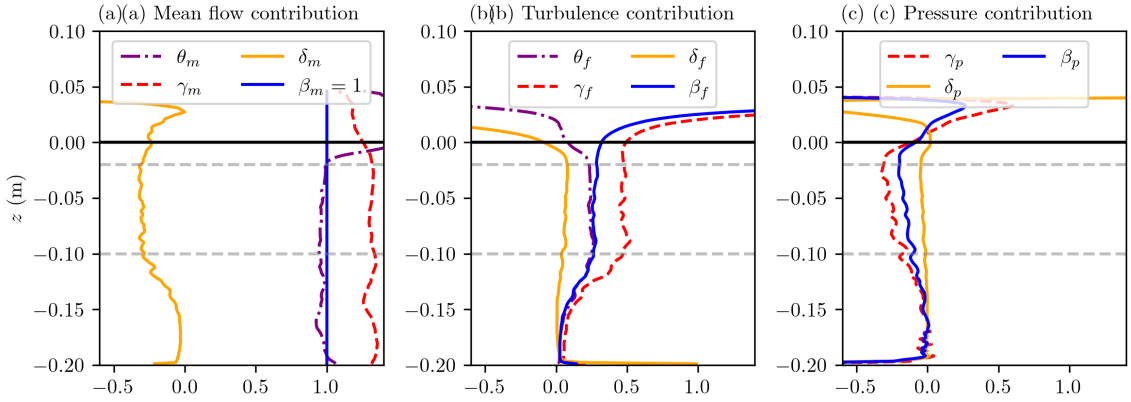

Fig. 2.14 As in figure 2.9 but calculated from simulation AS2. Grey dashed lines indicate the forcing region. The solid black line indicates the bottom of the initial stratified layer. The profile coefficients become constant before the plume penetrates the stratified layer.

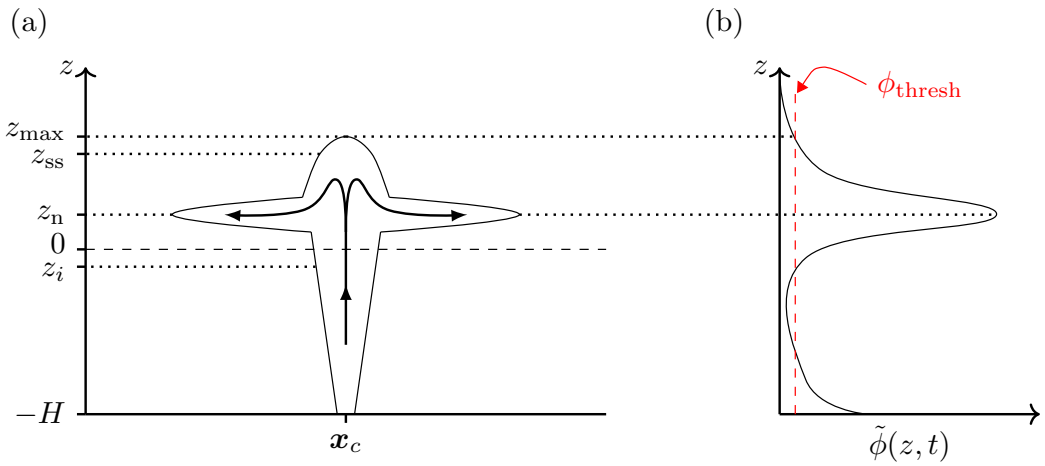

Fig. 2.15 Schematic of (a) characteristic heights for a buoyant plume centred at $\boldsymbol{x}_c$ penetrating into a stably stratified layer and (b) calculation method using the horizontally averaged tracer concentration. The maximum penetration height $z_{\max}$ is slightly above the quasi-steady state height z_{ss}. The intrusion forms at the equilibrium height z_{n}. The interface height z_i is slightly below the bottom of the initial stratified layer $z = 0$ to account for perturbation of the interface by the plume. The heights $z_{\max}$ and z_{n} are calculated from the horizontal mean of the tracer concentration $\tilde{\phi}$ and a threshold ϕ_{thresh}: $z_{\max}$ is the largest height at which $\tilde{\phi} > \phi_{\text{thresh}}$ and z_{n} is the height where $\tilde{\phi}$ is maximised. Note this requires sufficient tracer to have accumulated in the intrusion.

in the plume has fully developed. Together these results demonstrate that a uniform layer of depth $H = 0.2\,\text{m}$ is sufficient for the plume to reach a steady state before penetrating into the stratified layer. We find that $\Gamma \approx 0.8$ at penetration in the stratified simulations (not shown), suggesting the plume is slightly 'forced', with a small excess of inertia compared to buoyancy at penetration.

We now verify that our simulations are consistent with experimental results by comparing characteristic flow quantities with those reported in AS10. As described in section 1.2 and illustrated schematically in figure 2.15, a buoyant plume penetrating into a stably stratified layer rises to a maximum penetration height $z_{\max}$ before overturning and forming a spreading intrusion at the equilibrium height z_n. The maximum height of the plume then oscillates around a lower 'quasi-steady state' height z_{ss}. These heights are calculated from simulation data using the horizontal mean tracer concentration $\tilde{\phi}(z,t)$ and a threshold ϕ_{thresh}. At any time t, the top of the plume is defined as the largest height at which $\tilde{\phi}$ exceeds ϕ_{thresh}. The maximum height $z_{\max}$ is the largest of these heights and $t_{\max}$ is the time when $z_{\max}$ is reached. The quasi-steady state height z_{ss} is the mean height of the top of the plume from $t_{\max}$ onwards. Since tracer accumulates in the intrusion at the equilibrium height, we calculate z_{n} as the height at

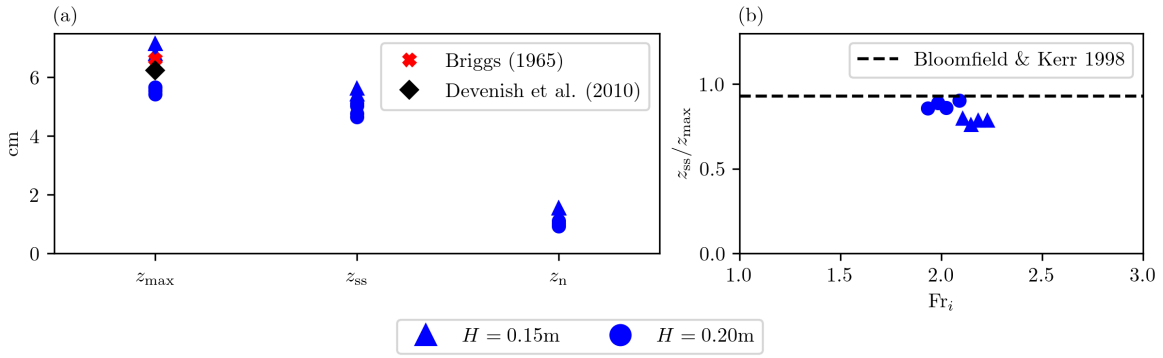

Fig. 2.16 Estimated maximum penetration height $z_{\max}$, quasi-steady state height $z_{\rm ss}$ and equilibrium height $z_{\rm n}$ (left) and comparison of the ratio $z_{\rm ss}/z_{\max}$ with the interfacial Froude number Fr_i defined by (2.41) in four runs of simulation AS1 and AS2 each.

which $\langle\phi\rangle_h$ is maximised. The calculation of $z_{\rm n}$ is only valid sufficiently long after $t_{\max}$ such that tracer has accumulated in the intrusion. In calculating the heights $z_{\max}, z_{\rm ss}$ there is some sensitivity to the tracer threshold $\phi_{\rm thresh}$. We ensure that $\phi_{\rm thresh}$ is large enough to avoid any numerical noise in the horizontal mean $\tilde{\phi}$. Unless otherwise stated, we use $\phi_{\rm thresh} = 10^{-3}$.

Following AS10 we also compute the interfacial Froude number Fr_i defined by

$$\mathrm{Fr}_i = \frac{w_m(z_i)}{\sqrt{b_m(z_i) r_m(z_i)}}, \tag{2.41}$$

where $z_i = -\frac{1}{10}H$ is the approximate height of the interface between the uniform and stratified layer. This value is slightly below the initial interface height $z = 0$ to account for perturbation of the interface as the plume rises and spreads. From MTT plume theory we expect $w_m(z_i) \sim H^{-1/3}, b_m(z_i) \sim H^{-5/3}$ and $r_m(z_i) \sim H$ hence $\mathrm{Fr}_i \sim 1$, i.e. Fr_i is roughly constant across a range of values of H. The interfacial Froude number is compared with the ratio of the quasi-steady state and maximum heights. For the case of a fountain in a linearly stratified environment (i.e. $H = 0, N_0^2 > 0$), Bloomfield and Kerr (1998) found an average $z_{\rm ss}/z_{\max} \approx 0.93$.

Figure 2.16 shows a summary of the results from the 8 simulations (4 runs each of AS1 and AS2). Our results can be compared with figures 6 and 7 in AS10. Figure 2.16(a) shows the characteristic heights $z_{\max}, z_{\rm ss}$ and $z_{\rm n}$. As noted in section 2.2, these heights scale with the length scale $L = F_0^{1/4} N_0^{-3/4}$. In particular, the experimental study of Briggs (1965) found that $z_{\max} \approx 3.8L$ and the LES study (in a fully stratified environment) of Devenish et al. (2010) found $z_{\max} \approx 1.36\alpha^{-1/2}L$. The simulation

results show good agreement with these estimates. It is difficult to compare our simulated values of z_n with AS10 results since in the laboratory it is difficult to distinguish between the interface and the intrusion. AS10 therefore only report z_n for experiments with $H \leq 10\,\text{cm}$, finding $z_n \approx 1\,\text{cm}$ in the $H = 10\,\text{cm}$ case. These values are similar to our simulation results despite the deeper uniform layer, though we note that the transition from the uniform layer to a fixed stratification above is likely not as sharp (i.e. the local buoyancy gradient increases more gradually immediately above the interface) in the AS10 experiments as in our simulations, which may weakly affect the height of the intrusion. The simulated values of z_{ss}/z_{max} shown in figure 2.16(b) are close to the empirical estimate by Bloomfield and Kerr (1998). However, we sample a much smaller range of interfacial Froude numbers compared with AS10. In particular, the Froude numbers we achieve are much smaller than in the AS10 experiments since we use a larger source radius r_0 and to attain a similar integral source buoyancy flux F_0 we prescribe a smaller vertical velocity and buoyancy at the source. Similarly, it was shown in § 2.3.1 that the realised forcing profiles when $\tau = 1$s do not exactly match the prescribed profiles, introducing a small imbalance in the forcing which results in a slightly forced plume state with $\Gamma < 1$. Nonetheless, we find Fr_i is approximately constant when H is varied between the two sets of simulations, as expected from MTT plume theory.

2.3.3 Gibbs ringing

In the horizontal pseudo-spectral numerical scheme used by `DIABLO`, the spectral cutoff filter introduces unphysical oscillations in the scalar fields throughout a horizontal level in response to sharp gradients on that level. This is known as Gibbs ringing (e.g. DeBonis (2019)) and is qualitatively similar to the oscillations that arise in the Fourier series representation of a finite step function using a finite number of modes. There are two regions where Gibbs ringing arises in the flow we consider: in the uniform layer, where b and ϕ are large on the plume centreline (and confined to small radii) and zero in the surrounding environment. Also, above the intrusion, the plume width is small compared to the domain size and the plume buoyancy is significantly smaller than the surrounding environment. This causes steep gradients in the buoyancy field in particular. These oscillations only occur along vertical slices that intersect the plume centreline at the middle of the domain and therefore does not have a significant impact on the plume *on average* (see figure 2.12) nor on the simulated buoyancy and tracer

fluxes (see figure 2.13). Note also that the numerical scheme conserves scalar fields in the absence of sources and sinks. Gibbs ringing primarily occurs on vertical slices crossing the plume centreline since the largest values in the buoyancy and vertical velocity fields occurs here. Figures in this thesis primarily show these vertical slices through the centreline, so Gibbs ringing artefacts are particularly apparent. The influence of Gibbs ringing can be reduced by decreasing the source buoyancy flux F_0 and tracer flux $F_0^{(\phi)}$, which acts to decrease the gradient in the scalar fields between the plume and environment. In analyses presented in the remainder of this thesis, we ensure that the results are not qualitatively influenced by the presence of Gibbs ringing. Where necessary, adjustments to the analyses to handle these numerical artefacts are introduced and described.

Chapter 3

Diagnosing tracer transport in convective penetration of a stably stratified layer

3.1 Introduction

Progress towards understanding the contribution of convective penetration to tracer transport in geophysical settings can be made by considering an idealised representation of the problem in which a region of strong stable stratification is penetrated by a turbulent buoyant plume generated in a region with weak or zero stratification. The objective of the study reported in this chapter is to diagnose the irreversible diapycnal tracer transport that results from turbulent mixing between plume fluid carrying a passive tracer and the surrounding environmental fluid in the stratified layer where no tracer is present. We aim to provide a quantitative description of the mixing involved in this diapycnal transport. Such descriptions are essential in forming parameterisations of convective penetration.

H	r_0	$N_h^2 \times N_z$	t_{end}	Δt	τ	L	L_c	L_p	Re	Pr
7.97	0.20	$512^2 \times 513$	15	0.25	1.00	23.9	0.80	0.40	6.29×10^6	0.70

Table 3.1 Non-dimensional parameters for the simulation with $N_0 = 1\,\text{s}^{-1}$ and $F_0 = 3.96 \times 10^{-7}\,\text{m}^4\text{s}^{-3}$ discussed in chapter 3.

We consider a single simulation of the setup described in chapter 2 in which a buoyant plume with source radius r_0 and source integral buoyancy flux F_0 generated in a uniform layer of depth H penetrates into a stably stratified layer with buoyancy frequency N_0. The source tracer flux $F_0^{(\phi)}$ has the same (dimensional) value as F_0. In this chapter, we non-dimensionalise using F_0 and N_0 such that the source buoyancy flux and stratification strength are both unity. We use simulation parameters which are similar to the experimental setup used by Ansong and Sutherland (2010) except for the source buoyancy flux, which is weaker here to reduce the influence of Gibbs ringing. The parameters are given in table 3.1 and non-dimensionalised by $N_0 = 1\,\mathrm{s}^{-1}$ and $F_0 = 3.96 \times 10^{-7}\,\mathrm{m}^4\mathrm{s}^{-3}$. In the remainder of this chapter, all values stated are non-dimensionalised with respect to this choice of F_0 and N_0.

Throughout the flow evolution, plume fluid is distinguished from environmental fluid by the presence of non-zero tracer concentration. Crucially, both the tracer concentration ϕ and buoyancy b are subjected to turbulent mixing, resulting in the entrainment of environmental fluid into the plume and modification of the relationship between buoyancy and tracer within the plume. Analysis of this relationship has previously been used to understand tracer transport and mixing. Plumb (2007) introduced a tracer-tracer probability density function to study rapid isentropic mixing in the stratosphere. Penney et al. (2020) utilised this method to study diapycnal mixing of passive tracers by Kelvin-Helmholtz billows arising in a stratified shear flow. Using buoyancy as one of the tracers, the redistribution of fluid in buoyancy-tracer space was used to interpret the mixing process.

In this chapter we introduce a buoyancy-tracer volume distribution which is a modified formulation of the tracer-tracer and buoyancy-tracer joint distributions presented in Plumb (2007) and Penney et al. (2020). In our formulation we consider the flow of fluid volume through a buoyancy-tracer phase space to understand the effect of mixing on the transport of a passive tracer in a buoyant plume penetrating a linearly stably stratified layer. In § 3.2 we discuss the evolution of the flow and tracer concentration. We then introduce our formulation of the buoyancy-tracer 'volume distribution' in § 3.3. We use this novel formulation of the method to show that the flow can be partitioned into three regions of buoyancy-tracer space: the 'source' region where plume fluid enters the stratified layer, a 'transport' region through which volume flows during initial mixing between the plume and environment, and an 'accumulation' region where mixed fluid settles and homogenises. Each of these regions of buoyancy-tracer space correspond to coherent regions of physical space that identify the essential structures

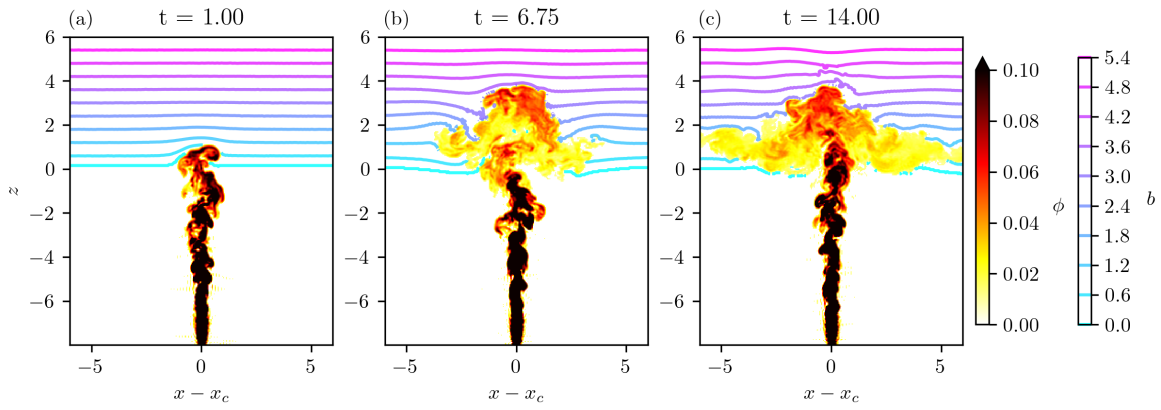

Fig. 3.1 Three stages of the flow evolution, shown as x-z cross-sections of the tracer concentration ϕ shown where ϕ exceeds 1% of its value on the plume centreline at the source $z = -H$. Buoyancy contours are shown otherwise. Cross-sections are taken at the plume centreline at non-dimensional times $t = 1, 6.75, 14$. From left to right, the panels show the plume during initial penetration, reaching maximum penetration height, and spreading of the intrusion.

of the flow, namely the rising plume, plume cap, and radially-spreading intrusion, respectively. These structures are indicated in figure 1.9. In § 3.4 we analyse diagnostics of the mixing process in each of these regions.

3.2 Flow & tracer structure

The flow evolution is presented in three vertical cross-sections through the plume centreline in figure 3.1. We identify the plume as regions with tracer concentration $\phi \geq \phi_{\min} \equiv 10^{-2}$, i.e. we threshold the tracer field at 1% of its value on the plume centreline at the source. In the tracer-less environment surrounding the plume we show contours of the buoyancy field. The bottom of the stratified layer, above which the buoyancy of the environment becomes non-zero, is indicated by the lowest buoyancy contour.

Figure 3.1(a) shows initial penetration of the stratified layer by the plume cap. As the plume rises through the stratified layer, its upward acceleration decreases as the relative buoyancy between the plume and the surrounding environment decreases. Once the environmental buoyancy exceeds that of the plume, the plume decelerates. Eventually, the rising fluid reverses direction, or 'overturns', and begins to subside from the maximum penetration height $z_{\max}$ (figure 3.1(b)). As plume fluid subsides,

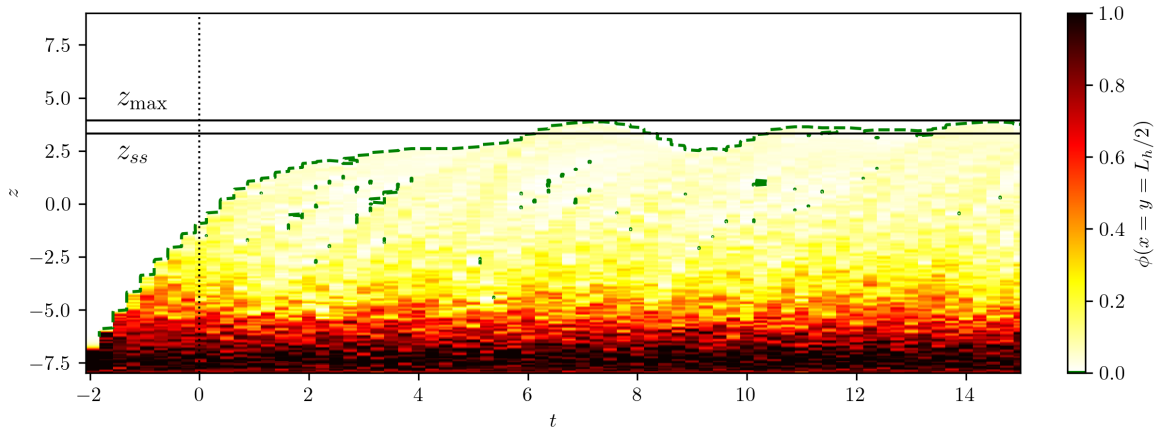

Fig. 3.2 Timeseries of the tracer concentration $\phi(L_h/2, L_h/2, z, t)$ in the $z - t$ plane at the centreline of the computational domain $x = y = L_h/2$. The green dashed contour denotes the plume threshold $\phi = \phi_{\min}$, i.e. where ϕ is 1% of its value on the plume centreline. The maximum penetration height $z_{\max}$ and the quasi-steady state height z_{ss} are marked.

its buoyancy relative to the surrounding environment increases until reaching the level of neutral buoyancy z_n where the plume fluid forms a radially-spreading intrusion – see figure 3.1(c). The dynamics observed in the simulation agree qualitatively with studies of similar set-ups in the literature, for example the experiments detailed in Ansong and Sutherland (2010) with an identical setup and similar physical parameters.

The evolution of the maximum height of the plume cap during penetration and the subsequent quasi-steady state is visualised as a time-series of tracer concentration on the plume centreline in figure 3.2. As has been noted in the literature, the maximum height of the plume tends to oscillate around a quasi-steady state height z_{ss} (Turner, 1966) but, to our knowledge, the mechanism setting the frequency of this oscillation (often referred to as 'plume bobbing') is not well understood (e.g. Ansong and Sutherland (2010)). In the simulation considered here, the quasi-steady state height z_{ss} is close to the maximum penetration height $z_{\max}$ and the oscillation is weak. For convenience, we will use $z_{\max}$ to refer to the maximum height of the plume. The maximum penetration height $z_{\max}$ determines the maximum height at which plume fluid can mix with the environment (Ansong et al., 2008), meaning the initial buoyancy at the maximum penetration height, $b = z_{\max}$, represents a plausible constraint on the maximum buoyancy accessible for mixing with the plume. However, this constraint can occasionally be exceeded when plume fluid subsiding from the plume cap pulls very buoyant environmental fluid downwards (see figure 3.1(b) to the left of the plume cap). Here we find $z_{\max} = 3.94$

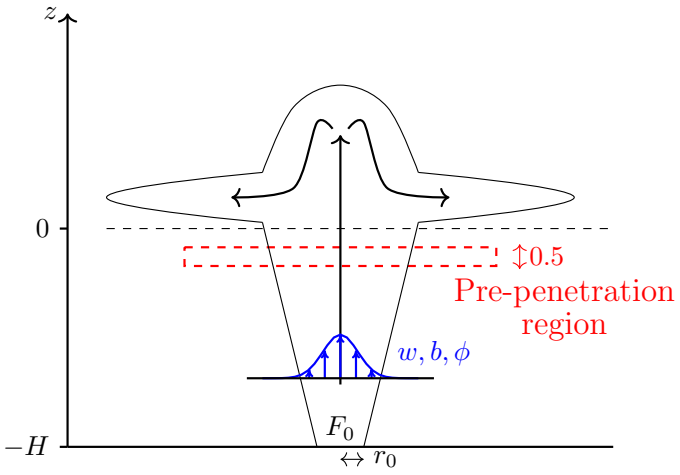

Fig. 3.3 Schematic illustration of the pre-penetration region defined in §3.2 for diagnostic purposes, shown in red. The (azimuthally averaged) Gaussian profiles of w, b and ϕ in the plume rising through the uniform layer are illustrated in blue.

which agrees with experimental estimates of the maximum penetration height in the literature, e.g. $z_{\max} \approx 3.8$ for a plume with a round source (List, 1982).

Internal gravity waves across a range of frequencies are generated during the penetration process. These waves are visible as small amplitude, long wavelength undulations in the buoyancy contours above $z \approx 4$ in figure 3.1(c). Whilst these waves may play some role in generating turbulence and hence mixing, we note from AS10 that the waves extract $\mathcal{O}(1 - 10\%)$ of the upward energy flux in the plume and in the absence of a mean flow the waves do not break, so this influence is expected to be small. We do not consider the particular contribution of these waves to mixing here; the generation of internal waves is considered in chapter 4 and their influence on mixing in the presence of vertical shear is considered in chapter 6.

In the uniform layer, the buoyancy and tracer evolve identically up to a linear factor, i.e. the undiluted plume fluid entering the stratified layer has a linear relationship between b and ϕ at each point. This follows from the self-similarity of the buoyancy and tracer concentration profiles in the steady state plume that penetrates the stratified layer (see chapter 2, figure 2.12). The radial profiles for b and ϕ are both Gaussian with the same width but different amplitudes, hence $b \propto \phi$. After penetrating the stratified layer, plume fluid with non-zero buoyancy and tracer concentration mixes with tracer-less environmental fluid and hence the buoyancy and tracer evolve differently. This effect can be quantified using a tracer probability density function (PDF) in buoyancy coordinates $\tilde{\phi}(b; t)$. The PDF is calculated within the stratified layer only. The value

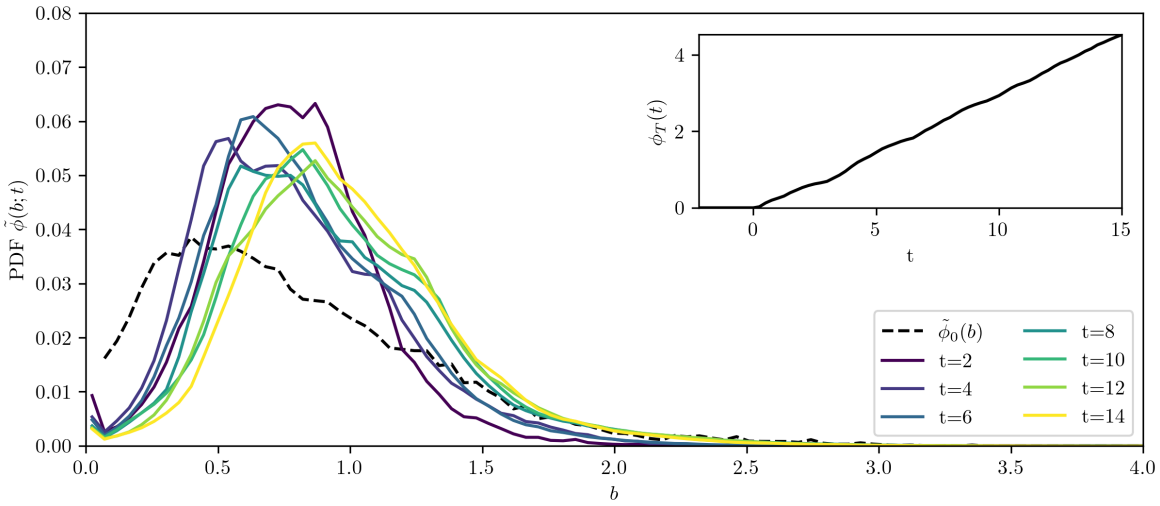

Fig. 3.4 Probability density function $\tilde{\phi}(b,t)$ of tracer as a function of buoyancy b in the stratified layer at fixed time intervals post-penetration shown as coloured lines. The black dashed line shows the time-averaged pre-penetration PDF $\tilde{\phi}_0(b)$, calculated with V chosen as the pre-penetration region indicated in figure 3.3 and time-averaged. The pre-penetration PDF $\tilde{\phi}_0(b)$ shows the tracer-buoyancy relationship within the plume prior to penetrating the stratified layer. Differences between $\tilde{\phi}_0$ and $\tilde{\phi}(b,t)$ represent the effect of mixing. Total tracer in the stratified layer $\phi_T(t)$ shown inset.

of the PDF $\tilde{\phi}(b;t)\,\mathrm{d}b$ is calculated as the total tracer with buoyancy within a range b to $b+\mathrm{d}b$ in the stratified layer, normalised by the total tracer in the stratified layer $\phi_T(t) = \sum_V \phi(\boldsymbol{x},t)\Delta V$, where V is the stratified layer and ΔV is the grid-cell volume. The definition of $\tilde{\phi}$ is such that $\sum_B \tilde{\phi}(B;t)\Delta B = 1$.

Figure 3.4 shows $\tilde{\phi}(b;t)$ in the stratified layer at fixed time intervals post-penetration. The total tracer in the stratified layer $\phi_T(t)$ is shown inset. The approximately linear increase in ϕ_T with time suggests a relatively uniform input of tracer to the stratified layer, carried by the penetrating plume. Owing to the self-similar nature of the penetrating plume, we expect the tracer that enters the stratified layer to have a fixed PDF (with some small variation). This *pre-penetration* PDF $\tilde{\phi}_0$ can be estimated using a domain V chosen as the pre-penetration region shown in figure 3.3. This region is a thin layer with (non-dimensional) depth 1/2 below the bottom of the stratified layer. The pre-penetration PDF, shown as a black dashed line in figure 3.4, represents the tracer PDF in the plume just before it penetrates the stratified layer. Without mixing, $\tilde{\phi}$ in the stratified layer would match the pre-penetration PDF. Mixing during the penetration process manifests as changes in the tracer PDF when compared with the pre-penetration PDF.

Evolution of the post-penetration PDF and changes compared with the pre-penetration tracer PDF highlight two mixing processes during penetration: mixing within the plume during penetration, and mixing between the plume and environment. Where plume fluid carries a large tracer concentration and mixes with the more buoyant surroundings, the positive tail of the tracer PDF increases. This is particularly evident after $t = 6.75$ when the plume has reached $z_{\max} = 3.94$, at which point very large values of buoyancy in the environment become accessible *and* large tracer concentrations at the centre of the plume are exposed to the environment as plume fluid overturns. At the edges of the plume where tracer concentration is smallest, mixing with the environment again moves tracer from lower to higher values of buoyancy and therefore the PDF decreases where b is small. This effect is supplemented by mixing within the plume, which acts to homogenise the large tracer concentration and buoyancy at the centre of the plume with the lower tracer concentration and buoyancy at the edge of the plume. This acts to narrow the PDF and hence decrease the PDF at large and small values of buoyancy but the effect is only evident before the plume reaches $z_{\max}$ at $t = 6.75$ and accesses much larger values of buoyancy. At late times, most tracer lies in the spreading intrusion at the neutral buoyancy height z_n, which coincides with the peak in the tracer PDF.

The buoyancy range of the tracer PDF is determined by the maximum penetration height of the plume as well as the rapidity of the mixing between the plume and environment occurring in the plume cap. If fluid quickly subsides after reaching $z_{\max}$, before substantial mixing with the environment occurs, only small amounts of the more buoyant environment are entrained and therefore the increase in the PDF at large values of buoyancy is modest compared with a scenario where plume fluid stalls during overturning and significant mixing with the environment occurs. In figure 3.4, the tracer PDF extent is $b \approx 3$ whilst the environmental buoyancy at $z_{\max}$ is approximately $b|_{z_{\max}} \approx 3.94$. This suggests the mixing timescale is slow compared to the dynamical timescale, i.e. mixing between the largest tracer concentrations first exposed during overturning and the environment is slow and continues during subsidence, where the buoyancy of the environment decreases.

The tracer PDF hints at competing effects of mixing within the plume and between the plume and the environment. Crucially, the buoyancy and tracer fields are mixed in different ways owing to the linearly increasing buoyancy and vanishing tracer concentration in the linearly stratified environment. Whilst changes in the tracer PDF considered here demonstrate the overall effect on the relationship between tracer and

buoyancy, it is difficult to extract information on the intensity of mixing between plume and environmental fluid and the specific buoyancy and tracer characteristics of the fluid parcels that mix. Furthermore, the tracer PDF $\tilde{\phi}(b;t)$ does not give information on the volume of fluid parcels at a given buoyancy; a peak in the tracer PDF may represent relatively few fluid parcels carrying large tracer concentrations or many fluid parcels carrying small amounts of tracer. The distinction is important, since the former can result in stronger gradients upon which diffusion acts and therefore more effective diapycnal transport of tracer.

3.3 Buoyancy-tracer volume distribution

The probability distributions of tracer concentration discussed in section 3.2 isolate the *irreversible* transport that results from turbulent mixing. The turbulent mixing of fluid parcels can be considered a two-step process (e.g. Davies Wykes and Dalziel (2014)), composed of stirring and molecular diffusion. Whilst stirring strengthens tracer gradients across buoyancy surfaces, it is – in principle – a reversible process. However, molecular diffusion results in irreversible changes to the buoyancy and tracer characteristics of fluid parcels and hence changes the tracer distribution.

Here, we use the distribution of volume in buoyancy-tracer space to diagnose mixing in the stratified layer. That is, we map from 3D physical space to a 2D phase space by using the buoyancy and tracer concentration fields to quantify the volume of plume fluid in the stratified layer with each value of b and ϕ. The total physical volume of plume fluid represented in the distribution changes in time and we do not normalise the distribution to form a PDF. Omitting this normalisation simplifies the interpretation of the distribution and its governing equation. The buoyancy-tracer volume distribution formalism presented here builds on previous density-tracer joint PDF formulations presented by Plumb (2007) and Penney et al. (2020).

3.3.1 Definition & properties

We define the *volume distribution* $W(B,\Phi;t)$ in buoyancy-tracer space such that the volume of fluid in a fixed volume V with $B < b(\boldsymbol{x},t) < B+\mathrm{d}B$ and $\Phi < \phi(\boldsymbol{x},t) < \Phi+\mathrm{d}\Phi$ is given by $W(B,\Phi;t)\mathrm{d}B\mathrm{d}\Phi$. This may be defined as

$$W(B,\Phi;t) = \int_V \delta(b(\boldsymbol{x},t)-B)\delta(\phi(\boldsymbol{x},t)-\Phi)\,\mathrm{d}V, \tag{3.1}$$

where $\delta(\cdot)$ is the Dirac delta function with the inverse dimension of its argument. Henceforth we choose the volume V to be the stratified layer. An evolution equation for W can be obtained using the governing equations for b and ϕ. See appendix 3.A for a full derivation. We have

$$\frac{\partial W}{\partial t} = -\nabla_{(B,\Phi)} \cdot \boldsymbol{F} + S, \tag{3.2}$$

where $\boldsymbol{F}(B, \Phi; t)$ is *mixing flux distribution* and $S(B, \Phi; t)$ is the *source distribution*. The mixing flux distribution $\boldsymbol{F}$ is a vector in buoyancy-tracer space with components formed from the volume-weighted average of the non-advective terms $\dot{b}$ and $\dot{\phi}$ in (2.15) and (2.16) respectively, representing the flux of W in buoyancy-tracer space due to mixing and is defined as

$$\boldsymbol{F}(B, \Phi; t) = (F_b, F_\phi) = \int_V (\dot{b}, \dot{\phi})\, \delta(b(\boldsymbol{x}, t) - B)\delta(\phi(\boldsymbol{x}, t) - \Phi)\, \mathrm{d}V, \tag{3.3}$$

where $\dot{b} = (\mathrm{RePr})^{-1}\nabla^2 b - \nabla \cdot \boldsymbol{\lambda}_b$ and $\dot{\phi} = (\mathrm{RePr})^{-1}\nabla^2 \phi - \nabla \cdot \boldsymbol{\lambda}_\phi$. Note that the plume forcing terms f_b and f_ϕ are excluded from $\dot{b}$ and $\dot{\phi}$ since the forcing vanishes in the stratified layer. The source distribution S represents a source or sink of W due to boundary fluxes across ∂V,

$$S(B, \Phi; t) = \int_{\partial V} \boldsymbol{u} \cdot \boldsymbol{n}\, \delta(b(\boldsymbol{x}, t) - B)\delta(\phi(\boldsymbol{x}, t) - \Phi)\, \mathrm{d}A, \tag{3.4}$$

where $\boldsymbol{u}$ is the velocity in physical space and $\boldsymbol{n}$ is the *inward* normal on the boundary ∂V of V. Since we are considering a flow upwards into V, $\boldsymbol{u} \cdot \boldsymbol{n}$ is positive and S acts as a source of W. Note that whilst S represents the effect of fluxes across the boundary ∂V in physical space, it is distributed in buoyancy-tracer space. Note that (3.2) contains no terms in which advection plays an explicit role except for the source term – which captures advection through the domain boundary – representing the fact that W remains unchanged under advection within the domain.

Turbulent mixing redistributes volume in buoyancy-tracer space, which results in changes to W via the mixing flux term $-\nabla_{(B,\Phi)} \cdot \boldsymbol{F}$. The change in W at a point (B, Φ) in buoyancy-tracer space as a result of turbulent mixing up to time t is therefore

$$M(B, \Phi; t) = -\int_0^t \nabla_{(B,\Phi)} \cdot \boldsymbol{F}(B, \Phi; t')\, \mathrm{d}t' = W(B, \Phi; t) - \int_0^t S(B, \Phi; t')\, \mathrm{d}t', \tag{3.5}$$

such that $M(B,\Phi;t)\mathrm{d}B\mathrm{d}\Phi$ is the change in volume of fluid with $B < b(\boldsymbol{x},t) < B+\mathrm{d}B$ and $\Phi < \phi(\boldsymbol{x},t) < \Phi+\mathrm{d}\Phi$ up to time t due to mixing. Therefore M represents the integrated effect of the mixing flux $\boldsymbol{F}$ and we refer to M as the *net mixing effect distribution*. The second equality in (3.5) follows from time-integrating (3.2) and noting that $W(B,\Phi;t=0)=0$ since there is no tracer in the initial stratified layer. Hence, M can be interpreted as a cumulative measure of the changes to W relative to the time-integrated source distribution, i.e. the changes in the volume distribution that arise solely from mixing. The final term in (3.5), which we refer to as the *cumulative source distribution*, represents the volume of fluid with buoyancy $B < b < B+\mathrm{d}B$ and tracer concentration $\Phi < \phi < \Phi+\mathrm{d}\Phi$ that has entered the stratified layer up to time t. The volume distribution $W \geq 0$ and the cumulative source distribution is also positive assuming there is a flow into V only. However, M can be positive or negative depending on the relative sizes of the volume distribution and the cumulative source distribution.

The net mixing effect distribution $M(B,\Phi;t)$ is *positive* in buoyancy-tracer space where more volume is present at time t than has entered the stratified layer up to time t, i.e. there is a net gain in the volume of fluid with buoyancy B and tracer concentration Φ due to mixing. Correspondingly, $M(B,\Phi;t)$ is *negative* where more volume has entered the stratified layer up to time t with buoyancy B and tracer concentration Φ than currently exists at time t, i.e. there is a net loss in the volume of fluid with buoyancy B and tracer concentration Φ due to mixing. The value of M therefore indicates the transfer of volume within W due to mixing; fluid leaves regions of buoyancy-tracer space with $M<0$ and enters regions with $M>0$.

To summarise, the distributions $W, S, \boldsymbol{F}$ and M together describe the flow in terms of its effect on buoyancy-tracer space. The volume distribution W is an instantaneous representation of the amount of fluid within the stratified layer with given ranges of values of buoyancy and tracer concentration. Large values of W indicate large volumes of fluid with a narrow range of b and ϕ, though the fluid parcels corresponding to this range are not necessarily co-located in physical space. The source distribution S represents the volume distribution of fluid that enters the stratified layer from the uniform layer. In the absence of mixing, W would be equivalent to the time integral of S. The mixing flux distribution $\boldsymbol{F}$ represents the redistribution of fluid in buoyancy-tracer space due to mixing. The net mixing flux distribution M captures the change in W relative to time-integrated S via $\boldsymbol{F}$ and indicates where there is accumulation or loss of volume due to mixing.

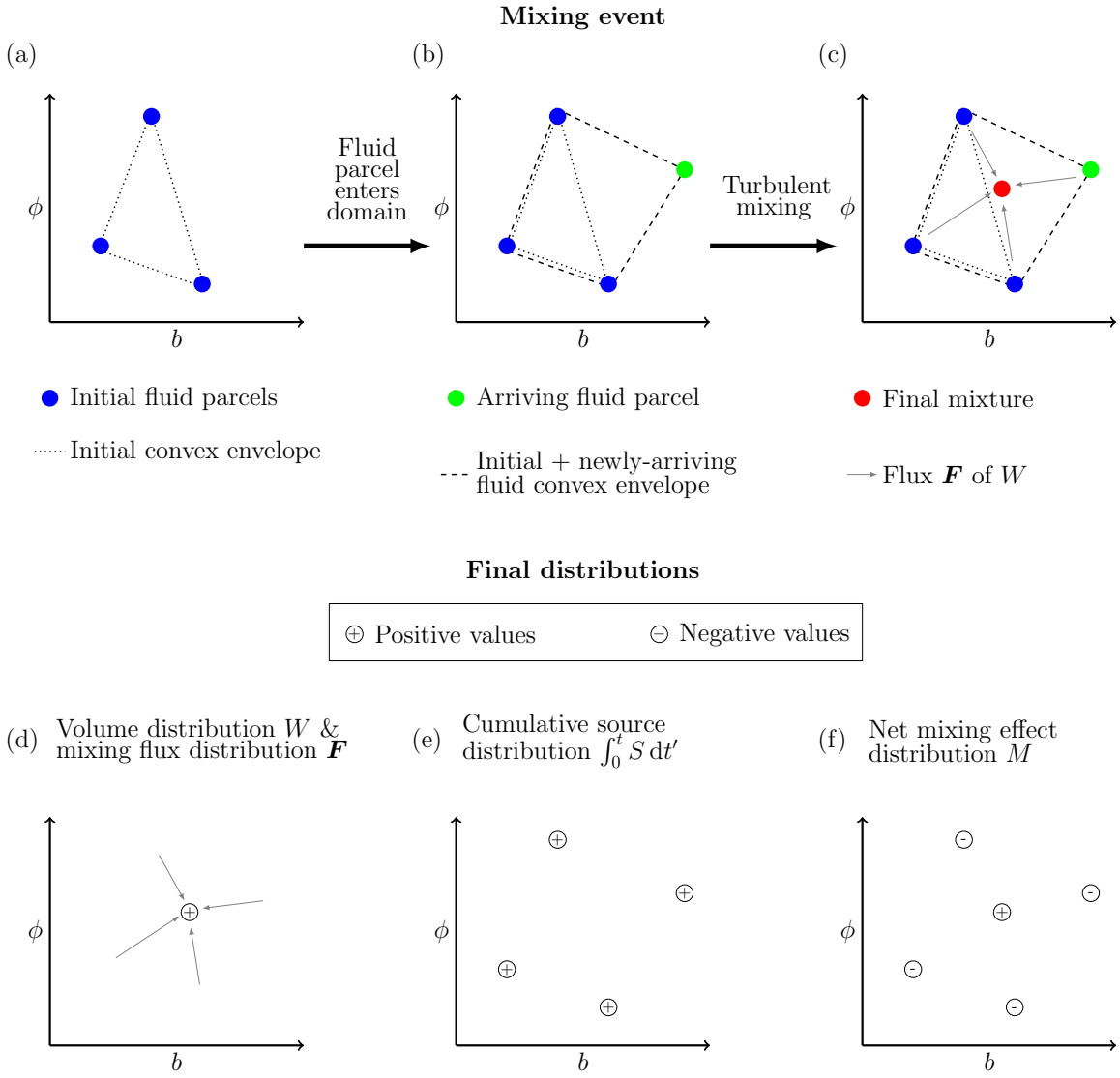

Fig. 3.5 Schematic diagram of the effect in buoyancy-tracer space of an idealised turbulent mixing event between a set of discrete fluid parcels that have entered the stratified layer (blue dots) and a fluid parcel that later enters the stratified layer (green dot). (a), (b) and (c) illustrate the convex envelope property of the volume distribution W, which implies that a mixture of a set of fluid parcels lies within the smallest envelope that contains the distribution of the fluid parcels that are mixed together. The distributions W, $\int S\,\mathrm{d}t$ and M following the idealised mixing event are shown in (d), (e) and (f), respectively. Positive (arbitrary) values of each distribution are indicated by a circled +, negative (arbitrary) values are indicated by a circled − in (d), (e) and (f). The mixing flux distribution vectors $\boldsymbol{F}$ are indicated by grey arrows in (c) and (d).

3.3.2 Idealised example

The effect of an idealised turbulent mixing event on buoyancy-tracer space is illustrated in figure 3.5. The top row shows the volume distribution containing three initial fluid parcels (blue points) which have entered the stratified layer. As turbulent stirring brings these fluid parcels together, another fluid parcel (green point) enters the domain and all four fluid parcels mix. The resulting mixed fluid parcel (red point) is a volume-weighted average of the fluid parcels involved in the mixing event. The bottom row shows the distributions after the mixing event. The volume distribution W is non-zero (and positive) only where the final mixture lies in buoyancy-tracer space and the direction of the mixing flux vectors $\boldsymbol{F}$ indicates the redistribution of volume. The cumulative source distribution $\int_0^t S \, \mathrm{d}t'$ is positive at the values of b and ϕ where the fluid parcels entered the domain and vanishes elsewhere. The net mixing effect distribution M is negative at these points, as volume has been lost, and positive where the mixed fluid parcel lies as volume has been gained. These principles can be used to understand the mixing processes in the physical flow that result in changes in the distribution in buoyancy-tracer space. Whilst it is not possible to isolate distinct fluid parcels that are mixing at any one time, we can identify physical regions of the flow that are subject to turbulent mixing and isolate the corresponding regions of buoyancy-tracer space.

Turbulent mixing acts to homogenise the buoyancy and tracer concentration of fluid parcels. Provided the molecular diffusivities of buoyancy and tracer are equal, a mixture of two fluid parcels lies on a line between the two parcels in buoyancy-tracer space (Penney et al., 2020). Therefore, as the buoyancy-tracer volume distribution W evolves, it is constrained to lie within its own past convex envelope, i.e. the smallest convex set that contains all non-zero points of the distribution. As illustrated in figure 3.5, this convex envelope must include fluid that enters the domain during the mixing process. The convex envelope of the initial volume distribution is indicated by the dotted envelope and the dashed envelope indicates the convex envelope including newly-arriving fluid parcels. We emphasise that the final mixed fluid parcel is contained within the convex envelope of initial and newly-arriving fluid, but not necessarily within the convex envelope of the initial fluid only. The principle of homogenising fluid parcels illustrated in figure 3.5 can be generalised to continuous mixing of fluid in a flow, in which case the convex envelope constraint applies to the volume distribution as a whole. This implies that in the absence of sources the convex envelope reduces over time and converges towards some compact distribution (Penney et al., 2020). In the setup

we consider, fluid entering the stratified layer causes the extremes of the distribution to persist, whilst turbulent mixing acts to continuously shift the buoyancy-tracer characteristics of fluid towards an accumulation region in buoyancy-tracer space.

3.3.3 Numerical implementation

To examine the numerical simulation detailed in § 3.2, we use a discrete formulation of the buoyancy-tracer volume distribution introduced in §3.3.1. We choose the domain V to be tracer-containing plume fluid within the stratified layer. The stratified layer initially corresponds to the volume $z \geq 0$. However, the plume can perturb the bottom of the stratified layer slightly below $z = 0$. We therefore define the domain as the region where $-1 \leq z \leq L_z$, $\phi > \phi_{\min}$, and $b > 0$. As a consequence, the 'reservoir' of environmental fluid where $\phi = 0$ is excluded. In interpreting results, we therefore consider the boundary $\phi = \phi_{\min}$ as a source where volume can enter the distribution from the environment. The entrainment of environmental fluid across this boundary in buoyancy-tracer space into the volume distribution is discussed in §3.3.7 and illustrated in figure 3.8.

The buoyancy and tracer domains are subdivided into N_b and N_ϕ equally sized bins of size $\delta B = (b_{\max} - b_{\min})/N_b$ and $\delta\Phi = (\phi_{\max} - \phi_{\min})/N_\phi$ respectively. We choose $b_{\min} = 0$ and $b_{\max} = 4$ since the largest accessible buoyancy is related to the maximum penetration height (Ansong et al., 2008) which is experimentally predicted to be $z_{\max} \leq 4$ (List, 1982). To accommodate fluctuations in tracer concentration, we choose $\phi_{\max}$ to be larger than the tracer concentration on the plume centreline $2\phi_m(0)$ at penetration height $z = 0$ using the profile predicted by the Morton et al. (1956) plume equations, $\phi_m(z)$, defined in (2.6) (see chapter 2 for details). We use $\phi_{\min} = 10^{-2}$, consistent with the plume threshold introduced in §3.2. Henceforth we use $N_b = N_\phi = 256$.

Denoting the centre of a given bin as (B_i, Φ_j), the associated value of the volume distribution is computed as

$$W_{ij}(t) = \sum_V I_{ij}(\boldsymbol{x}, t)\Delta x \Delta y \Delta z \tag{3.6}$$

where the sum is over all grid points within the domain V, $\Delta x, \Delta y, \Delta z$ are the grid-cell widths, and the indicator $I_{ij}(\boldsymbol{x}, t)$ is defined as

$$I_{ij}(\boldsymbol{x},t) = \begin{cases} 1 & (b(\boldsymbol{x},t) - B_i, \phi(\boldsymbol{x},t) - \Phi_j) \in \left(-\frac{1}{2}\delta B, \frac{1}{2}\delta B\right] \times \left(-\frac{1}{2}\delta\Phi, \frac{1}{2}\delta\Phi\right], \\ 0 & \text{otherwise.} \end{cases} \tag{3.7}$$

The value of $W_{ij}(t)$ therefore represents the total volume within V where the buoyancy lies within $\delta B/2$ of B_i and the tracer concentration lies within $\delta\Phi/2$ of Φ_j. Note that in the continuous formulation, the volume distribution $W(B, \Phi; t)$ defined by (3.1) must be integrated over B and Φ to yield a volume, whilst $W_{ij}(t)$ itself has dimensions of volume and need only be summed over i and j. The continuous and discrete formulations coincide in the limit $\delta B, \delta\Phi \to 0$, such that

$$\lim_{\delta B, \delta\Phi \to 0} \frac{W_{ij}(t)}{\delta B \delta \Phi} = W(B_i, \Phi_j; t). \tag{3.8}$$

The equivalence (3.8) also applies to the discrete mixing flux distribution $\boldsymbol{F}_{ij}(t)$, the discrete source distribution $S_{ij}(t)$ and the discrete net mixing effect distribution $M_{ij}(t)$ defined by

$$\boldsymbol{F}_{ij}(t) = (F^b_{ij}(t), F^\phi_{ij}(t)) = \sum_V I_{ij}(\boldsymbol{x}, t)(\dot{b}, \dot{\phi})\Delta x \Delta y \Delta z, \tag{3.9}$$

$$S_{ij}(t) = \sum_{\partial V} I_{ij}(\boldsymbol{x}|_{z=-1}, t) w(\boldsymbol{x}|_{z=-1}, t)\Delta x \Delta y, \tag{3.10}$$

$$M_{ij}(t) = W_{ij}(t) - \sum_{t'} S_{ij}(t')\Delta t', \tag{3.11}$$

where $\Delta t'$ is the simulation time step shown in table 3.1. In (3.9), $\dot{b}$ and $\dot{\phi}$ are the non-advective terms in the scalar evolution equations (2.15), (2.16) of b, ϕ respectively, as defined in §3.3.1. In (3.10) we have used the fact that $\boldsymbol{n} = \hat{\boldsymbol{k}}$ on the bottom boundary of the domain V.

To validate use of the buoyancy-tracer volume distribution, and to verify that mixing is well represented in our LES, we ensure that quantities of interest are sufficiently well resolved and that the results are not strongly dependent on the model resolution. We primarily focus on the volume distribution W. Figure 3.6 shows the volume distribution $W(b, \phi; t)$ at non-dimensional time $t = 10$ in four simulations with identical parameters (as described in § 3.1) except for the resolution: $128^2 \times 129$, $256^2 \times 257$, $512^2 \times 513$

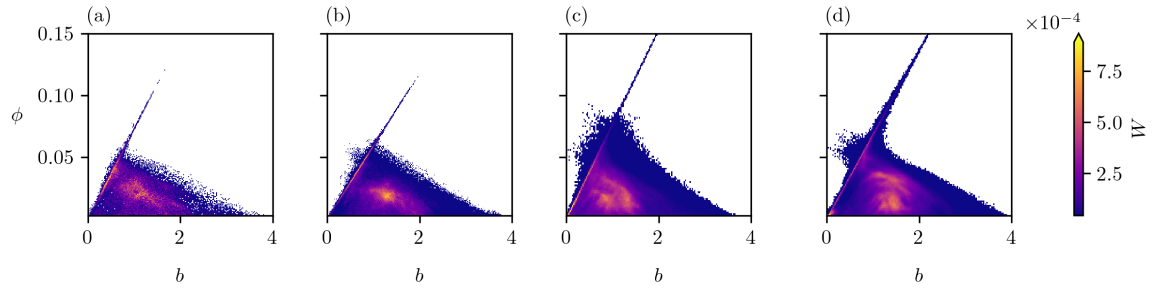

Fig. 3.6 Buoyancy-tracer volume distribution $W(b, \phi; t)$, defined in § 3.3.1, at $t = 10$ in four simulations with resolution $128^2 \times 129$, $256^2 \times 257$, $512^2 \times 513$ and $1024^2 \times 1025$ left to right.

(the main simulation presented in this chapter), and $1024^2 \times 1025$. To aid comparison, W is normalised by the full plume volume $\sum_{ij} W_{ij}(t)$. The structure of the distribution is similar at all resolutions – details of this structure are discussed in the following section. There is some noise in the distribution at lower resolution, since the smaller number of grid cells offers a smaller sample of the values of buoyancy and tracer concentration. The only element of the volume distribution structure that notably changes with resolution is the extent of the source line where $b \propto \phi$. This can be attributed to poor representation of the forcing profile at lower resolution as discussed in § 2.3 which effectively reduces the source buoyancy flux.

Unphysical oscillations referred to as Gibbs ringing (see § 2.3.3) affect the volume distribution in two regions of physical space where particularly strong gradients of b and ϕ arise. Ringing that occurs in the plume cap, above the intrusion, imprints on the value of the buoyancy in the plume, shifting a small amount of volume to the left of the main distribution in buoyancy-tracer space which produces a 'bulge' in the volume distribution. This is evident in figure 3.6, particularly panels (c) and (d). Whilst the effect appears prominent, this is largely a result of the chosen colour map; the bulge contains only 0.77% of the full plume volume at $t = 10$ in the main $512^2 \times 513$ simulation presented in this chapter. To aid clarity, the bulge is excluded from figures presented henceforth. Fluid associated with the bulge is treated as if in the main bulk of the distribution by replacing its buoyancy with the corresponding value in the main distribution (i.e. on the 'source line' which is described in the following section). To handle negative values of b and ϕ we use the absolute value of the buoyancy and tracer concentration fields, $|b|$ and $|\phi|$, to calculate the source distribution S and the mixing flux distribution $\boldsymbol{F}$. Note this has no effect on the calculation except for fluid affected by Gibbs ringing since ϕ and b are positive otherwise.

3.3.4 Results

The discrete formulation of the distributions given in §3.3.3 provides an approximation to the continuous formulation and is presented in all figures shown below. However, the interpretation is the same in both the continuous and discrete formulations and we will refer to the continuous formulation in all discussions. Quantities derived from the distributions are given in both continuous and discrete forms for completeness. In defining the discrete and continuous formulations we use the arguments B and Φ, which represent values of buoyancy and tracer concentration respectively. We treat W, $\boldsymbol{F}$, S and M as functions of b and ϕ to aid clarity, e.g. $W(b, \phi; t)$, with the interpretation that b and ϕ represent values of buoyancy and tracer concentration found in the flow in the same way as B and Φ in §3.3.1 and §3.3.3.

Figure 3.7 shows the buoyancy-tracer volume distribution $W(b, \phi; t)$ (middle row), the source distribution $S(b, \phi; t)$ (bottom row), and x-z cross-sections of the tracer concentration field and buoyancy contours (top row). These results are shown at three time steps representative of stages in the flow evolution as in figure 3.1. The distributions are shown only where non-zero, i.e. regions of buoyancy-tracer space which are not coloured indicate that there is no fluid with buoyancy and tracer concentration in that range. In each snapshot of W, the red dashed lines show the convex envelope that constrains the evolution of the volume distribution. As seen in the figure, the source distribution lies within the convex envelope of $W(b, \phi; t)$. Furthermore, as the plume rises and accesses more buoyant fluid in the surrounding environment, the convex envelope is extended along the $\phi = 0$ axis as new environmental fluid becomes accessible via mixing.

The results shown in figure 3.7 illustrate how the volume distribution captures the dynamics and mixing processes at each stage of the flow evolution. We first note that the source distribution $S(b, \phi; t)$ takes positive values only, since there is only a flow *into* the stratified layer. Furthermore, S is non-zero only on a line through the origin as expected from the linear relationship between b and ϕ in the rising plume. We refer to this as the *source line*. Given that the convex envelope of a set of points on a line segment is the same line segment, mixing of undiluted plume fluid within the plume only redistributes fluid on the source line. When undiluted plume fluid mixes with the surrounding environment, it is moved away from the source line. This offers a clear distinction between undiluted and mixed plume fluid, as illustrated schematically in figure 3.8. In the buoyancy-tracer volume distribution W shown on the middle row of

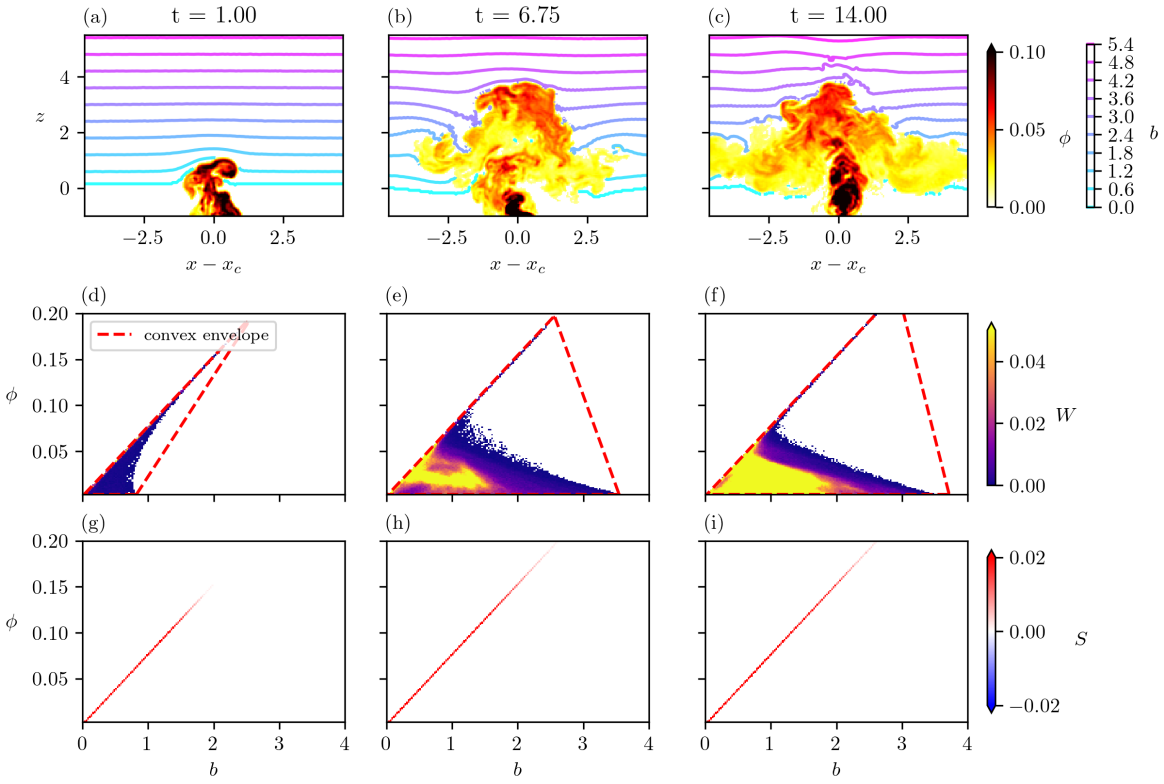

Fig. 3.7 Three instantaneous snapshots showing the evolution of the buoyancy-tracer volume distribution $W(b, \phi; t)$ (middle) and source distribution $S(b, \phi; t)$ (bottom) at non-dimensional times $t = 1, 6.75, 14$ corresponding with figure 3.1. The convex envelope of the volume distribution W at time t is shown as a red dashed line in the middle panel. To aid interpretation, we also show x-z cross-sections of the tracer concentration and buoyancy contours, as in figure 3.2 (top)

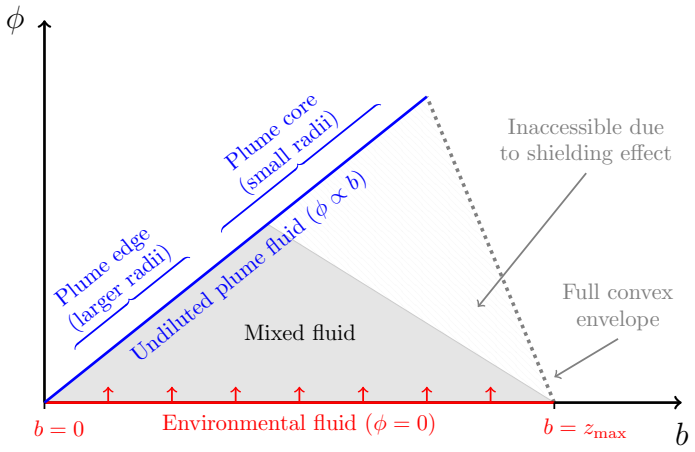

Fig. 3.8 Schematic diagram illustrating the correspondence between regions in physical space and regions in buoyancy-tracer space. Environmental fluid is represented by the b axis where $\phi = 0$ (red), between the bottom of the stratified layer where $b = 0$ and the maximum penetration height where $b = z_{\max}$. Undiluted plume fluid lies on the source line where $\phi \propto b$ (blue), with large b and ϕ in the core of the plume and small b and ϕ towards the edges. Mixed fluid lies between these two lines, within their convex envelope (dotted gray). Some regions of the convex envelope (hatched area) are inaccessible due to the shielding effect of the plume edge (where ϕ is non-zero but small) and the intrusion surrounding the rising plume. Volume entering the distribution due to entrainment of environmental fluid is indicated by the red arrows.

figure 3.7, fluid appearing away from the source line therefore represents a mixture of plume and environmental fluid. Further information on the regions of the undiluted plume that mix with the environment is gained by noting that, owing to the Gaussian profiles of the plume pre-penetration, b and ϕ are larger near the centreline of the plume and smaller towards the edge of the plume (see figure 3.7(c)). Hence fluid near the 'plume edge' lies nearest the origin on the source line whilst fluid in the 'plume core' lies at the extreme end of the source line.

Figure 3.7(a) shows the plume shortly after penetrating the stratified layer and before reaching its maximum penetration height. At this stage, only the edges of the plume are exposed to the environment in the lower part of the stratified layer which has a relatively small buoyancy. We therefore find volume appearing in a small region of the convex envelope closest to the origin in buoyancy-tracer space. In figure 3.7(b), the plume has reached its maximum penetration height and undiluted plume fluid in the plume core, which has until this stage been shielded from the environment by the edges of the plume, overturns and becomes exposed to environmental fluid near $z_{\max}$ with relatively large buoyancy. The volume distribution at this time covers a wider

range of b and ϕ as environmental fluid with a large range of buoyancy is able to mix with much of the undiluted plume fluid lying on the source line. However, note that we do not see mixing between the extreme end of the source line and the environment (see hatched region in figure 3.8). As undiluted plume fluid in the core of the plume rises, turbulent mixing acts to homogenise the buoyancy and tracer concentration within the source distribution, reducing the largest values of b and ϕ near the centreline of the plume. Hence when this fluid is first exposed to the environment in the plume cap, it lies closer to the middle of the source line. We refer to this as the shielding effect. Note that the large values of b and ϕ on the source line appear to persist, and may increase, due to new undiluted plume fluid entering the stratified layer.

Figure 3.7(c) shows the quasi-steady state plume where there is a continuous input of undiluted plume fluid along the source line $\phi \propto b$, mixing between the plume and environment up to values of buoyancy corresponding to heights near $z_{\max}$ and an accumulation of fluid at lower values of buoyancy and tracer concentration corresponding to the radially spreading intrusion. The intrusion dominates the total volume of the plume at late times and is represented by the region of large W at intermediate values of buoyancy and tracer concentration. Note that the intrusion enhances the shielding effect by preventing undiluted plume fluid from accessing the environment before reaching the plume cap.

3.3.5 Quasi-steady state

In this flow, quasi-steady state refers to the long-term behaviour established once an intrusion has formed. In this state, undiluted plume fluid continuously arrives in the stratified layer, mixes with the environment, and accumulates in the intrusion. This means that in quasi-steady state the volume of undiluted plume fluid in the stratified layer remains roughly constant whilst the full plume volume (i.e. the sum of the rising undiluted plume, plume cap and intrusion), and in particular the volume of the intrusion, increases monotonically.

To quantitatively identify the time at which quasi-steady state (QSS) starts, first we define the source line more generally as the region where the cumulative source volume is positive, $\mathcal{S} = \{(b,\phi)|\int_0^t S(b,\phi;t')\,\mathrm{d}t' > 0\}$. Next we can define the volume associated with any region $\mathcal{R}$ of buoyancy-tracer space at time t as

$$V(\mathcal{R};t) = \int_{\mathcal{R}} W(b,\phi;t)\,\mathrm{d}b\mathrm{d}\phi = \sum_{\mathcal{R}} W_{ij}(t). \tag{3.12}$$

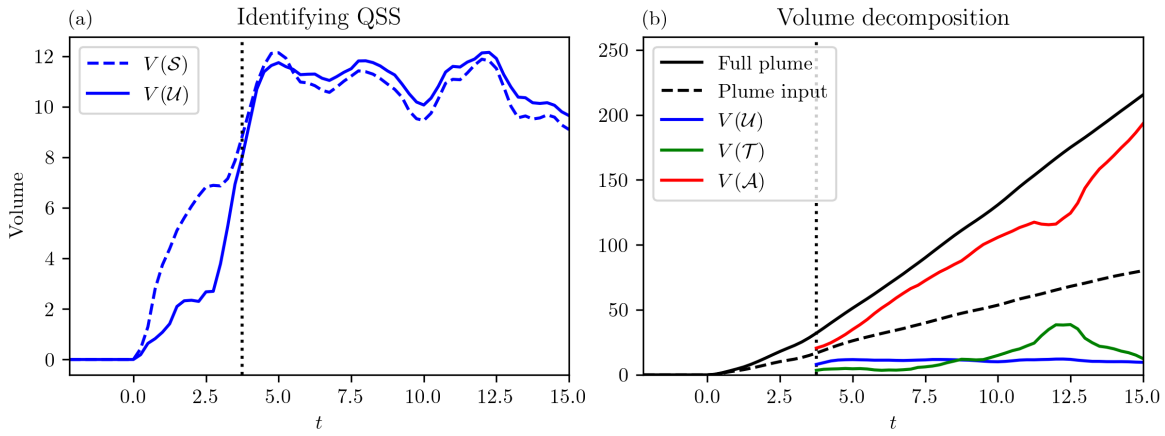

Fig. 3.9 (a) Volume of the source line $\mathcal{S} = \{\int_0^t S(b, \phi; t')\,\mathrm{d}t' > 0\}$ (dashed line) and the region $\mathcal{U} = \{M(b, \phi; t) < 0\}$ (solid line). The start of quasi-steady state (vertical dotted line) is identified as the time when these volumes agree to within 10%. (b) Decomposition of the full plume volume into undiluted plume fluid, plume cap, and intrusion (solid coloured lines) using the partitioning introduced in §3.3.6. The total plume input volume up to time t (black dashed line) is shown for reference.

We expect that in quasi-steady state $\mathrm{d}V(\mathcal{S})/\mathrm{d}t \approx 0$. However, 'plume bobbing' (i.e. the up-and-down motion of the plume cap noted in §3.2) results in some variation of the volume of the source line. The quasi-steady volume of undiluted plume fluid $V(\mathcal{S})$ can also gradually increase over time owing to the shielding effect. We therefore introduce an alternative constraint which utilises the net mixing effect distribution M. As illustrated in figure 3.8, the source line represents undiluted plume fluid arriving in the stratified layer, which introduces volume into the distribution that is eventually mixed away from the source line. In the transient penetration stage, turbulent mixing redistributes fluid on the source line before mixing with the environment. Hence there is some accumulation on parts of the source line and $M > 0$. However, once the plume reaches QSS and mixing with the environment continuously removes volume from the source line, M must become negative. Away from the source line, S vanishes so M is necessarily positive according to (3.5). We define the region $\mathcal{U} = \{(b, \phi) | M(b, \phi; t) < 0\}$ and identify QSS as the time when the volume associated with $\mathcal{U}$, $V(\mathcal{U})$, is within 10% of the volume of the source line $V(\mathcal{S})$. These volumes and the time we identify as the start of QSS, $t_{\mathrm{QSS}} \approx 3.5$, are shown in figure 3.9(a).

3.3.6 Source, transport and accumulation regions

We now restrict attention to quasi-steady state (QSS) $t > t_{\mathrm{QSS}}$, i.e. ignoring any transient dynamics during initial penetration. Here, we discuss the results for M and show that this distribution can be used to partition plume fluid into three classes which identify coherent regions of the plume.

Figure 3.10 shows the net mixing effect distribution in both physical and buoyancy-tracer space at $t = 14$, with the mixing flux distribution vectors $\boldsymbol{F}$ overlaid in buoyancy-tracer space. The distribution is represented in physical space by using the buoyancy and tracer concentration to map between buoyancy-tracer space and physical space, i.e. we plot $M(b(\boldsymbol{x}, t), \phi(\boldsymbol{x}, t); t)$. To avoid confusion between regions of buoyancy-tracer space and the corresponding fluid in physical space, we refer to the former as regions and the latter as classes of fluid. Recall that the net mixing effect distribution, M, quantifies the integrated effect of the mixing flux distribution, $\boldsymbol{F}$, or, equivalently, the volume difference between the volume distribution and the cumulative source distribution, representing the volume change due to mixing. Note that fluid associated with the erroneous bulge formed due to Gibbs ringing is coloured as if it lies on the source line with the same value of ϕ but modified value of b. As expected, we find $M < 0$ on the source line where undiluted plume fluid is continuously supplied before being mixed away into the $M > 0$ region. Environmental fluid is entrained into the plume via mixing and accumulates in the intrusion where M is maximised. We define *class U* as undiluted plume fluid corresponding to the *source region* $\mathcal{U} = \{M < 0\}$, introduced in the definition of QSS in §3.3.5. For convenience, we use the notation $\{M < 0\}$ as shorthand for $\{(b, \phi) | M(b, \phi; t) < 0\}$ henceforth. The mixing flux vectors point along the source line, indicating that mixing within $\mathcal{U}$ is mostly within the plume rather than between the plume and environment, owing to the shielding effect. Once undiluted plume fluid is exposed to the environment, there is a strong mixing flux between $\mathcal{U}$ and the $\phi = \phi_{\min}$ axis where environmental fluid joins the distribution.

As discussed in §3.3.1, we expect volume to accumulate in some region of buoyancy-tracer space. This is clearly demonstrated in physical space, where fluid collects in the intrusion after mixing with the environment. We can distinguish the accumulation region from the 'transport' region through which volume moves to reach the accumulation region by identifying a region in which M is small and approximately constant. In this region, plume fluid is actively mixing with the environment and transporting volume away from the source line, but fluid does not accumulate in this region. Then, fluid

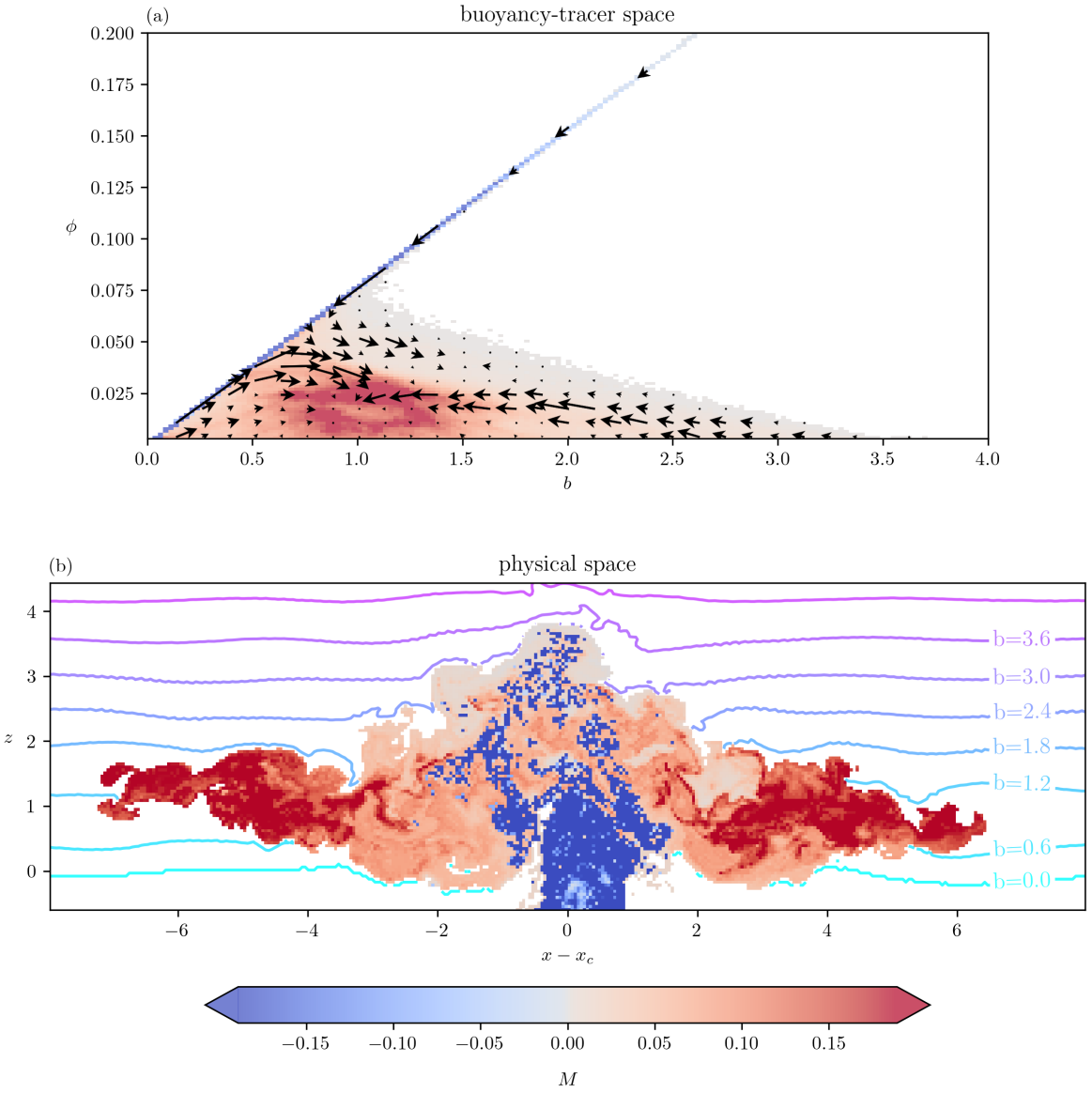

Fig. 3.10 Snapshots at non-dimensional time $t = 14$ of the buoyancy-tracer net mixing effect distribution, $M(b, \phi; t)$, in buoyancy-tracer space (top) and (bottom) in an x-z cross-section of physical space. Buoyancy contours are shown in the surrounding environment. The mixing flux distribution, $\boldsymbol{F}$, is overlaid in the top panel and the vectors are uniformly scaled to be visible.

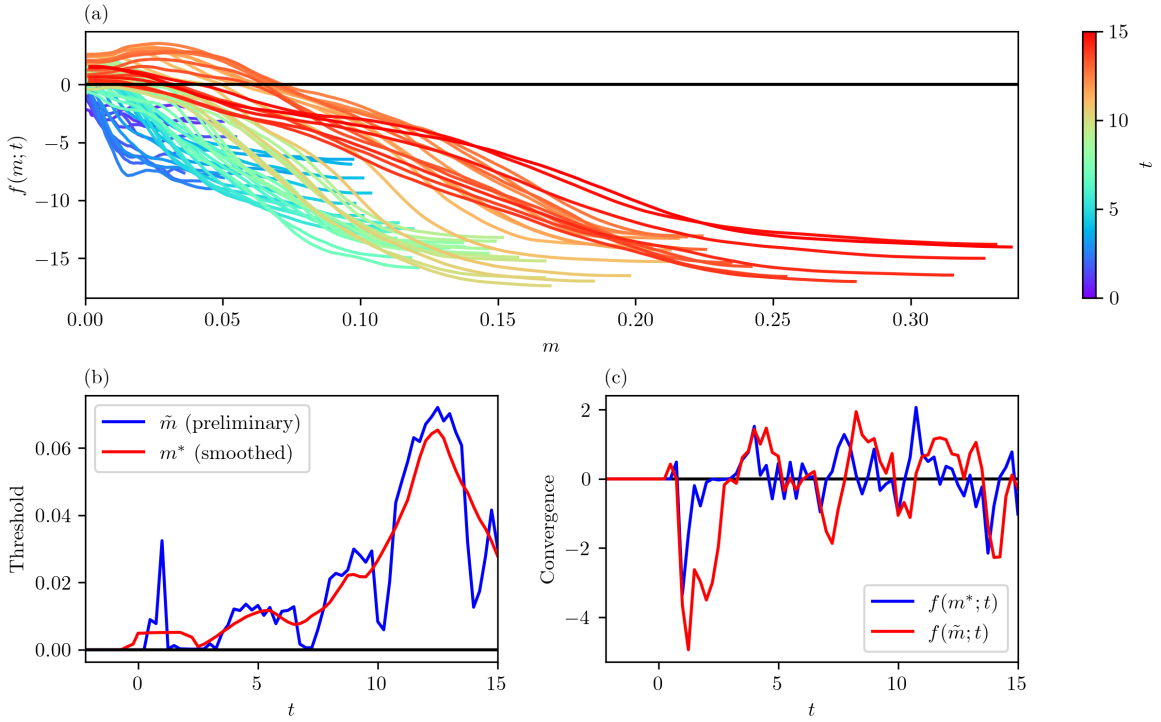

Fig. 3.11 (a) Total flux divergence $f(m;t)$ defined in (3.13) and (b) resulting preliminary and smoothed threshold choices. (c) Error in f from smoothing process.

that has undergone significant mixing and accumulates in the intrusion corresponds with a region where M is increasing with time. The regions are distinguished by a time-dependent threshold $m^*(t)$ such that the *transport region*, where much of the transition from undiluted to mixed plume fluid occurs, is $\mathcal{T} = \{0 < M \leq m^*\}$ and we refer to fluid corresponding to this region as *class T*. The *accumulation region* is $\mathcal{A} = \{M > m^*\}$ with corresponding mixed fluid accumulating in the intrusion referred to as *class A*. The threshold $m^*(t)$ is found by identifying the value m which minimises the total mixing flux convergence $f(m;t)$ associated with a region $\{0 < M \leq m(t)\}$ at each time t, where

$$f(m;t) = \int_{\{0<M\leq m\}} \frac{\mathrm{d}W}{\mathrm{d}t} - S\,\mathrm{d}b\mathrm{d}\phi = -\int_{\{0<M\leq m\}} \nabla_{(b,\phi)} \cdot \boldsymbol{F}\,\mathrm{d}b\mathrm{d}\phi, \tag{3.13}$$

so that the volume that enters the region $\mathcal{T}$ is approximately equal to the volume leaving $\mathcal{T}$. Then, remaining mixed fluid lies in the region $\mathcal{A}$ which must capture the accumulation of mixed fluid, formed from undiluted plume fluid that has entered the stratified layer and entrained environmental fluid.

This method is numerically implemented using the discrete form of the volume distributions. At each timestep k,

1. identify the current maximum value of M throughout buoyancy-tracer space, denoted $\mathcal{M} = \max_{i,j} M_{ij}(t_k)$;

2. for each of N_M test values of M, $m = 0, \ldots, \mathcal{M}$, calculate

$$f(m; t_k) \approx \sum_{i,j|0<M_{ij}\leq m} \left[\frac{W_{ij}(t_{k+1}) - W_{ij}(t_k)}{\Delta t} - S_{ij}(t_k) \right]; \tag{3.14}$$

3. identify the test value $\tilde{m}(t_k)$ which minimises $f(m; t_k)$.

Then, once a threshold $\tilde{m}(t_k)$ has been chosen for each timestep t_k, the final threshold $m^*(t)$ is chosen by applying a rolling average with an appropriate number of timesteps. We choose $N_M = 200$ and a rolling average width of 10 timesteps. The motivation for applying a rolling average is to smooth the threshold $m^*(t)$ so that the regions $\mathcal{T}$ and $\mathcal{A}$ do not grow and shrink dramatically in response to short-term changes in the flux divergence. Figure 3.11(a) shows the total flux convergence $f(m; t)$ for all times post-penetration and figure 3.11(b) shows the time variation of the corresponding preliminary thresholds $\tilde{m}(t)$ and the final thresholds $m^*(t)$. The total mixing flux convergence of class T for the preliminary and final thresholds over time is shown in figure 3.11(c), indicating the (generally small) error introduced by smoothing the thresholds.

The net mixing effect distribution with this partitioning is shown in figure 3.12, with class U coloured blue, class T coloured green and class A coloured red. Within classes U and A, the volume weighted centre-of-mass is shown by a coloured triangle, approximately indicating the position in buoyancy-tracer space towards which mixing acts to move fluid within each class. Internal plume mixing of undiluted plume fluid redistributes volume on the source line towards the blue triangle and homogenisation of mixed fluid in the intrusion accumulates volume near the red triangle. Figure 3.12 demonstrates the correspondence between the regions $\mathcal{U}$, $\mathcal{T}$ and $\mathcal{A}$ and coherent structures of the plume. The source region $\mathcal{U}$ identifies the rising undiluted plume. The accumulation region $\mathcal{A}$ identifies the radially spreading intrusion. The transport region $\mathcal{T}$ corresponds with newly-generated mixtures in the plume cap and subsiding fluid joining the intrusion. The partition of the full plume volume into the undiluted plume, plume cap, and intrusion volume is shown in figure 3.9(b) for $t > t_{\mathrm{QSS}}$. As

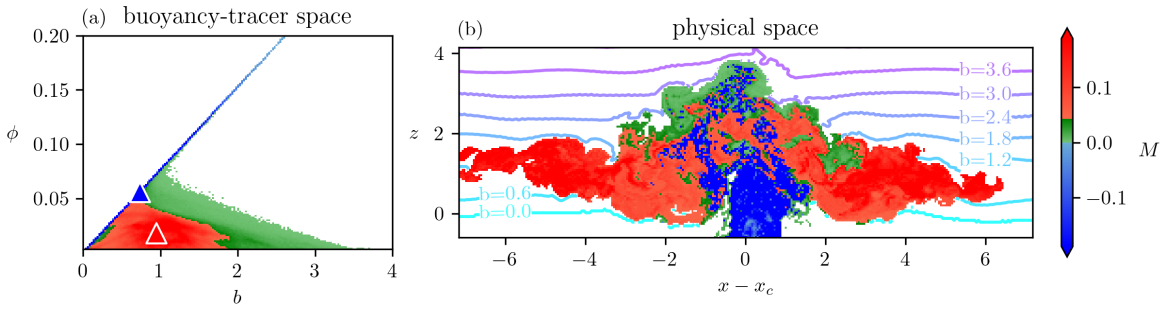

Fig. 3.12 As in figure 3.10, with the distribution partitioned into three regions: $\mathcal{U}$ (blue) where $M \leq 0$, $\mathcal{T}$ (green) where $0 < M \leq m^*(t)$ and $\mathcal{A}$ (red) where $M > m^*(t)$. The threshold $m^*(t)$ minimises the total mixing flux convergence defined by (3.13). Corresponding fluid classes U, T and A (respectively) shown in physical space. Triangles represent the volume-weighted centre-of-mass in class U (blue) and class A (red). Undiluted plume fluid in $\mathcal{U}$ is mixed towards the blue triangle whilst fluid accumulating in $\mathcal{A}$ is mixed towards the red triangle.

expected, we find that the volume of the intrusion (class A) dominates the plume at late times, as the volume of undiluted plume fluid and the plume cap each remain approximately constant.

3.3.7 Entrainment

We calculate the entrained volume $E(t)$ as the difference between the volume of the full plume and the cumulative volume of the source term S up to time t, so that E represents the volume of environmental fluid that has been mixed into the plume up to time t. We have

$$E(t) \equiv \int_{\{W>0\}} W(b,\phi;t)\,\mathrm{d}b\mathrm{d}\phi - \int_0^t \int_{\{W>0\}} S(b,\phi;t')\,\mathrm{d}b\mathrm{d}\phi\mathrm{d}t' \tag{3.15}$$

$$= -\int_0^t \int_{\{W>0\}} \nabla_{(b,\phi)} \cdot \boldsymbol{F}(b,\phi;t')\,\mathrm{d}b\mathrm{d}\phi\mathrm{d}t' \tag{3.16}$$

$$= \int_0^t \int_{\{\phi=\phi_{\min}\}} F_\phi(b,0;t')\,\mathrm{d}b\mathrm{d}t' \approx \sum_{t'}\sum_i \frac{F^\phi_{i,j=0}(t')}{\Delta\phi}\Delta t', \tag{3.17}$$

where the second equality follows from time-integrating (3.2) and the final equality follows from Green's theorem and the fact that the mixing flux $\boldsymbol{F}$ vanishes on the boundary of the $\{W > 0\}$ region except on the surface $\phi = \phi_{\min}$ where environmental

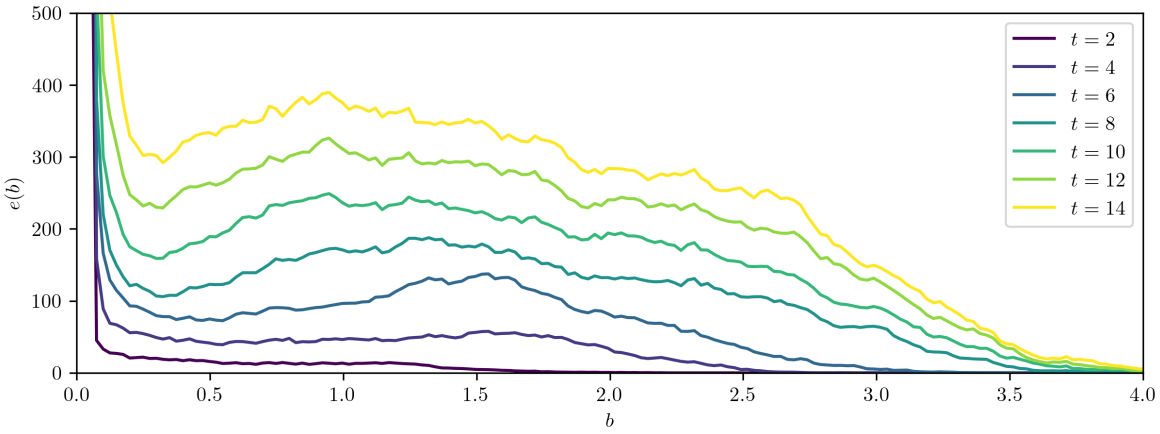

Fig. 3.13 Entrainment profile $e(b,t)$ defined by (3.18) at fixed time intervals post-penetration. The value $e(b,t)$ is the volume of environmental fluid entrained up to time t, per unit buoyancy, as a function of buoyancy b.

fluid enters the volume distribution via entrainment. The numerical calculation of E using the discrete form of the mixing flux distribution F_{ij}^{ϕ} is given by (3.17).

A common definition of an 'entrainment profile' with respect to height is the fractional volume (or mass) increase with height (e.g. De Rooy et al. (2013)). This is not a useful definition in the case where the plume overturns, since the rate of change with height captures multiple components of the plume which act to entrain fluid in (potentially) different ways. Exploiting the linear increase of buoyancy with height in the initially linearly stratified environment, we treat buoyancy as a rough proxy for height and define an entrainment profile with respect to buoyancy,

$$e(b_i,t) = \int_0^t F_\phi(b_i,0;t')\,\mathrm{d}t' \approx \sum_{t'} \frac{F^{\phi}_{i,j=0}(t')}{\Delta\phi\Delta b}\Delta t', \tag{3.18}$$

which represents the volume of environmental fluid entrained up to time t per unit buoyancy. We can then define the volume entrained into a region $\mathcal{R}$ of buoyancy-tracer space which intersects the $\phi = \phi_{\min}$ boundary as

$$E(\mathcal{R},t) = \int_0^t \int_{\{\phi=\phi_{\min}\}\cap\mathcal{R}} F_\phi(b,0;t')\,\mathrm{d}b\mathrm{d}t' = \int_{\{\phi=\phi_{\min}\}\cap\mathcal{R}} e(b,t)\,\mathrm{d}b, \tag{3.19}$$

which is numerically calculated by summing over the indices i in (3.18) which belong to the intersection of $\mathcal{R}$ with the boundary $\phi = \phi_{\min}$. Note this definition implicitly assumes that the intersection between $\mathcal{R}$ and $\{\phi = \phi_{\min}\}$ is time-independent. We define the entrainment rate as the time rate of change of the entrained volume into a

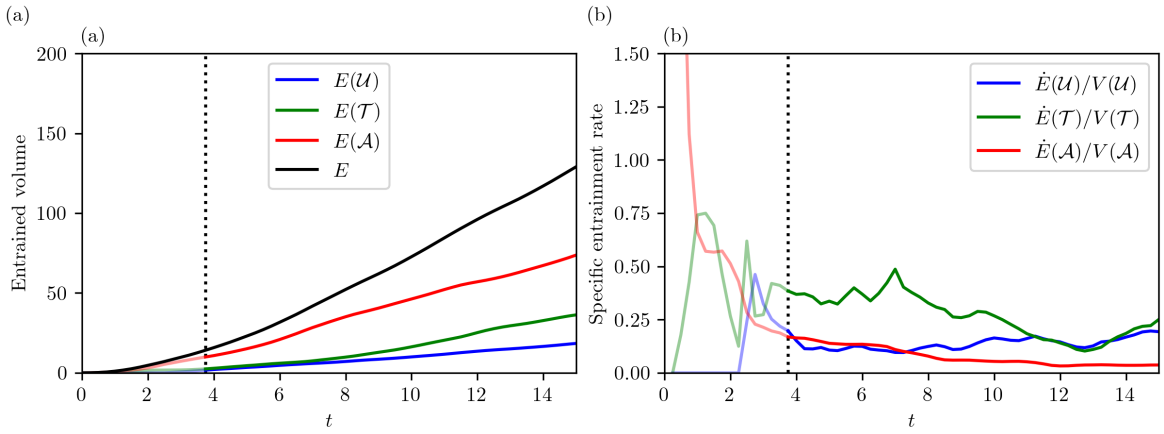

Fig. 3.14 (a) Volume of environmental fluid entrained up to time t (black line) and its decomposition into entrainment into the regions $\mathcal{U}, \mathcal{T}$ and $\mathcal{A}$ (coloured lines). These regions are defined in §3.3.6 and the entrained volumes $E(\mathcal{U}), E(\mathcal{T})$ and $E(\mathcal{A})$ are computed using (3.19). (b) Specific entrainment rate in each class, defined as the ratio of the rate of change of the entrained volume and the volume, e.g. $\dot{E}(\mathcal{U})/V(\mathcal{U})$. In both plots, the vertical dotted line indicates the start of the quasi-steady state.

region $\mathcal{R}$, i.e. $\dot{E}(\mathcal{R}) = \partial_t E(\mathcal{R})$. This quantifies the rate at which volume is entrained into a physical volume represented by a region $\mathcal{R}$ in buoyancy-tracer space. Whilst we expect vigorous mixing at the boundary between a sub-volume of the plume and the environment to result in entrainment, the entrainment rate $\dot{E}$ does not necessarily quantify this since larger volumes would be expected to entrain more volume over time even if the 'strength' of the mixing is weaker (assuming that fluid parcels lying in the region $\mathcal{R}$ of buoyancy-tracer space are approximately co-located in physical space). To quantify the strength of the entrainment into each sub-volume of physical space corresponding to a partitioning of buoyancy-tracer space, we define the *specific entrainment rate* as the ratio of the entrainment rate with the volume of each sub-region itself, i.e. $\dot{E}(\mathcal{R})/V(\mathcal{R})$ for each region $\mathcal{R} = \mathcal{U}, \mathcal{T}, \mathcal{A}$.

Figure 3.13 shows the evolution of the entrainment profile through the simulation. Significant entrainment occurs over a large range of intermediate buoyancy values, indicating that most entrained volume is from the environmental fluid surrounding the intrusion. Using the partitioning introduced in §3.3.6, the entrained volume can be decomposed into the volume entrained into the plume cap $E(\mathcal{T})$, the volume entrained into the intrusion $E(\mathcal{A})$, and the volume entrained just before penetrating the stratified layer $E(\mathcal{U})$. Figure 3.14(a) shows the entrained volume as well as its decomposition. Here, a correction has been made to $E(t)$ to account for numerical artefacts: volume associated with the bulge is included as part of class U when computing the volume

of undiluted plume fluid $V(\mathcal{U})$. Figure 3.14(b) shows the entrainment rate in each of the regions $\mathcal{U}, \mathcal{A}$ and $\mathcal{T}$. The relative contribution of plume cap entrainment and 'lateral' entrainment in the intrusion to the overall entrainment is noted as an open question in the study of fountains by Hunt and Burridge (2015), where the plume cap is analogous to the 'fountain-top'. Here we find that the contribution to the entrained volume from the plume cap (class T) is weak compared with the intrusion (class A) when in quasi-steady state. Under the definition of quasi-steady state for this flow given in section 3.3.5, volume continuously accumulates in the intrusion and hence the volume of the intrusion dominates the volume of the full plume at late times. Since the intrusion spreads radially, there is a greater contact area between the intrusion and the surrounding environmental fluid compared with the plume cap and the rising plume. This allows a greater volume of environmental fluid to be entrained into the intrusion. This suggests that entrainment of environmental fluid from the lower part of the stratified layer into the intrusion is important for setting the centre-of-mass of the quasi-steady state buoyancy-tracer distribution, primarily by diluting the tracer concentration (b is relatively unchanged since the intrusion is, by definition, neutrally buoyant). However, mixing during the overturning process in the plume cap near $z_{\max}$ is important for setting the maximum accessible buoyancy of the volume distribution after mixing, and therefore the extent of the accumulation region in buoyancy-tracer space. The specific entrainment rate is larger in class T than in class A, indicating stronger mixing with the environment in the plume cap in quasi-steady state compared with the intrusion.

3.3.8 Three-stage mixing process

Together, the results presented in this section suggest a multi-stage mixing process in quasi-steady state convective penetration. This is summarised in figure 3.15, in which we show schematics of the volume distribution partitioned into three regions $\mathcal{U}, \mathcal{T}$, and $\mathcal{A}$ of buoyancy-tracer space, and the corresponding classes of fluid in cross-sections of the plume. Fluid moves through each stage of mixing from top to bottom, corresponding with an increasing value of the net mixing effect M, though occasionally the primary mixing stage may be skipped – see following discussion. In each stage, the convex envelope of fluid involved in mixing is indicated by a gray dashed line in (b, ϕ)-space; arrows in (b, ϕ)-space indicate the movement of individual fluid parcels due to the mixing process; and circular arrows in the x-z cross-section indicate the

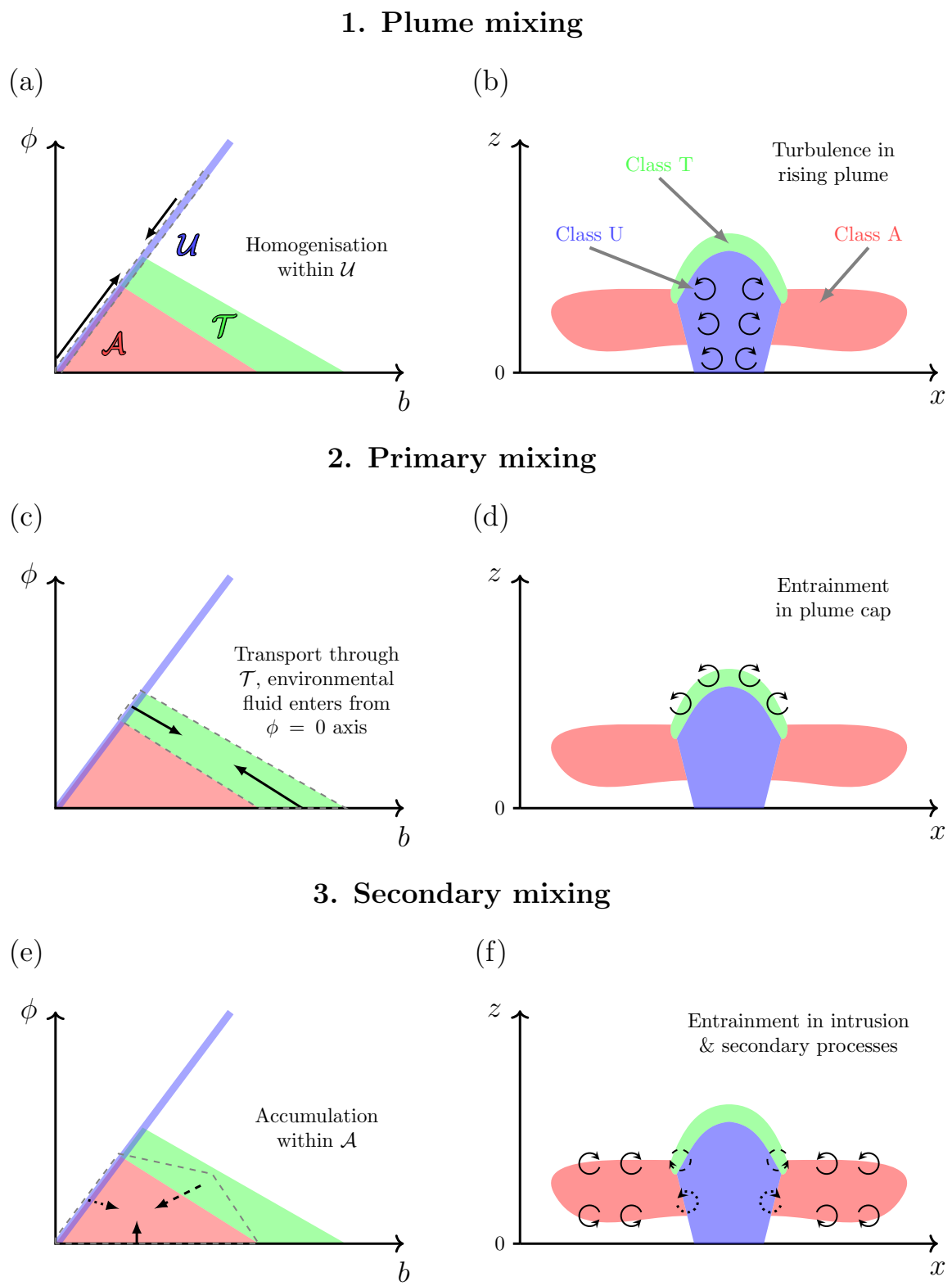

Fig. 3.15 Schematic of the three stage mixing process in quasi-steady state convective penetration of a buoyant plume into a stably stratified layer, identified by the partitioned buoyancy-tracer volume distribution. Buoyancy-tracer space is shown in (a), (c) and (e), with arrows indicating the movement of volume within each mixing stage. The region of buoyancy-tracer space affected by mixing in each stage is indicated by a gray dashed envelope. Physical space is shown in (b), (d) and (f), with circular arrows indicating where mixing is located. In the secondary mixing stage in (e) and (f) the three distinct mixing processes are shown as dotted, dashed and solid arrows, both in physical and buoyancy-tracer space.

location of mixing in physical space. These circular arrows are illustrative and are not intended to indicate the physical nature of the mixing mechanism in each stage. In the secondary mixing stage where multiple mixing processes occur simultaneously, three arrow types are shown which correspond between physical and buoyancy- tracer space. The mixing stages in QSS convective penetration are as follows:

1. Mixing within the rising plume as undiluted plume fluid penetrates into the stratified layer. This fluid is shielded from the surrounding environment. Thus, in buoyancy-tracer space, internal mixing of undiluted plume fluid acts within $\mathcal{U}$ only, homogenising the distribution and consequently moving fluid towards the centre-of-mass of class U indicated by the blue triangle in figure 3.12. This sets the buoyancy-tracer characteristics of plume fluid that is first exposed to environmental fluid near $z_{\max}$.

2. Primary mixing between the plume and environment occurs in the plume cap. This mixing may extend below the plume cap into the intrusion as the mixing timescale is slow compared to the dynamical timescale. In buoyancy-tracer space, the primary mixing stage acts on the undiluted plume fluid concentrated near the class U centre-of-mass and the surrounding environmental fluid with values of buoyancy close to $b = z_{\max}$. The resulting mixtures are transported towards intermediate values of buoyancy as indicated by the mixing flux distribution in figure 3.10(a).

3. After primary mixing with the environmental fluid, subsiding mixed fluid joins the intrusion and homogenises with its surroundings, moving from class T to class A (dashed arrows). A number of mixing processes act on the fluid accumulating in class A. In buoyancy-tracer space, mixing occurs between four regions of fluid as indicated by the convex envelope in figure 3.15. Secondary mixing with the environment occurs as environmental fluid lower in the stratified layer is entrained into the intrusion as it spreads (solid arrows), dominating the volume entrained by the full plume at late times. At the edges of the rising plume, undiluted plume fluid mixes with fluid already in the intrusion, resulting in some fluid parcels moving directly from class U to class A without entering the primary mixing stage (dotted arrows) as seen in figure 3.10(a). Finally, mixing in the interior of the intrusion homogenises the buoyancy-tracer distribution of fluid that accumulates within region $\mathcal{A}$. As fluid moves radially, large volumes of fluid

in class A are concentrated near the centre-of-mass in (b, ϕ)-space, where M (and W) are largest.

3.4 Mixing diagnostics

In this section we use the partitioning introduced in § 3.3.6 to examine the statistics of mixing in each stage of the plume evolution.

3.4.1 Characterising mixing

To characterise the physical nature of the mixing in each stage, we consider the mixing efficiency which relates the total energy expended in turbulent mixing with the actual mixing achieved (e.g. Davies Wykes et al. (2015)). The most useful definition depends on context, e.g. Gregg et al. (2018) for oceanographic contexts and Chemel and Staquet (2007) for an atmospheric setting. In buoyancy-driven stratified flows, the mixing efficiency is quantified by utilising the partitioning of potential energy into available potential energy (APE) and background potential energy (BPE). For an incompressible, Boussinesq flow BPE is the potential energy that is not available to do work whilst APE represents the energy stored in the buoyancy field if the flow is not in gravitational equilibrium (Davies Wykes et al., 2015; Lorenz, 1955). Turbulent mixing irreversibly converts APE into BPE and results in dissipation of turbulent kinetic energy (TKE). The conversion of APE into BPE quantifies the energy expenditure that results in mixing of the buoyancy field and its sum with the TKE dissipation represents the total energy expended by turbulent mixing. The ratio of these two quantities forms the mixing efficiency. Following Howland et al. (2020) and Holliday and Mcintyre (1981), in the case where $\partial_z b$ is constant in the initial stratified environment we may treat the quadratic form of the potential energy,

$$E_p = \frac{1}{2}\langle b'^2 \rangle, \tag{3.20}$$

as a proxy for available potential energy. Here, $b'(\boldsymbol{x}, t) = b(\boldsymbol{x}, t) - z$ is the departure from the linear initial stratification and $\langle \cdot \rangle$ denotes a volume average. We refer to E_p as the perturbation potential energy (PE). A full derivation of the perturbation PE budget is given in appendix 3.B, which follows the derivation as described in Howland et al. (2020) except with SGS terms included. The irreversible conversion of perturbation PE

to BPE that results from the reduction of buoyancy gradients by mixing is captured by the buoyancy variance dissipation rate,

$$\chi = \kappa_{\text{tot}} \left|\nabla b'\right|^2, \tag{3.21}$$

where $\kappa_{\text{tot}} = (\text{RePr})^{-1} + \kappa_{\text{SGS}}^{(b)}$ is the total diffusivity of buoyancy. The buoyancy variance dissipation rate represents the primary sink of E_p. The instantaneous energy dissipated via turbulent mixing is the sum of χ and the dissipation rate of TKE,

$$\varepsilon = \nu_{\text{tot}} \frac{\partial u_i}{\partial x_j} \frac{\partial u_i}{\partial x_j}, \tag{3.22}$$

where $\nu_{\text{tot}} = \text{Re}^{-1} + \nu_{\text{SGS}}$ is the total viscosity. The TKE dissipation rate acts as the primary sink of turbulent kinetic energy. The instantaneous mixing efficiency η is then

$$\eta = \frac{\langle \chi \rangle}{\langle \chi \rangle + \langle \varepsilon \rangle}, \tag{3.23}$$

as in e.g. Howland et al. (2020); Peltier and Caulfield (2003). We use $\langle \cdot \rangle$ to denote a volume average. It is instructive to examine the spatial structure of the dissipation rates. In particular, regions of large χ indicate intense buoyancy gradients and regions of large ε indicate intense turbulent motion.

Further information on the state of turbulence in stratified flows is often drawn from the buoyancy Reynolds number $\text{Re}_b \equiv \langle \varepsilon \rangle / \nu N_0^2$. We define a pointwise activity parameter I and its mean $\langle I \rangle$,

$$I = \frac{\frac{\partial u_i}{\partial x_j} \frac{\partial u_i}{\partial x_j}}{\left|\frac{\partial b}{\partial z}\right|} = \frac{\varepsilon}{\nu_{\text{tot}} \left|\frac{\partial b}{\partial z}\right|}, \quad \langle I \rangle = \frac{\langle \varepsilon / \nu_{\text{tot}} \rangle}{\langle \left|\frac{\partial b}{\partial z}\right| \rangle}. \tag{3.24}$$

The bulk property $\langle I \rangle$ is analogous to Re_b except with SGS contributions to viscosity included. Also, we replace the global buoyancy timescale N_0^{-1} with a local measure of the buoyancy timescale $|\partial_z b|^{-1}$ given by the local buoyancy gradient. This is a more appropriate measure since buoyancy gradients within the plume differ significantly from the background linear stratification and are more representative of the regime in which mixing occurs inside the plume. As with Re_b, the mean activity parameter $\langle I \rangle$ can be interpreted as the ratio of the destabilising effects of turbulent stirring to the stabilising effects of buoyancy and viscosity. Similarly, I may be treated as the ratio of the (local) buoyancy timescale $(\partial b / \partial z)^{-1/2}$ to the timescale of development of turbulent

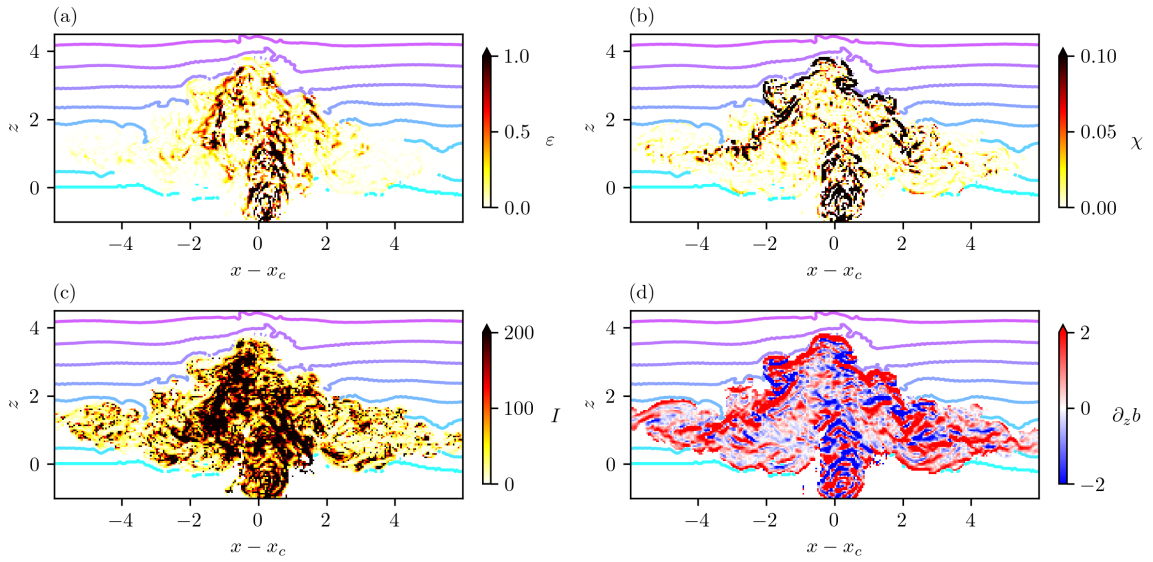

Fig. 3.16 x-z cross sections of the mixing diagnostics ε, χ, I and $\partial_z b$ within the plume, where $\phi > \phi_{\min}$ at non-dimensional time $t = 14$. Mixing diagnostics are defined in §3.4.1. Cross-sections are taken at the plume centreline. Buoyancy contours are shown outside the plume.

effects $(\varepsilon/\nu_{\text{tot}})^{-1/2}$ (Ivey et al., 2008). Regions of large I indicate active turbulence (García-Villalba and Del Álamo, 2011) that is weakly affected by stratification.

3.4.2 Results & discussion

Cross-sections in physical space of the dissipation rates ε and χ, activity parameter I and local buoyancy gradient $\partial_z b$ are shown in figure 3.16. These diagnostics are only shown in the plume, where $\phi > \phi_{\min}$. In the surrounding environment, buoyancy contours are shown. The mixing diagnostics within the plume structures identified by classes U, T and A are quantified by histograms separated into each class in figure 3.17. The colours for each class correspond with those used in §3.3 (e.g. figure 3.15). The black dashed lines show the histograms for the full plume, i.e. all fluid within the stratified layer where $\phi > \phi_{\min}$. This full histogram is normalised to form a PDF. The partitioned histograms are scaled so that the sum of the class U, T and A histograms equals the full plume PDF. These histograms are summarised by volume averages of the mixing diagnostics within each class, as well as the full plume volume average, in table 3.2.

The histograms for TKE dissipation in figure 3.17(a) and buoyancy variance dissipation in figure 3.17(c) are further separated based on where ν_{SGS} and κ_{SGS},

respectively, are non-zero or vanish. This distinction is made since the total viscosity ν_{tot} and total dissipation κ_{tot} are bimodal with a peak where the SGS contribution vanishes (where the simulation effectively switches from LES to direct numerical simulation, such that ν_{tot} and κ_{tot} reduce to the molecular values) and a peak where the SGS contribution is non-zero – see figures 3.17(b) and (d). The separation of the histograms based on non-zero and zero SGS contribution demonstrates that the bimodality of the histograms for ε and χ is a consequence of the bimodal total viscosity and diffusivity alone. The vertical buoyancy gradient histogram is shown on a logarithmic scale since the most extreme values are rare but remain important for mixing.

The results show that the mixing statistics are quantitatively different in each class, suggesting that the mixing regimes differ in each of the three stages of the plume evolution highlighted in §3.3.8. The cross-sections in figure 3.16 show that TKE dissipation ε is particularly large in the rising undiluted plume and in some regions of the plume cap. This is supported by the histograms which show that TKE dissipation is an order of magnitude larger in class U and T compared to class A. The activity parameter is also largest in the rising undiluted plume but comparable in the plume cap and intrusion. The largest values (both positive and negative) of the vertical buoyancy gradient $\partial_z b$ are found in the plume cap (class T) with a clear positive bias. The relatively tighter spread of the $\partial_z b$ distribution in class U in figure 3.17(f) suggests that smaller vertical buoyancy gradients are more common in the undiluted plume fluid as compared with the plume cap and intrusion. This explains the increased magnitude of the activity parameter in class U compared with class T despite similar magnitudes of TKE dissipation; ε is large in both classes but $\partial_z b$ is generally larger in class T and hence I, proportional to the ratio $\varepsilon/\partial_z b$, is smaller in class T. The strongest buoyancy gradients as measured by χ are found in the primary mixing region (class T), where fluid overturns and subsides fluid in the plume cap. Intense buoyancy gradients are also found in the rising column of undiluted plume fluid, but χ is more sparse here than in the plume cap. The strong buoyancy gradients found at the top edge of the plume cap are a result of the relatively less buoyant plume impinging on the more buoyant surrounding environmental fluid. Note that the largest values of χ at the extreme positive tail of the full plume PDF are almost all from class T.

We summarise the mixing regimes described by the mixing diagnostics as follows. In class U, we find active turbulence with large dissipation of TKE, consistent with the undiluted plume being unaffected by the surrounding stratified environment due

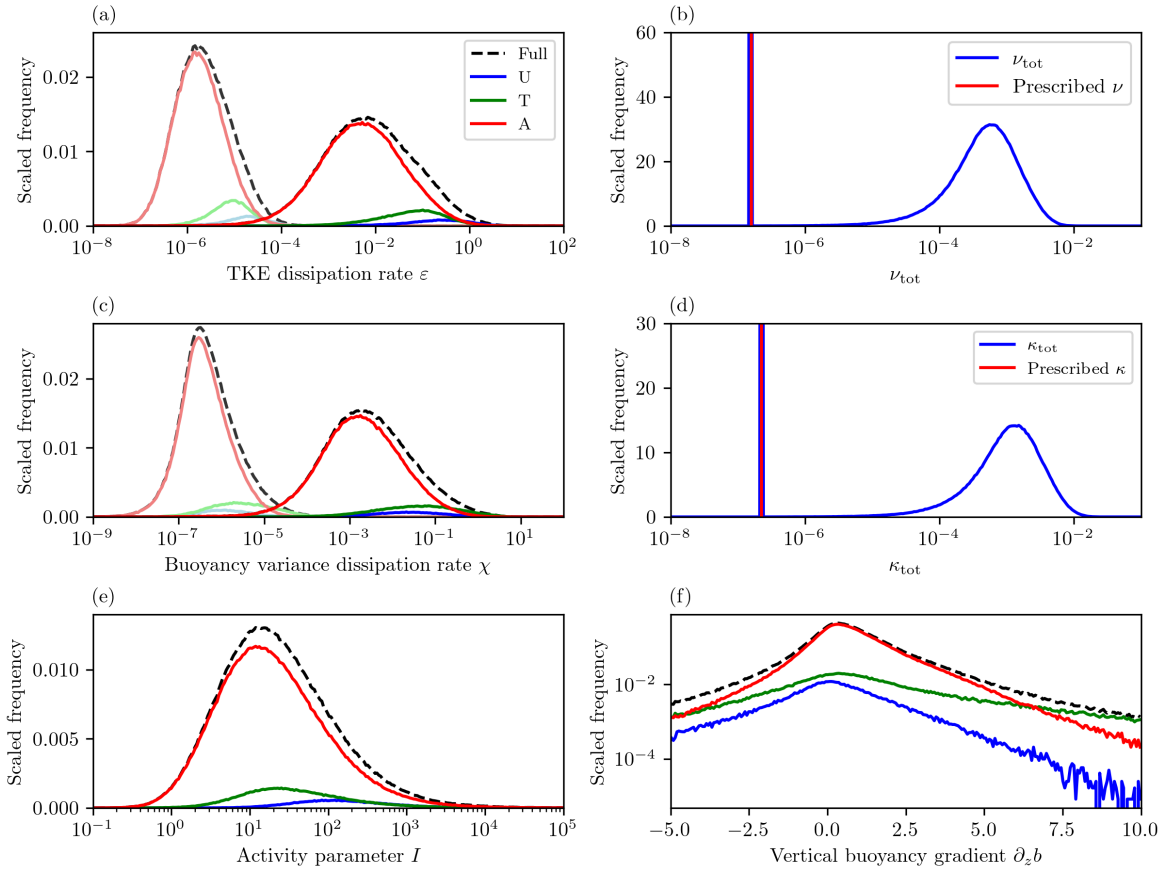

Fig. 3.17 (a), (c), (e), (f) show histograms of the mixing diagnostics ε, χ, I and $\partial_z b$ defined in §3.4.1 (black dashed line) decomposed into histograms within class U, T, A (coloured lines). The histograms within each class are scaled so that their sum is the histogram of the full plume. In (a) and (c), the histograms are further separated into those with $\nu_{\mathrm{SGS}} = 0$ and $\kappa^{(b)}_{\mathrm{SGS}} = 0$ (light colours) and with ν_{SGS} and $\kappa^{(b)}_{\mathrm{SGS}}$ non-zero (usual colours). (b) and (d) show histograms of the total viscosity ν_{tot} and total buoyancy diffusivity κ_{tot} respectively. All histograms are computed at $t = 15$. All vertical axes show the scaled histogram frequency. The scaling is such that the total area is unity for the full plume histograms and the sum of the partitioned histograms equals the full plume histogram. Similarly in (b) and (d) the frequency is scaled so that the total area is unity.

	Full plume	Class U	Class T	Class A
Volume %	100	3.64	9.88	86.5
Activity parameter $\langle I \rangle$	16.8	81.6	18.8	12.8
Vertical buoyancy gradient $\langle \lvert\partial_z b\rvert \rangle$	1.29	1.41	2.88	1.11
TKE dissipation rate $\langle \varepsilon \rangle$	0.0466	0.347	0.127	0.0247
Buoyancy variance dissipation rate $\langle \chi \rangle$	0.0238	0.0595	0.129	0.0103
Instantaneous mixing efficiency η	0.339	0.147	0.504	0.294

Table 3.2 Volume-averaged mixing quantities $\varepsilon, \chi, I, \partial_z b$ and mixing efficiency η defined in §3.4.1 at $t = 15$. Averages are computed over the full plume and within class U, T and A. The percentage of the full plume volume associated with each class is given to indicate the relative contribution of each class to the full plume average.

to the shielding effect. Since the undiluted plume fluid becomes well-mixed during its rise through the uniform layer, there are relatively small buoyancy gradients. As a result, there is relatively little PE dissipation. In class T, rising plume fluid impinges upon the more buoyant surrounding environmental fluid, generating particularly strong vertical buoyancy gradients. Horizontal buoyancy gradients are also generated by overturning. Turbulence advected upwards in class U is carried over into class T but gradually suppressed by the intense buoyancy gradients present in the plume cap, thus reducing the activity parameter. As the turbulent motion stirs these buoyancy gradients, significant PE dissipation occurs and consequently a large mixing efficiency is achieved, around 50%. Finally in class A, which eventually dominates the volume of the full plume as the intrusion grows, the interior of the intrusion becomes well-mixed resulting in weak buoyancy gradients and becomes close to neutrally buoyant with respect to the surrounding environment. There is some indication of a weak stratification and layering forming within the intrusion. Secondary mixing processes between the intrusion and environmental fluid at the bottom of the stratified layer can introduce larger vertical buoyancy gradients and result in some PE dissipation. Overall, TKE dissipation is weak as the buoyant forces driving turbulent motion are weakened by earlier mixing (i.e. TKE has been dissipated in earlier mixing stages). Whilst both TKE and PE dissipation are weak in class A, they are of similar magnitude and hence a greater mixing efficiency is achieved compared with class U. This could be attributed to the continued entrainment of environmental fluid above and below the intrusion, introducing small-scale buoyancy gradients which are acted upon by the weak turbulent motion.

3.5 Conclusions

In this chapter we have analysed a large-eddy simulation of a buoyant pure plume penetrating into a linearly stably stratified layer. We have outlined the buoyancy-tracer volume distribution formalism to examine tracer transport via turbulent mixing. Using this formalism, we developed a method for objectively partitioning buoyancy-tracer space into three regions based on the net change in volume due to mixing. Each of the regions identified corresponds with a class of fluid lying in coherent regions of the plume in physical space. The method distinguishes undiluted plume fluid (class U) from mixtures of plume and environmental fluid. Mixed fluid is further partitioned into newly-generated mixtures in the plume cap that are actively mixing with the environment (class T), and fluid in the radially spreading intrusion that has already undergone significant mixing (class A). In buoyancy-tracer space, the intrusion corresponds with an accumulation region (corresponding with class A) where volume collects and homogenises. Active mixing with the environment in the plume cap moves volume from the source region, through a transport region (corresponding with class T), into the accumulation region. The accumulation region represents the majority of the plume volume at late times. To quantify the mixing regime in each class of fluid, we use the buoyancy variance dissipation rate, turbulent kinetic energy dissipation rate, vertical buoyancy gradient and an activity parameter as diagnostic variables in each sub-volume of the plume. The instantaneous mixing efficiency is also calculated by treating the buoyancy variance dissipation rate as a proxy for the energy dissipated in turbulent mixing that actually results in mixing of buoyancy.

Our results demonstrate a three-stage mixing process in quasi-steady state penetration of a plume into a stably stratified layer. In the first 'plume mixing' stage (class U), turbulence within the undiluted rising plume homogenises the buoyancy-tracer distribution as fluid rises into the stratified layer. The turbulent motion near the centreline of the plume is relatively unaffected by the surrounding stratification owing to a shielding effect from the plume edge and surrounding intrusion. This homogenisation process sets the range of buoyancy and tracer concentration which is first exposed to the environment when fluid overturns near the maximum penetration height. The 'primary mixing' stage occurs as rising fluid impinges on the more buoyant environment, establishing intense buoyancy gradients in the plume cap (class T). The mixing of undiluted plume fluid with the surrounding environment near $z_{\max}$ has a particularly large mixing efficiency. The maximum penetration height approximately determines the

buoyancy of the environmental fluid involved in the primary mixing stage and sets the extent of the buoyancy-tracer convex envelope for the remainder of the mixing process. As newly-generated mixed fluid joins the intrusion and homogenises with fluid already in the intrusion (class A), the intensity of turbulence decreases and buoyancy gradients weaken. Several secondary mixing processes occur in the intrusion. This includes the entrainment of environmental fluid surrounding the intrusion, and mixing with small amounts of undiluted plume fluid at the edge of the rising plume that immediately join the intrusion without entering the plume cap. The volume of environmental fluid entrained into the intrusion during quasi-steady state dominates the volume into the plume as a whole at late times, but entrainment in the plume cap is 'strongest' in the sense of the largest fractional rate of increase in volume.

The statistical properties of turbulence are different in each of the three stages. The undiluted plume core is the most turbulent (as measured by the activity parameter) with TKE dissipation significantly larger than PE dissipation. In the plume cap, the intense buoyancy gradients result in large PE dissipation and small TKE dissipation and hence the entrainment of the surrounding environment achieves a large mixing efficiency, with around 50% of the total energy dissipated by turbulence resulting in mixing. As mixed fluid homogenises in the intrusion and further environmental fluid is entrained, weak buoyancy gradients are continually introduced and eroded by weak turbulence with low TKE dissipation. The mixing efficiency in the intrusion is moderately large, though smaller than in the plume cap.

Models of convective penetration which cannot resolve the processes responsible for mixing and entrainment must parameterise the effects of mixing on the flow. The markedly different statistics in each class suggest that each stage of mixing should be parameterised separately. Parameterisations of mixing in convective penetration could exploit the changing proportion of the full plume volume in each sub-region. For example, at early times before the formation of an intrusion, the plume is dominated by undiluted plume fluid in the plume core with intense turbulence but the mixing efficiency is small. At late times as fluid accumulates in the intrusion, the plume volume is dominated by the intrusion with weaker buoyancy gradients and turbulence and a greater mixing efficiency. Therefore the turbulent statistics associated with the full plume volume must change over time.

The partitioning method presented here, as well as the buoyancy-tracer volume distribution formalism as a whole, offers a way to analyse mixing in numerical simulations of stratified flows. Physical arguments can be made that restrict the regions of

buoyancy-tracer space accessible via mixing, and consideration of terms in the volume distribution budget equation (3.2) highlights the mixing processes that occur and the resulting tracer transport.

Appendix 3.A Buoyancy-tracer volume distribution evolution equation

In §3.3.1 we define the volume distribution $W(B, \Phi; t)$ and its governing equation

$$\frac{\partial W}{\partial t} = -\nabla_{(B,\Phi)} \cdot \boldsymbol{F} + S, \tag{3.25}$$

where $\boldsymbol{F}$ and S represent the flux and boundary source/sink of W respectively. We derive this evolution equation for the volume distribution W by starting with two scalar fields $b(\boldsymbol{x}, t)$ and $\phi(\boldsymbol{x}, t)$ satisfying

$$\frac{\partial b}{\partial t} + \boldsymbol{u} \cdot \nabla b = \dot{b}, \tag{3.26}$$

$$\frac{\partial \phi}{\partial t} + \boldsymbol{u} \cdot \nabla \phi = \dot{\phi}, \tag{3.27}$$

with $\nabla \cdot \boldsymbol{u} = 0$. Here, we use $\dot{b}$ and $\dot{\phi}$ to represent general forcing terms which are replaced in §3.3.1 with the non-advective forcing on buoyancy b and tracer concentration ϕ. Consider a fixed volume V in which (3.26) and (3.27) hold and define

$$g_{\mathcal{F}} = \int_V \mathcal{F}(b, \phi) \mathrm{d}V, \tag{3.28}$$

where $\mathcal{F}(b, \phi)$ is an arbitrary function of b and ϕ. Then

$$\begin{aligned}
\frac{\partial g_{\mathcal{F}}}{\partial t} &= \int_V \frac{\partial \mathcal{F}}{\partial b}\frac{\partial b}{\partial t} + \frac{\partial \mathcal{F}}{\partial \phi}\frac{\partial \phi}{\partial t}\,\mathrm{d}V \\
&= \int_V \frac{\partial \mathcal{F}}{\partial b}\left(\dot{b} - \boldsymbol{u}\cdot\nabla b\right) + \frac{\partial \mathcal{F}}{\partial \phi}\left(\dot{\phi} - \boldsymbol{u}\cdot\nabla\phi\right)\,\mathrm{d}V \\
&= \int_V \frac{\partial \mathcal{F}}{\partial b}\dot{b} + \frac{\partial \mathcal{F}}{\partial \phi}\dot{\phi}\,\mathrm{d}V - \int_V \left(\boldsymbol{u}\cdot\nabla b\right)\frac{\partial \mathcal{F}}{\partial b} + \left(\boldsymbol{u}\cdot\nabla\phi\right)\frac{\partial \mathcal{F}}{\partial \phi}\,\mathrm{d}V \\
&= \int_V \frac{\partial \mathcal{F}}{\partial b}\dot{b} + \frac{\partial \mathcal{F}}{\partial \phi}\dot{\phi}\,\mathrm{d}V - \int_V \nabla\cdot\left(\boldsymbol{u}\mathcal{F}(b,\phi)\right)\,\mathrm{d}V,
\end{aligned} \tag{3.29}$$

since $\nabla \cdot \boldsymbol{u} = 0$. By the divergence theorem we have

$$\frac{\partial g_{\mathcal{F}}}{\partial t} = \int_V \frac{\partial \mathcal{F}}{\partial b}\dot{b} + \frac{\partial \mathcal{F}}{\partial \phi}\dot{\phi}\,\mathrm{d}V + \int_{\partial V} \boldsymbol{u}\cdot\boldsymbol{n}\,\mathcal{F}(b,\phi)\,\mathrm{d}S, \tag{3.30}$$

where ∂V is the boundary of V and $\boldsymbol{n}$ is the *inward* normal on ∂V. This forms an evolution equation for $g_{\mathcal{F}}$. Note that we choose an inward normal so that the final term is positive when fluid flows *into* V.

We now consider the specific choice $\mathcal{F}(b,\phi;B,\Phi) = I(b;B)I(\phi;\Phi)$ where, for a field $\psi(\boldsymbol{x},t)$ defined in V, $I(\psi;\Psi)$ is the indicator function for the subset of V where $\psi(\boldsymbol{x},t) > \Psi$, i.e.

$$I(\psi;\Psi) = \begin{cases} 1 & \psi(\boldsymbol{x},t) > \Psi \\ 0 & \psi(\boldsymbol{x},t) \leq \Psi. \end{cases} \tag{3.31}$$

With this choice of $\mathcal{F}$, the function $g_{\mathcal{F}}$ is the volume of fluid in V with $b > B$ and $\phi > \Phi$. Furthermore $\frac{\partial^2}{\partial B \partial \Phi} g_{\mathcal{F}}$ is the 'volume density', i.e. $\frac{\partial^2}{\partial B \partial \Phi} g_{\mathcal{F}} \delta b \delta \phi$ is the volume of fluid in V with $B < b(\boldsymbol{x},t) < B + \delta b$ and $\Phi < \phi(\boldsymbol{x},t) < \Phi + \delta\phi$. This leads to the choice of name 'buoyancy-tracer volume distribution' for W.

We now simplify the right-hand side terms in (3.30) for the choice $\mathcal{F}(b,\phi;B,\Phi) = I(b;B)I(\phi;\Phi)$. We have

$$\begin{aligned} \int_V \frac{\partial \mathcal{F}}{\partial b} \dot{b} \,\mathrm{d}V &= \int_V \dot{b}\, \delta(b(\boldsymbol{x},t) - B) I(\phi;\Phi)\,\mathrm{d}V \\ &= \int_{S(B,\Phi)} \dot{b}\, \frac{\mathrm{d}S}{\partial b / \partial \boldsymbol{m}} \\ &= -\frac{\partial}{\partial B} \int_V \dot{b}\, I(b;B) I(\phi;\Phi) \mathrm{d}V, \end{aligned} \tag{3.32}$$

where $S(B,\Phi)$ is the surface in V where $b(\boldsymbol{x},t) = B$ and $\phi(\boldsymbol{x},t) > \Phi$, and $\boldsymbol{m}$ is the normal to the surface $S(B,\Phi)$. Similarly,

$$\int_V \frac{\partial \mathcal{F}}{\partial \phi} \dot{\phi} \,\mathrm{d}V = -\frac{\partial}{\partial \Phi} \int_V \dot{\phi} I(b;B) I(\phi;\Phi)\,\mathrm{d}V. \tag{3.33}$$

Then the evolution equation (3.30) with the choice $\mathcal{F}(b,\phi;B,\Phi) = I(b;B)I(\phi;\Phi)$ gives the integral form (3.34) of the evolution equation (3.25), which governs the buoyancy-tracer *cumulative* volume distribution:

$$\begin{aligned} \frac{\partial}{\partial t} \int_V I(b;B) I(\phi;\Phi)\,\mathrm{d}V = &-\frac{\partial}{\partial B} \left[\int_V \dot{b}\, I(b;B) I(\phi;\Phi)\,\mathrm{d}V \right] \\ &- \frac{\partial}{\partial \Phi} \left[\int_V \dot{\phi}\, I(b;B) I(\phi;\Phi)\,\mathrm{d}V \right] \\ &+ \int_{\partial V} \boldsymbol{u} \cdot \boldsymbol{n}\, I(b;B) I(\phi;\Phi)\,\mathrm{d}S. \end{aligned} \tag{3.34}$$

The governing equation for the buoyancy-tracer volume distribution $W(B,\Phi;t)$ is obtained by taking $\partial^2/\partial B\partial\Phi$ of (3.34) to get

$$\begin{aligned}\frac{\partial}{\partial t}\int_V \delta(b(\boldsymbol{x},t)-B)\delta(\phi(\boldsymbol{x},t)-\Phi)\,\mathrm{d}V = &-\frac{\partial}{\partial B}\left[\int_V \dot{b}\,\delta(b(\boldsymbol{x},t)-B)\delta(\phi(\boldsymbol{x},t)-\Phi)\,\mathrm{d}V\right]\\ &-\frac{\partial}{\partial \Phi}\left[\int_V \dot{\phi}\,\delta(b(\boldsymbol{x},t)-B)\delta(\phi(\boldsymbol{x},t)-\Phi)\,\mathrm{d}V\right]\\ &+\int_{\partial V}\boldsymbol{u}\cdot\boldsymbol{n}\,\delta(b(\boldsymbol{x},t)-B)\delta(\phi(\boldsymbol{x},t)-\Phi)\,\mathrm{d}S.\end{aligned} \tag{3.35}$$

Since each integral is taken over the volume V, we are left with functions of B,Φ and t alone. With the definitions

$$W(B,\Phi;t) = \int_V \delta(b(\boldsymbol{x},t)-B)\delta(\phi(\boldsymbol{x},t)-\Phi)\,\mathrm{d}V, \tag{3.36}$$

$$F_b(B,\Phi;t) = \int_V \dot{b}\,\delta(b(\boldsymbol{x},t)-B)\delta(\phi(\boldsymbol{x},t)-\Phi)\,\mathrm{d}V, \tag{3.37}$$

$$F_\phi(B,\Phi;t) = \int_V \dot{\phi}\,\delta(b(\boldsymbol{x},t)-B)\delta(\phi(\boldsymbol{x},t)-\Phi)\,\mathrm{d}V, \tag{3.38}$$

$$S(B,\Phi;t) = \int_{\partial V}\boldsymbol{u}\cdot\boldsymbol{n}\,\delta(b(\boldsymbol{x},t)-B)\delta(\phi(\boldsymbol{x},t)-\Phi)\,\mathrm{d}S, \tag{3.39}$$

then (3.35) can be written as

$$\frac{\partial W}{\partial t} = -\nabla_{(B,\Phi)}\cdot\boldsymbol{F} + S, \tag{3.40}$$

where $\boldsymbol{F} = (F_b, F_\phi)$, which completes the derivation.

Appendix 3.B Potential energy budget

In section 3.4.1 we introduce the perturbation potential energy $E_p = \frac{1}{2}\langle b'^2\rangle$ where b' is the departure from the initial linear stratification, i.e. $b(\boldsymbol{x},t) = b'(\boldsymbol{x},t) + z$. This form of the potential energy may be derived from equation (2.15) of Holliday and Mcintyre (1981) under the assumption of a constant buoyancy gradient in the initial stratified environment. The perturbation PE may be treated as a proxy for available potential energy. To examine the mixing processes in the plume we wish to identify the primary sink of E_p in order to calculate the mixing efficiency. We must therefore form a budget equation for the perturbation potential energy E_p.

We start with the governing equations (2.13) – (2.15) including the SGS terms and drop the hat notation. Substituting the buoyancy decomposition defined above, $b = z + b'$, the buoyancy evolution equation becomes

$$\frac{\partial b'}{\partial t} + w + \boldsymbol{u} \cdot \nabla b' = \frac{1}{\mathrm{RePr}} \nabla^2 b' + \nabla \cdot \left(\kappa_{\mathrm{SGS}}^{(b)} \nabla b' \right) + \frac{\partial}{\partial z} \kappa_{\mathrm{SGS}}^{(b)} + f_b. \tag{3.41}$$

Now, multiplying by the buoyancy departure from the initial stratification b' and volume averaging over a fixed volume V gives

$$\frac{\mathrm{d}E_p}{\mathrm{d}t} = \int_{\partial V} \left[\frac{1}{\mathrm{RePr}} + \kappa_{\mathrm{SGS}}^{(b)} \right] b' \nabla b' \cdot \mathbf{d}\boldsymbol{S} - \langle \chi \rangle - \langle J_b \rangle - \langle b' \frac{\partial \kappa_{\mathrm{SGS}}^{(b)}}{\partial z} \rangle \tag{3.42}$$

where $\langle \cdot \rangle$ denotes a volume average over V. Note that the term involving f_b has been neglected since the buoyancy forcing vanishes above the forcing region and we will apply this perturbation PE budget in the stratified layer. The first term on the RHS represents the diffusive buoyancy flux across the boundary ∂V, which is non-zero only where the plume penetrates the stratified layer. The second term is the volume averaged buoyancy variance dissipation rate

$$\langle \chi \rangle = \left\langle \left(\frac{1}{\mathrm{RePr}} + \kappa_{\mathrm{SGS}}^{(b)} \right) |\nabla b'|^2 \right\rangle, \tag{3.43}$$

which represents the primary sink of perturbation potential energy. The third term is the volume averaged buoyancy flux

$$\langle J_b \rangle = \langle b' w \rangle \tag{3.44}$$

which represents an exchange between kinetic and potential energy. The last term captures the effect of the spatially-varying SGS diffusivity acting on the background stratification.

Chapter 4

Internal waves generated by a plume impinging on a stratified fluid

4.1 Introduction

Internal (gravity) waves propagate horizontally and vertically through stratified fluid, driven by buoyancy forces. Because they vertically transport horizontal momentum, they can significantly influence atmospheric winds and, consequently, weather and climate. The waves can be generated by a variety of processes, including flow over topography, frontogenesis, and convective storms (Fritts and Nastrom, 1992). Of the last of these, internal waves can be excited when the top of a convective system impinges upon the base of the stratosphere. In the absence of mean winds and heating within the body of the plume, it has been proposed that internal waves can be excited by the vertically fluctuating motion of the cloud tops (Fritts and Alexander, 2003). This perspective was drawn into question by laboratory experiments examining internal wave generation by a vertical plume impinging upon a stratified fluid layer (Ansong and Sutherland, 2010). After penetrating into the stratified layer the plume became negatively buoyant, transforming into a fountain. AS10 showed that the frequency spectrum of internal waves emanating from the plume was narrow and not related to the broad-banded spectrum associated with fluctuations of the turbulent/non-turbulent interface of the plume cap (corresponding with the cloud top in Fritts and Alexander (2003)).

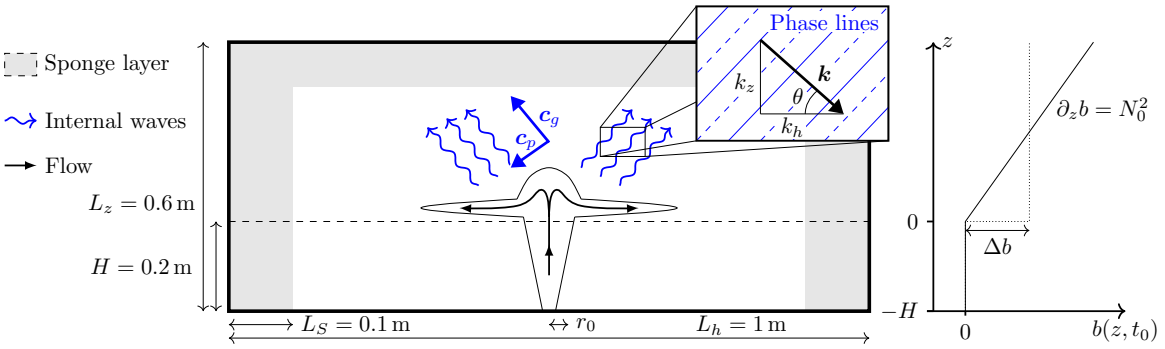

Fig. 4.1 Schematic showing simulation setup (left) and initial buoyancy profile $b(\boldsymbol{x}, t_0)$ (right) in the stratified (solid) and two-layer (dotted) simulations. The stratification begins at a height $H = 0.2\,\mathrm{m}$ above the bottom of the domain (black dashed line). In the two-layer simulation, there is a buoyancy jump Δb at $z = 0$. The plume lies on the centreline $x = y = L_h/2$ of the domain of width $L_h = 1\,\mathrm{m}$ and height $L_z = 0.6\,\mathrm{m}$. Sponge layers shaded in grey. Internal waves indicated by blue wavy lines with wavevector $\boldsymbol{k}$ as shown. The flow within the plume is indicated by solid black arrows.

Here we perform large-eddy simulations (LES) of a plume impinging upon a stably stratified fluid layer in order to gain insight into the mechanism for generation of narrow-banded internal waves from broad-banded convective turbulent motion. Note that the wavelength of the dominant internal waves that we analyse here is always much larger than the grid spacing. In all regions of the domain, the LES captures the energy-containing scales and the smallest resolved motions contain comparatively little energy. We therefore conclude that using LES to analyse the internal wave field is justified. Modifications to the numerical model are detailed in section 4.2. In section 4.3 we describe the flow and compare the generated wavefield observed in a set of simulations in which the squared buoyancy frequency of the stratified layer varies over two orders of magnitude. In section 4.4 we focus on a high-resolution simulation and present analyses which demonstrate that waves originate from within the plume cap rather than at the turbulent/non-turbulent interface. This simulation is compared with a two-layer flow in which waves are not present in order to isolate and examine the influence of waves on the flow.

4.2 Numerical setup

We consider LES with the numerical method and simulation setup described in chapter 2 and shown in figure 4.1 except with minor modifications to allow longer integration times. In particular, the simulation domain width $L_h = 1\,\mathrm{m}$ is wider than in earlier

Sim.	N_0^2 (s^{-2})	$N_h^2 \times N_z$	t_1	t_2	Δ_t	Re ($\times 10^7$)
N0	1	$512^2 \times 257$	2	8	0.02	2.2
N1	10	$512^2 \times 257$	2	8	0.02	1.25
N2	100	$512^2 \times 257$	2	8	0.02	0.71
HR	0.25	$1024^2 \times 513$	3	13	0.02	2.66
2L	0	$1024^2 \times 513$	3	13	0.02	2.66

Table 4.1 Simulation and time window parameters. N_x, N_y, and N_z are the number of grid cells in each direction.

simulations so that – although the intrusion still reaches the simulation boundary – there is a sufficiently wide region without edge effects to examine the internal waves. The wider domain also allows introduction of a sponge layer of width $L_S = 0.1\,\mathrm{m}$ on the four sides of the horizontally periodic domain to prevent low-frequency internal waves with a shallow angle from wrapping around the computational domain. To account for the wider domain, the number of horizontal grid cells here is $N_h = 2(N_z - 1)$ (compared with $N_h = N_z - 1$ in simulations in chapters 2 and 3). The plume source values and the domain size are chosen to be similar to those of the laboratory experiments of AS10 so that, in all simulations, the generated plume has source radius $r_0 = 0.005\,\mathrm{m}$ and integral source buoyancy flux $F_0 = 4.2 \times 10^{-7}\,\mathrm{m^4 s^{-3}}$. In the stratified layer, the squared buoyancy frequency N_0^2 is varied from 1 to $100\,\mathrm{s}^{-2}$ in moderate-resolution simulations and is $0.25\,\mathrm{s}^{-2}$ in a high-resolution simulation. We also include a high-resolution 'two-layer' simulation in which $N_0^2 = 0\,\mathrm{s}^{-2}$ with a buoyancy jump Δb at $z = 0$ (see Talluru et al. (2022) for an experimental study of a similar setup, without a uniform layer, and Hunt and Debugne (2016) for an analytic study). The jump $\Delta b = \frac{1}{2} b_0(z_{\mathrm{ss}})$ is chosen to be half the buoyancy of the initial stratification at the quasi-steady state height z_{ss} in the high-resolution simulation with $N_0^2 = 0.25\,\mathrm{s}^{-2}$, such that the plume penetrates to a similar maximum and quasi-steady state height in both the stratified and two-layer simulations. Relevant simulation parameters are summarised in table 4.1.

All simulations are first run until the plume front reaches the base of the stratified layer, which we define to occur at time $t = 0$. Before beginning our analyses, the wave field is allowed to develop until time $t_1 T_b$, where $T_b = 2\pi/N_0$ is the buoyancy period. We then collect data at a fine temporal resolution $\Delta_t T_b$ until time $t_2 T_b$. Values of the non-dimensional quantities t_1, t_2 and Δ_t for various simulations are listed in table 4.1. Unless otherwise stated, analyses are performed on a spatial window excluding the sponge layers and focused on the stratified layer: $L_S \leq x, y \leq L_h - L_S$

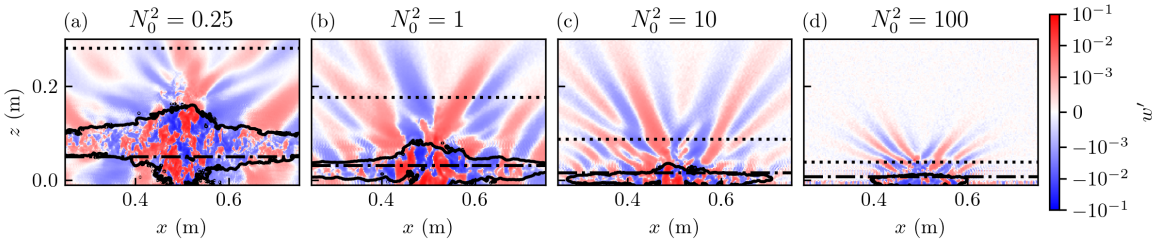

Fig. 4.2 Instantaneous x-z slices of w' showing the internal wave field in the stratified layer in simulations HR, N0, N1 and N2 at $t = 5\,T_b$. Horizontal dotted and dash-dotted lines indicates the height at which spectra are calculated in figure 4.4. The passive tracer contour in black indicates the extent of the plume.

and $0 \leq z \leq L_z - H - L_S$. Throughout this chapter, perturbation components are calculated by subtracting a running mean of the azimuthally averaged field over one buoyancy period T_b. The plume volume flux is small and the large-scale flow reaches a quasi-steady state in which the background stratification and flow vary more slowly than the averaging period, motivating this choice. Practical constraints mean that azimuthal averages are stored for the buoyancy and velocity components only. Analyses are therefore restricted to using horizontal slices. Horizontal averages are weighted by the radial distance from the plume centreline. Finally, note that whilst (2.13)–(2.15) are stated in non-dimensional form, we state all values in dimensional units henceforth to avoid confusion when varying N_0. For clarity and completeness, figure 4.1 shows a version of figure 2.1 with dimensional values used in the simulation setup in this chapter.

4.3 Comparison of plume and wavefield evolution

In each simulation, the plume rises through the uniform layer and penetrates into the stratified layer after around 3 seconds. The plume overturns at its maximum penetration height above the bottom of the stratified layer, $z_{\max} \propto F_0^{1/4} N_0^{-3/4}$, once it becomes relatively less buoyant than its surroundings, before transforming into a fountain and forming a radially spreading intrusion at the neutral buoyancy height. The scaling for $z_{\max}$ was introduced in chapter 2 and fits the simulation data with a proportionality constant 4.4 ± 0.2. A quasi-steady state is reached in which fluid is continuously supplied by the plume to the stratified layer and spreads as an intrusion after mixing with the buoyant environment near the plume cap (see section 3.3) with

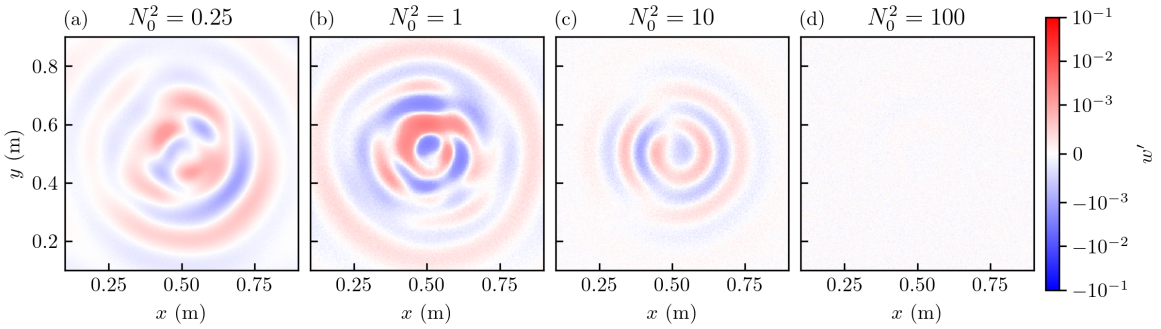

Fig. 4.3 Instantaneous horizontal slices of w' showing concentric rings of the internal wave field at $z = 0.3\,\mathrm{m}$ in simulations HR, N0, N1 and N2 at $t = 5\,T_b$.

mean steady-state height z_{ss} below $z_{\max}$. We ensure that this quasi-steady state is reached before time $t_1 T_b$ when fine-resolution data collection begins. As noted in experimental studies, internal waves are not observed during rise to the maximum penetration height (AS10), instead appearing once plume fluid first overturns.

Figure 4.2 shows instantaneous x-z slices through the plume centreline of the perturbation vertical velocity w' for all simulations and figure 4.3 shows horizontal slices at $z = 0.3\,\mathrm{m}$. Snapshots are taken at $t = 5\,T_b$, during quasi-steady state. A contour of the passive tracer field is shown to indicate the extent of the plume. The internal wave field is evident, with coherent wave beams propagating upwards and outwards in the ambient fluid above the plume cap. The simulated internal waves are consistent with results presented in AS10. Figure 4.4(a) shows the time-averaged vertical energy flux, $F_{\mathrm{wave}} = \int \langle wp \rangle \,\mathrm{d}A$, computed from a Fourier–Bessel decomposition of $\langle w \rangle$ as detailed in AS10. Our results with $N_0^2 = 1$ (closest to the value used by AS10) show that $F_{\mathrm{wave}} \approx O(10^{-7})$ throughout the stratified layer, consistent with AS10 results. Moreover, the similar wave flux in the (high-resolution) $N_0^2 = 0.25$ simulation and the (mid-resolution) $N_0^2 = 1$ simulation verifies that wave generation processes are sufficiently well resolved, i.e. not resolution dependent. The dotted line in figure 4.4(a) shows the theoretical scaling for F_{wave} derived by Couston et al. (2018) for waves generated by Reynolds stresses due to eddies in an (isotropically) turbulent region below a very strongly stratified layer. Whilst there is poor agreement in the weakly stratified cases, the $N_0^2 = 100$ case matches the predicted scaling reasonably well in the far field.

Frequency and horizontal wavenumber spectra are calculated from the (kinetic) energy density $E(k_h, \omega; z) = \frac{1}{2} \sum_i |A^{(u_i')}|^2$, where $A^{(u_i')}(\omega, k_h; z)$ are the 2D fast Fourier transform (FFT) amplitudes of each perturbation velocity component u_i' at height

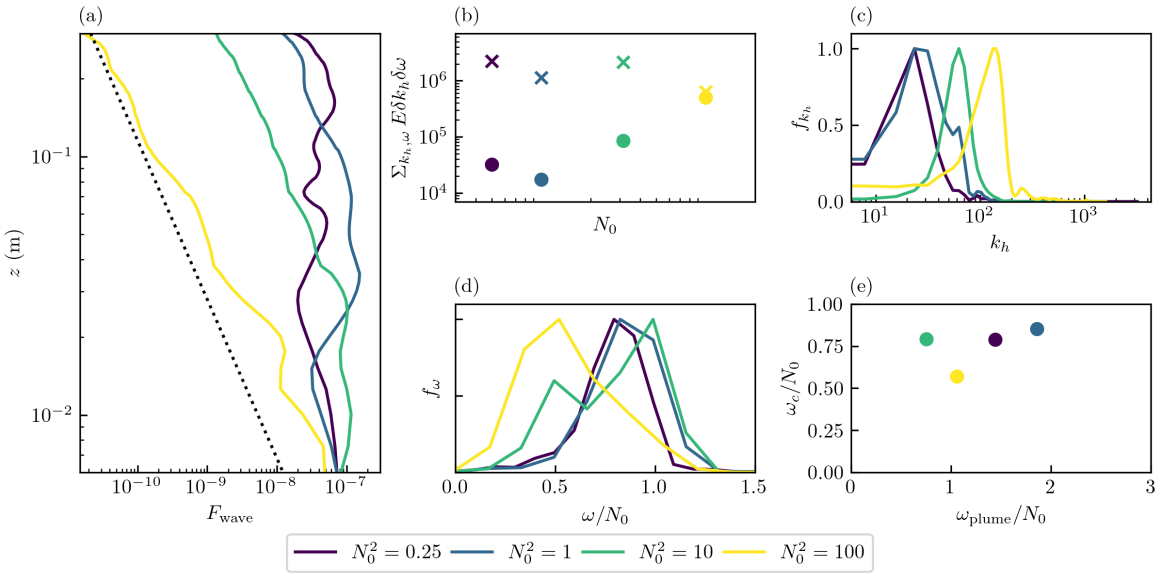

Fig. 4.4 Analyses of simulations HR, N0, N1 and N2 showing (a) time-averaged vertical energy flux, F_{wave}, compared with the theoretical prediction of Couston et al. (2018) for a strongly stratified regime with a stiff interface: $F_{\text{wave}} \sim z^{-13/8}$ (black dotted line), (b) total energy $\sum_{k_h,\omega} E\delta k_h \delta\omega$ at $z/z_{\max} = 0.25, 1.4$ (crosses, circles), (c) horizontal wavenumber spectrum f_{k_h} and (d) frequency spectrum f_ω at $z/z_{\max} = 1.4$. (e) compares the characteristic wave frequency ω_c and the plume forcing frequency ω_{plume}.

z. We apply an energy-corrected Hann window before computing the time FFT. The frequency spectrum is then $f_\omega(\omega; z) = \sum_{k_h} E\delta k_h$ and the horizontal wavenumber spectrum is $f_{k_h}(k_h; z) = \sum_\omega E\delta\omega$ where δk_h and $\delta\omega$ are the spacings in spectral space. Figure 4.4(b) shows the total energy $\sum_{k_h,\omega} E\delta k_h \delta\omega$ above (within) the plume, at $z/z_{\max} = 1.4$ (0.25), indicated by crosses (circles). The two heights are indicated by the dotted and dot-dashed lines in figure 4.2. The energy at heights inside the turbulent plume is approximately two orders of magnitude larger than in the internal wave field above the plume. The separation in energy scales is similar for $N_0^2 = 0.25, 1, 10$ and decreases when $N_0^2 = 100$.

Figure 4.4(c) and (d) shows f_{k_h} and f_ω, respectively, above the plume at $z/z_{\max} = 1.4$. The characteristic horizontal wavenumber $k_{h,c}$, calculated as a power-weighted average from f_{k_h}, scales with N_0 as $k_{h,c} \propto N_0^{0.5\pm0.05}$. Thus the horizontal wavelength of the wave beams decreases with N_0, as is evident in figure 4.2. The frequency spectra in figure 4.4(d) suggest that the characteristic wave frequency ω_c, calculated as a power-weighted average, remains approximately constant as a fraction of N_0 with $0.6 < \omega_c/N_0 < 1$. This is consistent with experiments of the same setup by AS10 which found $0.4 < \omega_c/N_0 < 0.9$. The characteristic wave frequency is not related to

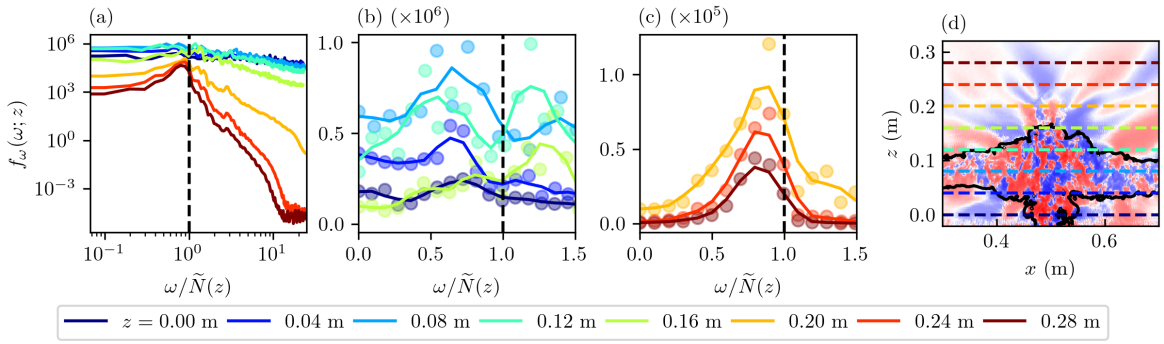

Fig. 4.5 Frequency spectrum $f_\omega(z)$ at a range of heights in simulation HR shown (a) at all heights on a log-log scale, (b) within the plume, and (c) above the plume. Dots indicate the raw spectrum which is smoothed to give the solid lines. Note the different scale between (b) and (c). The heights at which spectra are calculated are indicated by dashed coloured lines in (d), an instantaneous x-z snapshot of w' at $t = 5T_b$ with the same colour bar as in figure 4.2. In (a), (b) and (c) the vertical dashed line indicates $\omega/\widetilde{N} = 1$.

the plume forcing frequency. This is shown by comparing ω_c with the characteristic frequency ω_{plume} of vertical fluctuations of the plume height around the quasi-steady state height z_{ss} (not shown). This comparison is shown in figure 4.4(e) and is consistent with AS10, showing no clear relation between the approximately fixed ω_c/N_0 and the varying ω_{plume}. The question therefore remains: what determines the wave frequency spectrum?

4.4 Analyses

We now focus on analyses of the high-resolution simulation with $N_0^2 = 0.25\,\text{s}^{-2}$, for which the plume cap reaches a steady state height of $z_{\text{ss}} \simeq 0.18\,\text{m}$.

4.4.1 Spectral analysis

Figure 4.5 shows the frequency spectrum f_ω at a range of heights within and above the plume. The raw spectrum is shown as coloured dots and smoothed in frequency space to give the coloured lines. The frequency axis is normalised by the time and horizontally averaged stratification strength $\widetilde{N}(z)$, where $\widetilde{N}(z) = N_0$ sufficiently far above the plume (see § 4.4.2). There is a sharp increase in the stratification strength at the plume cap where intense buoyancy gradients are established between the plume and the more buoyant environment (see chapter 3) whilst the stratification is weaker deep inside the plume. Internal waves can propagate locally where $0 < \omega/\widetilde{N}(z) < 1$.

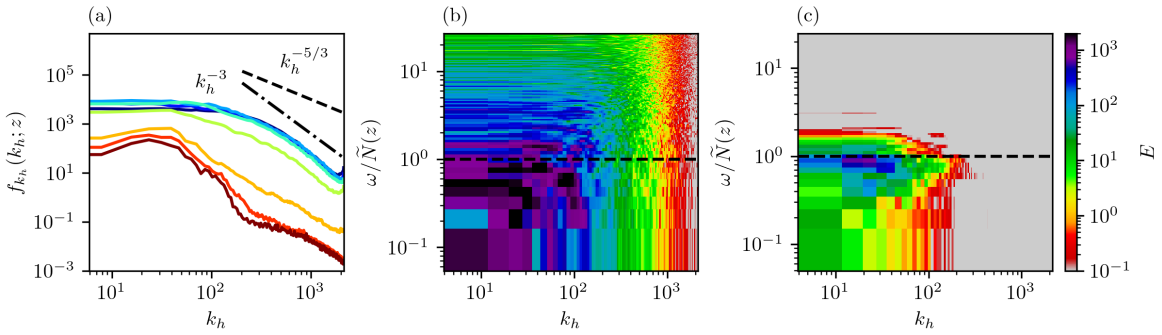

Fig. 4.6 (a) Horizontal wavenumber spectrum $f_{k_h}(k_h, z)$ at a range of heights in simulation HR, compared with an isotropic and axisymmetric turbulence scaling, $k_h^{-5/3}$ and k_h^{-3}, shown as dashed and dot-dashed black lines, respectively. Line colours as in figure 4.5. (b), (c) Energy spectrum E at $z/z_{\max} = 0.25, 1.4$. The black dashed line indicates $\omega/\widetilde{N}(z) = 1$.

Within the plume ($z \leq 0.18$ m, figure 4.5(b)), the frequency spectrum $f_\omega(z)$ is broad and decays with increasing frequency, as expected for turbulent flow. Above the plume (figure 4.5(c)), the spectrum is narrow and peaks around $0.7 \leq \omega/\widetilde{N} \leq 1$. This is consistent with the spectra in figure 4.4(b) and results in AS10. In figure 4.5(b) there is evidence of the spectrum forming a peak at frequencies close to, but larger than, $\widetilde{N}(z)$ at heights $z = 0.12, 0.16$ m in the plume cap.

Figure 4.6(a) shows the wavenumber spectrum $f_{k_h}(k_h, z)$ at a range of heights. The dashed line shows an isotropic turbulence spectrum $f_{k_h} \sim k_h^{-5/3}$ and the dot-dashed line shows a 2D (axisymmetric) turbulence spectrum $f_{k_h} \sim k_h^{-3}$. The axisymmetric scaling most closely matches the observed spectra within the plume, consistent with DNS studies of plumes in a uniform environment, e.g. Van Reeuwijk et al. (2016) whose results are demonstrated in figure 2.11 in chapter 2. Figure 4.6(b) and (c) show the energy (density) spectrum E at $z/z_{\max} = 0.25$ and 1.4 respectively, clearly showing the broad structure within the plume and restriction to small wavenumbers and a narrow frequency band above the plume.

4.4.2 Viscous internal wave model

Taylor and Sarkar (2007) (henceforth TS07) present a simple linear model to explain selection of a dominant range of frequencies in the spectrum of internal waves generated by a turbulent Ekman layer. The method starts with known wave amplitudes $A^{(w')}(\omega, k_h; z_0)$ computed from w' at some initial height z_0. Henceforth we drop the superscript and assume amplitudes are computed from w'. For § 4.4.2 only, we use an amplitude-corrected Hann window instead of energy-corrected. The amplitudes

$A^*(\omega, k_h; z)$ at an arbitrary height z are calculated based on the expected vertical propagation speed and viscous decay rate, assuming that the waves satisfy the linear dispersion relation

$$\omega^2 = \widetilde{N}^2 \frac{k_h^2}{k_h^2 + k_z^2} = \widetilde{N}^2 \frac{k_h^2}{|\boldsymbol{k}|^2}, \tag{4.1}$$

and that the background fields are slowly varying in space and time. Here, following TS07, the spectrum $P(\omega; z)$ is calculated from amplitudes A as $P(\omega; z) = \sqrt{\sum_{k_h} A(\omega, k_h; z)^2}$. Compared with the original study, we move from a Cartesian to an axisymmetric wave geometry, implicitly assuming that the curvature in the waves is small enough to be approximated as plane waves. We account for the energy-conserving amplitude decrease of a spreading axisymmetric wave beam from a virtual point source at height $z_s \leq z_0$ with a factor $\sqrt{r(z_0)/r(z)} = \sqrt{(z_0 - z_s)/(z - z_s)}$ where $r(z)$ is the along-beam distance from the virtual source to the waves at height z (Flynn et al., 2003). In effect z_s is an unknown that may be estimated by choosing the value that minimises the error between predictions and observations. The predicted amplitude $A^*(\omega, k_h; z)$ for a given frequency ω and horizontal wavenumber k_h at height z is then

$$\frac{A^*(\omega, k_h; z)}{A(\omega, k_h; z_0)} = \frac{\widetilde{N}(z_0)}{\widetilde{N}(z)} \sqrt{\frac{z_0 - z_s}{z - z_s}} \exp\left[-\frac{k_h^3}{\omega^4} \int_{z_0}^{z} \widetilde{N}^4(z') \widetilde{\nu}_{\mathrm{tot}}^{\mathrm{plume}}(z') \left(\widetilde{N}^2(z') - \omega^2 \right)^{-1/2} \mathrm{d}z' \right], \tag{4.2}$$

where the total viscosity is the sum of the molecular and SGS viscosity, $\nu_{\mathrm{tot}} = \nu + \nu_{\mathrm{SGS}}$, and $\widetilde{\nu}_{\mathrm{tot}}^{\mathrm{plume}}$ is the time and horizontal average of ν_{tot} within the plume.

Figure 4.7 compares the full horizontal average with the plume average of the stratification strength N and total viscosity ν_{tot}. Figure 4.7(a) also shows two profiles of the spatially varying but time-averaged stratification strength $\widetilde{N}^t(x, z)$, one on the plume centreline and another at the edge of the plume cap. Points close to the plume centreline and near the bottom of the stratified layer where $(\widetilde{N}^t)^2 < 0$ are set to zero and the profile is smoothed with a running mean. The amplitude prediction (4.2) uses the full horizontal average $\widetilde{N}(z)$ since this more faithfully represents the stratification in the region away from the centreline where the waves propagate outward – compare the dotted and dashed green lines in figure 4.7. At heights within the plume, ν_{tot} is between two and three orders of magnitude larger than the molecular viscosity ν, owing to strong turbulence, and limits to ν in the ambient. For the total viscosity, the plume average appears to better reflect the turbulent structure noted in Powell et al. (2024), with stronger/weaker turbulence in the plume cap/intrusion respectively. We therefore use the plume average $\widetilde{\nu}_{\mathrm{tot}}^{\mathrm{plume}}$ in (4.2). The results are qualitatively the same with the

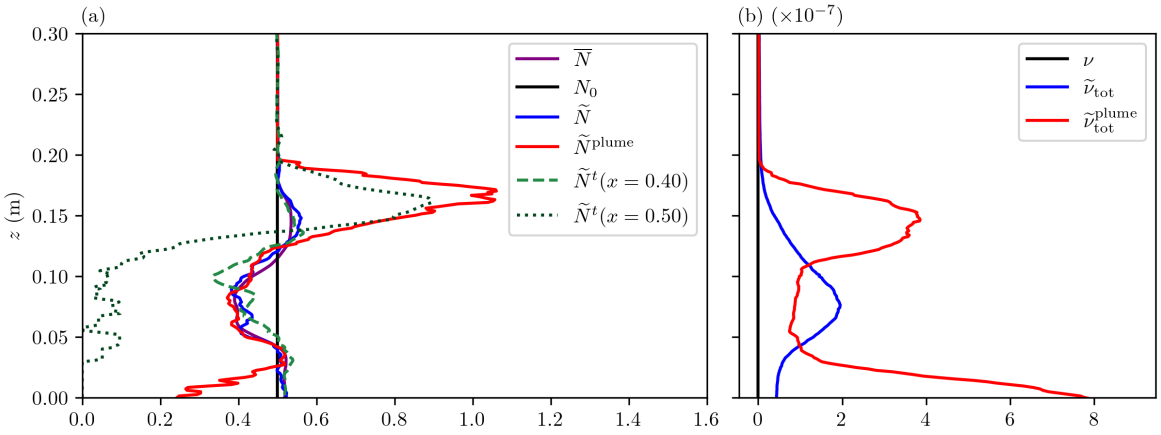

Fig. 4.7 Vertical profiles of (a) time and horizontal average stratification strength $\widetilde{N}$, time and horizontal average within the plume $\widetilde{N}^{\text{plume}}$, time and azimuthal average $\overline{N}$, background stratification N_0, and two profiles of the time-average $\widetilde{N}^t(x, z)$ on the plume centreline $x = 0.5\,\text{m}$ and at $x = 0.4\,\text{m}$. (b) vertical profiles of time and horizontal average total viscosity $\widetilde{\nu}_{\text{tot}}$, time and horizontal average within the plume $\widetilde{\nu}_{\text{tot}}^{\text{plume}}$, and molecular viscosity ν.

optimal choice of z_0 and z_s (see below) when using $\widetilde{\nu}_{\text{tot}}$ instead, but the plume average improves the prediction when z_0 lies within the plume.

As an example of applying the TS07 model, figure 4.8(a) shows the observed spectrum $P(\omega; z_0)$ at the initial height $z_0 = 0.16\,\text{m}$. Using this initial spectrum, the predicted spectrum $P^*(\omega; z)$ at heights $z = 0.2$ and $0.28\,\text{m}$ given a virtual source at $z_s = 0.12\,\text{m}$ are plotted as dashed lines in figure 4.8(b) and compared with the corresponding observed spectrum at the two heights, plotted as solid lines. We compare predictions with observations quantitatively by computing the mean squared error between them and normalising by the mean of the squared observed spectrum. This normalised mean-squared-error (NMSE) averaged over predictions at $0.24\,\text{m} \leq z \leq 0.28\,\text{m}$ every $\Delta z = 0.01\,\text{m}$ is plotted as a function of initial height, z_0, in figure 4.8 for a range of virtual source heights $z_s \leq z_0$. For all values of z_s, the error between predicted and observed waves well above the plume cap is minimised if the initial observation height is $z_0 \geq 0.16\,\text{m}$. This height is close to, but below, the plume cap. The lowest error is achieved with virtual source heights well within the plume, around the height of the intrusion. Even with these optimal parameters, as in figure 4.8(b), the viscous decay model does not perform as well here as in TS07. In particular, whilst the model does capture the selection of high frequency waves and the overall decay in power is well represented, the shape of the spectrum is poorly predicted, with the decay of intermediate frequencies underestimated. TS07 note

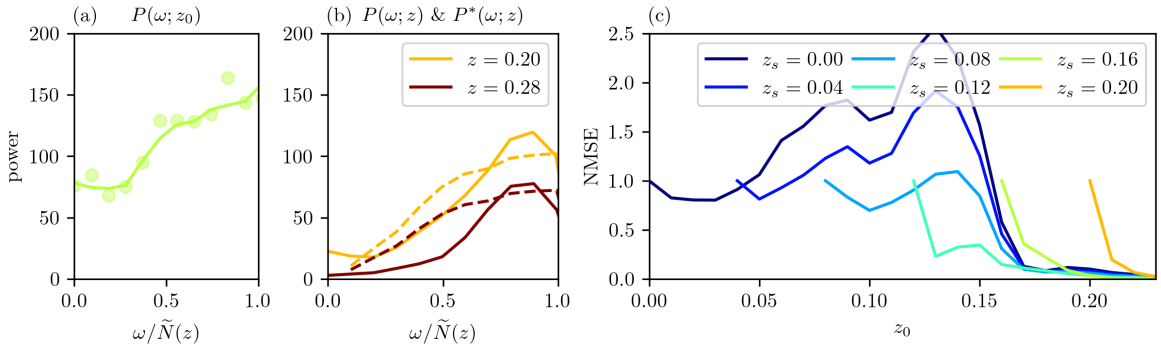

Fig. 4.8 Application of the viscous internal wave model from TS07 to simulation HR. Line colours as in figure 4.5. (a) Observed spectrum $P(\omega; z_0)$ at initial height $z_0 = 0.16\,\mathrm{m}$. (b) Comparison of predicted spectrum $P^*(\omega; z)$ (dashed line) and observed spectrum $P(\omega; z)$ (solid line) with virtual source height $z_s = 0.12\,\mathrm{m}$ at $z = 0.2\,\mathrm{m}$ and $0.28\,\mathrm{m}$. (c) Normalised mean square error between the predicted and observed spectrum, averaged over $0.24\,\mathrm{m} \leq z \leq 0.28\,\mathrm{m}$, as a function of initial height z_0 for a range of virtual source heights $z_s \leq z_0$ (indicated in colour).

that the predicted shape is sensitive to the shape of the initial spectrum. However, a key observation from (4.2) is that the maximum amplitude for a given height z and horizontal wavenumber k_h, assuming a fixed stratification and viscosity and a flat initial spectrum, occurs at $\omega/N_0 = \sqrt{4/5} \approx 0.9$ which is close to the peak in the observed spectra seen in figure 4.5(c) and 4.8(b). Overall, this analysis gives an indication that waves are generated within the body of the plume, though their spectrum there is not clearly established.

4.4.3 Dynamic mode decomposition and ray tracing

Motivated by the implication that internal waves are generated within the plume, we use the dynamic mode decomposition (DMD) method (Schmid, 2010) to extract spatial structures associated with internal wave frequencies $0 < \omega/N_0 < 1$. We then use ray tracing to identify coherent wave beams within these structures. Modal decomposition has previously been used to study internal waves in turbulent flows (Nidhan et al., 2022); the advantage of DMD in particular is that the modes need not be orthogonal. To apply DMD we construct a 'data matrix' X from snapshots of x-z slices through the plume centreline, with four observables: the perturbation horizontal velocity u', buoyancy b', vertical velocity w', and out-of-plane vorticity $\zeta_y = \partial_z u - \partial_x w$. The capability to use multiple observables as input data lends itself to extracting wave modes which are spatiotemporally coherent across all observables and reduces sensitivity to noise.

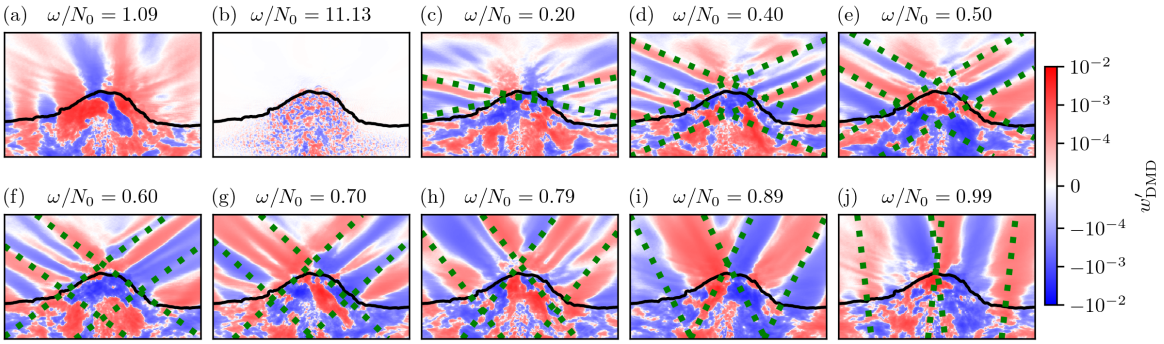

Fig. 4.9 Examples of DMD modes. Here, w'_{DMD} as defined in (4.3) is plotted. (a) evanescent mode, (b) turbulent mode, and (c)–(j) internal wave modes. In (c)–(j), green dotted lines indicate the wave beam angle $\theta = \arccos(\omega_j/N_0)$ derived from the mode frequency ω_j.

The snapshots are restricted to $0.3\,\mathrm{m} \leq x \leq 0.7\,\mathrm{m}$ and $0.04\,\mathrm{m} \leq z \leq 0.3\,\mathrm{m}$ to avoid any transient signal from the front of the spreading intrusion. Each column of the data matrix corresponds to a discrete time $t_k = k\Delta T$ in the range $t_1 \leq t/T_b \leq t_2$ with t_1, t_2 as given in table 4.1. A second matrix X' is constructed by advancing each column by one time step (and assuming periodicity, so that the last column becomes the first). The 'exact DMD' algorithm computes the eigen-decomposition of the linear operator A which advances X to $\mathsf{X}' \approx \mathsf{AX}$. The decomposition yields eigenvalues whose imaginary part represents the temporal frequency ω_j of mode j and real part represents the growth rate (which is close to zero here). The spatial structure of each observable i associated with mode j is given by the eigenvectors $\mathbf{\Phi}_j^{(i)}$ and amplitudes $\mathcal{A}_j$, which come in complex conjugate pairs for real input data. The spatial structure of w' (for example) in mode j with conjugate mode j^* is

$$w'_{\mathrm{DMD}}(\omega_j) = \mathcal{R}\left[\mathcal{A}_j \Phi_j^{w'} + \mathcal{A}_{j^*} \Phi_{j^*}^{w'}\right], \tag{4.3}$$

where $\mathcal{R}$ denotes the real component.

The spatial structure of the DMD modes determined from simulation HR is summarised in figure 4.9. The modes can be broadly categorised into three types: internal wave modes with $0 < \omega_j/N_0 < 1$, evanescent wave modes with $\omega_j/N_0 \gtrsim 1$, and turbulent modes with $\omega_j/N_0 \gg 1$. For the internal wave modes shown, we use the polarisation relation $\omega = N_0 \cos\theta$ to plot dotted lines with the wave beam angle expected from the mode frequency. The close agreement with the phase lines demonstrates that these DMD modes successfully capture internal waves matching the mode frequency.

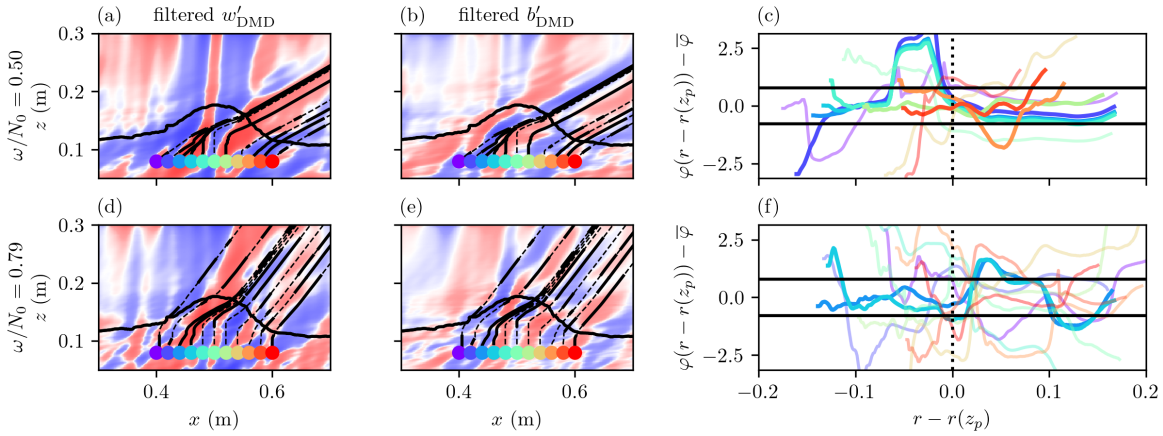

Fig. 4.10 Ray tracing in DMD modes 6 and 7 with $\omega/N_0 = 0.6, 0.7$ from an initial height $z_0 = 0.28\,\mathrm{m}$ and horizontal starting positions $0.4\,\mathrm{m} \leq x_0 \leq 0.6\,\mathrm{m}$ shown by coloured dots. (a), (d): filtered w'_{DMD} and (b), (e): filtered b'_{DMD} as described in the text. Colour bar the same as in figure 4.9. (c), (f): phase perturbation $\varphi - \overline{\varphi}$ as a function of along-beam distance $r - r(z_p)$ from the plume edge at height z_p. Lines are coloured according to starting position and highlighted where 50% of the ray within the plume is coherent. Rays are solid black (thin dashed) in (a), (b), (d), (e) where coherent (incoherent), being coherent when the phase perturbation in (c), (f) lies within the solid black lines of those plots.

We now use ray-tracing to examine whether the time-periodic structures determined by the DMD analysis can be interpreted as internal wave beams originating from within the plume. Linear ray theory implicitly assumes slowly varying background fields, meaning turbulent fluctuations are neglected here. We also neglect the mean flow when propagating rays, which is justified since the group velocity of waves with wavenumber $k_{h,c}$ and frequency ω_c is an order of magnitude larger than the mean velocities in the plume. To avoid interference from left- and right-moving waves, we first apply a Hilbert transform (Mercier et al., 2008) and filter each DMD mode into left-moving internal waves with $k_h < 0, k_z < 0$ and right-moving internal waves with $k_h > 0, k_z < 0$. The filtering introduces artefacts close to the horizontal centreline of the mode, which are reduced by applying a low-pass filter $|k_h| < 250$, but still present. From ray theory, the path of waves in the x-z plane is given by $\mathrm{d}x/\mathrm{d}z = \tan\theta$ in which θ is the angle formed between lines of constant phase and the vertical (Sutherland, 2010). This angle is determined implicitly by the polarisation relation $\omega_j = \widetilde{N}^t(x, z)\cos\theta$, giving θ as a function of x and z for fixed ω_j. Representative profiles of $\widetilde{N}^t(x, z)$ are shown in figure 4.7. For a particular DMD mode, we integrate starting from a height $z_0 = 0.08\,\mathrm{m}$ and at a range of horizontal starting positions $0.4\,\mathrm{m} \leq x_0 \leq 0.6\,\mathrm{m}$. Along each ray, we calculate the phase φ associated with the buoyancy and vertical velocity fields of the

DMD modes. Under the plane wave assumption $b'_{\mathrm{DMD}} = \hat{b}e^{i\varphi}$, $w'_{\mathrm{DMD}} = \hat{w}e^{i\varphi}$, with the amplitudes being related by the polarisation relation $\hat{b}\omega\cos\varphi = \hat{w}N_0^2\sin\varphi$ (Sutherland, 2010). Since the phase is constant along an internal wave beam, we identify coherent sections of each ray where the phase is within $\pi/4$ of the mean phase along the ray, $\overline{\varphi}$: $|\varphi - \overline{\varphi}| \leq \pi/4$. This method implicitly neglects interference from out-of-plane wave beams. Motivated by the coherent wave beam structure observed in horizontal cross-sections in figure 4.3, we assume that this interference is weak.

Figure 4.10 shows an example of the ray-tracing results for modes with $\omega_j/N_0 \approx 0.5, 0.8$. Rays are shown as thick solid black lines where coherent and dashed otherwise. The mean-subtracted phase along each ray is shown by coloured lines in figure 4.10(c) and (f). It is expected that there is some noise in the phase, especially where $\widetilde{N}^t(x,z)$ is noisy near the plume boundary. The artefacts introduced by filtering the waves, as well as the imperfect nature of the modal decomposition, also contributes noise. Nonetheless there are several rays in each mode along which the phase is approximately constant. This demonstrates that internal waves apparent in the region above the plume can be traced to a source within the plume.

4.5 Comparison with a two-layer flow

In this section we compare the high-resolution stratified simulation HR with the high-resolution two layer simulation 2L.

4.5.1 Two-layer flow structure

The two-layer and stratified flows are structurally similar but the upper uniform layer does not permit propagation of internal waves in the environmental fluid surrounding the plume in the two-layer case. We compare the two flows to asses the influence of internal waves on the flow spectra. Figure 4.11 shows the turbulent vertical velocity w' in both simulations. In the two-layer flow, the plume is less buoyant than the upper uniform layer and (by design) penetrates to a similar $z_{\max}$ and z_{ss} as in the stratified flow due to its excess momentum at penetration. Mixtures of plume and environmental fluid in the intrusion are more buoyant than the lower layer but less buoyant than the upper layer, so the intrusion spreads along the interface at $z = 0$. It is clear from the figure that no internal waves propagate through the stratified environment. However, there is a spatially oscillating signal in a thin layer immediately surrounding the plume

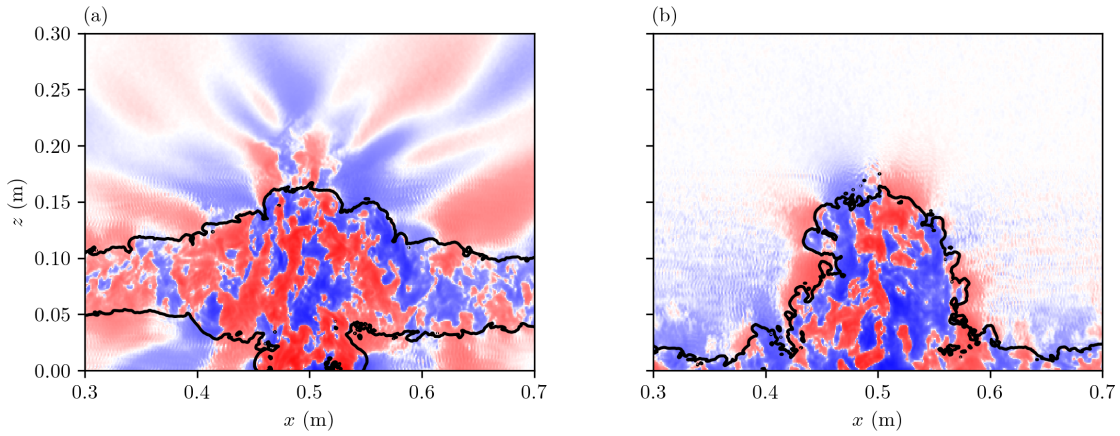

Fig. 4.11 Turbulent vertical velocity w' at time $t = 5T_b$ in simulation HR (left) and 2L (right).

cap which can likely be attributed to evanescent modes. In the remainder of the upper layer, the turbulent vertical velocity is significantly weaker in simulation 2L compared with simulation HR and no wave signal is apparent at all above $z = 0.2\,\mathrm{m}$.

Figure 4.12 shows profiles of the stratification strength and total viscosity as in figure 4.7 but for simulation 2L. Unlike simulation HR, where fluid within the plume was more weakly stratified than the environment other than in a thin layer at the top of the plume, here the stratification within the plume is stronger than the surrounding (uniform) environment at all heights. The time averaged profile $\widetilde{N}^t$ at $x = 0.4$, as well as the time and horizontal average $\widetilde{N}$ and time and azimuthal average $\overline{N}$, shows a weak stratification in the ambient fluid above the intrusion which vanishes above $z = 0.2\,\mathrm{m}$. There is a peak in the stratification strength at the top of the plume as in the stratified case. However, the structure of the total viscosity profile differs between simulation HR and 2L; in the two-layer case there is no sharp peak in the total viscosity at the top of the plume cap. Instead, the profile is flatter and the total viscosity throughout $0.05 \leq z \leq 0.15$ is similar to that found in the plume cap in the stratified case. Together this suggests that, whilst sharp buoyancy gradients form at the top of the plume in the two-layer case, the most vigorous turbulence is not confined to a thin layer at the interface between the plume cap and environment as in the stratified case.

4.5.2 Spectral analysis

Here we repeat the spectral analysis shown in § 4.4. Figure 4.13 shows frequency spectra at various heights in the domain within and above the plume, which can be

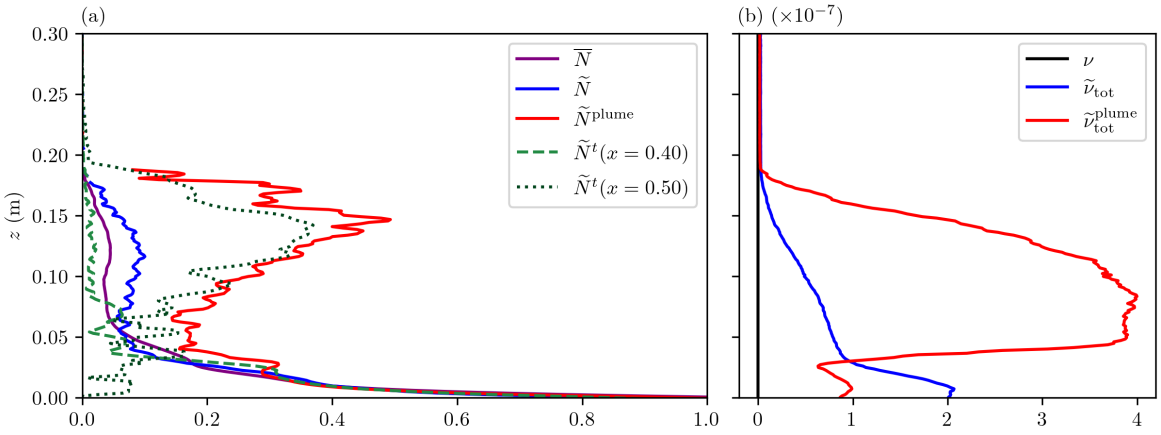

Fig. 4.12 Vertical profiles of (a) stratification strength and (b) total viscosity as in figure 4.7 but for simulation 2L.

compared with figure 4.5. Figure 4.14 shows the wavenumber and energy spectra which can be compared with figure 4.6. Although $N_0 = 0$ in simulation 2L, in figure 4.13 and 4.14 we normalise the frequency axis by $N_0 = 0.5\,\text{s}^{-1}$ to aid comparison with the relevant figures for simulation HR. In the frequency spectra, the power is similar at heights within the plume but an order of magnitude smaller above the plume (note the exponent shown above the plot). In simulation HR, within the plume, the spectral power increased with height up to the intrusion and then decreased (see figure 4.5(a)). In the two-layer case the spectral power also peaks at the height of the intrusion which now lies at $z = 0$. Above the plume, the spectra peak at $\omega = 0$ and rapidly decay with increasing frequency. The wave signal identified in figure 4.11 in a thin layer surrounding the plume cap corresponds with the peak in the spectrum at $z = 0.2\,\text{m}$ with $\omega \approx 0.25$. This frequency is close to but slightly smaller than the buoyancy frequency within the plume in simulation 2L. As the stratification decreases with height, these waves become evanescent above the plume and hence their amplitude decays exponentially. Thus the peak in the frequency spectrum is less pronounced at $z = 0.24\,\text{m}$ and absent at $z = 0.28\,\text{m}$.

Within the plume, the wavenumber spectrum in simulation 2L follows the same axisymmetric scaling $f_{k_h} \sim k_h^{-3}$ observed in simulation HR. It is perhaps surprising that the axisymmetric turbulence identified in the uniform layer in chapter 2 retains this spectrum in the upper layer (both uniform and stratified) since the flow is more complex and subject to increased shear as rising plume fluid overturns. Above the plume the spectral power is much lower in simulation 2L compared with HR, as seen in the frequency spectra, and drops off at smaller wavenumbers. Comparing the relative

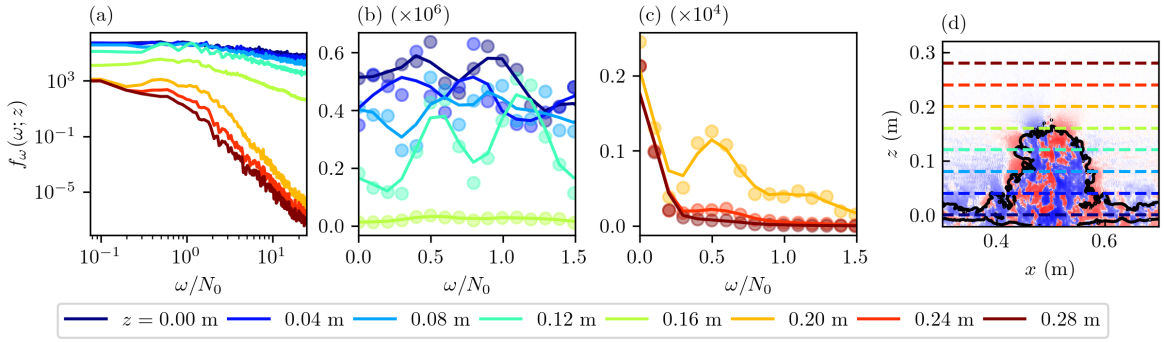

Fig. 4.13 Frequency spectra (a) at all heights, (b) within the plume and (c) above the plume and (d) w' at $t = 5T_b$ with the heights marked by coloured dashed lines as in figure 4.5 but for simulation 2L. The frequency axis is normalised by $N_0 = 0.5$ to aid comparison with simulation HR.

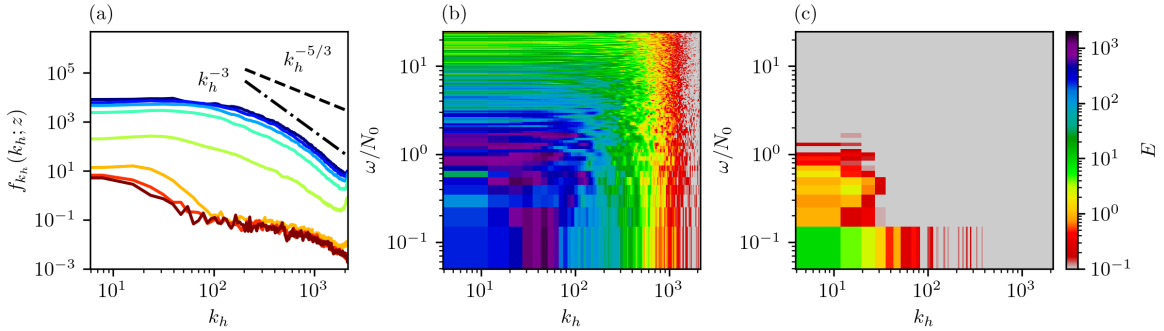

Fig. 4.14 (a) Horizontal wavenumber spectrum, (b) and (c) energy spectrum within and above the plume, as in figure 4.6 but for simulation 2L. Frequencies normalised by $N_0 = 0.5$ to aid comparison with simulation HR.

decrease in spectral power between the two-layer and stratified flows clearly illustrates the impact of internal waves propagating energy from the plume into the ambient fluid. In the stratified case, spectral power is around two orders of magnitude smaller in the waves above the plume compared with the turbulence within the plume. In the two-layer case, spectral power is around four orders of magnitude smaller in the absence of internal waves carrying energy into the environment. The same observations are apparent in the energy spectra; above the plume – in figure 4.14(c) – power is confined to smaller wavenumbers than in simulation HR and smaller frequencies. The energy spectra within the plume – compare figure 4.14(b) and figure 4.6(b) – appear largely similar.

4.6 Discussion and conclusions

Inspired by the laboratory experiments of AS10, we have performed large-eddy simulations of a buoyant plume penetrating into a stably stratified layer that then transforms into a fountain and excites internal waves that propagate horizontally and vertically away from the plume cap. In all simulations the plume source conditions were identical with the plume encountering the base of the stratified layer 0.2 m above the bottom of the domain. Across a range of different simulations the strength of the stratification, N_0^2, varied over two orders of magnitude from 0.25 to 100 s^{-2}.

Although the depth of penetration of the plume into the stratified layer decreases significantly with increasing N_0^2, the frequency spectrum above the fountain was found to be narrow-banded with energy concentrated in the range $0.6 < \omega/N_0 < 1$ and a peak frequency at a near constant fraction of N_0 around $\omega/N_0 = 0.9$. We applied a viscous internal wave model, introduced by Taylor and Sarkar (2007), to help understand the origin of this narrow spectrum, concluding that the model can sufficiently capture the power decay and frequency selection of the far-field internal wave spectrum when initialised from a spectrum taken near the top of the fountain $z_0 = 0.36$ m and assuming a virtual source height $z_s = 0.32$ m within the fountain, near the intrusion height. Using Dynamic Mode Decomposition, we were able to extract flow structures associated with internal wave frequencies and used ray-tracing to demonstrate that internal wave beams can be traced from inside the fountain. This method is subject to significant noise in the phase reconstruction owing to filtering of the wave modes; superior methods of identifying a wave signature in the turbulent flow within the plume may exist. Whilst our analyses do not elucidate the wave generation mechanism, the results imply waves are generated within the fountain and not at the turbulent/non-turbulent interface between the plume cap and ambient fluid.

A simulation with a uniform instead of stratified upper layer was run to provide comparison between two structurally similar flows, one with internal waves present in the ambient fluid and one without, with the aim of identifying differences in the flow spectra. The buoyancy jump between the bottom and top uniform layer was chosen so that the plume penetrates to a similar maximum and quasi-steady state height. Comparison of the energy spectra at heights within and above the plume showed that, in the absence of waves in the two-layer case, spectral power is two orders of magnitude smaller above the plume compared to within, drops off at smaller wavenumbers than in the stratified case, and is confined to very low frequencies. There was evidence for

evanescent waves in a thin layer surrounding the plume cap where the ambient fluid becomes weakly stratified. Whilst this analysis did not elucidate the wave generation mechanism, the evanescent wave modes surrounding the plume cap were found to correspond with frequencies close to but smaller than the buoyancy frequency inside the plume. Thus, whilst waves cannot propagate in the ambient, their generation and propagation within the plume in the two-layer case appears consistent with the stratified case.

Other numerical studies of convection interacting with a stratified layer have likewise shown the excitation of internal waves with their source originating within the convective region (Couston et al., 2018; Lecoanet et al., 2015; Lecoanet and Quataert, 2013; Pinçon et al., 2016). However, in those studies convective cells scoured the underside of a strongly stratified layer having buoyancy frequency far exceeding the characteristic convective frequency. In this 'scouring' regime, multiple convective plumes impinged upon and perturbed the interface between the turbulent lower layer and the stratified upper layer but did not penetrate into the upper layer. The convection excited horizontally long, hydrostatic waves with a relatively wide but low frequency spectrum. The separation of spatial and temporal scales between the convective and stratified regions allowed them reasonably to adapt Lighthill's theory for the generation of sound waves by turbulence (Lighthill, 1952) to the problem of internal waves generated by convection. Thus they showed that internal waves were excited by Reynolds stresses within the convecting region with a spectrum that decayed rapidly with increasing frequency. By contrast, our study focuses on a 'penetrative' regime with internal waves generated by spatially localised penetrative convection, in which the frequencies associated with turbulence in the plume cap overlap with the observed frequencies of generated non-hydrostatic internal waves. The lack of spatial and temporal scale separation in our problem means that Lighthill theory cannot be applied, nor could it explain the observed narrow frequency band at which waves are excited. Indeed, comparison of energy spectra in figure 4.6 with those shown in Couston et al. (2018) clearly shows different structures in spectral space. However, our simulation with $N_0^2 = 100$ appears to mark a transition between the penetrative convection regime and the scouring regime: the energy scale separation between the turbulent plume and waves is much smaller (figure 4.4(b)) and the vertical energy flux in figure 4.4(a) more closely matches the theoretical scaling derived by Couston et al. (2018) compared with weaker N_0. This trend continues in simulations with $N_0^2 = 1000$, not shown here, though the nature of the transition between the penetrative and scouring regimes remains unclear.

Whatever the strength of the stratification, internal waves are generated within the turbulent region, though we argue the excitation mechanism differs for penetrative convection.

Chapter 5

Minimal model of moist effects in convective hydration of the TTL

5.1 Introduction

In chapters 5 and 6 we focus our attention directly on convective hydration of the TTL. The aim is to establish a parameterisation of microphysical processes that are thought to be relevant to the irreversible transport of water vapour into the TTL via penetrative convection. In particular, we seek a *minimal* moisture model which retains only the most essential processes, to aid interpretation and understanding of the mechanisms that contribute to moisture transport and the interaction between them. The key difference between earlier simulations and the 'moist' simulations presented henceforth is the temperature-dependent nature of the tracer concentration(s) present in the flow. As in earlier chapters, the moist tracers are passive in the sense that they do not affect dynamics in the flow, but the evolution of the tracers now depends on temperature. Although the moist tracers are no longer 'tracers' in the typical sense, we continue to use this term for consistency with earlier chapters.

To formulate our minimal model, in § 5.2 we first discuss in detail the mechanisms that lead to hydration of the TTL by overshooting convection and identify the essential processes as condensation, sublimation, and sedimentation. We then explore how these processes are modelled in comprehensive and simplified microphysical schemes. The objective is to determine (a) the simplest functional forms that represent each process and (b) a representation of temperature that is consistent with the Boussinesq assumption implicit in our numerical scheme. In § 5.3 we describe our minimal

moisture model and validate its behaviour in § 5.4. As part of this validation, we define dimensionless 'regime numbers' that quantify the importance of each process in a given simulation. Finally in § 5.5 we introduce a moist variation of the buoyancy-tracer volume distribution formalism introduced in chapter 3. In chapter 6, we use our idealised model of convective hydration to explore the interaction between microphysics, convective intensity, mixing, and large-scale vertical shear in convective hydration of a stratified layer.

5.2 Literature review

5.2.1 Convective hydration of the TTL

Recent modelling studies in combination with in-situ and remote observations have progressed our understanding of the mechanisms that lead to vertical transport of water vapour into the TTL and ultimately the tropical lower stratosphere (TLS). Dauhut et al. (2018) studied numerical simulations of "Hector the convector", a large thunderstorm complex that forms frequently in austral summer near Darwin, Australia. Over their 10 hour simulation, 1500 overshoots were identified, of which around 20 penetrate deep into the TTL. Their study focuses on the processes occurring as these overshoots penetrate and collapse, on the time scale of several minutes. Lee et al. (2019) consider the evolution of a moist anomaly long after the overshooting convection has subsided; processes on these longer time scales can strongly modify the amount of water vapour that ultimately reaches the TLS. Here, we summarise the present understanding of the hydration mechanism which is also illustrated in figure 5.1.

As convective clouds rise through the troposphere and penetrate into the TTL, air parcels are adiabatically cooled which reduces the saturation vapour concentration, thus freeze-drying water during ascent. Excess water vapour condenses into droplets which freeze to form a variety of frozen hydrometeor species. Together these can be treated collectively as 'ice' condensates (Hassim and Lane, 2010). In an individual overshoot penetrating deep into the TTL, the ice concentration is typically 100-1000x larger than the water vapour concentration which is around 10 ppmv (Dauhut et al., 2018). In particular, overshoots which cross the CPT are significantly colder and more ice-rich than the surrounding dry (i.e. subsaturated) TTL environment which warms with height above the CPT. Owing to the large temperature difference, the overshoot becomes negatively buoyant and collapses, generating shear between the rising updraft

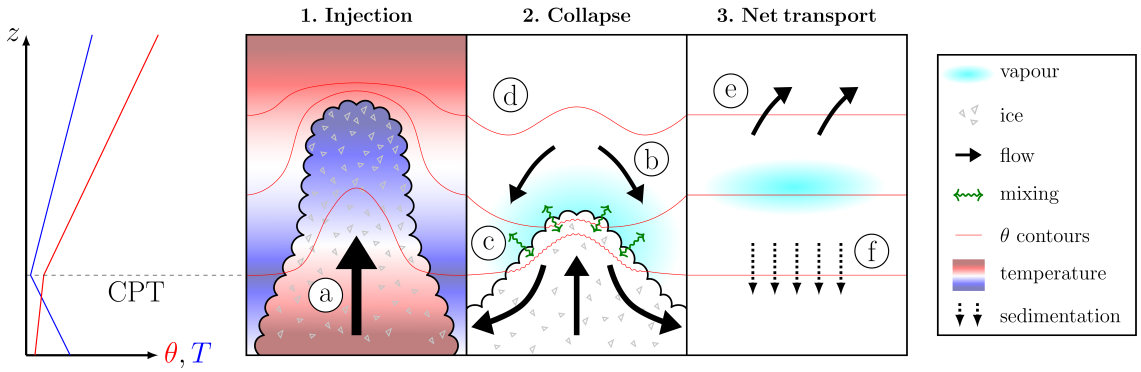

Fig. 5.1 Schematic illustration of the mechanism for convective hydration of the TTL. Axes on the left show representative profiles of the environmental temperature T and potential temperature θ profile in the TTL, as well as the cold-point tropopause (CPT). Panel 1: penetration of a convective overshoot deep into the TTL, with (a) a strong updraft and significant ice loading. Shading indicates temperature. Red lines are contours of potential temperature θ. Panel 2: the overshoot collapses, causing (b) air to subside around the overshoot, enhancing (c) mixing between cold tropospheric air at the top of the overshoot and surrounding warm TTL air. Ice sublimates in the warmer air, producing a water vapour anomaly (indicated by light blue shading). (d) Gravity wave breaking may further promote mixing and associated vertical displacements can loft water vapour deeper into the TTL. Panel 3: net transport of water vapour into the TLS occurs due to (e) large-scale uplift, but can be reduced by (f) the formation and sedimentation of ice.

and subsiding flow surrounding it. Turbulence drives intense mixing between the overshoot and environment, which may be enhanced by shear within the overshoot. Large-scale wind shear in the TTL can also promote mixing. The mixing of cold and ice-rich tropospheric air with warm and dry TTL air leads to the sublimation of ice and formation of a vapour-rich pocket at the top of the overshoot. As the overshoot collapses to its level of neutral buoyancy, anomalous concentrations of water vapour remain at greater heights in the TTL.

The hydration mechanism relies on the entrainment of subsaturated air from the upper TTL into the overshoot so that sublimated ice can increase the vapour content. However, if air in the TTL is supersaturated then the overshooting process can result in dehydration via 'ice scavenging' (Hassim and Lane, 2010; Khaykin et al., 2022), where excess vapour condenses onto convectively lofted ice particles which grow and sediment out of the TTL. Ice scavenging drives the TTL environment back towards saturation, producing a net dehydration of the TTL. This tends to occur in overshoots which do not penetrate far into the TTL; relative humidity is typically low in the upper TTL and TLS so the rare occasions where deep convection penetrates well above the CPT

almost always result in hydration (Jensen et al., 2020). However, Khaykin et al. (2022) note a single flight in the StratoClim campaign during the Asian Summer Monsoon with evidence of supersaturated regions above the CPT that had been dehydrated by convective penetration events.

Notwithstanding the fact that moistening of the TTL occurs, for overshoots that cross the CPT but do not reach the TLS, the amount of water vapour that is irreversibly transported into the TLS strongly depends on processes on longer time scales, from hours to days, during the quasi-horizontal motion that accompanies slow upwelling through the TTL. For example, gravity-wave associated temperature perturbations can temporarily cool anomalously moist regions during transit through the TTL, leading to the formation of ice which may sediment out of the TTL and reduce the net hydration of the TLS (e.g. Pan et al. (2019); Tissier and Legras (2016); Wright et al. (2011)). Larger-scale dynamically induced temperature anomalies can have a similar effect.

Convective overshoots generate gravity waves which propagate outwards and upwards, producing remote effects as well as local influence on the overshoot (e.g. Hassim and Lane (2010); Lee et al. (2019); Sang et al. (2018)). These waves have associated temperature and vertical velocity perturbations which propagate through the TTL and become amplified when waves break in the presence of vertical wind shear. Sang et al. (2018) argued that gravity-wave breaking promotes mixing at the top of the overshoot, thereby increasing the net hydration of the TTL by entraining larger volumes of warm stratosphere air which then sublimates greater amounts of ice. Sang et al. (2018) also suggested that the presence of large-scale vertical shear near the CPT limits the amplitude of gravity waves and reduces the overall transport as a result. The remote effects of gravity waves have been invoked as an explanation for the 'jumping cirrus' phenomenon where hydration occurs up to 1–3 km above the overshoot (Iwasaki and Yamaguchi, 2022; Wang, 2003). The mechanism was examined by Hassim and Lane (2010) using numerical simulations which showed that upward displacement of TTL air by breaking gravity waves results in ice formation by adiabatic cooling, which is then mixed into the subsaturated (and warmer) environment of the upper TTL and TLS. However, it is unclear whether the large air-parcel displacements are solely associated with gravity wave breaking – which necessitates sufficient vertical wind shear in the TTL environment – or associated with motion of the overshoot itself (Frey et al., 2015).

The TTL temperature structure plays an important role in determining the hydration potential of an overshoot. A cooler TTL environment limits the amount of sublimated ice that can remain after convective injection since the saturation vapour

concentration is lower. The increase of TTL temperatures with height above the CPT makes the maximum penetration height of a convective overshoot a key factor (Dauhut et al., 2018). A larger maximum height allows mixing of even warmer air from the upper TTL into the overshoot, increasing the saturation concentration and allowing more ice particles to sublimate. This supports an earlier study by Sherwood and Dessler (2001) in which an idealised convective overshooting scheme coupled to a model of the large-scale circulation showed particular sensitivity to the distribution of heights where mixing with air in the TTL occurs.

In an idealised model of convective hydration of the TTL we are primarily concerned with how much vapour remains in convectively lofted fluid parcels that have mixed with the TTL environment and therefore warmed and sublimated some of their ice content. We focus on this transient process of hydrating the immediate surroundings of convective overshoots rather than the slow ascent occurring afterwards. Whilst ice may remain in fluid parcels, we implicitly assume that this ice sediments out of the TTL on longer timescales. We choose not to consider the influence of the TTL environment, instead opting for a completely subsaturated TTL environment to simplify interpretation. We therefore focus exclusively on *hydration* of the TTL and do not consider the apparently less frequent dehydration events; this allows us to formulate a simpler model that does not represent supersaturation at all.

To conclude, our model need only represent two moist species, vapour and ice, and must represent three microphysical processes: condensation of vapour to form ice, sublimation of ice to form vapour, and sedimentation of ice. The timescale on which these processes occur will play a role in determining the net hydration of the TTL; for example, the growth rate of ice determines the size distribution of ice crystals which itself determines the sedimentation velocity. However, by choosing to represent ice using a tracer concentration (as with the passive tracer used in earlier chapters) we neglect any representation of crystal size. We will also choose sedimentation to be independent of ice concentration, such that the sedimentation velocity is fixed, which aids interpretation of its effect relative to other processes such as mixing and conversion between vapour and ice.

5.2.2 Minimal moisture models

Moisture schemes range in complexity from comprehensive models that represent multiple moist species and use detailed microphysical schemes to describe each species

(i.e. representing ice number concentration, crystal sizes, etc.), to simplified cloud models which describe vapour, condensate, and precipitate forms of water and use bulk parameterisations to represent microphysical processes. Moisture schemes can be further idealised by considering the limit in which one conversion process is fast relative to others, for example allowing intermediate forms of moisture between vapour and precipitate to be neglected. Here, we discuss the model presented by Hernandez-Duenas et al. (2013) (henceforth HD13) which represents vapour and precipitate (rain water) only and can be viewed as a limiting case of the more complex cloud microphysics model presented by Grabowski (1998) (henceforth G98). H13 present simplified representations of the conversion between vapour and precipitate which are modified for use in our own moisture scheme. Figure 5.2 summarises the H13 and G98 models along with our minimal moisture model detailed in § 5.3.

The G98 simplified cloud model is designed to be applicable to large-scale tropical circulations whilst remaining computationally practical for large domain cloud-resolving models. Their moisture scheme models the mixing ratios of water vapour q_v, cloud water (condensate) q_c and rain water (precipitate) q_p which sediments via a terminal velocity V_T which depends on temperature and other thermodynamic properties of rain water. Condensation of vapour to form cloud water occurs via the term C_d and deposition of vapour onto rain water occurs via the term D_p. Cloud water forms rain water via autoconversion A_c and accretion A_r. Each of these conversion terms is represented by a bulk parameterisation derived from detailed microphysical models.

H13 consider the limit where autoconversion of cloud water into rain water is fast, so that condensed cloud water quickly forms into rain droplets that precipitate. Hence cloud water is neglected as a moist species in their model. There are then only three moist processes: condensation of water vapour into rain water C_d, evaporation of rain water into water vapour E_r and precipitation of rain water at a fixed velocity V_T. Unlike the G98 model in which the parameterisations are bulk parameterisations of detailed cloud microphysics, H13 choose the conversion terms to have the simplest non-trivial functional forms for condensation and evaporation whilst retaining the essential features of precipitating convection. Following Majda et al. (2010) the closures adopted are

$$C_d = \frac{q_v - q_{vs}(z)}{\tau_c}\mathcal{H}(q_v - q_{vs}(z)), \tag{5.1}$$

$$E_r = \frac{q_{vs}(z) - q_v}{\tau_e}\frac{q_r}{q_*}\mathcal{H}(q_{vs}(z) - q_v), \tag{5.2}$$

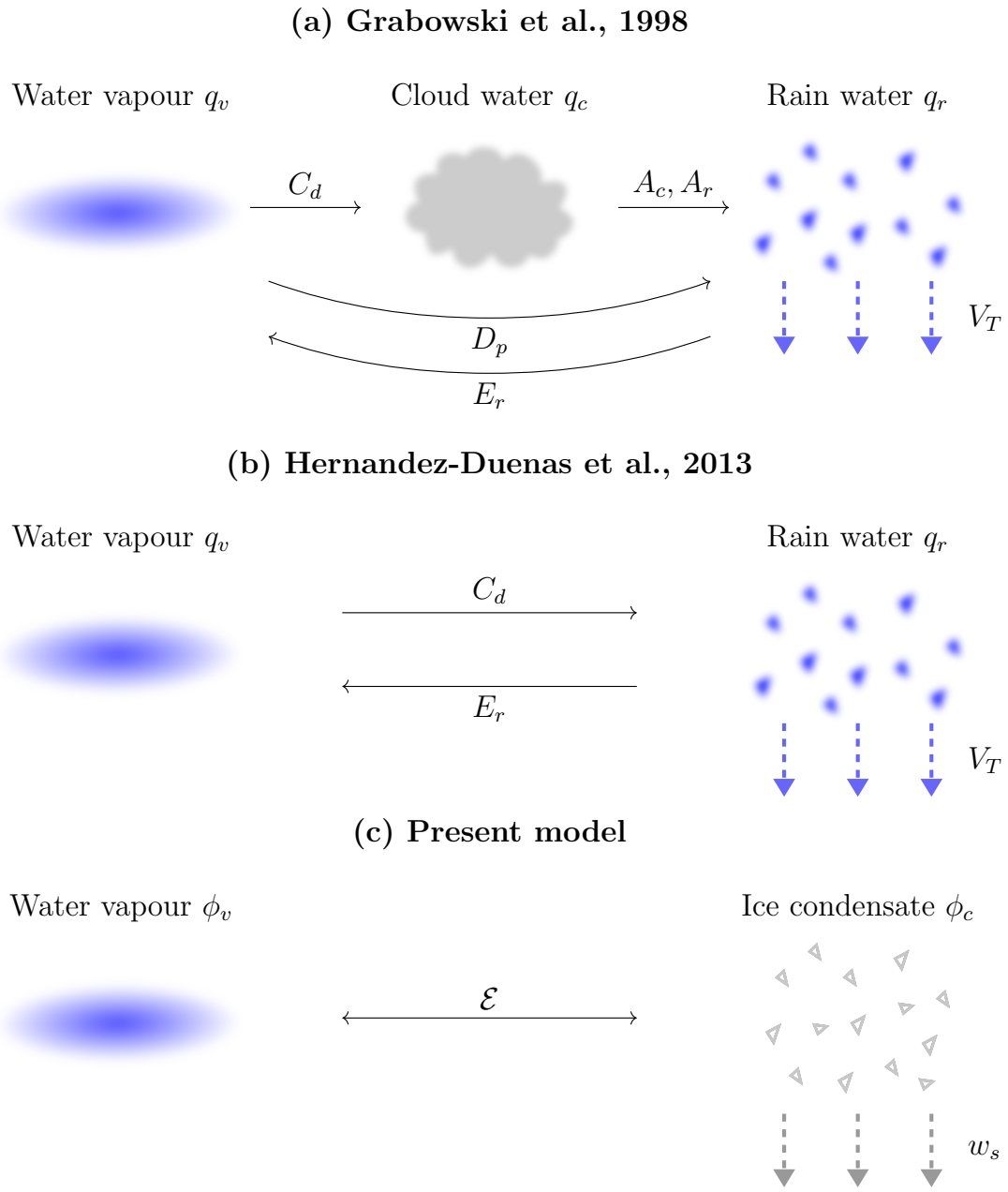

Fig. 5.2 Schematic of moisture schemes: (a) comprehensive scheme used by Grabowski (1998), (b) fast autoconversion limit used by Hernandez-Duenas et al. (2013), (c) minimal moisture model introduced in §5.3.

where $\mathcal{H}$ is the Heaviside step function, $q_{vs}(z)$ is the height-dependent saturation specific humidity and q_* is a reference specific humidity. Note the different meaning of q in the G98 model, representing a mixing ratio, and the H13 model where q is the specific humidity of each moist species, meaning the ratio of the mass of the moist species to the mass of the moist air parcel. The difference between the mixing ratio and specific humidity is typically small and either form is valid in the closures given above. The form of C_d and E_r mean that when the amount of vapour q_v exceeds the saturation specific humidity q_{vs} then q_v reduces to q_{vs} on a timescale τ_c and is converted to rain water q_r on a timescale τ_e. Conversely when air is subsaturated, i.e. q_v is smaller than q_{vs}, if rain water is present then it is converted into vapour. The condensation timescale τ_c is typically assumed to be smaller than the evaporation timescale τ_e, i.e. condensation occurs more quickly than evaporation.

The conversion terms between vapour and precipitate (which we will later assume to be frozen) depend on a saturation value which limits the amount of vapour. H13 use the anelastic approximation which treats pressure and temperature, and hence q_{vs}, as functions of height only. However, our model will be formulated under the Boussinesq approximation. We follow the study by Vallis et al. (2019) which presents a simple extension of the Rayleigh-Bénard convection model with the addition of a water vapour field that experiences condensation alone. The Boussinesq framework derived by Vallis et al. (2019) provides a form for q_{vs} which is a valuable starting point for our own moisture scheme owing to its simplicity. This form ultimately relies on a representation of temperature that is consistent with the Boussinesq assumption, which is derived as follows. For an ideal gas, the first law of thermodynamics states

$$c_p \frac{\mathrm{D}T}{\mathrm{D}t} - \frac{1}{\rho}\frac{\mathrm{D}p}{\mathrm{D}t} = \mathcal{Q}, \tag{5.3}$$

where $\mathcal{Q}$ is the heating (which includes diffusion) and c_p is the specific heat capacity of air. Under the Boussinesq approximation and using the hydrostatic equation, the second term is approximated by

$$\frac{1}{\rho}\frac{\mathrm{D}p}{\mathrm{D}t} \approx \frac{w}{\rho_0}\frac{\mathrm{d}p_0}{\mathrm{d}z} = -wg. \tag{5.4}$$

The first law then becomes

$$\frac{\mathrm{D}\theta}{\mathrm{D}t} = \frac{\mathcal{Q}}{c_p}, \tag{5.5}$$

where the potential temperature θ is

$$\theta = T + \frac{g}{c_p} z, \tag{5.6}$$

meaning g/c_p acts as the dry adiabatic lapse rate for this model. Assuming that deviations from a neutral profile are small and that $\partial_z T \approx -g/c_p$ (i.e. that the temperature profile is nearly adiabatic) then $\delta\rho/\rho_0 \approx -\delta\theta/T_0$, where $\delta\theta = \theta - \theta_0$ is the potential temperature perturbation and $\theta_0 = T_0$ is a reference potential temperature, equivalent to the reference absolute temperature T_0. For consistency with earlier chapters, we will focus on temperature and buoyancy as the key thermodynamic variables, with the knowledge that potential temperature is related to the buoyancy via

$$b = \frac{g}{\theta_0}\delta\theta, \tag{5.7}$$

and can be derived from the temperature according to (5.6). The temperature T and buoyancy b are related by

$$T = T_0 + \delta T = T_0 + \frac{T_0}{g} b - \frac{g}{c_p} z. \tag{5.8}$$

The form for the saturation specific humidity q_{vs} in Vallis et al. (2019) is derived from an approximation to the ideal gas solution of the Clausius-Clapeyron equation assuming that the latent heat of condensation $\mathcal{L}$ is constant. Assuming small variations in absolute temperature T, the saturation vapour pressure e_s is approximated by

$$e_s = e_0 \exp\left(\frac{\mathcal{L}}{R_v T_0^2}\delta T\right), \tag{5.9}$$

where $\delta T = T - T_0$ is the temperature perturbation, R_v is the gas constant for water vapour and e_0 and T_0 are constants. The specific humidity q is related to the vapour pressure e by

$$q = \varepsilon_m \frac{e}{p - e} \approx \varepsilon_m \frac{e}{p}, \tag{5.10}$$

where $\varepsilon_m \approx 0.62$ is the ratio of the molar mass of water vapour to dry air and the approximation $p \gg e$, which is valid for Earth's atmosphere, has been used. To proceed

further we use the relation between pressure, temperature and potential temperature

$$p = p_0 \left(\frac{T}{\theta}\right)^{c_p/R_d} \approx p_0 \left(\frac{T}{\theta_0}\right)^{c_p/R_d}, \tag{5.11}$$

assuming that variations in θ away from $\theta_0 = T_0$ are small, and where R_d is the gas constant of dry air. Given variations in T away from T_0 are also small then

$$p = p_0 \exp\left(\frac{c_p \delta T}{R_d T_0}\right), \tag{5.12}$$

using $T_0 = \theta_0$. Finally, the saturation specific humidity can be written as

$$q_s = q_0 \exp\left(\alpha \delta T\right), \tag{5.13}$$

where α is a constant that determines the exponential growth rate of saturation specific humidity with temperature, defined by

$$\alpha = \mathcal{L}/(R_v T_0^2) - c_p/(R_d T_0). \tag{5.14}$$

5.3 Idealised model of moist convection

In this section we give a complete description of the minimal model of moist convection that we use to explore convective hydration of a stably stratified layer. Our model resembles the moisture scheme presented by H13 with one further simplification: we use the same 'moist conversion' term to represent both condensation and evaporation, which we assume to occur on the same timescale τ_m. The representation of temperature and the saturation vapour concentration is based on the Boussinesq framework introduced by Vallis et al. (2019). Whilst the Boussinesq approximation that temperature variations away from the mean are small does not hold over the depth of the whole domain, in the shallow regions we focus on (i.e. the overshoot in the stratified layer) the approximation is valid. We consider a regime representative of the TTL where condensate is frozen and latent heating is neglected.

5.3.1 Model formulation

In earlier chapters we have quantified the passive tracer carried by the flow using the (dimensionless) concentration ϕ. Moist species, such as water vapour or ice, can be

quantified in various ways, for example absolute, relative or specific humidity, partial pressure, or mixing ratio. The moisture schemes discussed in §5.2.2 use the specific humidity and mixing ratio to quantify moist species, both of which are dimensionless. For consistency with earlier chapters, in our own moisture scheme we will continue to quantify tracers using their (dimensionless) concentration. This treatment – with ϕ_v as the vapour concentration and ϕ_{vs} as the saturation vapour concentration – is equivalent to using mixing ratio with an appropriate scaling. The relative humidity is defined as $r_h = \phi_v/\phi_{vs}$.

We consider two moist species: water vapour with concentration $\phi_v(\boldsymbol{x}, t)$ and ice condensate with concentration $\phi_c(\boldsymbol{x}, t)$. The forcing is chosen such that only vapour is carried by the plume initially, with ice produced via condensation only. We assume a fixed sedimentation velocity w_s for ice and assume for simplicity that vapour condenses into ice and ice sublimates into vapour according to the same conversion term $\mathcal{E}$ (but with opposite signs) on the same timescale τ_m. We also assume the fast condensation limit discussed in Vallis et al. (2019), such that $\tau_m \ll \tau_d$ where τ_d is the dynamical timescale (defined explicitly later). Upon reaching saturation, any water vapour exceeding the saturation vapour concentration ϕ_{vs} is rapidly converted into ice and when subsaturated, ice (if present) sublimates back into water vapour. This means that supersaturated air is not permitted in our model. Finally, to aid in interpreting results, we include a fully passive tracer ϕ_p with the same forcing as ϕ_v except with no condensation or sublimation processes. The tracer ϕ_p is equivalent to the tracer ϕ used in earlier chapters. In cases with sedimentation (when ϕ_c does not precisely follow the flow) this allows consistent definition of 'plume fluid' using a fixed contour $\phi_p \geq 10^{-3}$ as in earlier chapters (cf. Hassim and Lane (2010) where the 'cloud' is defined using a fixed contour of the sum of cloud water and ice). We refer to ϕ_p as the 'passive total water' since $\phi_p = \phi_v + \phi_c$ in the absence of sedimentation (except for minor variation due to the SGS diffusivity). The minimal moisture model is illustrated in figure 5.2.

The governing equations for the vapour, ice and passive total water concentration are

$$\frac{\mathrm{D}\phi_v}{\mathrm{D}t} = \kappa\nabla^2\phi_v - \mathcal{E}, \tag{5.15}$$

$$\frac{\mathrm{D}\phi_c}{\mathrm{D}t} - w_s\frac{\partial\phi_c}{\partial z} = \kappa\nabla^2\phi_c + \mathcal{E}, \tag{5.16}$$

$$\frac{\mathrm{D}\phi_p}{\mathrm{D}t} = \kappa\nabla^2\phi_p, \tag{5.17}$$

respectively, where w_s is the constant sedimentation velocity (meaning that ϕ_c is conserved) and the moist conversion term $\mathcal{E}$ is given by

$$\mathcal{E} = \frac{\phi_v - \phi_{vs}}{\tau_m} \mathcal{H}(\max\{\phi_c, \phi_v - \phi_{vs}\}), \tag{5.18}$$

where $\mathcal{H}$ is a Heaviside step function. The form of $\mathcal{E}$ is chosen such that condensation occurs when $\phi_v > \phi_{vs}$, converting vapour to ice, and sublimation occurs if $\phi_v < \phi_{vs}$ and $\phi_c > 0$, converting ice to vapour.

In order to represent moist processes in the TTL realistically, all variables and constants must be converted from geophysical scales to the laboratory scale used in our simulations. To do this, we choose characteristic time and length scales in each setting and use these as scaling factors. This is equivalent to first non-dimensionalising the system and then re-dimensionalising for our chosen scale. For the lengthscale l we choose the depth of the uniform layer $H = 0.2\,\mathrm{m}$ which corresponds with the depth of the troposphere $H_{\mathrm{atm}} = 14\,\mathrm{km}$, giving a lengthscale factor $R_l = H_{\mathrm{atm}}/H = 7 \times 10^4$. For the timescale we choose the time taken for a convective overshoot to penetrate, collapse and settle in the TTL, τ_p. From Dauhut et al. (2018) we estimate $\tau_{p,\mathrm{atm}} \approx 10\,\mathrm{min.}$, whilst in our simulations $\tau_{p,\mathrm{sim}} \approx 15\,\mathrm{s}$ based on the forcing used in earlier chapters which we continue with here. The time scale factor from simulation to atmospheric scales is then $R_t = \tau_{p,\mathrm{atm}}/\tau_{p,\mathrm{sim}} = 40$. Under this scaling, a typical value of the stratification strength in the TTL $N^2_{\mathrm{atm}} \approx 6 \times 10^{-4}\,\mathrm{s}^{-2}$ translates to $N_0^2 \approx 0.96\,s^{-2}$ in our simulations. These conversions are summarised in table 5.1. Note that choosing a horizontal lengthscale, such as the plume radius at penetration, may be more appropriate given its direct influence on transport into the stratified layer. However, it is difficult to calculate the corresponding scale in the TTL since overshoots vary significantly in width (Dauhut et al., 2018) and the choice between the radius of the entire overshoot complex or the central updraft is not clear.

There is no natural choice of temperature scaling in our simulations, so we continue to use temperature values corresponding to a choice of reference temperature $T_0 = 300\,\mathrm{K}$. With the scale factors R_t and R_l, the temperature in our model is

$$T = T_0 + \Theta b - \Gamma(z + H), \tag{5.19}$$

where $\Theta = T_0 R_l/(gR_t^2)$ is the conversion between buoyancy and potential temperature perturbation, such that $\delta\theta = \Theta b$, and $\Gamma = gR_l/c_p$ is the 'dry adiabatic' lapse rate in

Quantity	Lab scale	Geophysical scale	Conversion factor
Uniform layer depth H	0.2 m	14 km	$R_l = 7 \times 10^4$
Overshoot timescale τ_p	15 s	10 min.	$R_t = 40$
Stratification N_0^2	0.96 (s^{-2})	6×10^{-4} (s^{-2})	R_t^{-2}

Table 5.1 Conversion between characteristic quantities in the TTL and our simulations.

our model. This provides a mechanism for (an analogue to) 'adiabatic cooling' and 'adiabatic warming' in our model, where fluid is cooled (warmed) as it moves upwards (downwards) which reduces (increases) ϕ_{vs}. The saturation vapour concentration is

$$\phi_{vs} = \phi_0 \exp\left[\alpha(T - T_0)\right] = \phi_0 \exp\left[\alpha\left(\Theta b - \Gamma(z + H)\right)\right], \tag{5.20}$$

where α is a constant defined in (5.14) which depends on other physical constants whilst ϕ_0 is the reference saturation concentration, a free parameter which can be set along with the plume forcing $F_0^{(\phi)}$ to determine how much condensation occurs (see §5.3.3). Note that by neglecting latent heating, the moist static energy is equivalent to the buoyancy b. The dry and saturated adiabatic lapse rates are also identical and no buoyancy or vapour sources or sinks are present in the domain except from in the forcing region where the plume is generated.

5.3.2 Simulation setup & numerical implementation

The simulation setup is identical to that detailed in chapter 2 except with minor modifications to the tracer initial conditions, the introduction of vertical shear in the stratified layer, and an additional factor in the plume forcing terms which switches off plume forcing at time t_{lim}. The full initial conditions are now

$$\boldsymbol{u}(\boldsymbol{x}, t_0) = \begin{cases} \boldsymbol{0} & -H \leq z \leq 0, \\ \lambda z\, \hat{\boldsymbol{x}} & 0 \leq z \leq L_z - H, \end{cases} \tag{5.21}$$

$$b(\boldsymbol{x}, t_0) = \begin{cases} 0 & -H \leq z \leq 0, \\ N_0^2 z & 0 \leq z \leq L_z - H, \end{cases} \tag{5.22}$$

$$\phi_{p,v,c}(\boldsymbol{x}, t_0) = \mathcal{N}, \tag{5.23}$$

where $\lambda = \partial_z u$ is the vertical shear rate in the stratified layer and $\mathcal{N}$ represents random noise of magnitude 10^{-8} applied to all tracers. Note that the stratified layer is chosen to be initially completely dry. The noise is included to handle a numerical instability in the SGS diffusivity calculation. From (5.22), the initial conditions for the temperature T are

$$T(\boldsymbol{x}, t_0) = \begin{cases} T_0 - \Gamma(z + H) & -H \leq z \leq 0, \\ T_0 + (\Theta N_0^2 - \Gamma)z - \Gamma H & 0 \leq z \leq L_z - H, \end{cases} \tag{5.24}$$

Note that with the intention to use this model to explore processes in the TTL, where temperatures increase with height above the CPT, we are restricted to $\Theta N_0^2 > \Gamma$ so that $\partial_z T > 0$ in the stratified layer. As in previous chapters, the boundary conditions on the top and bottom boundaries are no-slip $\partial_z u = \partial_z v = 0$, no-penetration $w = 0$ and no-flux $\partial_z b = \partial_z \phi = 0$.

The full, non-dimensional governing equations are as previously stated for velocity $\boldsymbol{u}$ and buoyancy b (equations (2.13) and (2.14)). The tracer evolution equations for ϕ_p, ϕ_v, ϕ_c include plume forcing for ϕ_p and ϕ_v, the moist conversion term for ϕ_v and ϕ_c, and sedimentation of ϕ_c. We have

$$\frac{\mathrm{D}\widehat{\phi}_p}{\mathrm{D}t} = \frac{1}{\mathrm{RePr}}\nabla^2\widehat{\phi}_p - \nabla \cdot \boldsymbol{\lambda}_{\phi_p} + f_{\phi_p}, \tag{5.25}$$

$$\frac{\mathrm{D}\widehat{\phi}_v}{\mathrm{D}t} = \frac{1}{\mathrm{RePr}}\nabla^2\widehat{\phi}_v - \nabla \cdot \boldsymbol{\lambda}_{\phi_v} - \widehat{\mathcal{E}} + f_{\phi_v}, \tag{5.26}$$

$$\frac{\mathrm{D}\widehat{\phi}_c}{\mathrm{D}t} = \frac{1}{\mathrm{RePr}}\nabla^2\widehat{\phi}_c - \nabla \cdot \boldsymbol{\lambda}_{\phi_c} + \widehat{\mathcal{E}} + w_s\frac{\partial\widehat{\phi}_c}{\partial z}, \tag{5.27}$$

where the plume tracer forcing terms f_{ϕ_p} and f_{ϕ_v} are as detailed in §2.2.3 and defined explicitly in (2.35) except with ϕ replaced by ϕ_p and ϕ_v respectively. The plume forcing terms f_{ϕ_p} and f_{ϕ_v} as well as f_w and f_b defined in (2.33) and (2.34), respectively, are multiplied by a factor

$$f_t(t) = \frac{1}{2}\left[1 - \tanh\left(\frac{t - t_{\mathrm{lim}}}{\tau_r}\right)\right], \tag{5.28}$$

which ends plume forcing at time $t \approx t_{\mathrm{lim}}$. The parameter $\tau_r = 0.5\,\mathrm{s}$ is the relaxation timescale for this forcing modulation. The SGS tracer fluxes $\lambda_{\phi_p}, \lambda_{\phi_v}$ and λ_{ϕ_c} are as defined in (2.19) with ϕ replaced by ϕ_p, ϕ_v and ϕ_c respectively. Finally, $\widehat{\mathcal{E}}$ is the moist conversion term with $\phi_{v,c}$ replaced by the filtered variables $\widehat{\phi}_{v,c}$. To avoid confusion when varying F_0, we drop the non-dimensionalisation in (5.25)–(5.27) henceforth.

Parameter	Definition	Meaning	Value (if fixed)
T_0	(5.8)	Reference temperature	300 K
w_s	(5.16)	Sedimentation velocity of ice	
τ_m	(5.18)	Moist conversion timescale	0.1 s
ϕ_0	(5.20)	Reference saturation concentration	
α	(5.14)	ϕ_{vs} exponential growth rate	0.05 K^{-1}
Θ	(5.19)	$\delta\theta = \Theta b$	1340 K^{-1} m^{-1} s^2
Γ	(5.19)	Dry adiabatic lapse rate	684 K m^{-1}
λ	(5.21)	Vertical shear rate in stratified layer	
L_h, L_z	Fig 2.1	Domain width & height	
F_0	(2.27)	Source buoyancy flux	
$F_0^{(\phi)}$	(2.28)	Source passive & vapour tracer flux	
N_0	(2.26)	Stratified layer buoyancy frequency	1.0 s^{-1}
H	(2.26)	Uniform layer depth	0.2 m
r_0	(2.34), (2.35)	Source plume radius	0.002 m
t_{end}	(2.34), (2.35)	Simulation end time	
τ_r	(5.28)	Limited forcing relaxation timescale	0.5 s
τ	(2.34), (2.35)	Forcing relaxation timescale	1.0 s
t_{lim}	(5.28)	Plume forcing end time	

Table 5.2 Minimal moisture model parameters and general simulation parameters with values if fixed in all simulations.

The random noise required for stability of the SGS diffusivity calculation introduces a complication in the numerical implementation. The form of the condensation/sublimation term in (5.15) and (5.16) means that ϕ_c and ϕ_p are modified when $\phi_v > \phi_{vs}$ or when $\phi_v < \phi_{vs}$ and $\phi_c > 0$. Given a time step Δt, from (5.15) the change in ϕ_v is approximately

$$|\Delta\phi_v| \approx |\phi_v - \phi_{vs}| \frac{\Delta t}{\tau_m}, \tag{5.29}$$

and similarly for ϕ_c. At the top of the domain, this introduces a numerical instability since ϕ_v is non-zero and small due to the imposed noise but ϕ_{vs} is extremely large, so $\Delta\phi_v$ far exceeds the amount of ice available to sublimate unless the time step Δt is restricted to being very small. To exclude the possibility that 'too much' sublimation occurs, and to avoid excessive constraints on the time step, we explicitly check when $\Delta\phi_v > \phi_c$ and instead set $\Delta\phi_v = \phi_c$ so that $\phi_v \mapsto \phi_v + \phi_c$ and $\phi_c \mapsto 0$.

For consistency with the fast condensation limit of Vallis et al. (2019), we choose the moist conversion (i.e. phase change) timescale τ_m to be much smaller than the dynamical timescale τ_d. The timescale τ_d could be defined in various ways; here we choose the time taken for fluid parcels to rise from penetration to the top of the plume which scales with N_0^{-1} (Devenish et al., 2010). This is approximated as the ratio of the quasi-steady state height of the plume $z_{\rm ss}$ and the average vertical velocity on the plume centreline $\boldsymbol{x}_p = (L_h/2, L_h/2, 0)$ at penetration:

$$\tau_d = \frac{z_{\rm ss}}{\overline{w}(\boldsymbol{x}_p)}. \tag{5.30}$$

We implicitly assume the fast condensation limit in our model, which requires $\tau_m/\tau_d \ll 1$. This requirement is enforced by choosing τ_m to be sufficiently small. On average, the simulations presented in this chapter have $\tau_m/\tau_d \approx 0.05$. Note this limit is representative of the tropical atmosphere; condensation and evaporation occur on timescales of a few seconds whilst the dynamics occur on the timescale of a few minutes (e.g. Hernandez-Duenas et al. (2013)).

The minimal moisture model introduces a number of simulation parameters which are summarised in table 5.2. For completeness, we also state simulation parameters introduced in chapter 2 and give values for parameters which are fixed in all simulations presented in the remainder of chapter 5 as well as in chapter 6.

5.3.3 Quantifying model regimes

Dimensionless numbers are often used to quantify the importance of one process relative to another, thus identifying regimes where one process or another is dominant. For example, in § 1.3, we introduced the Reynolds number and buoyancy-Reynolds number which characterise the turbulent nature of the flow and the relative importance of turbulence and stratification. Here, we introduce dimensionless 'regime numbers' $R_{\rm H}, R_{\rm S}$, and $R_{\rm SH}$, which quantify the importance of phase change, sedimentation, and large-scale vertical shear, respectively. These regime numbers are fixed in each simulation and controlled by the sedimentation velocity w_s, the reference saturation concentration ϕ_0, the vertical shear rate λ and the source buoyancy and tracer fluxes F_0 and $F_0^{(\phi)}$.

As described in § 5.3, our minimal moisture model introduces two new moist processes into the simulations: moist conversion between vapour and ice (condensa-

tion/sublimation) and sedimentation of the ice tracer. There are two aspects of this process which are important for our focus on hydration of the stratified layer: the extent to which condensation of vapour into ice occurs as the plume rises through the uniform layer (which sets the partitioning of moisture into vapour and ice as the plume penetrates), and how fast this conversion occurs relative to the mixing and dynamics, which is quantified by the ratio of the moist timescale τ_m and the dynamical timescale τ_d. We quantify the extent to which moist conversion occurs as the plume rises through the uniform layer using a 'conserved' relative humidity

$$R_{\mathrm{H}} = \frac{\overline{\phi}_p(\boldsymbol{x}_p)}{\phi_0 \exp\left[\alpha\left(\overline{b}(\boldsymbol{x}_p) - \beta H\right)\right]}, \tag{5.31}$$

which is the ratio of the time- and azimuthally-averaged passive tracer ϕ_p and the saturation vapour concentration ϕ_{vs} on the plume centreline at penetration $\boldsymbol{x}_p = (L_h/2, L_h/2, 0)$. The time average is taken over $0 \leq t \leq t_{\mathrm{lim}}$. The dimensionless number R_{H} can be interpreted as the mean relative humidity on the plume centreline at penetration assuming moist conversion does not occur. Hence R_{H} determines the extent to which condensation occurs: when $R_{\mathrm{H}} \ll 1$ the typical water vapour concentration at penetration is well below the saturation vapour concentration so little condensation occurs as the plume rises through the uniform layer and most moisture is in vapour form at penetration. Conversely, when $R_{\mathrm{H}} \gg 1$ condensation occurs as the plume rises through the uniform layer, so the plume is 'ice-loaded' at penetration. The regime number R_{H} is controlled by two parameters: the plume buoyancy and tracer fluxes F_0 and $F_0^{(\phi)}$, which modify ϕ_p, ϕ_v and b in the plume, and the reference saturation vapour concentration ϕ_0, which varies the environmental saturation profile and thus modifies the amount of vapour needed to reach saturation. Note that because of excessive Gibbs ringing when F_0 and $F_0^{(\phi)}$ are large (see § 2.3.3), we cannot explore regimes where R_{H} is extremely large. Test simulations showed that $R_{\mathrm{H}} \approx 15$ is the practical limit with our numerical setup.

The importance of sedimentation is expressed by a dimensionless number

$$R_{\mathrm{S}} = \frac{w_s}{w_{\mathrm{eddy}}}, \tag{5.32}$$

which is the ratio of the sedimentation velocity w_s and the mean turbulent vertical velocity in the plume,

$$w_{\mathrm{eddy}} = \langle w' \rangle^{\mathrm{plume}}, \tag{5.33}$$

Regime	R_{H}	R_{S}	ϕ_0	w_s
$R_{\mathrm{H}} \gg 1$	8.54	0	0.2	0
$R_{\mathrm{H}} \sim 1$	0.89	0	2.0	0
$R_{\mathrm{H}} \ll 1$	0.10	0	15	0
$R_{\mathrm{S}} \gg 1$	2.49	6.45	0.5	5×10^{-2}
$R_{\mathrm{S}} \sim 1$	2.09	0.66	0.5	5×10^{-3}
$R_{\mathrm{S}} \ll 1$	2.15	0.01	0.5	5×10^{-5}

Table 5.3 Simulation parameters for the regime-exploring simulations presented in § 5.4. Fixed parameters are $N_0 = 1$, $\lambda = 0$, $F_0 = 8 \times 10^{-7}$, $F_0^{(\phi)} = 1.04 \times 10^{-6}$, resolution $N_h \times N_z = 512 \times 513$, simulation end time $t_{\mathrm{end}} = 15\,\mathrm{s}$ and plume forcing end time $t_{\mathrm{lim}} = 10\,\mathrm{s}$.

where $\langle\cdot\rangle^{\mathrm{plume}}$ indicates the plume average within the stratified layer and over the time range $0 \leq t \leq t_{\mathrm{lim}}$, and w' is the turbulent component of the vertical velocity, calculated as in chapter 4 by subtracting the running mean of the azimuthally averaged velocity. Here, the running mean is taken over a time period of 25 turnover times $T_{\{F_0,r_0\}} = r_0^{4/3} F_0^{-1/3}$ (see § 2.2 for further details), which smooths out eddy fluctuations. When $R_{\mathrm{S}} \gg 1$ the turbulent vertical velocity within the plume is significantly weaker than the sedimentation velocity and we expect that ice falls out of suspension and therefore does not reach as far into the stratified layer. When $R_{\mathrm{S}} \ll 1$ the sedimentation velocity is weak compared with the turbulent eddies in the plume and therefore sedimentation plays little role in the dynamics.

Finally, the strength of the vertical shear in the horizontal velocity in the environment, relative to plume velocities, is quantified by the dimensionless number

$$R_{\mathrm{SH}} = \frac{\tau_d}{\lambda^{-1}} \tag{5.34}$$

which is the ratio of the dynamical timescale τ_d and the shear timescale λ^{-1}, where $\lambda = \partial_z u$ as defined in (5.21). Thus when $R_{\mathrm{SH}} \gg 1$ the shear timescale is much shorter than the dynamic timescale so shear effects are strong and the plume cap becomes significantly distorted by the large-scale horizontal flow in the stratified layer. When $R_{\mathrm{SH}} \ll 1$ the shear plays little role in the dynamics.

5.4 Exploring model behaviour

In this section we explore the behaviour of our minimal moisture model in two regimes, each with one of R_{H} and R_{S} fixed and the other varied by changing ϕ_0 and w_s

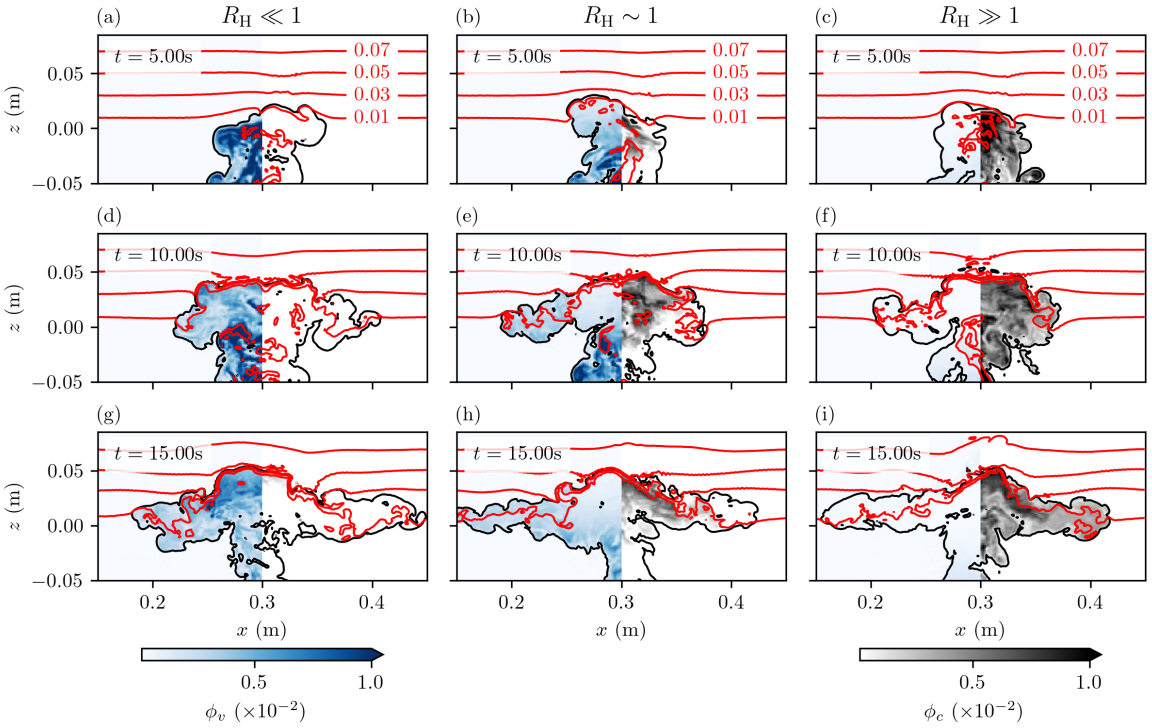

Fig. 5.3 Snapshots of simulations with varied ϕ_0 and $w_s = 0$ at $t = 5, 10, 15$ s showing the vapour concentration ϕ_v and ice concentration ϕ_c in each panel. These simulations are representative of regimes with $R_H \ll 1, R_H \sim 1$ and $R_H \gg 1$ respectively. Buoyancy contours are shown in red every 0.02 from $b = 0.01\,\mathrm{m\,s^{-2}}$. The black line indicates the plume contour $\phi_p = 10^{-3}$.

respectively. First, we vary the reference saturation concentration ϕ_0, yielding regimes with $R_H \gg 1, R_H \sim 1$ and $R_H \ll 1$. For this set of simulations the plume forcing is fixed and there is no sedimentation or shear. Separately, we vary the sedimentation velocity w_s, yielding regimes with $R_S \gg 1, R_S \sim 1$ and $R_S \ll 1$, keeping the plume forcing and ϕ_0 fixed and with no shear. All simulations are run to time $t_{\mathrm{end}} = 15\,\mathrm{s}$ and plume forcing ends at time $t_{\mathrm{lim}} = 10\,\mathrm{s}$. As previously, the plume is identified by the contour $\phi_p = 10^{-3}$. Parameters for the simulations presented here are summarised in table 5.3. The focus here is solely on the behaviour of the model, how this depends on ϕ_0 and w_s, and the relation to the hydration mechanism in the TTL; a deeper discussion of the mechanisms and interactions in convective hydration of a stably stratified layer is given in chapter 6.

Figure 5.3 shows snapshots of the simulations with varied reference saturation concentration ϕ_0 at various times post-penetration. In each plot, we show the vapour concentration ϕ_v and ice concentration ϕ_c with buoyancy contours shown every 0.02

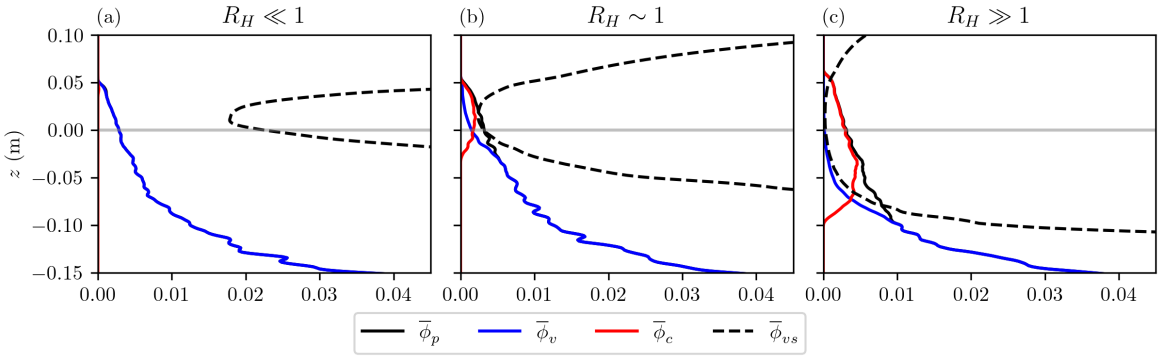

Fig. 5.4 Vertical profiles of the time- and azimuthally-averaged tracer concentrations ϕ_p, ϕ_v, ϕ_c and saturation vapour concentration ϕ_{vs} on the plume centreline, averaged over $0 \leq t \leq t_{\text{lim}}$. Only the reference saturation concentration ϕ_0 is varied between simulations. The gray horizontal line indicates the 'cold point' $z = 0$ where the environmental temperature is minimised.

from $b = 0.01\,\text{m s}^{-2}$ – note that with $N_0 = 1\,\text{s}^{-1}$, buoyancy and height are (numerically) equivalent in the stratified environment. Although plume forcing ends at time $t_{\text{lim}} = 10\,\text{s}$, plume fluid continues to rise through the uniform layer up to the end of the simulation. Figure 5.3 demonstrates how R_{H} relates to the partitioning of moisture into vapour and ice: when $R_{\text{H}} \ll 1$ the vapour concentration remains well below saturation at penetration and hence we find very little ice in the stratified layer. Some ice is produced at the very top of the plume at $t = 15\,\text{s}$ as plume fluid is adiabatically cooled during its rise to z_{max}. Conversely, when $R_{\text{H}} \gg 1$, relatively little vapour reaches the stratified layer and the plume is ice-loaded, with large concentrations of ice present. In the intermediate regime, $R_{\text{H}} \sim 1$, some but not all of the vapour has condensed so the plume carries moderate concentrations of both vapour and ice into the stratified layer. This effect is also seen using vertical profiles of the azimuthally averaged tracer concentrations $\overline{\phi}_p, \overline{\phi}_v$ and $\overline{\phi}_c$ on the plume centreline $r = 0$, as shown in figure 5.4. As noted earlier, without sedimentation then $\phi_p = \phi_v + \phi_c$. In the $R_{\text{H}} \ll 1$ case, the vapour concentration never reaches saturation so $\phi_p \approx \phi_v$. When ϕ_0 is reduced so that $R_{\text{H}} \gtrsim 1$, the plume reaches saturation lower in the uniform layer.

The $R_{\text{H}} \gg 1$ simulation in figure 5.3(c), (f), (i) and figure 5.4(c) is representative of the TTL regime; plume fluid is freeze-dried as it rises through the uniform layer and penetrates the stratified layer carrying large amounts of ice. As temperature increases in the stratified layer, the saturation vapour concentration increases exponentially with height. Thus larger concentrations of vapour can exist at the top of the plume where plume and environmental fluid mix, so some of the ice content is sublimated to produce

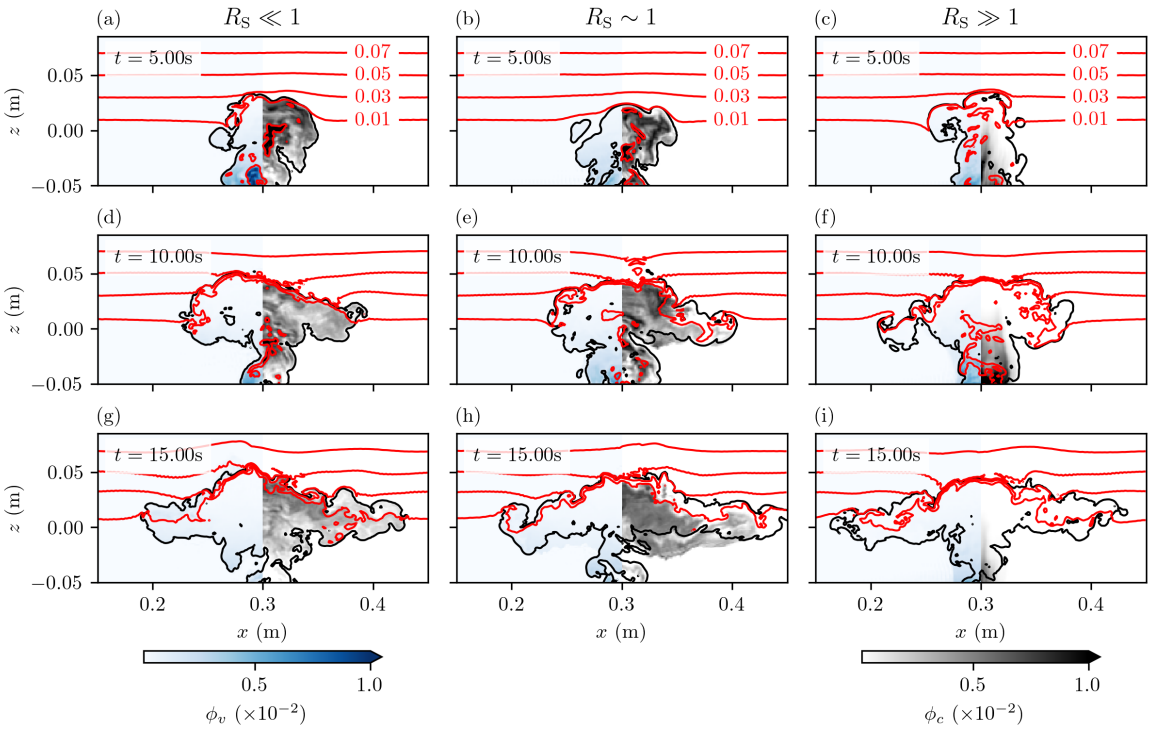

Fig. 5.5 Snapshots of simulations with varied w_s at $t = 5, 10, 15$ s showing vapour ϕ_v and ice ϕ_c in each panel. These simulations are representative of regimes with $R_S \ll 1, R_S \sim 1$ and $R_S \gg 1$ respectively. Here, $R_H \approx 2$. Buoyancy contours are shown in red every 0.02 from $b = 0.01\,\mathrm{m\ s^{-2}}$. The black line indicates the plume contour $\phi_p = 10^{-3}$.

vapour. Note that figure 5.4 shows averaged profiles which do not reflect local changes in ϕ_{vs} from mixing between the plume and the significantly more buoyant surroundings which could allow more substantial concentrations of vapour to form. In § 5.5 we use the buoyancy-tracer volume distribution to explore this in more detail.

Figure 5.5 shows snapshots of the simulations with fixed reference saturation concentration $\phi_0 = 0.5$ and varied sedimentation velocity w_s. For these simulations, $R_H \approx 2$ so the $R_S \ll 1$ case (with essentially no sedimentation) lies between the $R_H \sim 1$ and $R_H \gg 1$ regimes shown in figure 5.3. However, it is qualitatively closest to the $R_H \sim 1$ regime with both ice and vapour present in the plume as it penetrates into the stratified layer, though the ice concentration is much larger than the vapour concentration within the stratified layer because of continued adiabatic cooling after penetration. In the $R_S \gg 1$ regime, it is evident that the sedimentation velocity dominates the upward plume velocity meaning very little ice reaches the stratified layer. When $w_s > 0$, ice is 'decoupled' from the plume in the sense that we no longer have $\phi_p \approx \phi_v + \phi_c$ because ϕ_c does not precisely follow the flow. This is particularly

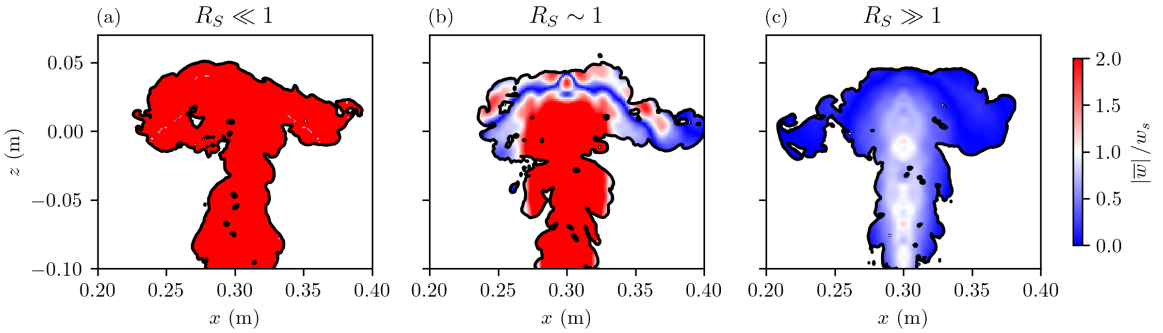

Fig. 5.6 x-z cross-sections through the plume centreline of simulations with $R_\mathrm{S} \ll 1, R_\mathrm{S} \sim 1$ and $R_\mathrm{S} \gg 1$, showing the ratio of the time and azimuthal average vertical velocity $\overline{w}$ and the sedimentation velocity w_s.

evident at $t = 15\,\mathrm{s}$ in the $R_\mathrm{S} \gg 1$ case where ice has fallen out of the plume into the subsaturated environment and sublimated to form vapour. Thus we find both vapour and ice outside of the $\phi_p = 10^{-3}$ contour. The intermediate regime $R_\mathrm{S} \sim 1$ appears similar to the $R_\mathrm{S} \ll 1$ case at $t = 5\,\mathrm{s}$, though there is less ice present at the plume boundary, because the centreline velocity of the plume still exceeds w_s in the $R_\mathrm{S} \sim 1$ case (see below). At $t = 10\,\mathrm{s}$ and particularly at $t = 15\,\mathrm{s}$ ice is sedimenting out of the intrusion, where the velocity is predominantly radial and does not counteract the downward sedimentation velocity.

The competition between the plume flow keeping ice in suspension, and sedimentation settling ice out of the plume, can be seen by comparing the magnitude of the time- and azimuthally-averaged vertical velocity $\overline{w}$ (calculated over $0 \leq t \leq t_\mathrm{lim}$) and the sedimentation velocity, as shown in figure 5.6. In the $R_\mathrm{S} \gg 1$ case, w_s is sufficiently large to dominate both the turbulent vertical velocity and the mean vertical velocity in most of the plume. However, on the plume centreline, w_s and $\overline{w}$ are of similar magnitude so ice is still lifted towards the stratified layer. In the intermediate regime $R_\mathrm{S} \sim 1$ the turbulent vertical velocity and sedimentation velocity are of similar velocity, so one might expect ice concentration to decrease with height since not all ice is kept in suspension by turbulent eddies. However, the mean vertical velocity on the plume centreline far exceeds w_s so ice is lifted into the stratified layer. Subsequently, as plume fluid collapses in the plume cap, the mean vertical velocity felt by fluid parcels is reduced (and changes sign) so ice begins to fall out of the plume. In summary, we expect that ice reaches the stratified layer even when $R_\mathrm{S} > 1$ owing to the strong updraft velocity on the plume centreline. However, provided w_s is non-negligible then

we expect ice to fall out of the plume once the upward flow overturns near $z_{\max}$ and subsides towards the intrusion.

5.5 Moist buoyancy-tracer volume distributions

To explore the combined effect of moist processes and mixing, here we modify the buoyancy-tracer volume distribution formalism introduced in § 3.3 to account for the additional moist terms in the governing equations. We then use the formalism to examine the effect of mixing on the vapour concentration in the regimes with varied R_{H} and R_{S}. Whilst we do not use the partitioning of the plume defined in chapter 3, the evolution of the volume distribution for vapour and ice gives a useful picture of how the hydration mechanism operates and in chapter 6 we use the passive tracer volume distribution to identify how large-scale vertical shear influences mixing.

The volume distribution for the passive tracer is as stated in § 3.3 except with ϕ replaced by ϕ_p. From the vapour and ice tracer governing equations (5.15) and (5.16), the vapour and ice volume distributions W_v and W_c evolve according to

$$\frac{\partial W_v}{\partial t} = -S_v - \nabla \cdot \boldsymbol{F}_v - \frac{\partial J_v}{\partial \phi_v}, \tag{5.35}$$

$$\frac{\partial W_c}{\partial t} = -S_c - \nabla \cdot \boldsymbol{F}_c - \frac{\partial J_c}{\partial \phi_c} - \frac{\partial K}{\partial \phi_c}, \tag{5.36}$$

where the buoyancy-vapour distributions in (5.35) are defined as

$$W_v(B, \Phi; t) = \int_V \delta(b(\boldsymbol{x}, t) - B)\delta(\phi_v(\boldsymbol{x}, t) - \Phi)\,\mathrm{d}V, \tag{5.37}$$

$$S_v(B, \Phi; t) = \int_{\partial V} \boldsymbol{u} \cdot \boldsymbol{n}\, \delta(b(\boldsymbol{x}, t) - B)\delta(\phi_v(\boldsymbol{x}, t) - \Phi)\,\mathrm{d}A, \tag{5.38}$$

$$\boldsymbol{F}_v(B, \Phi; t) = \int_V (\dot{b}, \dot{\phi})\, \delta(b(\boldsymbol{x}, t) - B)\delta(\phi_v(\boldsymbol{x}, t) - \Phi)\,\mathrm{d}V, \tag{5.39}$$

where $\dot{b} = \kappa\nabla^2 b - \nabla \cdot \boldsymbol{\lambda}_b$ and $\dot{\phi}_v = \kappa\nabla^2\phi_v - \nabla \cdot \boldsymbol{\lambda}_\phi$ represent the effect of diffusive mixing on b and ϕ_v. The ice distributions $W_c(b, \phi_c; t)$, $S_c(b, \phi_c; t)$, and $\boldsymbol{F}_c(b, \phi_c; t)$ are defined as in (5.37)–(5.39) except with ϕ_v replaced by ϕ_c. The additional 'moist' terms

in (5.35) and (5.36) are

$$J_v(B,\Phi;t) = -\int_V \left[\frac{\phi_v - \phi_{vs}}{\tau_m}\,\mathcal{H}(\max\{\phi_c, \phi_v - \phi_{vs}\})\right]\delta(b(\boldsymbol{x},t) - B)\,\delta(\phi_v(\boldsymbol{x},t) - \Phi)\,\mathrm{d}V, \tag{5.40}$$

$$J_c(B,\Phi;t) = \int_V \left[\frac{\phi_v - \phi_{vs}}{\tau_m}\,\mathcal{H}(\max\{\phi_c, \phi_v - \phi_{vs}\})\right]\delta(b(\boldsymbol{x},t) - B)\,\delta(\phi_c(\boldsymbol{x},t) - \Phi)\,\mathrm{d}V, \tag{5.41}$$

$$K(B,\Phi;t) = \int_V \left[w_s\frac{\partial \phi_c}{\partial z}\right]\delta(b(\boldsymbol{x},t) - B)\,\delta(\phi_c(\boldsymbol{x},t) - \Phi)\,\mathrm{d}V, \tag{5.42}$$

which are referred to as the vapour condensation flux, ice sublimation flux, and sedimentation flux respectively. These terms arise by replacing $\dot{\phi}$ in equation 3.3 in § 3.3.1 with $\dot{\phi}_v = -\mathcal{E}$ and $\dot{\phi}_c = \mathcal{E} + w_s\frac{\partial \phi_c}{\partial z}$, respectively, and separating the terms. Note that (5.40)–(5.42) are written as functions of (B,Φ) to aid clarity and for consistency with definitions given in § 3.3 but henceforth all 'vapour' distributions (with a subscript v) are written as functions of (b,ϕ_v) and all 'ice' distributions (with a subscript c) are written as functions of (b,ϕ_c).

In chapter 3, we used the volume distribution to explore the effect of turbulent mixing on the distribution of tracer in the flow. Recall that W_v represents the amount of fluid in the plume within the stratified layer with buoyancy and vapour concentration within a given range. Mixing acts to move volume through (b,ϕ_v)-space which is captured by $\boldsymbol{F}_v$, whilst J_v describes changes in the vapour concentration due to condensation. The source distribution S_v captures plume fluid entering the stratified layer. Compared with the approach used in chapter 3, there is the added complexity of the conversion between vapour and ice, each of which is associated with its own phase space (b,ϕ_v) or (b,ϕ_c) with its own set of distributions. We also have additional terms J_v, J_c and K which could be interpreted as vectors in (b,ϕ_v)-space (for J_v) or (b,ϕ_c)-space (for J_c and K) with no component in the b direction, representing the fact that moist conversion and sedimentation acts on the tracer concentration(s) alone, with no effect on the buoyancy of fluid parcels. The distributions are calculated as described in § 3.3.3, with the number of buoyancy and tracer bins in the discrete calculation set as $N_b = N_\phi = 256$. As before, we use $b_{\min} = 0$ so that all fluid with non-zero buoyancy is represented in the distribution, i.e. excluding fluid from the uniform layer. The minimum vapour, ice and passive tracer concentrations $\phi_{v,\min}, \phi_{c,\min}$ and $\phi_{p,\min}$ are chosen so that Gibbs ringing artefacts do not appear in the distribution. In some

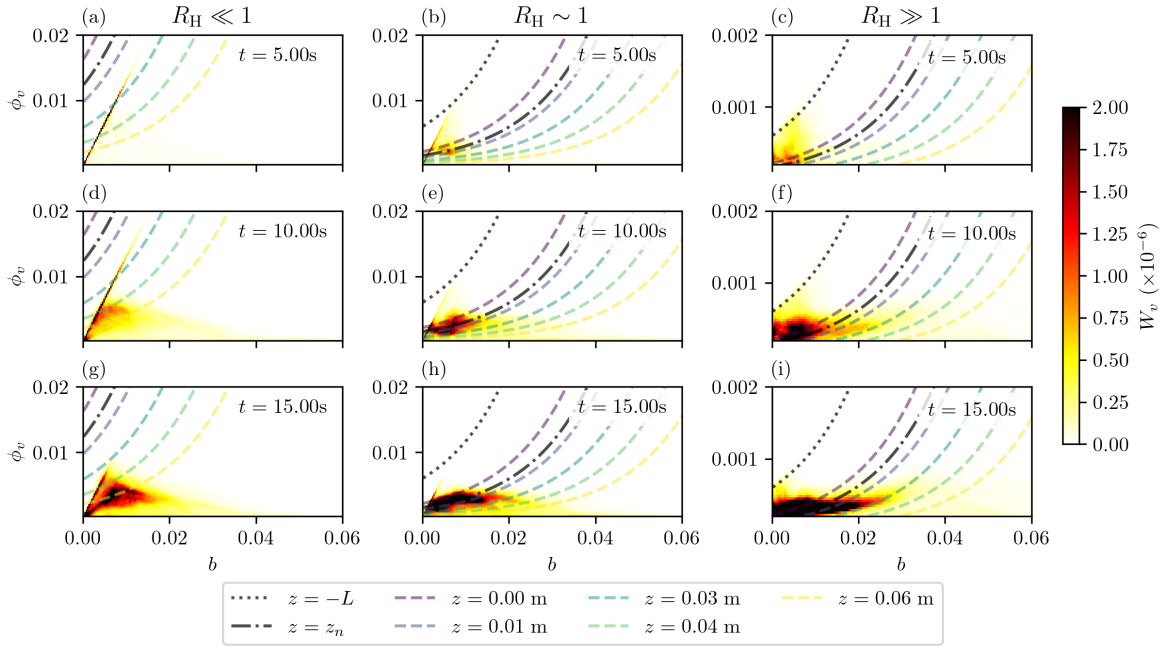

Fig. 5.7 Buoyancy-vapour volume distribution W_v in simulations with $R_H \ll 1, R_H \sim 1$ and $R_H \gg 1$ at times $t = 5, 10, 15$ s. Saturation curves $\phi_v = \phi_0 \exp(\alpha(\Theta b - \Gamma(z + H)))$ with $z = -L$ (black dotted), $z = z_n$ (black dot-dashed), and heights $z = 0.01, 0.03, 0.05, 0.07, 0.09$ m (dashed colour lines).

cases, particularly when $R_H \gg 1$, the minimum saturation concentration can fall below $\phi_{v,\min}$. However, this issue applies to relatively few fluid parcels in the domain and does not qualitatively influence our conclusions. In simulations presented here and in chapter 6 we use $\phi_{v,\min} = \phi_{c,\min} = \phi_{p,\min} = 2 \times 10^{-4}$. Note that, as in chapter 3, we define the 'stratified layer' (where the volume distribution is computed) to be $z \geq -L$ where $L = F_0^{1/4} N_0^{-3/4}$ is the characteristic lengthscale when non-dimensionalising with F_0 and N_0.

As discussed in § 5.2, our primary focus is on the distribution of vapour in the stratified layer post-penetration. We therefore focus on the vapour volume distribution W_v first. Figure 5.7 shows W_v at $t = 5, 10, 15$ s in the simulations with $R_H \ll 1, R_H \sim 1$ and $R_H \gg 1$ and figure 5.8 shows W_v at the same times in simulations with $R_S \ll 1, R_S \sim 1$ and $R_S \gg 1$. In each plot, we show 'saturation curves' $\phi_v = \phi_{vs}(b, z)$ as a function of b for a range of values of z. Vapour concentrations exceeding the saturation curve at a given height will condense until ϕ_v reduces to the saturation curve (with b unchanged). The black dotted line shows the saturation curve at $z = -L$ where the source distributions S_v and S_c are calculated and therefore acts as a limit on the maximum vapour concentrations at penetration. The black dash-dotted line shows the

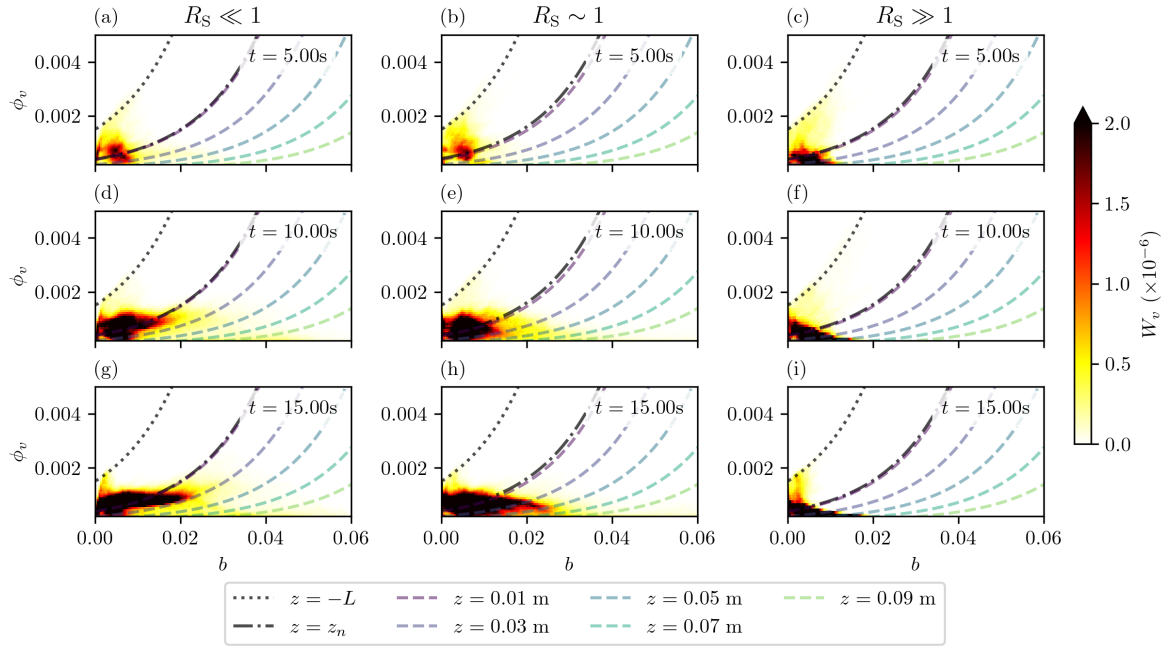

Fig. 5.8 Buoyancy-vapour volume distribution W_v in simulations with $R_S \ll 1, R_S \sim 1$ and $R_S \gg 1$ at times $t = 5, 10, 15$ s. Saturation curves $\phi_v = \phi_0 \exp(\alpha(\Theta b - \Gamma(z+H)))$ with $z = -L$ (black dotted), $z = z_n$ (black dot-dashed), and heights $z = 0.01, 0.03, 0.05, 0.07, 0.09$ m (dashed colour lines).

saturation curve at $z = z_n$ where the intrusion forms; we expect vapour to accumulate near this curve at late times. The remaining coloured dashed lines show the saturation curve at heights $z = 0.01, 0.03, 0.05, 0.07, 0.09$ m. This aids comparison of the volume distributions in figure 5.7 and figure 5.8 with cross-sections in physical space shown in figure 5.3 and figure 5.5 respectively.

Moist processes play essentially no role in the $R_H \ll 1$ simulation, so the vapour distribution W_v behaves qualitatively the same as the passive tracer in chapter 3. At all times, the vapour concentrations on the source line remain well below the saturation curves except for the extreme end of the source line where some fluid shielded from the surroundings is adiabatically cooled during rise to z_{max}, condensing some vapour. In the $R_H \sim 1$ case most of the source line remains below the saturation curve at penetration, so condensation only occurs close to the plume centreline where vapour concentrations are large enough to exceed the saturation concentration. As fluid rises into the stratified layer, the saturation curve quickly limits vapour concentrations so most fluid parcels experience some condensation during rise towards z_{max}. As fluid parcels join the intrusion, they are limited by the saturation curves close to $z = z_n$ which limits the region of (b, ϕ_v) space where fluid accumulates at late times.

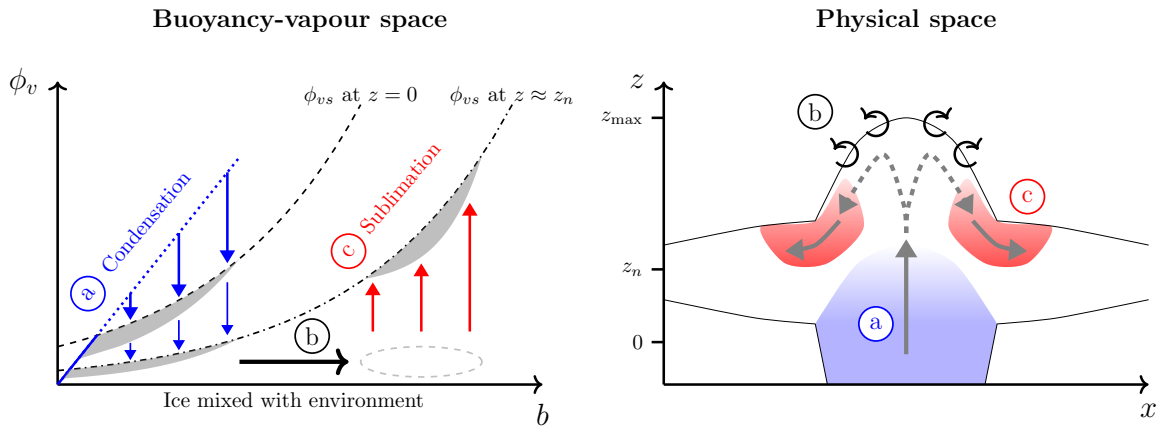

Fig. 5.9 Schematic illustration of convective hydration of the stratified layer in the $R_{\mathrm{H}} \gg 1$ regime where the plume is ice-loaded at penetration. Left panel shows processes in (b, ϕ_v)-space. Right panel shows corresponding effect in physical space with the flow indicated by solid gray arrows (when carrying vapour) and dashed gray arrows (without vapour). Coloured arrows in the left panel correspond with coloured regions in the right panel. (a) Plume fluid on the source line experiences condensation during rise through the uniform layer (blue arrows). At penetration, vapour concentrations (left, gray region at small b) are limited by the saturation curve with $z = 0$ (left, dashed black curve). (b) Ice carried by the plume is transported to larger buoyancies via mixing with more buoyant environmental fluid near $z_{\max}$ (left, gray dashed ellipse; right, circular arrows). Warmer mixed fluid permits larger vapour concentrations. (c) Sublimation of ice (red arrows) produces large vapour concentrations at large b (gray region at large b) which is aided by adiabatic warming as fluid descends and joins the intrusion. Fluid accumulates close to the saturation curve with $z = z_n$ (dot dashed black curve).

The evolution of W_v in the $R_{\mathrm{H}} \gg 1$ simulation is qualitatively different to the $R_{\mathrm{H}} \ll 1$ and $R_{\mathrm{H}} \sim 1$ cases; most fluid parcels undergo condensation during rise through the uniform layer so the evolution of W_v heavily depends on the evolution of W_c and subsequent conversion from ice back to vapour. The saturation curve at penetration significantly restricts vapour concentrations on the source line. As plume fluid mixes with the environment, ice and vapour is shifted towards larger b where the saturation concentration ϕ_{vs} is (exponentially) larger, allowing ice to sublimate. Thus W_v increases at large b even without direct transport in (b, ϕ_v)-space. The abundance of ice in the $R_{\mathrm{H}} \gg 1$ regime means that mixtures of plume and environmental fluid quickly reach saturation. Thus the volume distribution at $t = 15\,\mathrm{s}$ accumulates near the saturation curve with $z = z_n$ with more substantial volume at larger values of b than found in the $R_{\mathrm{H}} \sim 1$ and $R_{\mathrm{H}} \ll 1$ cases. This process, which is representative of the TTL hydration mechanism, is illustrated schematically in figure 5.9.

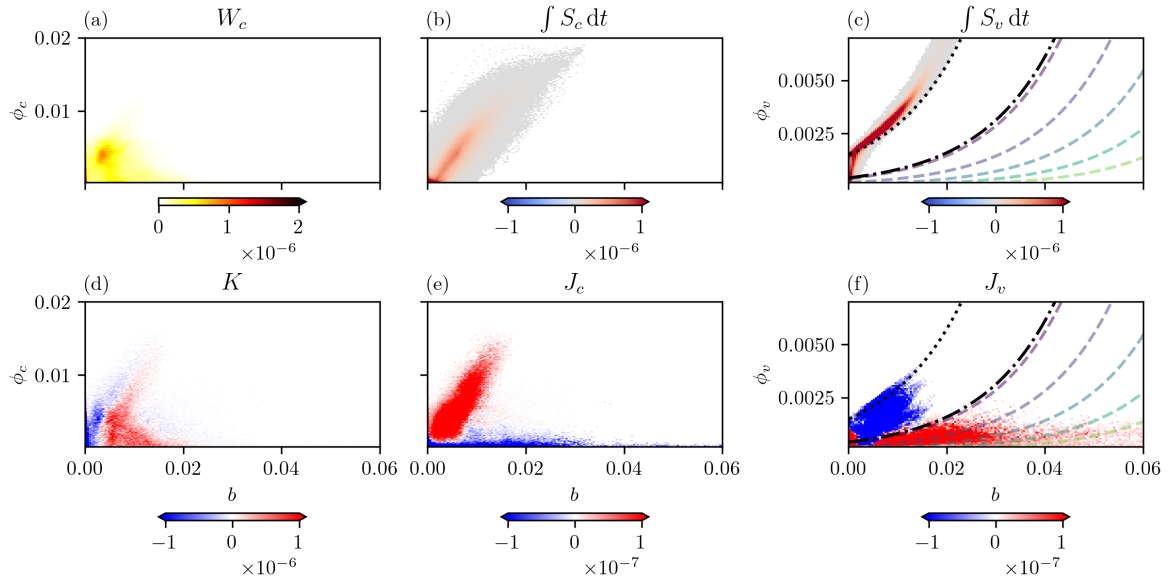

Fig. 5.10 Ice tracer volume distribution W_c, cumulative source ice and vapour distributions $\int S_c\,\mathrm{d}t$ and $\int S_v\,\mathrm{d}t$, sedimentation flux K, sublimation flux J_c, and condensation flux J_v at $t = 10\,\mathrm{s}$ in the simulation with $R_\mathrm{S} \sim 1$. In the two rightmost panels showing (b, ϕ_v) space, saturation curves are shown as in figure 5.7 and 5.8.

In the simulation with $R_\mathrm{S} \ll 1$ we see similar behaviour to the $R_\mathrm{H} \gg 1$ simulation but when R_S increases, the region of (b, ϕ_v) space where fluid accumulates is gradually restricted to smaller b and ϕ_v because settling of ice out of the plume limits the effectiveness of mixing with the environment in producing vapour via sublimation. Instead, vapour concentrations are reduced because of dilution by dry environmental fluid.

For completeness, figure 5.10 shows the remaining distributions W_c, J_c, J_v, K as well as the cumulative source distributions for vapour $\int S_v\,\mathrm{d}t$ and ice $\int S_c\,\mathrm{d}t$ at a single time $t = 10\,\mathrm{s}$ in the $R_\mathrm{S} \sim 1$ regime. As stated earlier, the sedimentation, sublimation and condensation fluxes are difficult to interpret since they represent a conversion between two different phase spaces. The ice concentration is not limited by saturation curves so, when ice is present in the stratified layer, W_c behaves in a similar manner to the passive tracer volume distribution in the 'dry' simulations considered in chapter 3. However, ice appears only when vapour condenses so the source line tends to be more diffuse than in the volume distribution for a fully passive tracer because varying amounts of ice appear depending on the extent to which the vapour concentration exceeds the saturation concentration. The cumulative source distribution for the ice tracer shows the distribution of ice that enters the stratified layer, which clearly shows the more

diffuse shape of the source line for the ice tracer relative to that seen for the vapour tracer which remains reasonably confined as seen in chapter 3. However, here the extreme end of the vapour source line is limited by the saturation curve at penetration. Regions where the condensation flux J_v is positive in (b, ϕ_v) space show where vapour is being converted to ice (blue), which appears in (b, ϕ_c) space where J_c is positive (red). Similarly, J_v is positive (red) where ice is being sublimated and corresponds with regions where J_c is negative (blue). This is consistent with the schematic illustration of the hydration process in figure 5.9 – ice is formed on the source line as the saturation curve limits vapour concentrations, which is then mixed towards large buoyancy via mixing with the more buoyant environment, and then sublimated to reach saturation at larger b where larger vapour concentrations are permitted. Alongside the moist conversion processes, sedimentation moves ice downwards. This is difficult to interpret in (b, ϕ_c) space. Figure 5.10 shows that K is negative at the 'top' of the source line (i.e. where ϕ_c is larger) since the volume of fluid with these larger concentrations is reduced. Correspondingly, the volume of fluid with smaller concentrations of ice increases so K is positive.

Chapter 6

The influence of convective intensity, turbulent mixing, sedimentation and vertical shear in convective hydration of a stratified layer

6.1 Introduction

In this chapter we use the minimal moisture model formulated in chapter 5, shown schematically in figure 6.1, to investigate the relative influence of mixing, convective intensity, microphysics and vertical shear in convective hydration of a stably stratified layer. Here, the term 'microphysics' is used to mean the three moist processes which are retained in our minimal moisture model: condensation of vapour into ice, sublimation of ice into vapour, and sedimentation of ice. In § 5.2 we detailed the mechanism for hydration of the TTL by convective overshoots, which relies on mixing of ice-loaded air parcels with warmer and drier stratospheric air, resulting in formation of anomalous vapour concentrations via sublimation of some of the ice content. Thus the 'hydration mechanism' depends on transport of moisture (primarily as ice), turbulent mixing of that moisture across buoyancy contours, and the microphysics of phase change, i.e. conversion between moist species. The mechanisms that lead to mixing between moist tropospheric air and dry stratospheric air have been proposed to include (internal)

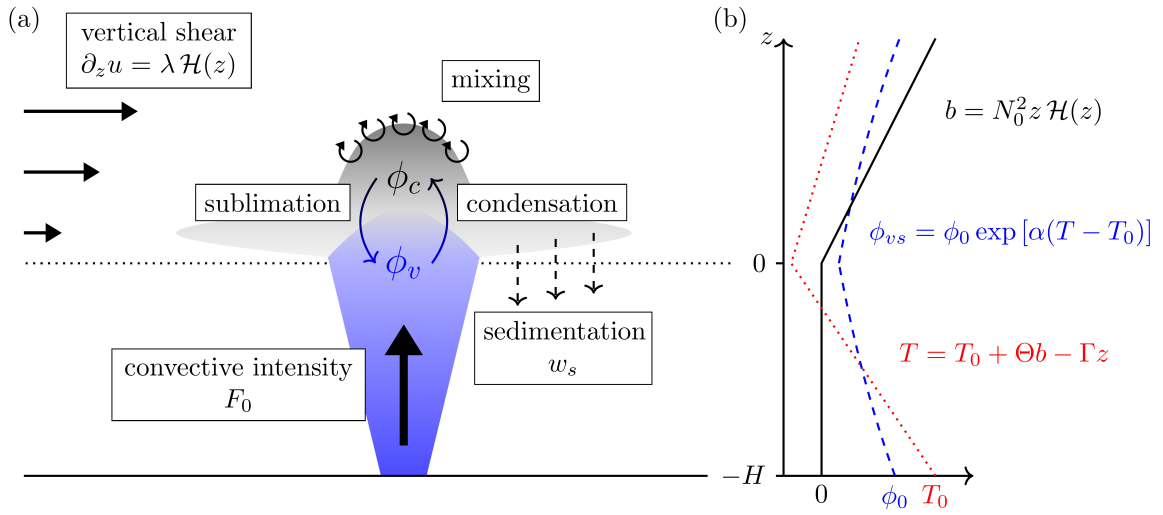

Fig. 6.1 Schematic diagram of the problem setup, showing (a) processes involved in convective hydration with their controlling parameters and (b) environmental profiles of buoyancy b, temperature T and saturation vapour concentration ϕ_{vs}.

gravity wave breaking, shear instabilities at the cloud edge, and vortices formed by the gravity wave response to convective penetration. Studies have attempted to identify the dominant process – i.e. whichever exerts the most control on the resulting hydration of the TTL – in numerical simulations of individual convective overshoots (or collections thereof) using complex microphysical models and observed environmental setups. Whilst realistic and directly comparable with observations, these studies are each limited to a narrow regime which is not necessarily representative of the breadth of regimes possible in the TTL and does not uncover how the interaction between processes may vary.

We address this problem by considering the representative flow in which a buoyant plume penetrates into a stably stratified layer. We include only processes which have been identified to play a role in controlling vapour transport and explore the interplay between these processes in regimes where each process is weak, influential, or dominant relative to others. These simulations are performed in a setting representative of the TTL where the plume is ice-loaded at penetration. Our use of a minimal model is advantageous over previous comprehensive modelling studies using complex meteorological models that are computationally expensive because our approach allows more experiments with limited resources. We can therefore explore multiple simulations which cover the full breadth of regimes.

The simulations are organised into one control run and three experiments, each with a single parameter varied relative to the control simulation, determining (1) the sedimentation strength, (2) plume forcing strength, and (3) large-scale vertical shear, respectively. We use the regime numbers R_{H}, R_{S} and R_{SH} introduced in § 5.3 to quantify each regime. To place our results in the context of the literature on hydration of the TTL, we refer to three studies: Hassim and Lane (2010), henceforth referred to as H10; Dauhut et al. (2018), henceforth D18; and Sang et al. (2018), henceforth S18. As in our simulations, these studies consider large-eddy simulations which parameterise the effects of sub-grid-scale turbulence. Our simulations are performed at the lab scale (as detailed in § 5.3) which means the scale at which energy is injected into the system (by the plume) is closer to the scale at which it is dissipated (by turbulence), so our results are less sensitive to the SGS model used in our LES compared with the simulations in H10, D18 and S18 with $\mathcal{O}(100\mathrm{m})$ grid spacing. Using results presented in chapter 3, in our simulations energy is injected at a $\sim 10^{-1}\,\mathrm{m}$ scale and dissipated at the Kolmogorov scale $\eta_k \sim 10^{-5}\,\mathrm{m}$ with a resolved grid scale $\sim 10^{-3}\,\mathrm{m}$. In atmospheric convection (Feist et al., 2019), energy is injected at a $\sim 10^{4}\,\mathrm{m}$ scale and dissipated at the Kolmogorov scale $\eta_k \sim 10^{-3}\,\mathrm{m}$ with a resolved grid scale $\sim 10^{2}\,\mathrm{m}$. Thus a larger fraction of the inertial subrange is resolved in the simulations presented in this thesis compared with those in the literature. In the remainder of § 6.1 we review the main findings in H10, D18 and S18. In § 6.2 we detail the experimental design and parameter choices. The control simulation is presented in § 6.3 and compared with our current understanding of convective hydration of the TTL. The results of the three experiments are presented in § 6.4–6.6 in the context of the research questions posed below. We summarise our findings in § 6.7.

In § 6.4 we consider the competition between sedimentation and mixing; sedimentation acts to settle ice out of the plume whilst mixing acts to sublimate ice into vapour. Mixing may overcome sedimentation by acting quickly enough for plume fluid to reach saturation before ice is fully removed from the plume, or sedimentation may be strong enough to heavily modulate the influence of mixing by removing ice quickly. These two extremes lead to different conclusions on the resulting hydration of the stratified layer, which can be assessed using semi-quantitative models that predict vapour concentrations indirectly by using the temperature of fluid parcels. In the former regime, which we refer to as the 'slow sedimentation' regime, we expect that vapour concentrations are determined by their current temperature since plume fluid remains close to saturation. In the latter regime, referred to as the 'fast sedimentation' regime,

vapour concentrations are determined by the minimum temperature experienced along parcel trajectories, which coincides with the minimum vapour concentration. Any excess moisture is removed by sedimentation. H10 found that mixing is more localised than the extensive patterns of moistening (or drying, in the case of a supersaturated environment) in their simulations, leading to the conclusion that microphysical processes prevail over the effects of small-scale mixing in determining vapour transport. H10 also note that there is little mixing outside the simulated overshoot, meaning mixing plays a limited role in redistributing water vapour; instead, microphysical control of ice crystal concentration and size distributions, and thus sedimentation velocity, determines the net hydration achieved. However, S18 instead found that turbulent mixing makes a significant contribution to the transport of small ice particles from the convective cloud top into the TTL environment. Smaller ice particles are less influenced by sedimentation and therefore mixing has a more influential role in determining net hydration. Using simulations with varied sedimentation velocity we are able to explore regimes where sedimentation is fast, slow, and of intermediate strength. With the fixed sedimentation velocity used in our minimal moisture model, these regimes are essentially representative of cases in the real atmosphere where the mean size of ice crystals tends to be large or small relative to the intermediate regime.

In § 6.5 we consider the effect of 'convective intensity' by considering simulations with strengthened plume forcing. Whilst the dynamical evolution of penetration, collapse and spreading is unchanged when convective intensity is increased (i.e. the plume is more buoyant), the time evolution of the flow may change as well as the intensity of mixing between the plume and environment. S18 considered simulations with convection initiated by a buoyant thermal, i.e. a plume forced for a short time, with varied initial temperature. It was found that the net water vapour transport increases with convective intensity whilst the convective 'lifecycle', i.e. the timescale on which overshoots penetrate and collapse, is unchanged. By varying the convective intensity, we are able to address the conclusion by D18 that the maximum penetration height is the key prognostic variable in determining water vapour transport since it determines the largest potential temperature of stratospheric air which is mixed into the overshoot, as discussed earlier in § 5.2. The stratification strength is fixed in the simulations presented in this chapter and $z_{\max} \sim F_0^{1/4} N_0^{-3/4}$ (see chapter 2) so by increasing F_0 we also increase $z_{\max}$. Whilst it is clear from chapter 3 that penetration to a greater $z_{\max}$ allows mixing of plume fluid to much greater buoyancies, the increased maximum height may result in larger quantities of vapour condensing via adiabatic

cooling during ascent, thus offering the potential for sedimentation to exert stronger control on hydration when convective intensity is increased.

Finally, in § 6.6 we consider the influence of large-scale vertical shear on mixing (and thus hydration) and the vortical and gravity wave response to convective penetration in the presence of shear. The dynamical evolution of the flow is significantly influenced by the presence of a mean flow; we consider the effect of these structural changes in the flow on turbulent mixing in general as well as the effect on hydration of the stratified layer. The influence of vertical shear was considered in detail by S18 who found that the net hydration decreases with increasing shear rate, though the vertical shear is found to have no influence on the strength of overshooting. The reduced vapour transport is attributed to a reduction in the occurrence of gravity wave breaking, with a reduction in gravity wave amplitudes. Although small-scale turbulent mixing is found to strengthen with shear rate, S18 find that the modulation of gravity wave breaking is more influential. The results of S18 appear to contradict the view that strong vertical wind shear tends to favour gravity wave breaking (e.g. Lane et al. (2003), and also noted in H10 and D18). As waves break, their amplitudes increase until non-linear effects become dominant and turbulence is generated. Internal gravity waves have been identified as key process in causing intense mixing between the overshoot and environment because of the production of successive vortices with alternating sign (Dauhut et al., 2018; Lane, 2008) that may lead to shear instabilities at the cloud edge. D18 also place importance on strong wind shear inside the overshoot that produces the strong cross-isentropic transport needed to warm ice-loaded air parcels. As a final addendum to our investigation of vertical shear, we address part of the study by H10 which identifies the mechanism for the jumping cirrus phenomenon, introduced in § 5.2, that results in moistening of the TTL well above the maximum penetration height. H10 identified large vertical displacements (around 1 km in magnitude) as the key mechanism for the formation of jumping cirrus, which acts to bring together and mix moist air lower in the TTL with relatively dry air higher in the TTL. The resulting moist air reaches saturation as it ascends towards its neutral buoyancy height, producing cirrus (i.e. clouds of ice). Gravity wave breaking has been invoked as the primary mechanism responsible for these large vertical displacements but it remains unclear if wave breaking is essential; large vertical displacements could instead be associated with collapse of the overshoot or propagating gravity waves and therefore may be present in regimes where the vertical shear is weak or absent (where critical layer wave breaking is not possible).

Simulation	N_h	L_h (m)	t_{end} (s)	F_0 ($\times 10^{-6}$) (m^4s^{-3})	w_s (m s^{-1})	R_{S}	λ (s^{-1})	R_{SH}
`control`	512	0.6	35	5	0	0	0	0
`weak_sed`	512	0.6	35	5	5×10^{-4}	0.06	0	0
`sed`	512	0.6	35	5	5×10^{-3}	0.6	0	0
`strong_sed`	512	0.6	35	5	5×10^{-2}	7.2	0	0
`control+F`	512	0.6	35	20	0	0	0	0
`sed+F`	512	0.6	35	20	5×10^{-3}	0.45	0	0
`strong_sed+F`	512	0.6	35	20	5×10^{-2}	4.0	0	0
`weak_shear`	1024	0.8	15	5	0	0	0.175	0.30
`shear`	1024	0.8	15	5	0	0	0.5	0.93
`strong_shear`	1024	0.8	15	5	0	0	1.2	2.0

Table 6.1 Simulation parameters. The parameters $N_0 = 1\,\text{s}^{-1}$, $F_0^{(\phi)} = 5 \times 10^{-6}\,\text{m}^3\text{s}^{-1}$, $\phi_0 = 0.2$, $t_{\text{lim}} = 10\,\text{s}$, $N_z = 513$ and $L_z = 0.5\,\text{m}$ are fixed. The mean attained plume buoyancy and tracer fluxes are $F_0^{(\phi)} = 5.5 \times 10^{-8}\,\text{m}^3\text{s}^{-1}$ and $F_0 = 5.5 \times 10^{-8}\,\text{m}^4\text{s}^{-3}$ in the control forcing simulations and $F_0 = 3.0 \times 10^{-7}\,\text{m}^4\text{s}^{-3}$ and $F_0^{(\phi)} = 7.5 \times 10^{-8}\,\text{m}^3\text{s}^{-1}$ in the strong forcing simulations.

6.2 Experimental design

The simulation setup and numerical method are as described in chapter 2 with specific alterations for the minimal moisture model as detailed in chapter 5. The simulation parameters used in the control simulation and three experiments are detailed in table 6.1. We refer to simulations using the name given in the first column, e.g. the control simulation is referred to as `control`. Remaining parameters are as detailed in chapter 5 and given in table 5.2.

Two important choices are made in setting the simulation parameters. First, we restrict attention to the model regime $R_{\text{H}} \gg 1$ since it is representative of the atmospheric case where convective overshoots penetrate into the TTL carrying significant concentrations of ice. This is verified by observational evidence and numerical simulations. For example, figure 7(d) of D18 shows the solid water (i.e. ice) mixing ratio around 10^4 ppmv and the vapour mixing ratio around 10 ppmv in an overshoot that results in a net hydration above the 380 K isentrope, which is used to define stratospheric air. Translating to the language of our setup, assuming that sedimentation is weak then $\phi_p = \phi_v + \phi_c \approx 10^4$ at penetration and hence $R_{\text{H}} \approx \phi_v/\phi_p \approx 10^3$. As discussed in § 5.3, this is not practically achievable in our simulations but nonetheless illustrates why

the $R_\mathrm{H} \gg 1$ regime is most relevant. In all simulations we use a reference saturation concentration $\phi_0 = 0.2$, yielding an average $R_\mathrm{H} \approx 12$ in simulations with the control plume forcing value shown in table 6.1. Simulations with the increased plume forcing yield an average $R_\mathrm{H} \approx 5$: the plume is more buoyant, hence warmer, so can support larger vapour concentrations. Thus given the same tracer forcing, condensation occurs higher in the uniform layer and the partitioning of total water into vapour and ice is shifted towards vapour at penetration, reducing R_H. The second choice is to limit plume forcing to a finite time and run simulations long enough to explore the 'relaxation' stage of the flow evolution that occurs after plume forcing ceases and the plume cap has collapsed. During this stage, buoyancy contours relax to their initial positions and re-establish the stratification of the environment that was disturbed by the plume. Plumes that are forced for a finite time are essentially thermals, i.e. transient releases of buoyant fluid. This setup can be considered representative of the atmospheric problem where the intense updraft that drives a convective overshoot is eventually cut off by a spreading cold pool at the surface – another justification is the use of a buoyant thermal to initiate convection in numerical studies such as H10 and S18. In our simulations, plume forcing ends at time $t_\mathrm{lim} = 10\,\mathrm{s}$, equivalent to $\mathcal{O}(10\,\mathrm{min})$ on atmospheric scales. Another motivation to continue simulations long after plume forcing ends, up to time $t_\mathrm{end} = 35\,\mathrm{s}$, is a clearer distinction between the net hydration in different cases, especially those with weak sedimentation where the effects are more clearly seen on long timescales. The longer simulation time means that the intrusion front reaches close to the edge of the (horizontally periodic) simulation domain. Test simulations showed that the radial spreading slows significantly after plume forcing ends at $t_\mathrm{lim} = 10\,\mathrm{s}$, so the continued spreading of the intrusion has a negligible effect on the flow evolution. Note that simulations with large-scale vertical shear are only run up to time $t_\mathrm{end} = 15\,\mathrm{s}$ so that the plume cannot not wrap around the horizontally periodic domain and interact with itself during the simulation.

The experiments are set up as follows. Table 6.2 shows the conversion of the simulation parameters from the lab scale to atmospheric scales, as well as characteristic dynamical quantities in each simulation: the typical turbulent vertical velocity in the plume w_eddy (defined in § 5.3.3), azimuthal average buoyancy and vertical velocity at penetration on the plume centreline $\overline{b}(r = 0, z = 0)$ and $\overline{w}(r = 0, z = 0)$ (averaged over $5 \leq t \leq 10\,\mathrm{s}$), maximum penetration height z_max, equilibrium height z_n, and dynamical timescale τ_d (defined in § 5.3.3).

Simulation(s)	Quantity	Lab scale	TTL scale
All	N_0^2 (s^{-2})	1	6.25×10^{-4}
All	t_{lim}	10 s	6.7 min
No shear	t_{end}	35 s	23.3 min
Shear	t_{end}	15 s	10 min
Control forcing	F_0 (m^4 s^{-3})	5.5×10^{-8}	2.1×10^{7}
Strong forcing		3.0×10^{-7}	1.1×10^{8}
`weak_sed` (`+F`)	w_s (m s^{-1})	5×10^{-4}	0.875
`sed` (`+F`)		5×10^{-3}	8.75
`strong_sed` (`+F`)		5×10^{-2}	87.5
`weak_shear`	λ (s^{-1})	0.175	4.4×10^{-3}
`shear`		0.5	1.3×10^{-2}
`strong_shear`		1.2	3.0×10^{-2}
No shear	w_{eddy} (m s^{-1})	7.7×10^{-3}	13.5
No shear (`+F`)		1.1×10^{-2}	19.3
`weak_shear`		7.1×10^{-3}	12.4
`shear`		9.3×10^{-3}	16.3
`strong_shear`		8.3×10^{-3}	14.5
Control forcing	$\overline{w}(r = 0, z = 0)$ (m s^{-1})	3.8×10^{-2}	67
Strong forcing		6.3×10^{-2}	110
Control forcing	$\overline{b}(r = 0, z = 0)$ (m s^{-2})	6.3×10^{-3}	0.28
Strong forcing		1.6×10^{-2}	0.70
No shear	z_{max}	5.2×10^{-2} m	3.6 km
No shear (`+F`)		8.2×10^{-2} m	5.7 km
`weak_shear`		5.1×10^{-2} m	3.6 km
`shear`		5.7×10^{-2} m	4.0 km
`strong_shear`		5.3×10^{-2} m	3.7 km
No shear	z_{n}	1.0×10^{-2} m	0.7 km
No shear (`+F`)		1.9×10^{-2} m	1.3 km
`weak_shear`		8.1×10^{-3} m	0.6 km
`shear`		1.3×10^{-2} m	0.9 km
`strong_shear`		1.8×10^{-2} m	1.3 km
No shear	τ_d (s)	2.10	84
No shear (`+F`)		1.80	72
`weak_shear`		1.72	69
`shear`		1.85	74
`strong_shear`		1.68	67

Table 6.2 Conversion of simulation parameters from the laboratory scale, as given in table 6.1 and described in the text, to atmospheric scales representative of the TTL. The scale factors R_t and R_l are derived in § 5.3.1 and given in table 5.1.

1. **Varied sedimentation strength.** The sedimentation velocity w_s is chosen to explore the regimes $R_\mathrm{S} \ll 1$, $R_\mathrm{S} \sim 1$ and $R_\mathrm{S} \gg 1$ in `weak_sed`, `sed`, and `strong_sed` respectively. Recall that $R_\mathrm{S} = w_s/w_\mathrm{eddy}$ is the ratio of the sedimentation velocity and the typical turbulent vertical velocity in the plume, w_eddy. Thus when $R_\mathrm{S} \ll 1$, ice is kept suspended in the plume by turbulent eddies, whilst when $R_\mathrm{S} \gg 1$ sedimentation acts to settle ice out of the plume rapidly. In simulation `weak_sed`, w_s is chosen to be representative of the atmospheric case: figure 2 of Grabowski (1998) shows the terminal velocity for rain and snow as a function of the mixing ratio using the Marshall-Palmer size distribution. For precipitating frozen water, equivalent to ice in our model, the velocity is on the order of $1\,\mathrm{ms}^{-1}$ on atmospheric scales which translates to $w_s = 5 \times 10^{-4}\,\mathrm{ms}^{-1}$ in our model.

2. **Varied forcing strength.** Simulations `control`, `sed`, and `strong_sed` are repeated with the source integral buoyancy flux F_0 quadrupled relative to the control simulation. Whilst the prescribed integral source tracer flux is fixed so that the tracer concentration carried by the plume remains the same, the measured tracer flux in the uniform layer is slightly larger than in the control forcing simulations because the vertical velocity is larger – note from § 2.2.3 that the vertical velocity forcing is controlled by F_0 as well as the buoyancy forcing.

3. **Varied vertical shear strength.** Large-scale vertical shear is introduced in the stratified layer with shear rate λ varied to give regimes $R_\mathrm{SH} \ll 1$, $R_\mathrm{SH} \sim 1$ and $R_\mathrm{SH} \gg 1$ in `weak_shear`, `shear`, and `strong_shear`, respectively. Recall that $R_\mathrm{SH} = \tau_d/\lambda^{-1}$ is the ratio of the dynamical timescale and the shear timescale. Thus when $R_\mathrm{SH} \ll 1$ the shear plays little role whilst when $R_\mathrm{SH} \gg 1$ the plume is significantly deformed. To accommodate the lateral deformation of the plume, the domain width is increased to $L_h = 0.8\,\mathrm{m}$ and the horizontal resolution is doubled to $N_h = 1024$. Values of the parameter λ are chosen to cover the wide range of vertical shear rates found in the TTL. The shear rate chosen for the $R_\mathrm{SH} \ll 1$ case is calculated from the mean shear between 15 and 18 km, 5°N-S from 2010 to 2015 using ERA5 reanalysis data, giving $\lambda_\mathrm{atmos} = 4.4 \times 10^{-3}\,\mathrm{s}^{-1}$ which translates to $\lambda = 0.175\,\mathrm{s}^{-1}$ at the lab scale. The choice of λ for the $R_\mathrm{SH} \gg 1$ regime is calculated from observations at individual locations over the Indian Peninsula, which give shear rates around $\lambda_\mathrm{atmos} \approx 3 \times 10^{-2}\,\mathrm{s}^{-1}$ on average during

summer monsoon months (Liu, 2017; Sunilkumar et al., 2015), which translates to $\lambda = 1.2\,\mathrm{s}^{-1}$ in our model.

Note that large-scale vertical shear combined with a stable stratification can lead to shear instability when the bulk Richardson number $\mathrm{Ri}_0 = N_0^2/\lambda^2 \leq 1/4$ (see § 1.3). The minimum Ri_0 is achieved in simulation `strong_shear`, with $\mathrm{Ri}_0 \approx 0.8$. Hence all simulations are initially stable, meaning shear instability will not spontaneously develop. However, internal wave breaking may lead to the generation of turbulence. To better resolve this process, and in anticipation of enhanced turbulent mixing, in the shear simulations the grid is stretched so that the vertical grid spacing is reduced between $z = 0$ and $z = 0.1\,\mathrm{m}$ (i.e. the resolution is increased).

6.3 Convective hydration of a stably stratified layer

In this section we examine the `control` simulation which acts a baseline for the experiments presented in the following sections. We discuss the evolution of the flow and introduce quantities used to assess mixing and vapour transport in the stratified layer.

6.3.1 Evolution of moist tracers and temperature

In the absence of a mean flow in the stratified layer, the evolution of the buoyancy field and flow proceeds as described in earlier chapters. Three stages of the flow evolution can be identified: penetration towards the maximum penetration height $z_{\max}$, collapse of the plume cap once plume forcing ends, and relaxation at late times. Here, we discuss the evolution of temperature T (which depends linearly on b and z, see (5.19)) and its effect on the moist tracer concentrations ϕ_v and ϕ_c via modification of the saturation vapour concentration $\phi_{vs}(T)$. It is also instructive to consider the relative humidity $r_h = \phi_v/\phi_{vs}$ – in studies of atmospheric models it is common to use the 'cloud contour' $r_h = 1$ to mark the edge of clouds (which are in the form of cirrus in the TTL). However, we continue to use the 'plume contour' $\phi_p = 10^{-3}$ for consistency with the 'dry' analysis in earlier chapters where definition of a cloud contour was not possible. The plume contour is also useful for the purposes of comparison between cases with varying sedimentation velocity; ice that sediments outside the plume contour is considered to be permanently lost from the plume. When sedimentation is weak or absent, vapour and ice concentrations are guaranteed to be small outside the plume

contour: $\phi_{v,c} \leq \phi_p \leq 10^{-3}$. Note that in the remainder of this chapter we use the terms 'moist' and 'dry' to refer to the size of the vapour concentration, i.e. if ϕ_{vs} is small then a region may be 'dry' in the sense it has a low vapour concentration ϕ_v but could carry large amounts of ice.

Figure 6.2 shows the time evolution of the vapour concentration ϕ_v, ice concentration ϕ_c, relative humidity r_h, and temperature T in x-z cross-sections through the plume centreline in simulation `control`. The strong central updraft lifts the plume to the maximum penetration height $z_{\max}$ shortly after $t = 5\,\mathrm{s}$. As the plume rises it cools (panel d) which freeze-dries the vapour content, forming a pocket of very cold fluid in the plume cap which is relatively dry (panel a) and loaded with ice (panel b). During this penetration stage, plume fluid is saturated whilst the surrounding environment is completely dry (panel c). At $t = 10\,\mathrm{s}$ the plume has started to collapse and form an intrusion. Mixing is evident at the top edge of the plume in panels (e)–(h): the $b = 0.01\,\mathrm{m\ s^{-2}}$ contour is significantly deformed and lies within the plume contour. The mixing of cold plume fluid with warm environmental fluid creates a shell of warmer fluid at the edge of the plume cap (panel h) where ϕ_v increases (panel e) and ϕ_c decreases (panel f) via sublimation. As mixed plume fluid subsides from the plume cap and joins the intrusion, it is adiabatically warmed (panel l) and continues to mix with the environment, further increasing ϕ_v (panel i) and decreasing ϕ_c (panel j). Note from panel (g) and (k) that mixtures of plume and environmental fluid remain saturated owing to the abundance of ice in the $R_{\mathrm{H}} \gg 1$ regime and the relatively low saturation concentration near the cold point, $z = 0$. Although plume forcing ends at time $t_{\mathrm{lim}} = 10\,\mathrm{s}$, plume fluid continues to rise through the uniform layer and can still be seen penetrating past the cold point at $t = 15\,\mathrm{s}$ in panels (i)–(l). The collapsing stage of the flow evolution continues through $t = 15\,\mathrm{s}$, with strong mixing evident in the plume cap and intrusion. Gravity waves are evident from the perturbation of the isentropes above the plume as well as perturbation of the environmental temperature in panels (l), (p), and (t). At $t = 25\,\mathrm{s}$ and $t = 35\,\mathrm{s}$ the plume has reached the relaxation stage; isopycnals gradually relax and the temperature difference between the plume and environment reduces – note that plume fluid becomes stratified like the surrounding environment (panel t). A moist region is evident in panel (m) between the $b = 0.01\,\mathrm{m\ s^{-2}}$ and $b = 0.04\,\mathrm{m\ s^{-2}}$ contours. Mixed plume fluid remains at saturation (panel s) and some ice remains in the plume (panel r), whilst some fluid surrounding the plume is slightly subsaturated and carries some vapour (panel q) but no ice.

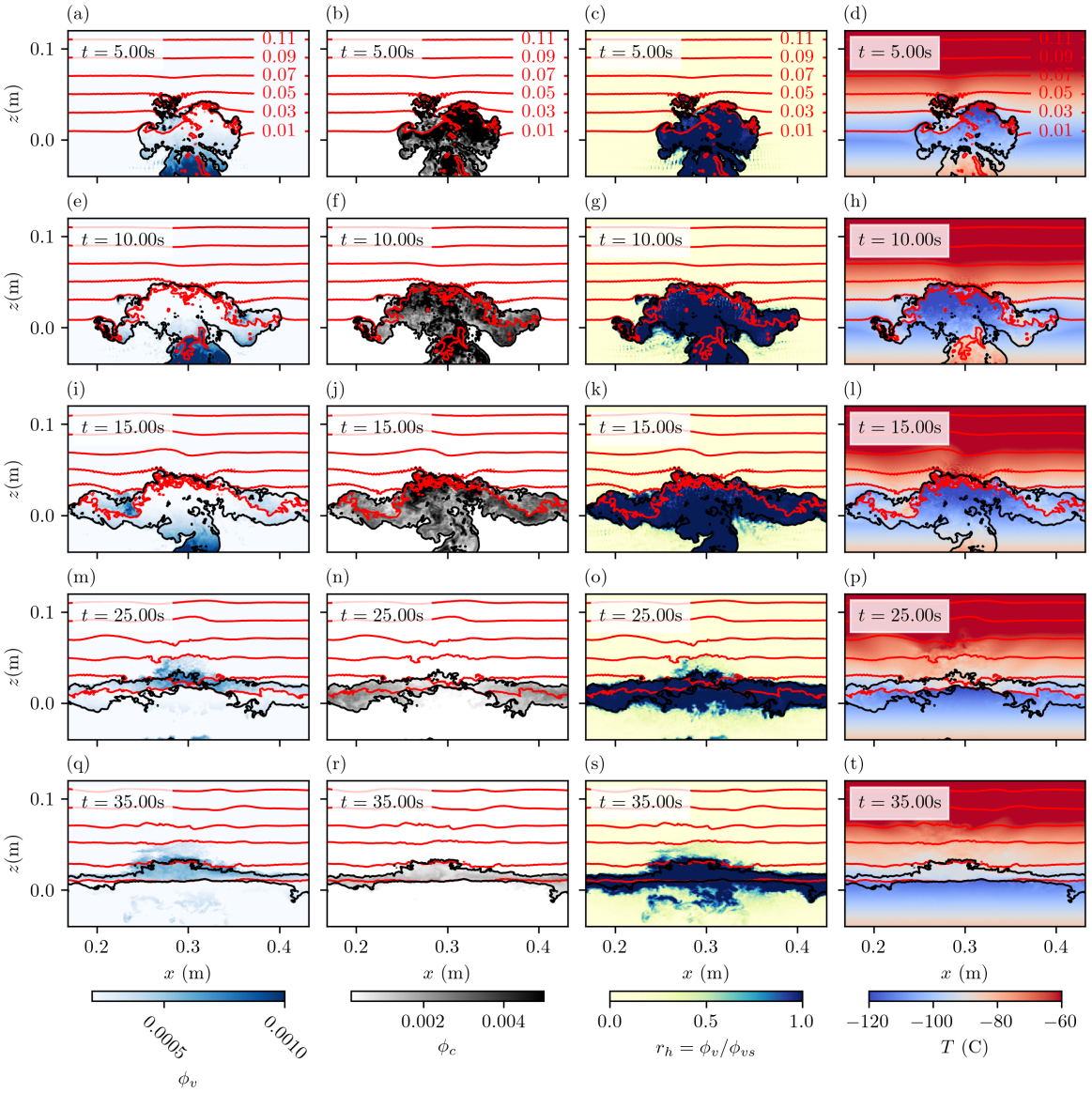

Fig. 6.2 Snapshots of simulation `control` at $t = 5, 10, 15, 25, 35$ s showing vapour concentration ϕ_v, ice concentration ϕ_c, relative humidity $r_h = \phi_v/\phi_{vs}$ and temperature T. The black outline indicates the plume contour $\phi_p = 10^{-3}$. In each plot, buoyancy contours are shown in red every 0.02 from $b = 0.01\,\mathrm{m\ s^{-2}}$.

6.3.2 Quantifying hydration of the stratified layer

To quantify the evolution of moist and passive tracers, we calculate the total amount of each tracer in the stratified layer at time t. The total amount of vapour is

$$\mathcal{T}_v(t) = \int_{\substack{z\geq -L \\ \phi_v \geq \phi_{v,\min}}} \phi_v(\boldsymbol{x}, t)\,\mathrm{d}V = \int W_v(b, \phi; t)\phi\,\mathrm{d}\phi, \tag{6.1}$$

where we exclude vapour concentrations $\phi_v \leq \phi_{v,\min}$ to handle any numerical artefacts, as with the moist volume distributions presented in § 5.5. The total amount of ice $\mathcal{T}_c$, and passive tracer $\mathcal{T}_p$, is defined as in (6.1) but with vapour quantities replaced by ice and passive tracer quantities, respectively. The total amount of vapour that has been directly transported into the stratified layer by the plume up to time t is

$$\mathcal{I}_v(t) = \int_0^t \int_{\substack{z=-L \\ \phi_v \geq \phi_{v,\min}}} \phi_v(\boldsymbol{x}, t) w(\boldsymbol{x}, t)\,\mathrm{d}S\mathrm{d}t = \int_0^t \int S_v(b, \phi; t)\phi\,\mathrm{d}\phi\mathrm{d}t, \tag{6.2}$$

and similarly for other tracers. We use the rate of change of $\mathcal{T}_v, \mathcal{T}_c$ and $\mathcal{T}_p$ to quantify the flux of each tracer into the stratified layer. It is also instructive to consider the 'retained fraction' of each tracer at time t, which is the ratio of the current amount of tracer and the input amount of tracer, i.e. $\mathcal{T}_v/\mathcal{I}_v$ for vapour and similarly for other tracers. In the following analysis we define the 'total hydration' as $\mathcal{T}_v(t_{\text{end}})$, i.e. the final amount of tracer in the stratified layer. This is analogous to the 'net hydration' often referred to in the atmospheric literature, except we do not use the term 'net' since there is no initial vapour content in the stratified layer. Transport of vapour into the stratified layer can be separated into direct transport, where vapour is carried by the plume, and indirect transport, where ice is carried by the plume and later sublimated into vapour. The 'excess hydration fraction' is defined as the final retained fraction of vapour $\mathcal{T}_v(t_{\text{end}})/\mathcal{I}_v(t_{\text{end}})$; this quantifies the indirect transport as a fraction of the direct transport. When the excess hydration fraction exceeds one then the indirect transport of vapour from sublimating ice dominates the total hydration. Note this is not guaranteed: adiabatic cooling during ascent freeze-dries large amounts of vapour into ice. Thus for there to be an excess hydration, sufficient mixing must occur for some or most of the ice to be sublimated back into vapour.

Figure 6.3 shows the tracer totals $\mathcal{T}_v, \mathcal{T}_c$ and $\mathcal{T}_p$, the rate of change of the tracer totals, and retained fraction of each tracer over time in simulation `control`. The tracer totals in figure 6.3(a) increase rapidly until a few seconds after plume forcing

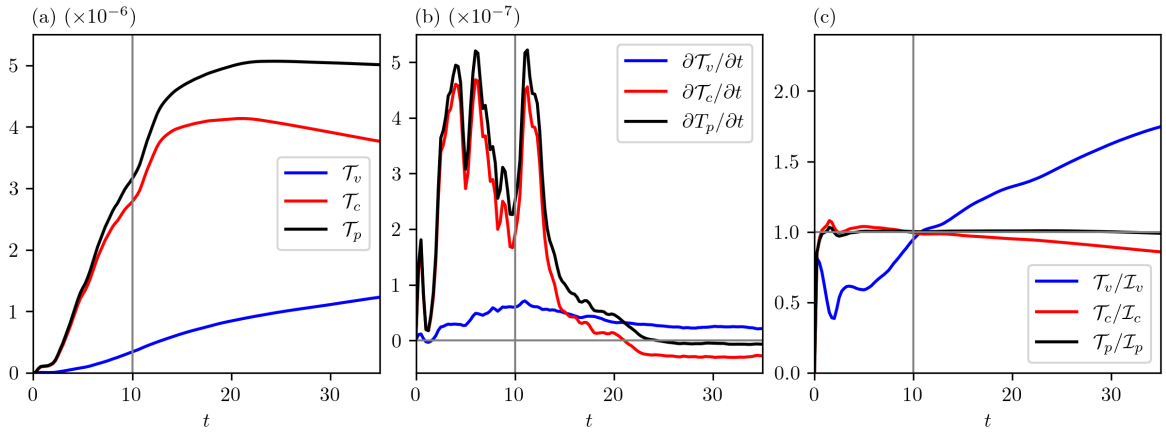

Fig. 6.3 Evolution of tracers in the stratified layer in simulation `control`. (a) Total vapour $\mathcal{T}_v$, ice $\mathcal{T}_c$ and passive tracer $\mathcal{T}_p$. (b) Rate of change of total vapour, ice and passive tracer. (c) Retained fraction of vapour, ice and passive tracer. The grey vertical line indicates the time $t = t_{\text{lim}}$ when plume forcing ends.

ends (indicated by a vertical grey line), when the majority of the plume fluid has risen through the uniform layer. The totals $\mathcal{T}_c$ and $\mathcal{T}_p$ increase at similar rates and $\mathcal{T}_v$ increases more slowly due to freeze-drying of vapour during ascent towards z_{max}. Nonetheless, $\mathcal{T}_v$ increases monotonically whilst from $t \approx 20\,\text{s}$ onwards $\mathcal{T}_c$ decreases as ice is sublimated – note the change of sign in $\partial_t \mathcal{T}_c$ in figure 6.3(b). Some of the reduction in $\mathcal{T}_c$ is due to parts of the plume falling below $z = -L$, though only a small fraction: note the small reduction in $\mathcal{T}_p$ which quantifies this effect. In the relaxation stage from $t \approx 20\,\text{s}$ onwards, there is an approximately constant conversion of ice into vapour. We hypothesise that this occurs as plume fluid descends and adiabatically warms as buoyancy contours relax towards their initial height. It is clear that this steady-state conversion cannot continue indefinitely since eventually fluid either reaches saturation or the ice content is depleted. Figure 6.3(c) shows that the retained fraction of vapour initially falls rapidly due to freeze-drying but begins to increase from $t \approx 2\,\text{s}$ onwards, indicating mixing begins to increase the vapour content via sublimation relatively early in the flow evolution. From $t \approx 10\,\text{s}$ onwards, the retained fraction of vapour $\mathcal{T}_v/\mathcal{I}_v > 1$ so there is an excess hydration. Correspondingly, the retained fraction of ice $\mathcal{T}_c/\mathcal{I}_c < 1$.

6.3.3 Evolution of mixing statistics

To quantify turbulent mixing and vertical transport by the plume we consider plume averages of the mean and turbulent vertical velocity as well as relevant mixing metrics introduced in chapter 3. The plume average $\langle\cdot\rangle^{\text{plume}}$ is calculated from x-z cross-sections

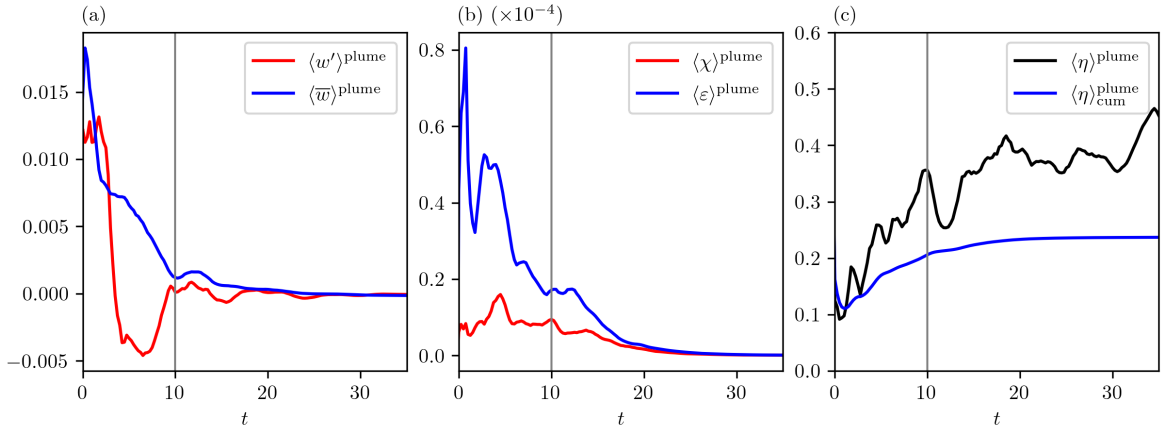

Fig. 6.4 Vertical velocity and mixing metrics in the `control` simulation. All quantities are averaged within the plume $\phi_p \geq 10^{-3}$ in the stratified layer $z \geq -L$. (a) Turbulent vertical velocity $\langle w' \rangle^{\text{plume}}$ and mean vertical velocity $\langle w \rangle^{\text{plume}}$. (b) Buoyancy variance dissipation rate $\langle \chi \rangle^{\text{plume}}$ and TKE dissipation rate $\langle \varepsilon \rangle^{\text{plume}}$. (c) Instantaneous mixing efficiency $\langle \eta \rangle^{\text{plume}}$ and cumulative mixing efficiency $\langle \eta \rangle^{\text{plume}}_{\text{cum}}$ defined in (6.3).

by averaging in the horizontal and vertical where $\phi_p \geq 10^{-3}$ and restricting to the stratified layer $z \geq -L$. Note that in this chapter, $\langle \cdot \rangle^{\text{plume}}$ does not include a time average (as opposed to the use of this notation in chapter 4 and 5). The horizontal component of the average is weighted by the radius from the plume centreline to emulate a volume average (hence the choice of notation, see § 3.4). A test simulation with the full 3D volume average computed at runtime showed negligible difference with the 2D approximation. The mean vertical velocity is defined as in chapter 4, with an azimuthal average and a running mean over one buoyancy period. Later, when vertical shear is introduced in the stratified layer, the weighting is modified to use the radius from the centre of the intrusion. The decomposition of the vertical velocity is not calculated for those simulations since the plume is no longer approximately axisymmetric. Turbulent mixing is quantified using the buoyancy variance dissipation rate $\chi(\boldsymbol{x}, t)$, which acts as a sink of potential energy due to mixing, and the turbulent kinetic energy dissipation rate $\varepsilon(\boldsymbol{x}, t)$, which acts as a sink of (turbulent) kinetic energy due to mixing. The quantities χ and ε are formally defined in § 3.4. The instantaneous mixing efficiency is defined as $\eta = \chi/(\chi + \varepsilon)$ and quantifies the fraction of dissipated energy that results in mixing (see § 3.4 for a more in depth discussion). The cumulative mixing efficiency,

$$\eta_{\text{cum}}(\boldsymbol{x}, t) = \frac{\int_0^t \chi \, \mathrm{d}t}{\int_0^t \chi \, \mathrm{d}t + \int_0^t \varepsilon \, \mathrm{d}t}, \tag{6.3}$$

is an integrated form of η which represents the energetic influence of a mixing event that occurs over a finite time period (Davies Wykes et al., 2015).

The vertical velocity and mixing statistics are explored in figure 6.4. There is an initially large mean vertical velocity in the plume which decreases over time. Note in particular that the turbulent vertical velocity is, on average, negative between $t \approx 4\,\mathrm{s}$ to $t \approx 10\,\mathrm{s}$ as plume fluid overturns and collapses. During this collapse, intense mixing between the plume and environment occurs. As the plume penetrates and collapses, $\langle\varepsilon\rangle^{\mathrm{plume}}$ remains large, whilst $\langle\chi\rangle^{\mathrm{plume}}$ increases during penetration and then remains steady from $t \approx 5\,\mathrm{s}$ to $t \approx 15\,\mathrm{s}$ as the plume collapses. As the flow restratifies, $\langle\chi\rangle^{\mathrm{plume}}$ and $\langle\varepsilon\rangle^{\mathrm{plume}}$ both reduce to zero. The more gradual increase in $\langle\chi\rangle^{\mathrm{plume}}$ relative to $\langle\varepsilon\rangle^{\mathrm{plume}}$ occurs because the plume already has energetic turbulence at penetration but it takes some time for intense buoyancy gradients to become established between the plume and environment. Therefore the mixing efficiency $\langle\eta\rangle^{\mathrm{plume}}$ in figure 6.4(c) increases over time. Interestingly, whilst the mixing metrics reduce in magnitude as the flow restratifies at late times, the instantaneous mixing efficiency remains roughly constant. Figure 6.4(c) also shows that cumulatively around 30% of the energy dissipated during convective penetration results in mixing, consistent with our results in chapter 3.

6.4 Competing effects of sedimentation and mixing

Here we consider simulations `control`, `weak_sed`, `sed`, and `strong_sed` which represent regimes with $R_{\mathrm{S}} = 0, 0.06, 0.6, 7.2$, respectively. This experiment is similar to that presented in § 5.3.3 so we only briefly summarise the flow evolution. In § 5.3.3 we found that when w_s is sufficiently large, but not necessarily larger than the typical turbulent vertical velocity in the plume, then ice that is kept in suspension by turbulent eddies is quickly lost from the plume once fluid overturns near z_{max} and subsides to form the intrusion. The dynamics and mixing are identical in the four simulations considered here; our focus is on the modulation of the hydration process by sedimentation, which starves the plume of ice and limits the effects of turbulent mixing. We also explore the extent to which semi-quantitative models based only on dynamics can predict the distribution of vapour concentrations after the flow restratifies.

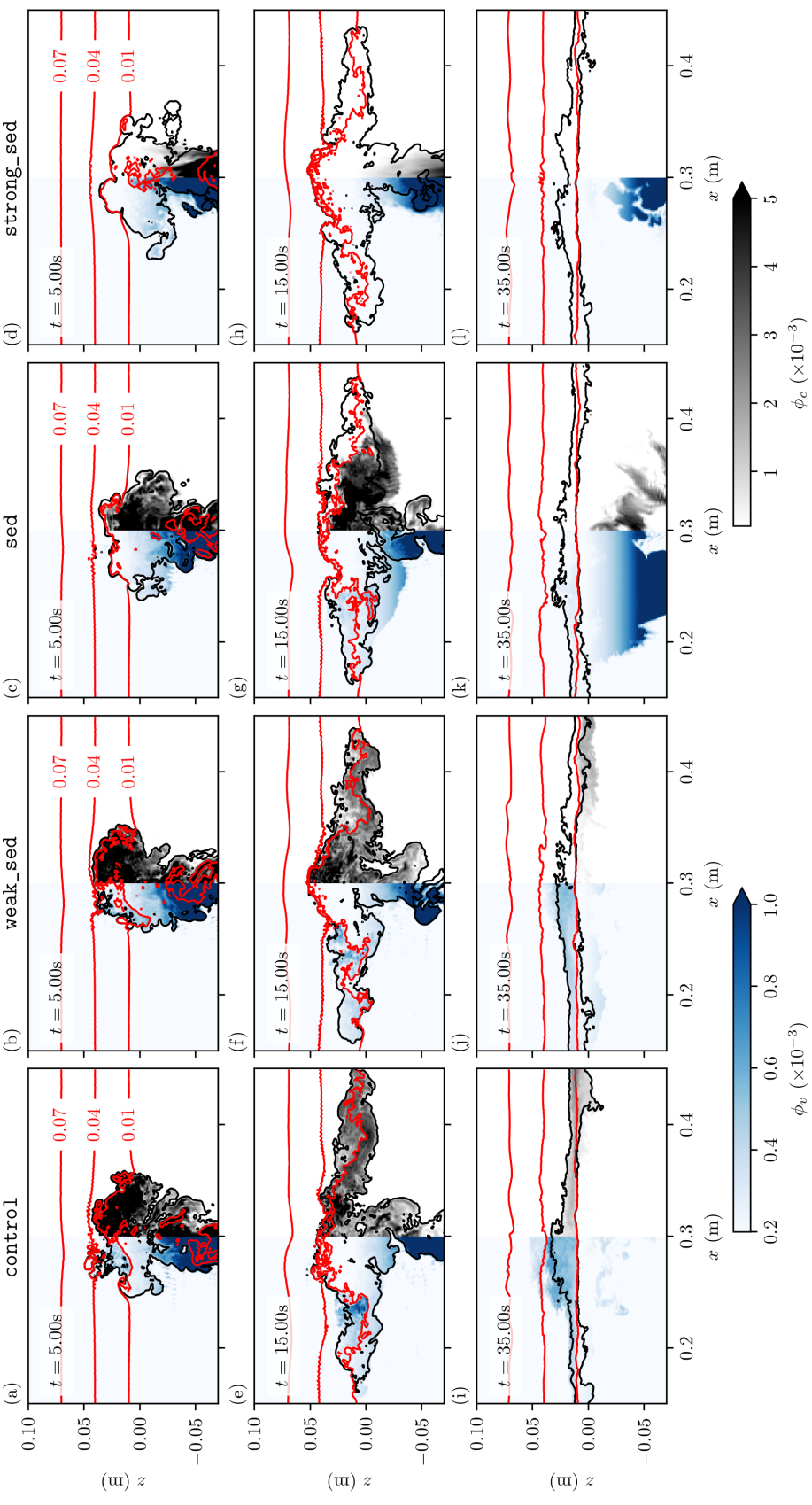

Fig. 6.5 Snapshots of simulations `control`, `weak_sed`, `sed` and `strong_sed` at $t = 5, 15, 35$ s showing the vapour concentration ϕ_v (left) and ice concentration ϕ_c (right) in each plot. The black outline indicates the plume contour $\phi_p = 10^{-3}$. In each plot, buoyancy contours are shown in red every 0.02 from $b = 0.01$ m s^{-2}.

6.4.1 Evolution of moist tracers

Figure 6.5 shows the vapour and ice concentration in the penetration, collapse and relaxation stages of the flow evolution in each simulation. Simulations `control` and `weak_sed` appear almost identical, with the effects of the very weak sedimentation in `weak_sed` appearing only at late times when ice finally settles out of the plume (panel j). There is some evidence that less ice reaches the top of the plume in `weak_sed`, since the vapour concentrations are slightly reduced relative to `control` at late times. Simulation `strong_sed` lies at the other extreme to `weak_sed`: very little ice is carried into the stratified layer and no ice reaches the intrusion. Thus vapour concentrations are considerably smaller than in the simulations with weaker sedimentation. The intermediate case in simulation `sed` lies between these two regimes. Ice is carried into the plume but relatively little reaches the edge of the plume cap where the most efficient mixing occurs between the plume and environment. Thus vapour concentrations are noticeably smaller than in simulations `control` and `weak_sed`.

Figure 6.6 quantifies the evolution of moist tracers as in figure 6.3. Black horizontal lines indicate the value of w_s in each simulation in figure 6.6(d), which shows the plume-averaged mean and turbulent vertical velocity as in figure 6.4(a). Note that w_s in simulation `strong_sed` is off the scale. In figure 6.6(b), the time derivative of the passive tracer total $\partial_t \mathcal{T}_p$ has been omitted for clarity. As stated earlier, the dynamics of the flow itself are unaffected by sedimentation, so the passive tracer (which is unaffected by microphysics) and the vertical velocities evolve in a similar manner in all four simulations, with some natural variation. The similar moist evolution in `weak_sed` and `control` is evident in figure 6.6, with only a minor reduction in the total hydration and excess hydration fraction. The rate of change of ice $\partial_t \mathcal{T}_c$ only becomes negative at $t \approx 20\,\mathrm{s}$ (panel b) when the mean vertical velocity falls below w_s (panel d).

In simulation `strong_sed`, although almost no ice or vapour is transported into the stratified layer, the small amounts of vapour that cross the $z = -L$ surface follow the same process of freeze drying as in other simulations, with a brief reduction in the retained fraction of vapour (panel c) because the plume has not yet adiabatically cooled so $\mathcal{T}_v$ initially increases more rapidly. Once the plume penetrates deeper into the stratified layer, most vapour is converted to ice and lost so the retained fraction reduces to zero. The intermediate case in simulation `sed` exhibits an interesting evolution: during penetration, $\mathcal{T}_c$ and $\mathcal{T}_v$ increase roughly in line with simulation `control` and `weak_sed`, though slightly reduced (panel a). From $t \approx 8\,\mathrm{s}$, the vertical velocity falls

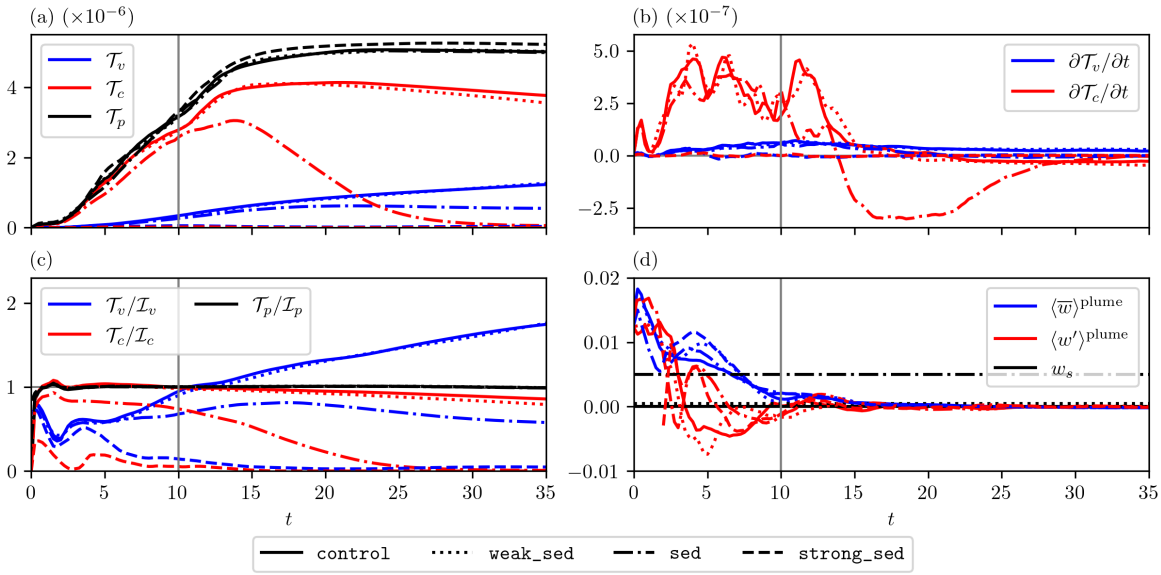

Fig. 6.6 Comparison of tracer totals and vertical velocity in simulations `control`, `weak_sed`, `sed`, and `strong_sed`. (a) Total vapour $\mathcal{T}_v$, ice $\mathcal{T}_c$ and passive tracer $\mathcal{T}_p$. (b) Rate of change of total vapour, ice and passive tracer. (c) Fraction of input vapour, ice and passive vapour remaining in the stratified layer at time t. (d) Mean $\overline{w}$ and turbulent w' vertical velocity compared with sedimentation velocity w_s (horizontal black lines). In (a)–(d), the vertical grey line indicates the time $t = t_{\text{lim}}$ when plume forcing ends.

below w_s (panel d) so the transport of ice slows down (panel b) and $\mathcal{T}_c$ decreases from $t \approx 15\,\text{s}$ (panel a). As the flow begins to relax, there is continued conversion of ice into vapour so the retained fraction of vapour increases up to $t \approx 20\,\text{s}$ and decreases thereafter (panel c), though the total amount of vapour $\mathcal{T}_v$ remains approximately steady until the end of the simulation. The total hydration is approximately halved relative to simulations `control` and `weak_sed`. There is no excess hydration in simulation `sed` as sedimentation restricts the amount of ice available to sublimate; the rate of change $\partial_t\mathcal{T}_v$ is reduced from $t \approx 15\,\text{s}$ (panel b) once sedimentation dominates the flow and ice has settled out of the plume.

6.4.2 Semi-quantitative hydration models

As described in § 6.1, we use two semi-quantitative models based on ‘fast’ and ‘slow’ sedimentation regimes to predict the distribution of vapour concentration ϕ_v at the end of the simulation, following restratification of the environment once the plume settles and isopycnals relax. Crucially, these distributions are determined by dynamics alone, with no information on the mixing process or microphysics. From each model

we compute a PDF of ϕ_v and compare with the observed PDF of ϕ_v at time $t = t_{\text{end}}$ in each simulation. The models are derived as follows:

- **Slow sedimentation (final T):** assume that vapour condensed into ice is kept suspended in the plume. Thus the vapour concentration in the relaxation stage of the flow evolution is determined by the saturation concentration once the plume reaches equilibrium with the environment. Hence ϕ_v is controlled by the environmental temperature at the height z_f where each fluid parcel settles. To estimate the PDF of ϕ_v, compute a PDF of the heights of plume fluid with $\phi_p \geq 10^{-3}$ at $t = t_{\text{end}}$. Given a height z_f, the saturation vapour concentration is then $\phi_{vs}(T_{\text{final}})$ where

$$T_{\text{final}} = T_0 + \Theta N_0^2 z_f - \Gamma(z_f + H). \tag{6.4}$$

  and ϕ_{vs} is defined in (5.20). Henceforth we refer to this as the 'Final T' model.

- **Fast sedimentation (minimum T):** assume that all vapour condensed into ice is lost via sedimentation. Thus the vapour concentration is determined by the saturation concentration at the minimum temperature along each fluid parcel trajectory. To estimate the PDF of ϕ_v, we compute a set of trajectories. The velocities are provided by x-z cross-sections through the plume centreline (as shown in e.g. figure 6.5) of the vertical and horizontal velocity every $\Delta t = 0.25\,\text{s}$. We initiate 64 trajectories at random points within the plume $\phi_p \geq 10^{-3}$ and within the height range $0.06\,\text{m} \leq z \leq 0.18\,\text{m}$ every $0.25\,\text{s}$ from $t = 0$ to $t = 10\,\text{s}$. Trajectories are propagated to the end of the simulation at time $t = t_{\text{end}}$ and rejected if the trajectory ends outside the plume. We compute a PDF of the minimum temperature T_{min} along the ~ 1200 trajectories. To account for the use of 2D data, the contribution of each trajectory to the PDF is weighted by its radial distance from the plume centreline. The PDF of ϕ_v is then computed using $\phi_{vs}(T_{\text{min}})$ as defined in (5.20). Henceforth we refer to this as the 'Min T' model.

Figure 6.7(a)–(d) compares the Final T and Min T models with the observed vapour distribution at $t = t_{\text{end}}$ in each simulation. The horizontal dashed lines indicate the mean of the model and observed distributions. Figure 6.7(e)–(h) shows the PDFs of T_{min} and T_{final} in the Min T and Final T model, respectively, and the environmental temperature at the equilibrium height $z = z_{\text{n}}$ and the maximum penetration height

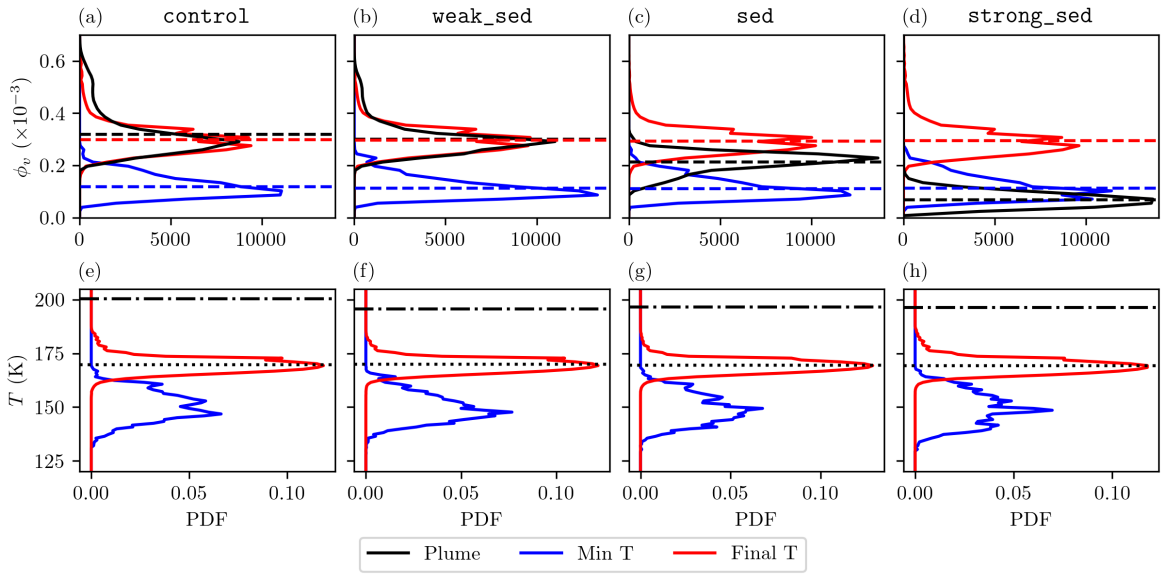

Fig. 6.7 Comparison of semi-quantitative hydration models with the observed vapour distribution within the plume $\phi_p \geq 10^{-3}$ at the end $t = t_{\text{end}}$ of simulations `control`, `weak_sed`, `sed` and `strong_sed`. (a)–(d) Comparison of observed PDF (black) with the Min T (blue) and Final T (red) predictions as described in the text. Horizontal dashed lines indicate the mean of each distribution. (e)–(h) Comparison of PDFs of the minimum temperature (blue) and final temperature (red) along parcel trajectories calculated as described in the text. Horizontal lines indicate the environmental temperature at $z = z_{\text{max}}$ (dot-dashed) and $z = z_{\text{n}}$ (dotted).

$z = z_{\text{max}}$. Note that the temperature distributions are qualitatively similar across the four simulations since the dynamics are unaffected by the variation in w_s. As expected, vapour concentrations are indeed determined by the final temperature along parcel trajectories in simulations `control` and `weak_sed`, both with regime numbers $R_{\text{S}} \ll 1$ and $R_{\text{H}} \gg 1$, in which ice is abundant in the plume. Note that the distribution of final temperatures is centred on the environmental temperature at $z = z_{\text{n}}$ since this represents the height of the intrusion where mixed plume fluid settles. There is a small discrepancy between the Final T model and the observed distribution at large ϕ_v, which corresponds with the warmest fluid parcels which may not have relaxed to the environmental temperature by $t = t_{\text{end}}$.

As w_s is increased, the observed vapour distribution moves closer to being controlled by the minimum temperature along parcel trajectories. In simulation `strong_sed`, with regime $R_{\text{S}} \gg 1$ where we expect the observed and Min T models to have the closest agreement, there is in fact an overestimation by the semi-quantitative model. We hypothesise that the reduction of vapour concentrations below $\phi_{vs}(T_{\text{min}})$ is caused

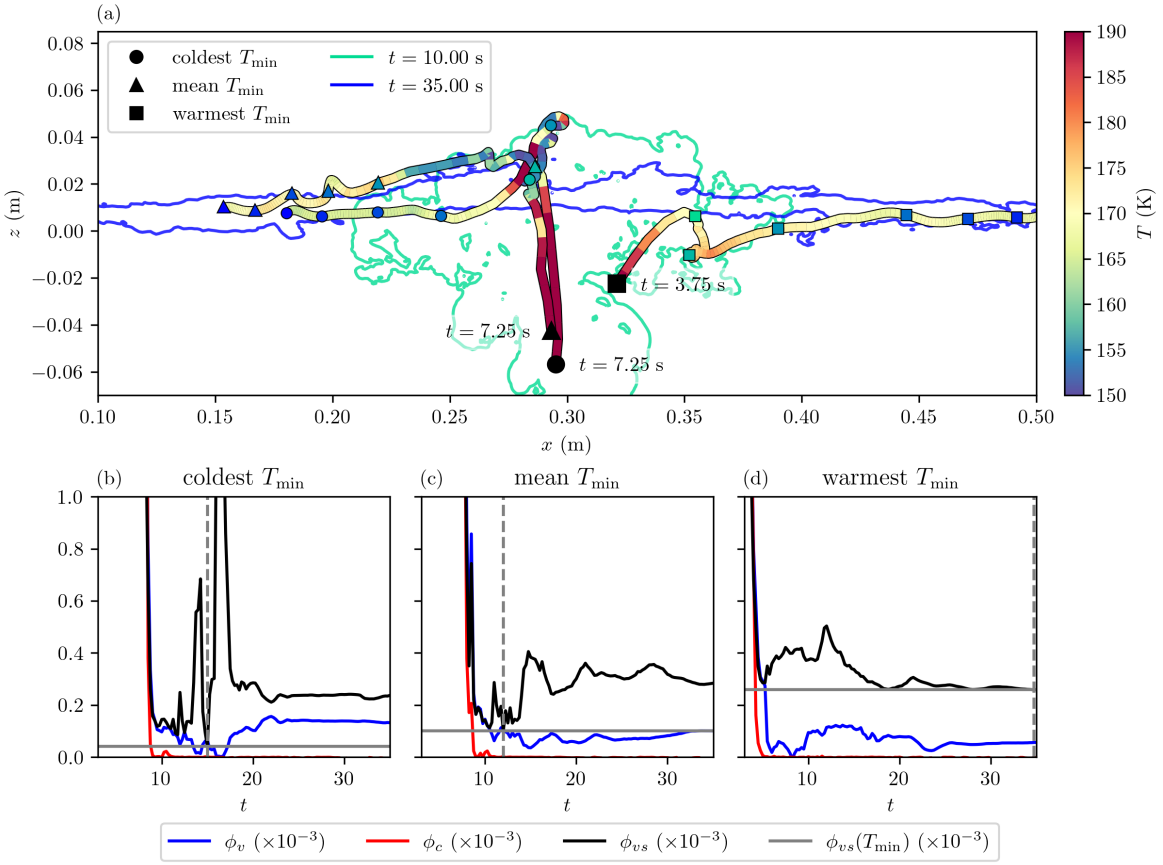

Fig. 6.8 Fluid parcel trajectories in simulation `strong_sed` associated with the coldest, mean and warmest minimum temperature $T_{\min}$. (a) Trajectories overlaid on plume contour at $t = 10\,\mathrm{s}$ and $t = 35\,\mathrm{s}$. Line colour indicates temperature T. Coloured symbols are shown at $t = 5, 10, 15, 20, 25, 30, 35\,\mathrm{s}$ along each trajectory. (b–d) vapour, ice, and saturation vapour concentration along the three trajectories. The horizontal grey line indicates the minimum saturation vapour concentration $\phi_{vs}(T_{\min})$ along the trajectory. The time when $T_{\min}$ is attained in each simulation is shown as a vertical grey line.

by dilution of plume fluid after reaching its minimum temperature $T_{\min}$ as a result of mixing with dry environmental fluid. Note that this does not reduce the total hydration – which is not fully captured by the observed PDF – since the total vapour is simply shared among a larger volume.

To illustrate the dilution effect, figure 6.8 shows three fluid parcel trajectories in simulations `strong_sed` overlaid on outlines of the plume at $t = 10\,\mathrm{s}$ and $t = 35\,\mathrm{s}$ in panel (a). The vapour, ice, and saturation vapour concentration along each trajectory are shown in panels (b)–(c). In these plots, the horizontal grey line indicates $\phi_{vs}(T_{\min})$ on each trajectory and the vertical dashed grey line indicates the time at which $T_{\min}$ was attained. Trajectories can be broadly categorised based on $T_{\min}$: trajectories which

enter the intrusion directly have the warmest $T_{\min}$, whilst trajectories that reach the top of the plume cap have the coldest $T_{\min}$. In the $R_{\mathrm{H}} \gg 1$ regime, plume fluid remains at saturation during penetration so ϕ_v is limited by ϕ_{vs} until reaching its maximum height in the stratified layer. The minimum temperature $T_{\min}$ is attained at this maximum height. As fluid parcels decelerate on approach to their maximum height (or begin to move laterally), sedimentation removes all ice content. Parcels are then warmed either by mixing with the warm environment (as in the cold and mild trajectories) or by mixing with warmer, mixed plume fluid in the intrusion. Correspondingly, ϕ_{vs} increases, but there is no increase in ϕ_v as there is no ice to sublimate. Mixing in the intrusion homogenises ϕ_v; the coldest trajectories gain vapour whilst the warmest trajectories lose vapour. Further mixing with dry environmental fluid surrounding the intrusion dilutes the vapour that remains in the plume, reducing ϕ_v.

Overall our results show that semi-quantitative models based on dynamics alone are able to produce reasonable estimates of the vapour PDF following relaxation of the flow, given some knowledge of the sedimentation regime determined by R_{S}. When w_s dominates velocities in the flow, along each trajectory ϕ_v is limited by $\phi_{vs}(T_{\min})$ and further diluted by mixing with the dry environment. Otherwise, ice remains suspended in the plume and keeps plume fluid close to saturation. The models as described are limited to predicting the distribution of vapour only. However, given additional knowledge of the moist partitioning, determined by R_{H}, and the plume tracer flux at penetration, then a prediction could be formulated for the total hydration.

6.5 Influence of convective intensity on hydration

In this section we consider simulations `control+F`, `sed+F` and `strong_sed+F` in which the integral source buoyancy flux F_0 is quadrupled relative to `control`, thus increasing the convective intensity. As has been noted throughout this thesis, in convective penetration of a buoyant plume into a stratified layer the maximum penetration height $z_{\max}$ is directly linked to the strength of the plume forcing: $z_{\max} \sim F_0^{1/4}$. D18 place $z_{\max}$ as the key quantity determining the net hydration by a convective overshoot, since penetration to a greater maximum height results in mixing with relatively warmer stratospheric air, thereby increasing ϕ_{vs} further and allowing sublimation of a larger amount of ice. Here we explore this effect and its competition with sedimentation. We also consider the influence of convective intensity on turbulent mixing.

6.5.1 Evolution of moist tracers

Figure 6.9 summarises the flow evolution and figure 6.10 summarises the evolution of the moist and passive tracers as in figure 6.5 and figure 6.6, respectively. The increase in convective intensity from quadrupling F_0 alters the flow evolution in two key respects: the maximum penetration height $z_{\max}$ is increased by a factor of $\sqrt{2}$ and the azimuthally averaged vertical velocity on the plume centreline $\overline{w} \sim F_0^{1/3}$ increases by a factor of $4^{1/3} \approx 1.6$ (see § 2.2.3 for further details on $\overline{w}$). Thus $z_{\max}$ is reached slightly faster than in `control`, and the transport of tracers into the stratified layer is increased – note the more rapid increase in $\mathcal{T}_p$ in figure 6.10(a). Penetration to a larger $z_{\max}$ allows the plume to mix across the $b = 0.07\,\mathrm{m\ s^{-2}}$ contour, compared with the $b = 0.04\,\mathrm{m\ s^{-2}}$ contour in simulation `control`. Similarly, the $b = 0.04\,\mathrm{m\ s^{-2}}$ contour shown in figure 6.9 is more significantly distorted in the strong forcing simulations. Consequently, vapour concentrations are increased in `control+F` relative to `control` and remain slightly higher in the domain (and therefore slightly warmer) after relaxation of the flow. As opposed to simulations `sed` and `strong_sed`, there is evidence of some vapour remaining in the plume at late times in `sed+F` and `strong_sed+F`. The extent of the dry environment below the plume, which is hydrated by ice sedimenting out of the plume, is wider, suggesting ice reaches further into the intrusion in the strong forcing simulations despite the strong sedimentation velocity.

The total hydration in the strong forcing simulations is increased, consistent with S18 and D18. We also note that the total hydration in `sed+F` is greater than half that in `control+F`, suggesting the competition between sedimentation and mixing is more in favour of mixing when convective intensity is increased. Indeed, this follows from the increased vertical velocity in the plume which modifies the R_{S} regime in `sed+F` and `strong_sed+F` to $R_{\mathrm{S}} = 0.45, 4.0$, respectively. These simulations remain comparable with the control forcing simulations `sed` and `strong_sed`, but the change in R_{S} signifies the reduced influence of sedimentation when convective intensity is increased that allows ice to remain suspended in the plume for longer – note the ice total $\mathcal{T}_c$ decreases more rapidly in simulations `sed` and `strong_sed` in figure 6.6(a) compared with `sed+F` and `strong_sed+F` in figure 6.10(a). As noted with the passive tracer, the increase in $\mathcal{T}_v$ is also more rapid in the strong forcing simulations, both because of the stronger updraft velocity as well as the increased buoyancy in the plume which supports larger vapour concentrations. Overall this suggests that the increased hydration is a function of increased transport, stronger mixing, as well as

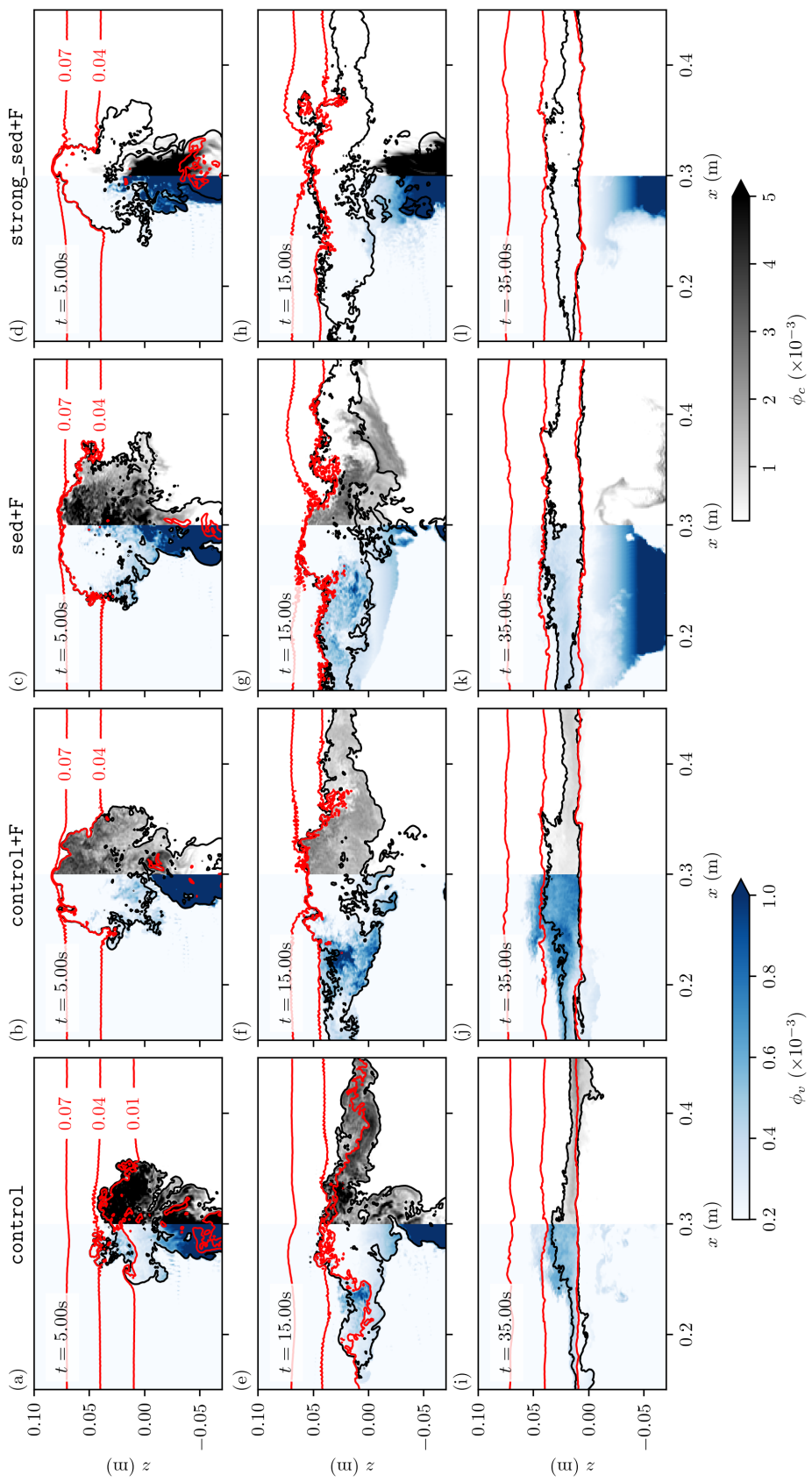

Fig. 6.9 Flow summary as in figure 6.5, for simulations `control`, `control+F`, `sed+F` and `strong_sed+F`. The $b = 0.1\,\mathrm{m\,s^{-2}}$ contour has been omitted in the strong forcing simulations on the top two rows for clarity.

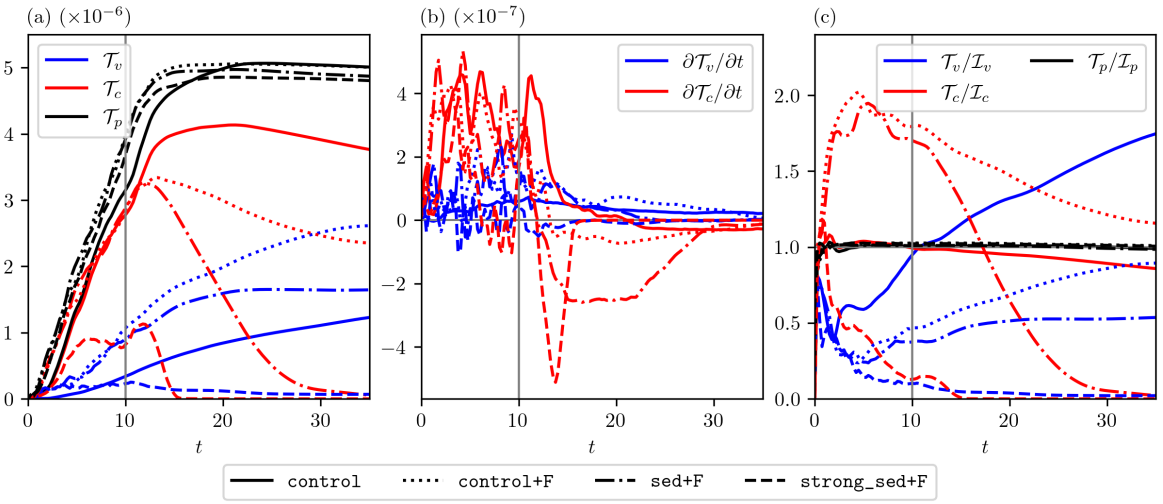

Fig. 6.10 Evolution of moist tracer totals as in figure 6.6(a-c), for simulations `control`, `control+F`, `sed+F`, and `strong_sed+F`.

access to greater potential temperatures. However, we note from figure 6.10(c) that despite the increased total hydration in `control+F` relative to `control`, there is no longer an excess hydration. During ascent towards $z_{\max}$, a larger amount of vapour is freeze-dried – note the lower minimum in the retained fraction of vapour in the strong forcing simulations. Therefore whilst access to greater potential temperatures in the environment is sufficient to increase the total hydration relative to the control forcing simulations, it is not sufficient to recover all of the vapour that is converted to ice during the penetration stage (bearing in mind that more vapour is also carried into the stratified layer during penetration).

6.5.2 Turbulent mixing

To assess the influence of convective intensity on turbulent mixing, in figure 6.11 we compare the vertical velocity and mixing metrics in `control` and `control+F`. Only one strong forcing simulation is shown since these quantities are controlled by the dynamics which is influenced by F_0 but not w_s.

Figure 6.11(a) shows that the turbulent vertical velocity is initially larger `control+F` relative to `control`, whilst the mean velocities are comparable. The difference in the turbulent velocity vanishes from $t \approx 5\,\mathrm{s}$ onwards, suggesting the collapsing stage of the flow evolution is less influenced by convective intensity. The plume averaged TKE dissipation rate $\langle\varepsilon\rangle^{\mathrm{plume}}$ and buoyancy variance dissipation rate $\langle\chi\rangle^{\mathrm{plume}}$ are systematically larger in `control+F` throughout the simulation. Thus the turbulence is more

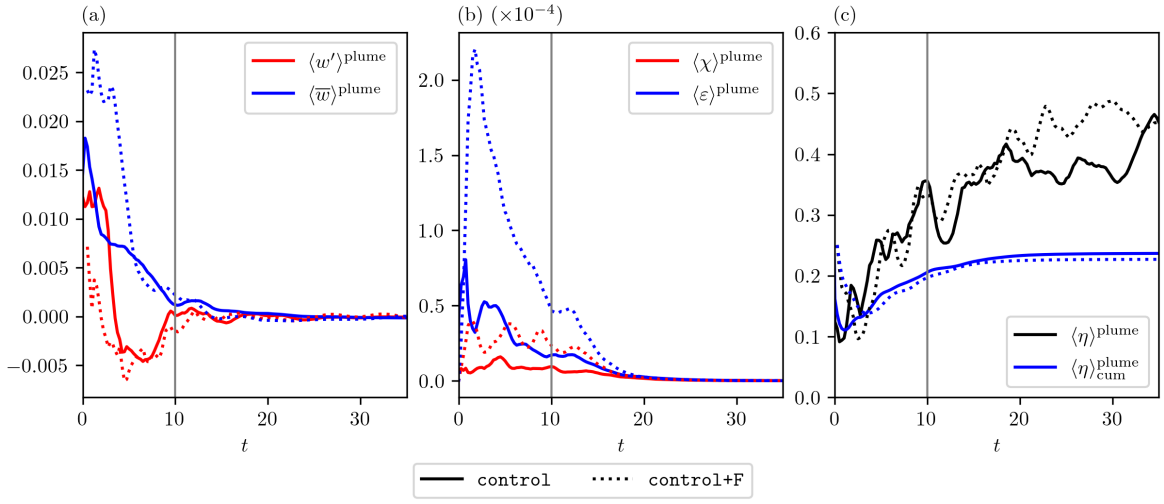

Fig. 6.11 As in figure 6.4, for simulations `control` and `control+F`.

energetic and the mixing more intense when the convective intensity is increased. Note that χ is a measure of the destruction of buoyancy gradients which depends on the magnitude of the buoyancy difference as well as the sharpness of the gradients. We can crudely estimate the buoyancy difference using characteristic scales from integral plume theory (see § 2.2.3). The plume centreline buoyancy $b_{\max}$ at the maximum penetration height $z_{\max} \sim F_0^{1/4}$ scales as $b_{\max} \sim F_0^{2/3} z_{\max}^{-5/3} \sim F_0^{1/4}$ whilst the environmental buoyancy b_{env} at $z_{\max}$ scales as $b_{\text{env}} \sim z_{\max} \sim F_0^{1/4}$. Therefore the buoyancy difference between the plume and environment only weakly scales with F_0, whilst the increase in $\langle\chi\rangle^{\text{plume}}$ is roughly a factor of 3. Hence we conclude that the buoyancy gradients generated between the plume and environment, that are eroded by turbulent mixing, become sharper as the convective intensity is increased in the sense that the change in buoyancy occurs over a shorter distance. Finally, we note from figure 6.11(c) that despite the increase in $\langle\chi\rangle^{\text{plume}}$ and $\langle\varepsilon\rangle^{\text{plume}}$, the fraction of dissipated energy that results in mixing does not depend on convective intensity: there is no clear difference in the instantaneous and cumulative mixing efficiency between `control` and `control+F`. However, a stronger plume is more energetic so, in total, more energy is dissipated as the plume impinges on the stratified layer, resulting in more intense mixing between the plume and environment.

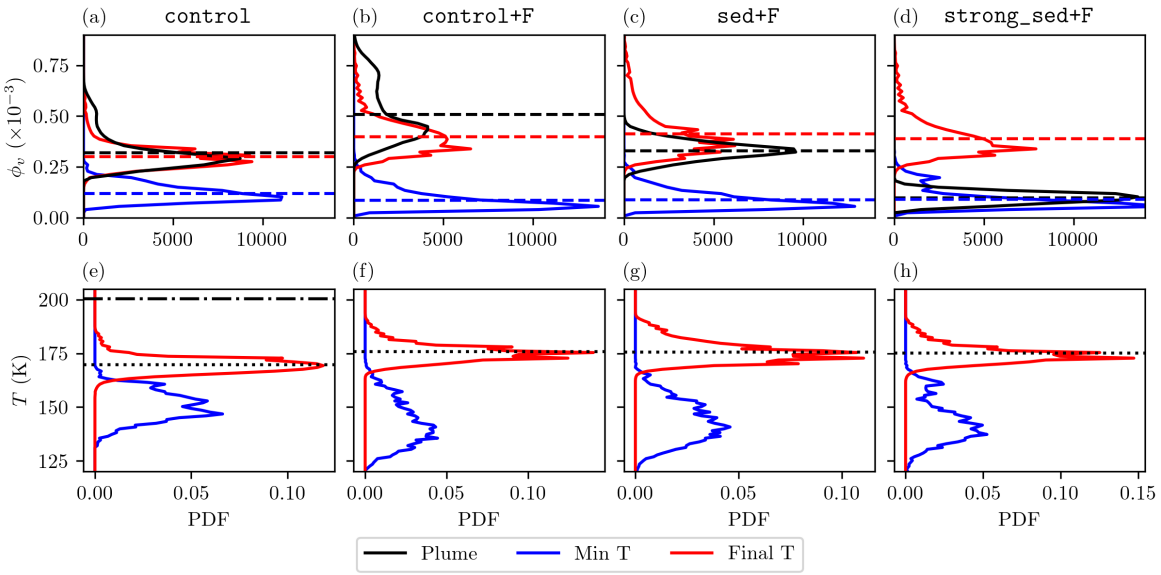

Fig. 6.12 As in figure 6.7, for simulations `control`, `control+F`, `sed+F`, and `strong_sed+F`.

6.5.3 Consequences for semi-quantitative models

We found in § 6.4 that sedimentation and mixing play a competing role in determining net hydration of the stratified layer, with vapour concentration in a fluid parcel determined by the minimum temperature along its trajectory when sedimentation is dominant or its final temperature when sedimentation is weak. Using the strong forcing simulations we can assess how convective intensity influences this conclusion.

Figure 6.12 shows the Min T and Final T models as described in § 6.4.2 compared with the observed vapour distributions at $t = t_{\text{end}}$ in the strong forcing simulations. As hypothesised by D18, increased convective intensity results in mixing with relatively warmer environmental fluid and thus an increase in the final temperature distribution of the flow. This is clearly shown in figure 6.12(f)–(h), noting as in § 6.4 that the distribution of T_{final} is governed by dynamics alone so the distributions are qualitatively similar. The observed vapour distribution in `control+F` is underestimated by the final T model. This is likely because the flow takes longer to relax relative to simulation `control` since plume fluid subsides from a greater maximum penetration height – compare panel (i) and (j) in figure 6.9. Hence if the simulation had been run for longer, we would expect the observed PDF to match the prediction from the Final T model. In simulation `strong_sed+F`, where sedimentation is dominant, the observed vapour distribution is close to but underestimated by the Min T model. Whilst dilution remains a factor, here the stronger turbulent and mean vertical velocities in

the plume keep ice suspended for longer – as noted in § 6.5.1 – which allows the vapour concentration to increase after the plume and environment begin to mix unlike in simulation `strong_sed`. A similar effect is seen in simulation `sed+F` which lies between the predictions of the Min T and Final T model predictions as in the control forcing case, though arguably closer to the Final T distribution in the strong forcing case. This again illustrates the reduced influence of sedimentation under increased convective forcing. The results for the strong forcing simulations shown in figure 6.12, as well as figure 6.7 with the control forcing, show that knowledge of the mixing process is not essential to predict the final ϕ_v PDF when sedimentation is weak; the equilibrium height $z = z_n$ is sufficient information.

6.6 Convective penetration in the presence of large-scale vertical shear

The final results we present in this chapter address the effect of large-scale vertical shear in the stratified layer in simulations `weak_shear`, `shear`, and `strong_shear`. Here, the behaviour of the flow is significantly modified by the presence of a mean flow. First, we explore the influence on hydration of the stratified layer, which is closely related to the enhancement of turbulent mixing. We revisit some analyses used in chapter 3 and § 5.5 to investigate changes in turbulent mixing using the (moist and passive) buoyancy-tracer volume distribution. Finally, we explore the impact of vertical shear on internal gravity wave breaking and modification of the associated vortical response. We also explore the link between vertical displacement of fluid parcels in the stratified layer and gravity wave breaking as part of the explanation for the 'jumping cirrus' phenomenon discussed in § 5.2.

6.6.1 Evolution of flow and moist tracers

The flow evolution in the three shear simulations is summarised in figure 6.13 and the evolution of moist tracers is shown in figure 6.14. Note in figure 6.13 we only show the vapour concentration unlike figures 6.5 and 6.9. We also indicate the flow with black arrows. In figure 6.14 the retained fraction of vapour is separated from the ice and passive tracers for clarity. The presence of vertical shear deforms the plume cap, which has two consequences: the intrusion is increasingly asymmetric as λ and therefore R_{SH} increase, with most mixed plume fluid lying downstream of the plume cap when shear

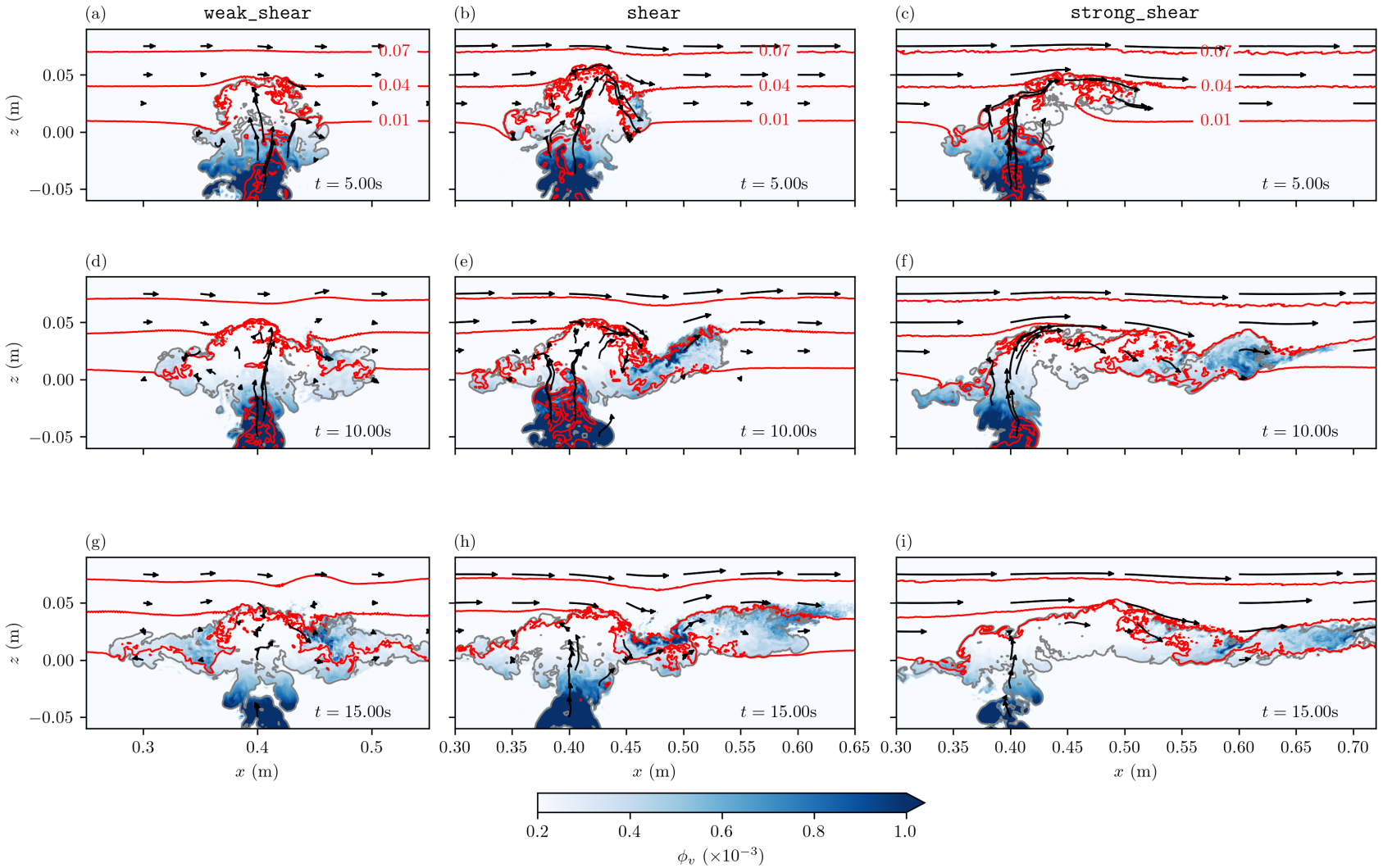

Fig. 6.13 Flow summary as in figure 6.5, except only showing the vapour concentration ϕ_v, for simulations `weak_shear`, `shear` and `strong_shear`, with $R_{\mathrm{SH}} \ll 1, \sim 1$ and $R_{\mathrm{SH}} \gg 1$ respectively. For these simulations, $R_{\mathrm{H}} \approx 12$ and $R_{\mathrm{S}} = 0$.

is strong, and modification of the path taken towards the maximum penetration height. As R_{SH} increases, the plume reaches $z_{\max}$ further downstream, meaning fluid parcels take longer to reach $z_{\max}$ and become exposed to environmental fluid earlier along their trajectory. The downstream shift of $z_{\max}$ also means the downward flow of fluid which typically inhibits the upward flow when there is no shear is both weaker and dislocated from the rising plume. This allows a more rapid transport of fluid into the stratified layer, which can be seen from the more rapid increase in $\mathcal{T}_p$ in figure 6.14(a).

The total hydration $\mathcal{T}_v(t_{\mathrm{end}})$ increases with shear rate, as well as the excess hydration fraction. An important caveat for figure 6.14 is that the shear simulations are run until $t = 15\,\mathrm{s}$ so do not reach the relaxation stage seen in other simulations from $t \approx 15\,\mathrm{s}$ onwards. It can be seen from figure 6.10 that the final vapour total $\mathcal{T}_v$ may evolve very differently in this stage (compare $\mathcal{T}_v$ in simulations `control` and `sed+F`). Nonetheless, the increased excess hydration fraction and the more rapid increase from $t \approx 5\,\mathrm{s}$ onwards suggests that the increase in hydration comes from increased sublimation of ice as a result of more intense mixing between the plume and environment. This is supported by increased deformation of buoyancy contours in e.g. panel (e) and (f) of figure 6.13. As noted in other experiments, the retained fraction of vapour $\mathcal{T}_v/\mathcal{I}_v$ in figure 6.14(b) initially decreases before later increasing and exceeding unity. This minimum is shallower (i.e. $\mathcal{T}_v/\mathcal{I}_v$ does not become as small) in the shear experiments, though the change is not monotonic – this may be related to stronger mixing between the plume and environment during the rise of fluid parcels towards $z_{\max}$, which begins to sublimate ice earlier in the evolution of the flow so the total vapour $\mathcal{T}_v$ does not decrease as much. The minimum in $\mathcal{T}_v/\mathcal{I}_v$ also occurs later because fluid parcels take longer to reach $z_{\max}$ when the plume cap is more significantly deformed by shear, so the significant increase in vapour content due to sublimation of ice at the top of the plume cap occurs later.

The spatial distribution of the moist regions formed via sublimation of ice is increasingly asymmetric as the shear rate increases and extends further along the intrusion. In the absence of shear, regions with larger ϕ_v formed surrounding the plume cap, whilst in simulations `shear` and `strong_shear` vapour forms downstream of the plume cap. Figure 6.13(f) appears to show a Kelvin-Helmholtz-like roll-up of the intrusion in simulation `strong_shear` at $t = 10\,\mathrm{s}$, with two 'billows' resulting in significant perturbations of the $b = 0.01\,\mathrm{m\ s^{-2}}$ and $b = 0.04\,\mathrm{m\ s^{-2}}$ contours. The roll-up relaxes by $t = 15\,\mathrm{s}$, though intense mixing continues at the top of the intrusion between $0.5\,\mathrm{m} \leq x \leq 0.6\,\mathrm{m}$. Kelvin-Helmholtz (KH) instabilities arise in regions of a

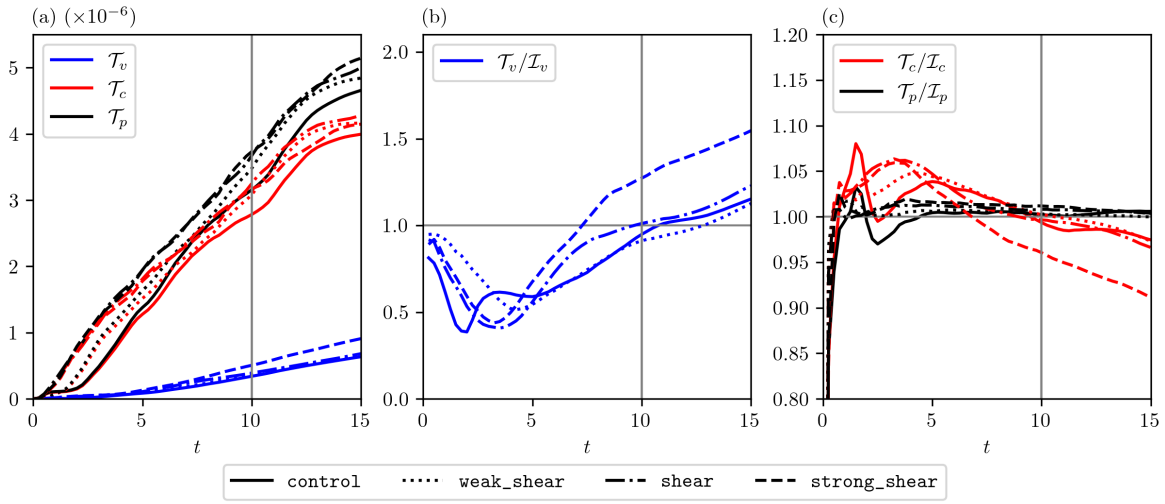

Fig. 6.14 As in figure 6.10(a) and (c), for simulations `weak_shear`, `shear`, and `strong_shear`.

stratified shear flow where $\mathrm{Ri}_g \leq \frac{1}{4}$, where Ri_g is the local gradient Richardson number defined in (1.9). Recall from § 6.2 that all of the shear simulations are initially stable, so KH instabilities cannot form spontaneously and must involve a local enhancement of shear rate or reduction in the local stratification. Indeed, we will show later that the large-scale shear flow induces a downward flow over the plume cap (e.g. panel (c) and (e) in particular) which can locally enhance the shear rate such that $\mathrm{Ri} \leq 1/4$, allowing shear instabilities to develop. Another interesting aspect of the flow structure in `shear` is the formation of a hydraulic jump-like feature, marked by the significant 'kink' in the forming intrusion at $t = 10\,\mathrm{s}$ and the persistence of this structure at $t = 15\,\mathrm{s}$. Again, we will revisit this point later in § 6.6.3 where we consider the residual circulation that forms above the plume, linked to the vortical and wave response to convective penetration in the presence of large-scale shear.

Evaluation of the semi-quantitative hydration models detailed in § 6.4 is difficult for the shear simulations because they do not reach the relaxation stage of the flow evolution. Nonetheless, in the absence of sedimentation we found that the Final T model accurately captures the observed vapour distribution. It is instructive to compare the distribution of final temperatures T_{final} and minimum temperatures T_{min} along parcel trajectories, as shown in figure 6.15. As the shear rate increases, the final temperatures become warmer owing to enhanced mixing between the plume and environment which more effectively warms plume fluid. This is consistent with figure 6.13 where it can be seen that the intrusion sits slightly higher in the simulations

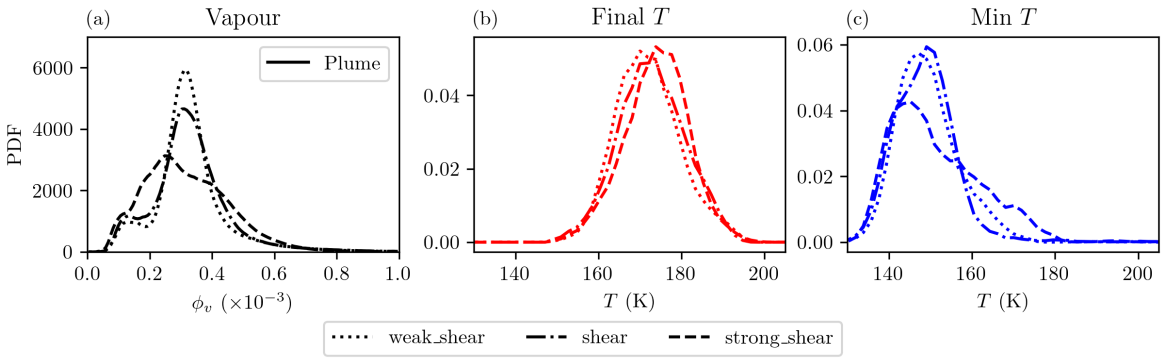

Fig. 6.15 Comparison of (a) observed vapour concentration PDF with the (b) Final T and (c) Min T model predictions as described in § 6.4. The temperature PDFs in (b) and (c) have been smoothed for clarity.

with stronger shear. The minimum temperatures in figure 6.15(c) are more widely distributed, primarily because of an increased number of trajectories with warmer $T_{\min}$. This suggests that more plume fluid enters the intrusion directly rather than rising towards $z_{\max}$. The observed vapour distribution in the shear simulations at $t = 15\,\mathrm{s}$ in figure 6.15(a) is similar in simulations `weak_shear` and `shear` but wider in `strong_shear`, again indicating enhanced mixing between the plume and environment.

The enhanced mixing between the plume and environment in simulations with stronger shear is well illustrated by the buoyancy-vapour and buoyancy-ice volume distributions W_v and W_c introduced in § 5.5 and shown here in figure 6.16 at $t = 15\,\mathrm{s}$ in the three shear simulations. As the shear rate increases, the transport of ice-loaded fluid towards large b (panel f) due to turbulent mixing is increased. In turn, the mixing of more fluid to large b allows a more significant proportion of ice to be sublimated since ϕ_{vs} is larger. Note that the largest buoyancy reached does not increase with the shear rate. We therefore conclude that large-scale vertical shear increases the total hydration by more effectively mixing plume and environmental fluid near the maximum penetration height and therefore increasing the transport of volume (hence ice) to the largest accessible buoyancy. Importantly, the enhanced hydration is not a result of increasing the transport of moisture into the stratified layer, nor increasing the maximum accessible buoyancy.

6.6.2 Influence on mixing

Having established that mixing is enhanced in the presence of strong vertical shear, here we focus on quantifying the effect and explore the spatial distribution of mixing.

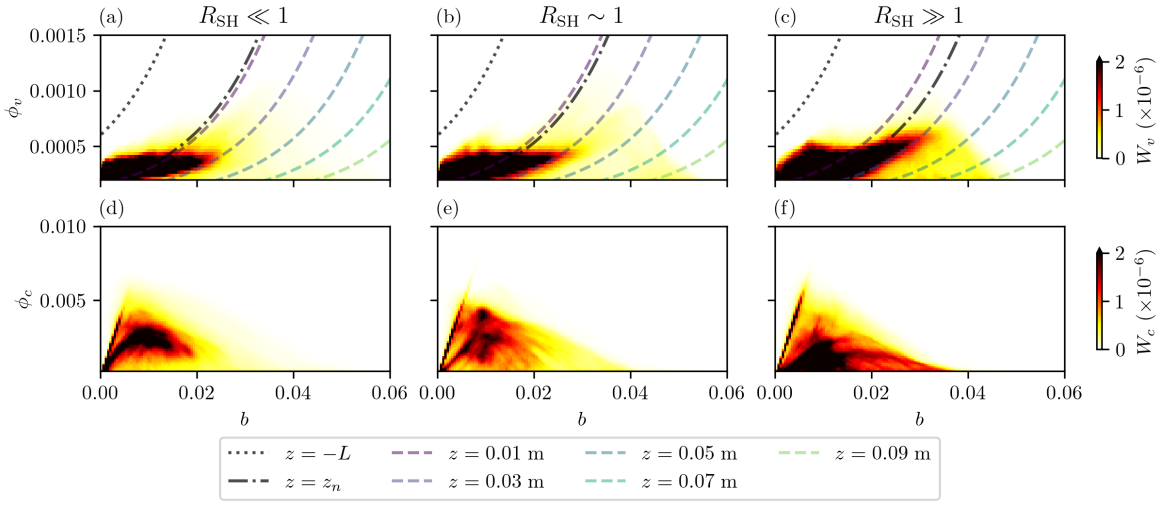

Fig. 6.16 Buoyancy-vapour and buoyancy-ice volume distributions W_v and W_c at $t = t_{\text{end}}$ in simulations `weak_shear`, `shear` and `strong_shear`, with $R_{\text{SH}} \ll 1, \sim 1$ and $R_{\text{SH}} \gg 1$ respectively. In (a)–(c), saturation curves $\phi_v = \phi_0 \exp(\alpha(\Theta b - \Gamma(z + H)))$ are shown with $z = -L$ (black dotted), $z = z_n$ (black dot-dashed), and heights $z = 0.01, 0.03, 0.05, 0.07, 0.09\,\text{m}$ (dashed colour lines).

Figure 6.17 shows the mixing metrics χ, ε, and the mixing efficiencies discussed earlier in § 6.4 and § 6.5. The TKE dissipation rate is slightly increased in the strong shear simulations, especially at early times. Although we only see the evolution of the mixing metrics up to $t = 15\,\text{s}$, there is evidence that the TKE dissipation rate is gradually decreasing in simulations `control`, `weak_shear`, and `shear`. However, the increased value of ε appears to persist for longer in simulation `strong_shear`. The buoyancy variance dissipation rate χ also tends to be larger in the shear simulations, especially in simulation `shear` with $R_{\text{SH}} \sim 1$ where there is a large peak after the plume reaches z_{max} at $t \approx 5\,\text{s}$ which may correspond with initial formation of a hydraulic jump. The evolution of the mixing is similar to simulations without shear, as noted in § 6.3, with η increasing over time since χ remains approximately steady once mixing between the plume and environment begins whilst the turbulence gradually becomes less energetic in the plume. The cumulative mixing efficiency is smaller in `weak_shear` and `strong_shear` relative to control whilst `shear` is more efficient. Given the increase in total hydration with shear rate, this suggests that the mixing efficiency is not a useful proxy for determining the influence of mixing on hydration.

Figure 6.18 shows the spatial distribution of χ in x-z cross-sections through the plume centreline, indicating where turbulent mixing is active in the flow. The structure seen in simulation `weak_shear` is consistent with that seen in the absence of shear

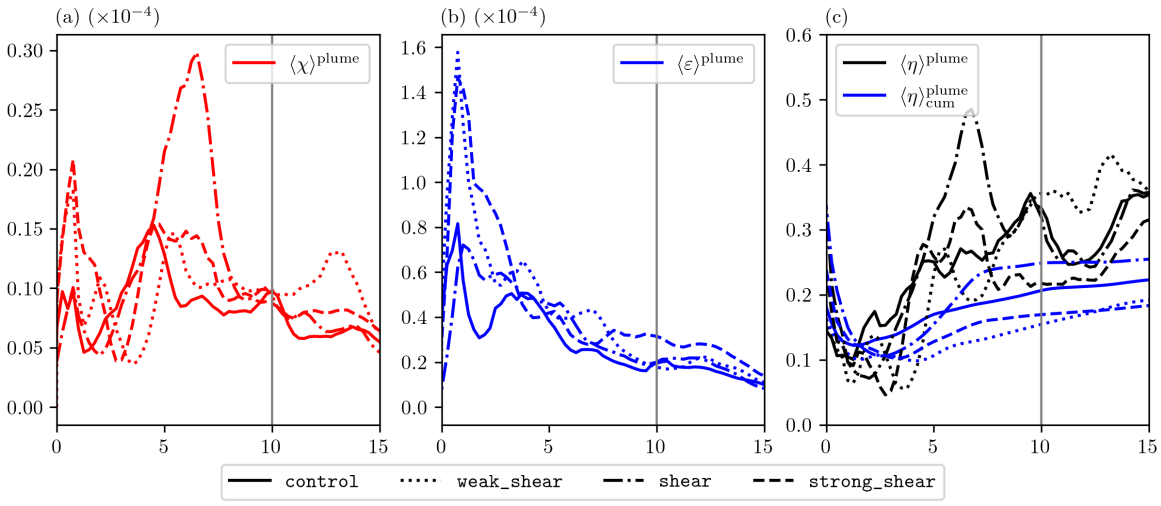

Fig. 6.17 Vertical velocity and turbulent mixing metrics as in figure 6.11, for simulations `control`, `weak_shear`, `shear`, and `strong_shear`.

as in chapter 3, where a thin layer of large χ forms at the edge of the plume cap as the plume impinges on the more buoyant environment. As the shear rate increases, the layer of large χ is stretched downstream and extends over a larger surface area. Regions with moderate χ are also evident in the environment and cover a larger area as the shear rate increases. In simulation `shear`, the largest values of χ are found immediately downstream of the plume cap, in the region earlier noted to resemble a hydraulic jump. In `strong_shear` there are layers with large χ present throughout the intrusion. There is also evidence of shear instabilities in these layers. Note also that this region of enhanced mixing does not appear to lift as it moves downstream unlike the $R_{\mathrm{SH}} \sim 1$ simulation.

Our results suggest a critical range of shear rates where the more energetic turbulence generated in the presence of large-scale shear results in more intense mixing which extends over large parts of the interface between the plume and environment. As we will see in the following subsection, the increased efficiency in simulation `shear` could be attributed to the presence of a hydraulic jump-like feature that results in a recirculating flow downstream of the plume cap, where mixing is significantly enhanced. In simulation `strong_shear` no hydraulic jump is seen and the enhanced mixing appears to instead result from internal wave breaking and shear instabilities at the top of the intrusion.

To explore the changes in the spatial distribution of mixing further we revisit the net mixing effect distribution M for the passive tracer ϕ_p that was used in chapter 3 to partition plume fluid between three stages of mixing. We do not explore the

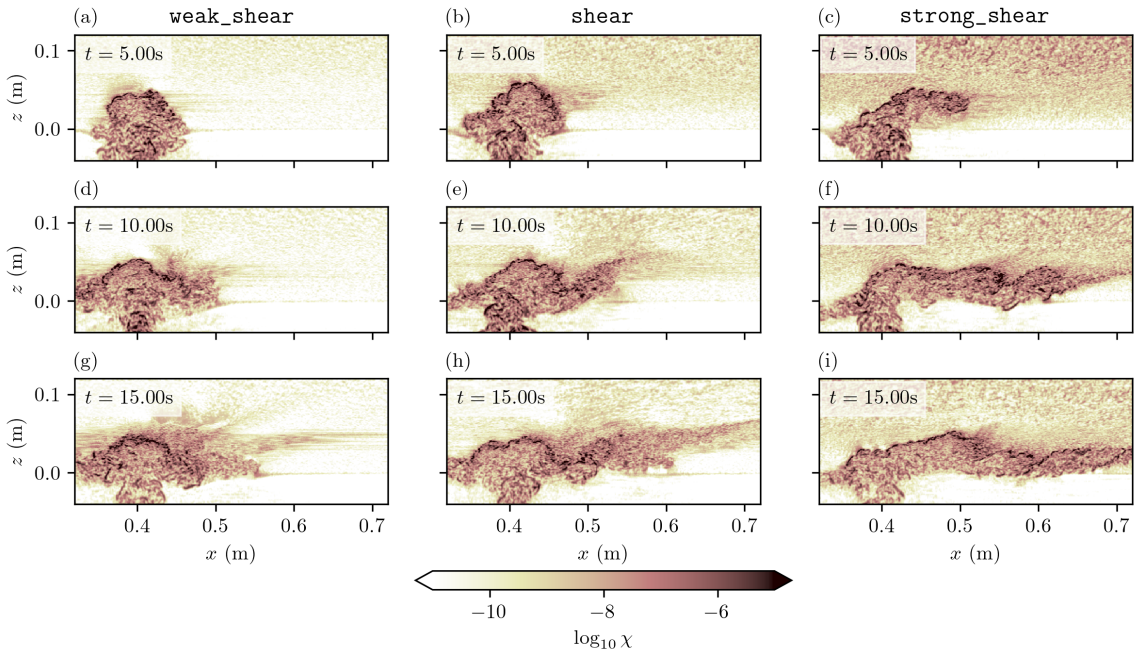

Fig. 6.18 x-z cross-section through the plume centreline of the buoyancy variance dissipation rate χ at $t = 5, 10, 15$ s in simulations `weak_shear`, `shear`, and `strong_shear`.

partitioning here since the flow does not reach a quasi-steady state, meaning the method presented in chapter 3 is not valid. Nonetheless, we can use the raw values of M to identify regions where turbulent mixing is particularly active, indicated by values of M which are positive but small. Mixed fluid with large (positive) M is 'older' in the sense that it has undergone more mixing. See § 3.3 for a more detailed discussion of the interpretation of M. Figure 6.19 shows the net mixing effect distribution in (b, ϕ_p)-space and physical space at $t = 12$ s in `control` and the three shear simulations. As has been noted previously, simulation `weak_shear` behaves in a similar manner to `control`. The layer of enhanced χ at the edge of the plume cap where the most efficient turbulent mixing occurs can be seen as a layer of small positive M. As mixed fluid subsides and joins the intrusion it becomes homogenised and the value of M increases. In the shear simulations, it can be seen that mixing between undiluted plume fluid with $M < 0$ and the rest of (b, ϕ_p)-space occurs over a wider range of b and ϕ_p. In simulation `strong_shear`, the layer of small positive M extends along the top of the intrusion, consistent with figure 6.18. Mixed fluid accumulates at the bottom and far downstream edge of the intrusion. Simulation `shear` is distinct in that much larger regions of intrusion have small values of M, suggesting intense mixing throughout the intrusion. This explains the observation from figure 6.17 that the mixing efficiency is

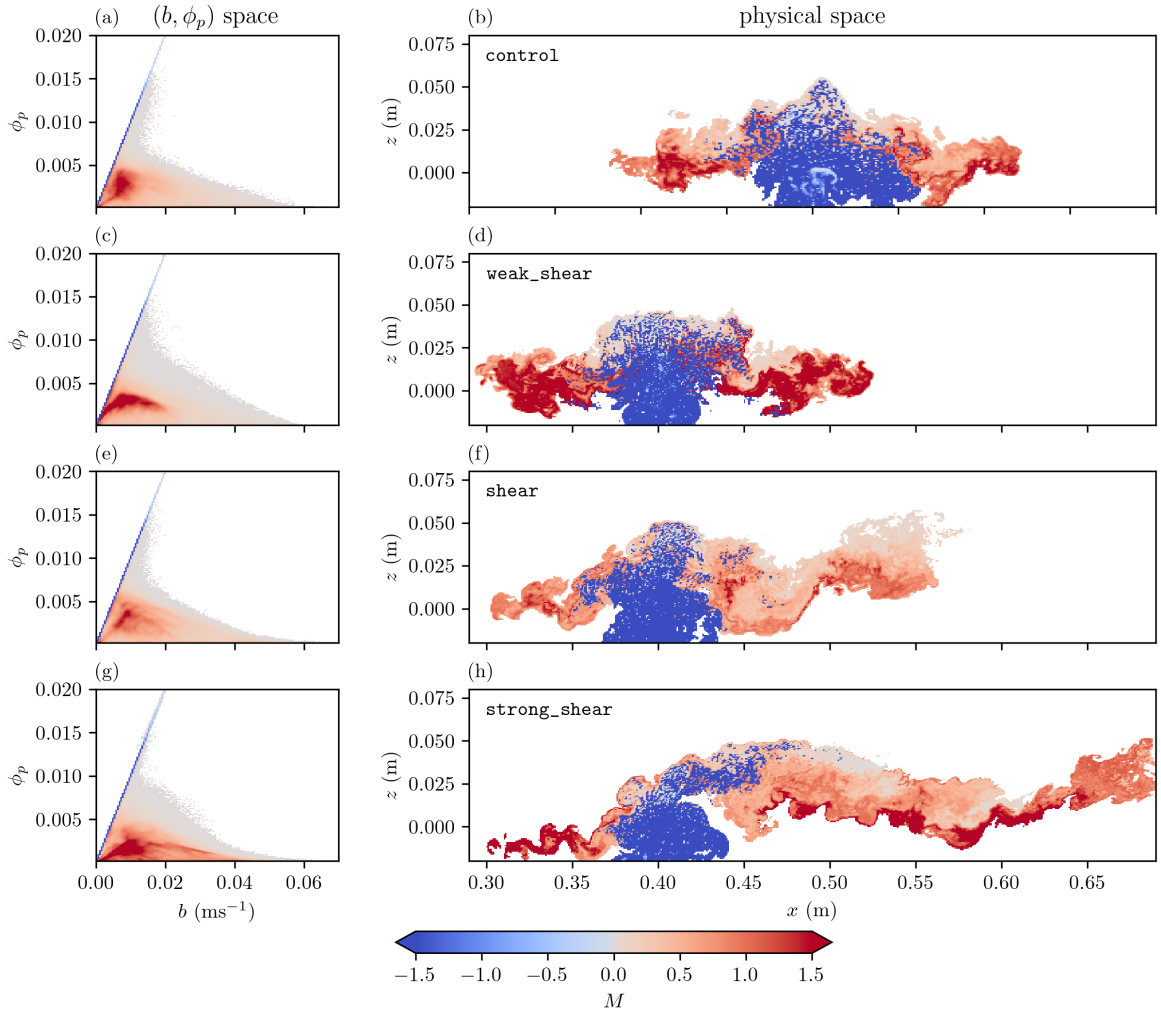

Fig. 6.19 Net mixing effect distribution M defined in § 3.3 at $t = 12\,\mathrm{s}$ in simulations `control`, `weak_shear`, `shear`, and `strong_shear`. M is shown in both (b, ϕ_p)-space and physical space.

largest in the $R_{\mathrm{SH}} \sim 1$ regime: the energetic turbulence results in mixing throughout the intrusion rather than just on the top edge as in the $R_{\mathrm{SH}} \gg 1$ regime, meaning a larger proportion of dissipated energy results in mixing. However, only mixing at the top of the plume contributes to hydration by warming plume fluid parcels, so the hydration is not enhanced to the same extent as simulation `strong_shear`, where the most intense mixing is more localised but effective at hydration.

6.6.3 Influence on internal gravity wave response

In chapter 4 we examined internal waves generated by convective penetration into a quiescent, stably stratified layer. Here we explore the effect of large-scale vertical shear in the stratified environment. Numerical studies suggest that large-scale vertical shear does not play a role in generating internal waves (Lane and Reeder, 2001), which is consistent with our results in chapter 4 that link internal wave generation with turbulence inside the plume cap that is unaffected by shear in the surrounding environment. Instead, the mean flow acts to introduce asymmetry in the internal wave beams as well as introducing critical layers where waves with a given frequency and wavenumber will break, leading to the development of turbulence and mixing in the region where they break. Turbulence above deep convection has been linked with internal wave breaking as small-scale gravity waves encounter a critical level (Lane et al., 2003), as well as secondary wave generation (Lane and Sharman, 2006).

Howland et al. (2021) explored shear-induced breaking of internal gravity waves in an idealised flow, showing that linear ray-tracing theory is qualitatively useful in describing refraction of waves by the shear despite the development of strong nonlinearities which make the assumption of a slowly-varying background invalid. Motivated by this conclusion, we use ray tracing to explore the effect of a mean flow with linear shear $\boldsymbol{U} = \lambda z \hat{\boldsymbol{x}}$ in the presence of a linear stratification $b = N_0^2 z$. Recall the dispersion relation for internal gravity waves is

$$\omega^2 = N_0^2 \frac{k_h^2}{k_h^2 + k_z^2}, \tag{6.5}$$

where k_h and k_z are the horizontal and vertical wavenumber, respectively. In the presence of a mean flow, the *extrinsic* frequency Ω observed travelling with the mean flow $\boldsymbol{U}$ satisfies the (stationary) dispersion relation in (6.5). This is distinct from the

intrinsic frequency,

$$\omega = \boldsymbol{U} \cdot \boldsymbol{k} + \Omega = \lambda z k_h + N_0 \frac{k_h}{\sqrt{k_h^2 + k_z^2}}, \tag{6.6}$$

measured by a stationary observer, where $\boldsymbol{k} = (k_h, k_z)$ is the wavevector and we have assumed that the large-scale shear may be treated as slowly-varying relative to the wave period (Sutherland, 2010).

With respect to a stationary observer, an internal wave will propagate along a ray whose position $\boldsymbol{x}$ is determined by the ray tracing equations,

$$\frac{\mathrm{d}\boldsymbol{x}}{\mathrm{d}t} = \nabla_{\boldsymbol{k}}\, \omega, \quad \frac{\mathrm{d}\boldsymbol{k}}{\mathrm{d}t} = -\nabla \omega, \tag{6.7}$$

where $\nabla_{\boldsymbol{k}}$ is the gradient in wavenumber space. Waves encounter a 'critical level' when the vertical wavenumber k_z becomes infinite and the extrinsic frequency drops to zero, meaning upward propagating rays appear to bend over and become horizontal. As an internal wave beam approaches its critical level, the wave amplitude and (with the mean flow we consider) the vertical wavenumber grow until instabilities develop which cause the wave to break. In the case of a linear shear, the intrinsic frequency ω and horizontal wavenumber k_h are conserved along a ray. Thus an internal wave beam encounters its critical level at a height z_c, determined by setting $\Omega = 0$ in (6.6), where

$$z_c = \frac{\omega}{\lambda k_h}. \tag{6.8}$$

We therefore expect that as the shear rate λ increases, waves with a given frequency and (horizontal) wavenumber encounter their critical level at a lower height. In particular, low frequency waves with large horizontal wavenumbers (i.e. narrow wave beams) are more likely to break lower in the stratified layer, close to the height of the penetrating plume and downstream intrusion.

Figure 6.20 shows horizontal cross-sections of the vertical velocity in `control` and the three shear simulations at $t = 10\,\mathrm{s}$. Rays computed according to (6.7) and initialised at $\boldsymbol{x}_0 = (0, L_h/2)$ are overlaid in green for $\omega/N_0 = 0.5, 0.9\,\mathrm{s}^{-1}$ and $k = 1, 10\,\mathrm{m}^{-1}$. Although the ray calculation assumes a slowly varying background and entirely neglects the effects of the penetrating plume, it gives a qualitative sense of the behaviour of internal wave beams which propagate upwards and outwards from the plume cap. To give a sense of the time-dependence of the wave response, figure 6.21 shows a time

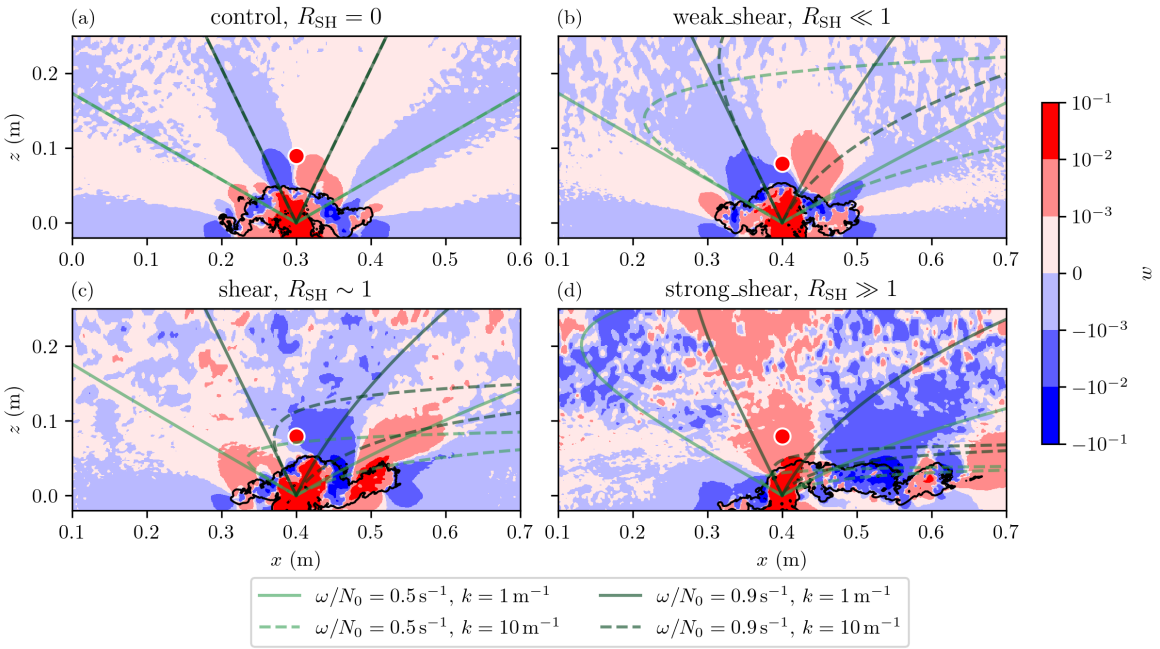

Fig. 6.20 x-z cross-sections through the plume centreline of the vertical velocity in simulations `control`, `weak_shear`, `shear`, and `strong_shear` at $t = 10\,s$ on a symmetric log scale. Green lines are computed using ray tracing (as described in the text) initialised at $x = L_h/2, z = 0$ with fixed values of ω/N_0 and k_h shown in the legend. Red dots indicate the location of the time series of w shown in figure 6.21.

series of the vertical velocity at a single height $z/z_{max} = 1.1$ on the centreline of each simulation, shown by a red dot in figure 6.20.

An important observation from figure 6.21 is that the wave response in simulations `control` and `weak_shear` is one of propagating internal waves, with oscillations in the vertical velocity evident above the plume. However, no oscillation is seen in simulations `shear` and `strong_shear`, suggesting the large-scale shear is strong enough to prevent upstream propagation of internal waves. Instead, we observe features consistent with internal wave breaking; whilst the internal wave response in simulation `weak_shear` in figure 6.20(b) is similar to that seen in `control` except with slight asymmetries, the wave response when $R_{SH} \gtrsim 1$ in figure 6.20(c) and (d) is structurally different. Consistent with linear ray theory, the horizontal scale of the wave structures increases with shear rate because smaller scale waves break (note that the dashed rays with larger k_h become horizontal, i.e. break, lower in the domain). The structures also become incoherent at lower heights which is consistent with the theoretical prediction in (6.8) that internal waves encounter their critical levels at lower heights when the shear rate increases. We also note that the amplitude of the vertical velocity is larger

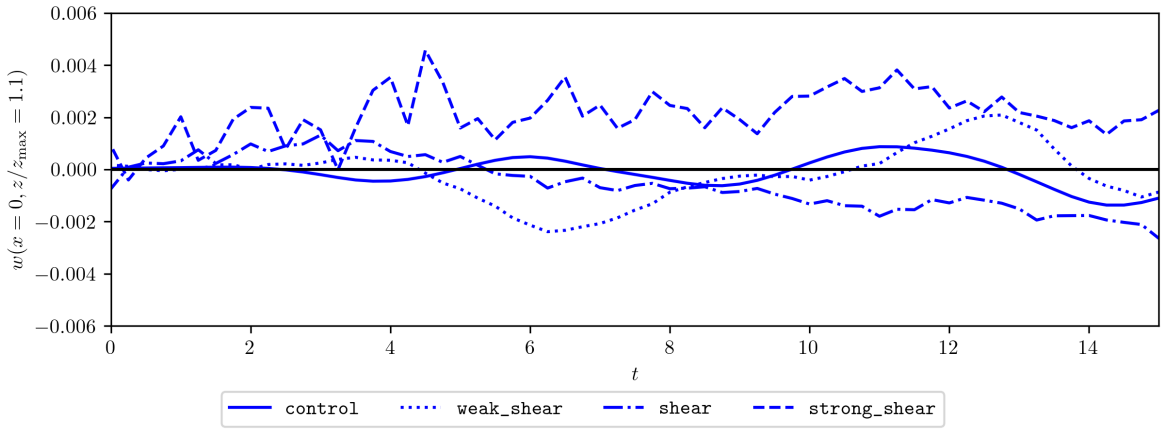

Fig. 6.21 Time series of vertical velocity w at $x = L_h/2, z/z_{\max} = 1.1$ in simulations `control`, `weak_shear`, `shear`, and `strong_shear`. Location in each simulation shown as a red dot in figure 6.20.

immediately above the plume when the shear rate is larger, consistent with breaking of small-scale (high wavenumber) gravity waves. Similarly, the noisy signal observed well above the plume in simulations `shear` and `strong_shear` is consistent with the generation of turbulence and instabilities in the environment. The amplitude of the vertical velocity appears larger close to the plume, especially where large-amplitude perturbations of the intrusion are observed, e.g. near the hydraulic jump-like feature in `shear` and the KH-like structures in `strong_shear`.

The internal wave response to penetrative convection is associated with a vortical response which is a half wavelength out of phase with the vertical velocity response. Lane (2008) consider the vortical response to convective penetration in an idealised flow where an axisymmetric thermal (i.e. a finite release of buoyant fluid) rises through a quiescent, stably stratified environment. A 'secondary circulation' of vortices with alternating sign forms above the thermal. It is interesting to note that waves they observe have a frequency very close to the environmental buoyancy frequency, again consistent with our findings in chapter 4. D18 identify the alternating vortices as a source of wind shear at the edge of a convective overshoot which can lead to instabilities and mixing. To explore this effect in the presence of large-scale vertical shear we define the residual circulation,

$$\boldsymbol{u}_r = \boldsymbol{u} - \lambda z \mathcal{H}(z), \tag{6.9}$$

and the out-of-plane residual vorticity in an x-z cross-section of the flow as

$$\zeta_r = \hat{\boldsymbol{y}} \cdot \nabla \times \boldsymbol{u}_r = \zeta_y - \lambda \mathcal{H}(z), \tag{6.10}$$

where $\zeta_y = \partial_z u - \partial_x w$ is the out-of-plane vorticity, as used in chapter 4.

Figure 6.22 shows the time evolution of residual vorticity in simulations `control` and `weak_shear` from $t = 5\,\mathrm{s}$ to $t = 15\,\mathrm{s}$. Simulations `weak_shear` and `strong_shear` are shown in figure 6.23. The residual circulation is overlaid as green arrows with length proportional to the speed $|\boldsymbol{u}_r|$ at its starting point and velocities set to zero inside the plume. Arrows whose length is shorter than the size of the arrow head are not shown. Stippling indicates regions where the local Richardson number $\mathrm{Ri}_g \leq 1/4$, with Ri_g defined as in (1.9), indicating regions of the flow which are susceptible to shear instability.

The circulation observed in figure 6.22 is consistent with the circulation described by Lane (2008) and D18; propagating internal waves form vortices of alternating signs, inducing a downward flow on some regions of the plume cap. The residual circulation may enhance mixing by inducing shear instabilities via two pathways: either by increasing the local shear rate or by reducing the local buoyancy gradient. We note that regions with $\mathrm{Ri}_g \leq 1/4$ appear in the presence of downward flows, which likely enhance the shear between the plume and environment, and upward flows, which likely act to reduce the buoyancy gradient by separating buoyancy contours – note the left side of the plume cap in figure 6.22(c) and the right side in figure 6.22(i). The same behaviour is observed in simulation `weak_shear` despite slight asymmetries in the internal wave (and therefore vortical) response. The regions susceptible to shear instability are larger in `weak_shear` due to the presence of a weak mean flow. The location of these regions appears consistent with the regions of moderate χ in the environment above the plume in figure 6.18(a) and the slight increase in $\langle\chi\rangle^{\mathrm{plume}}$ in figure 6.17(b).

As shown in figure 6.23, the vortical response is more complex in simulations `shear` and `strong_shear` where the internal wave and vortical response is approximately stationary. Regions susceptible to shear instability extend further into the environment. The formation of a hydraulic jump-like feature in simulation `shear` noted earlier appears consistent with the formation of a stationary vortex downstream of the plume cap, where $\mathrm{Ri}_g \leq 1/4$, which recirculates the flow and produces a strong downward flow on the plume cap that acts to enhance mixing (see figure 6.18). Readjustment of the perturbed flow downstream acts to lift up the far end of the intrusion. Note that the time when the recirculating vortex is strongest coincides with the peak in $\langle\chi\rangle^{\mathrm{plume}}$ in figure 6.17. The regimes in which a hydraulic jump forms can be deduced by defining a Froude number Fr in terms of the mean-flow velocity U at the obstacle

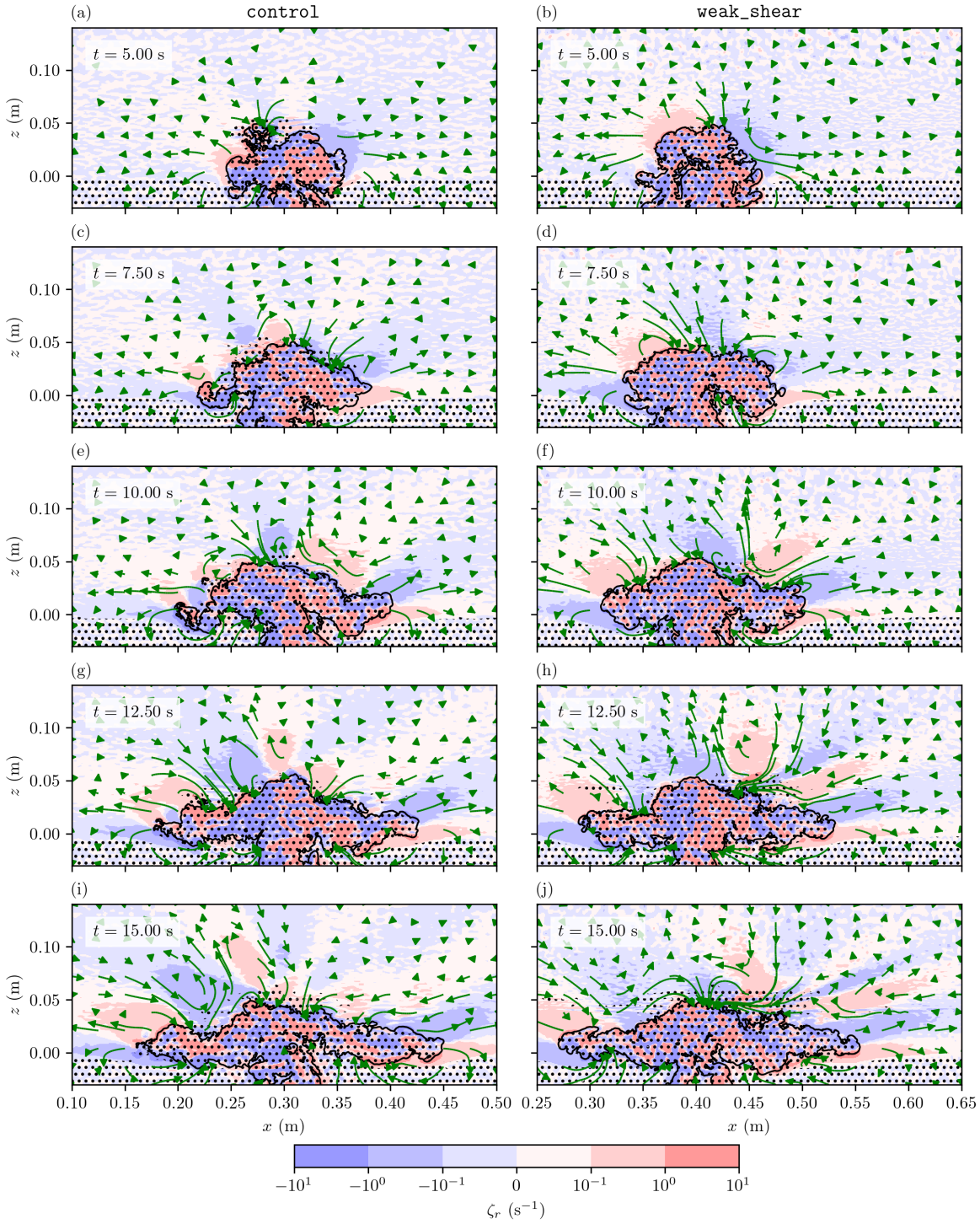

Fig. 6.22 x-z cross-sections of simulations `control` and `weak_shear` at $t = 5, 7.5, 10, 12.5, 15$ s showing the residual vorticity ζ_r (colour, symmetric log scale) and the residual circulation $\boldsymbol{u}_r$ (green arrows). Arrow length is proportional to the speed at the start point. The velocities are set to zero within the black line which indicates the plume contour $\phi_p = 10^{-3}$. Hatching indicates regions where the local Richardson number $\mathrm{Ri}_g \leq 1/4$, meaning the flow is susceptible to shear instability.

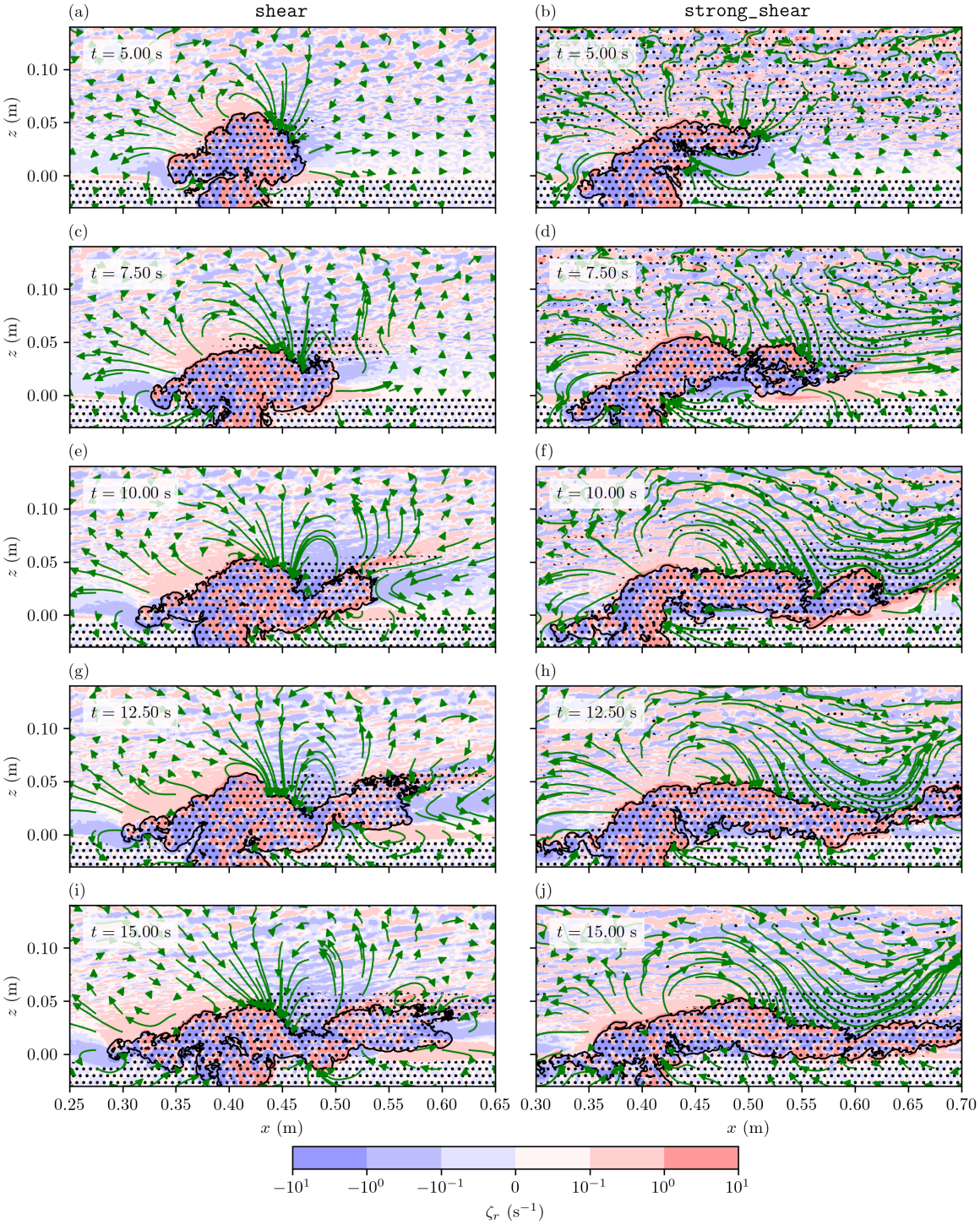

Fig. 6.23 As in figure 6.22, for simulations `shear` and `strong_shear`.

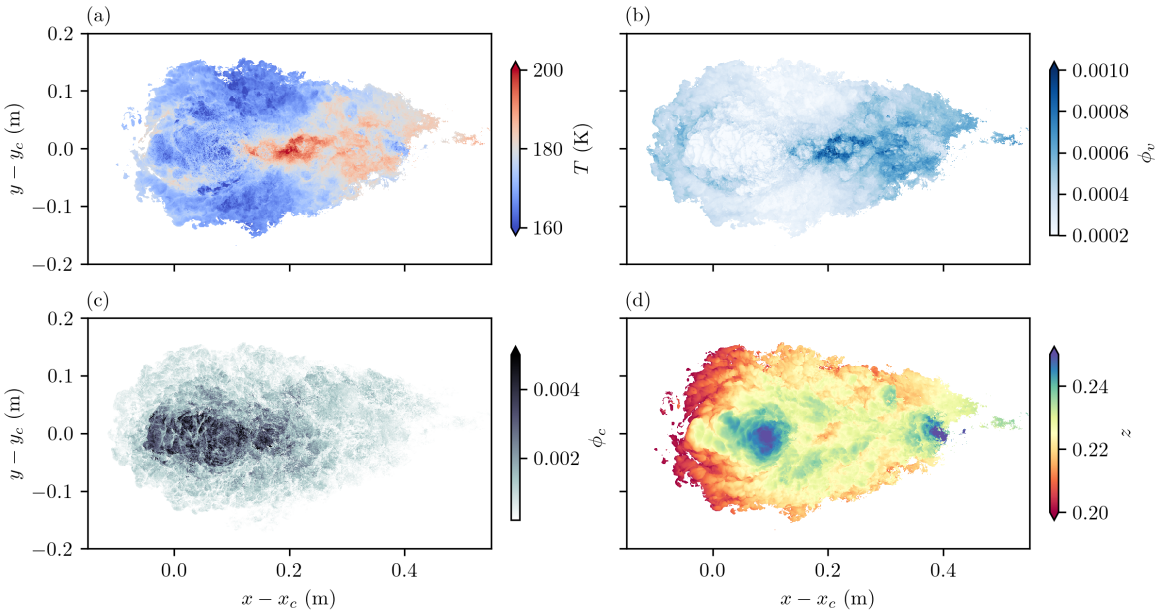

Fig. 6.24 Top-down view of the plume (where $\phi_p \geq 10^{-3}$) in simulation `strong_shear`, showing (a) temperature T, (b) water vapour concentration ϕ_v, (c) ice concentration ϕ_c, and (d) height z on the top surface of the plume at the end of the simulation, $t = t_{\text{end}}$ s. The axes are centered on the plume centreline $x_c = y_c = L_h/2$.

height h,

$$\text{Fr} = \frac{U}{N_0 h} = \frac{\lambda z_{\max}}{N_0 z_{\max}} = \frac{\lambda}{N_0} \tag{6.11}$$

where h is chosen to be the maximum penetration height $z_{\max}$ (Homeyer et al., 2017; O'Neill et al., 2021). A hydraulic jump is expected to form when the flow is 'supercritical' with Fr > 1, though 2D modelling and observations have shown that they may form when Fr $\gtrsim 0.4$ (Durran, 1986). In simulation `shear`, Fr $= 0.5$. The vortical structure and residual circulation in simulation `strong_shear` appears different to simulation `shear` since the downward flow forms over the downstream end of the intrusion rather than the plume cap. This suggests simulation `shear` lies in a critical range of shear rates where a standing gravity wave structure forms just downstream of the plume cap, rather than far downstream over the intrusion. Nonetheless, in simulation `strong_shear` the downward flow results in a horizontally extended region where shear instabilities may form owing to the increased local shear rate. The observation of KH-like structures in the intrusion at $t = 10$ s coincides with the region where $\text{Ri}_g \leq \frac{1}{4}$. However, the enhanced buoyancy gradient from the downward flow appears to limit the amplitude of the KH structure from $t \approx 10$ s onwards, a process which has been noted in idealised simulations of stratified shear flows (VanDine et al., 2021).

To conclude our assessment of the internal wave response to convective penetration in the presence of large-scale shear, we address the link between internal wave breaking and large vertical displacements in the stratified layer. In the TTL, observations of 'remote' hydration of the stratosphere occurring well above the maximum penetration height of a convective overshoot have been linked with the formation of cirrus (ice) clouds referred to as 'jumping cirrus' (Wang, 2004). Recall from § 5.2 that H10 examined this phenomenon, suggesting that upward displacement of TTL air by internal wave breaking results in in-situ formation of ice via adiabatic cooling, which is then mixed into the subsaturated (and warmer) environment higher up in the TTL and TLS.

There is a distinction between the formation of jumping cirrus, which to a large extent represents redistribution of moisture already present in the TTL, and direct injection of water vapour into the stratosphere via turbulent mixing between an overshoot and the surrounding TTL environment. Direct injection and mixing of moisture into the TTL is linked with 'above-anvil cirrus plumes' (AACPs), where moist regions that resemble chimney plumes extend downstream of overshooting tops (Homeyer et al., 2017). AACPs have been linked with severe weather at the surface and are often associated with a 'cold U / warm centre' structure in satellite observations (Luderer et al., 2007). The warm centre indicates air that has mixed with the stratosphere and become warmer, forming a plume of moist air well above the thunderstorm 'anvil' that forms at the tropopause from parts of the cloud that are not energetic enough to penetrate into the stratosphere (Homeyer, 2014). The penetrating plume in our simulations essentially represent these AACPs. In the presence of shear, the 'warm centre' structure is evident: figure 6.24 shows a top-down view of `strong_shear`, showing the temperature, vapour and ice concentration, and vertical height on the top surface of the plume. Warm regions form at the top of the plume due to mixing with the warmer environment, forming moist regions that extend downstream of the overshooting plume cap.

Our simulations have shown that penetration of the plume significantly perturbs the surrounding environment which can result in vertical displacement of fluid away from the plume, either directly (e.g. when the plume collapses) or indirectly (e.g. from propagating internal waves). Crucially, there is a mechanism for these displacements to occur *without* internal wave breaking, which only occurs due to the presence of large-scale vertical shear in simulations `shear` and `strong_shear`. We are therefore motivated to explore whether internal wave breaking is necessary for the formation of jumping cirrus. Whilst in-situ formation of ice cannot occur in our model due to the dry

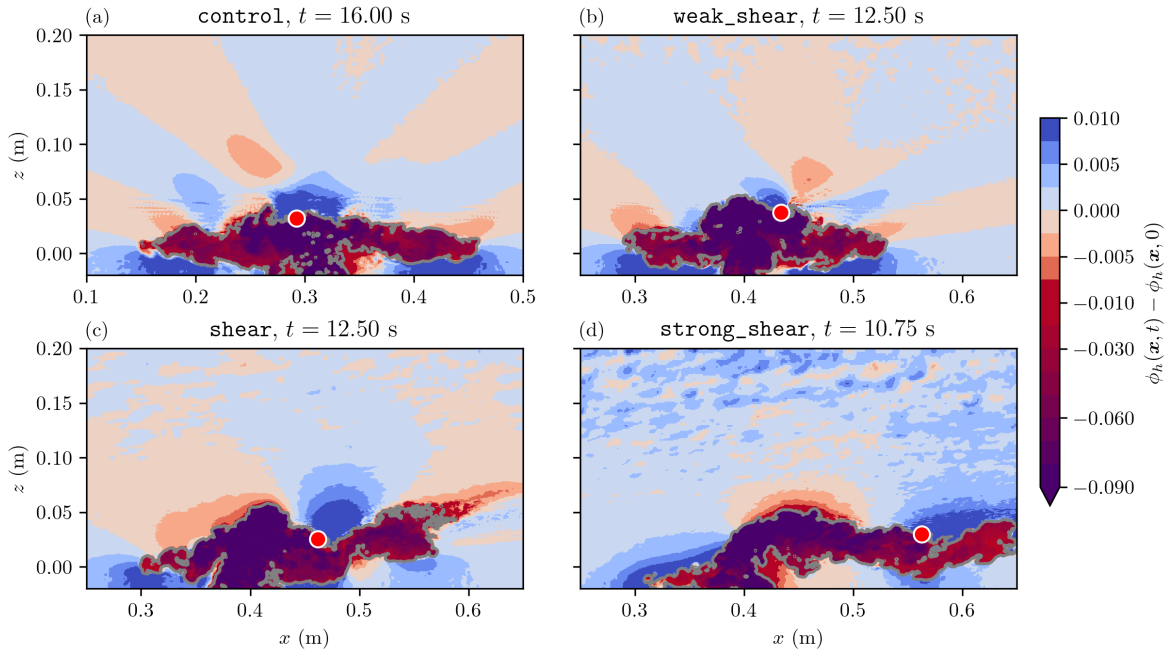

Fig. 6.25 x-z cross-sections through the plume centreline of the initial height tracer perturbation $\phi_h(\boldsymbol{x}, t) - \phi_h(\boldsymbol{x}, 0)$ in simulations `control`, `weak_shear`, `shear`, and `strong_shear`. For each simulation, the time shown is when the positive initial height perturbation is maximised. The location where this maximum is achieved is shown by a red dot with a white outline.

environment, we test the underlying assumption that large vertical displacements are related to gravity wave breaking by comparing these displacements in the `control` and varied shear simulations.

Motivated by the analysis reported by H10, the `control` and varied shear simulations include an additional passive 'initial height' tracer ϕ_h which obeys the same governing equation (5.25) as ϕ_p but with no diffusion and with initial condition

$$\phi_h(\boldsymbol{x}, t_0) = z, \tag{6.12}$$

with ϕ_h fixed on the top and bottom boundary. Thus at any time t, the vertical displacement of a fluid parcel is $\phi_h(\boldsymbol{x}, t) - \phi_h(\boldsymbol{x}, t_0)$ with positive values indicating downward displacement and vice versa. We use this analytical method to explore the differences in vertical displacements of fluid parcels in the `control` and varied shear simulations. In particular, we ask whether the displacements are solely a gravity wave effect or whether large vertical displacements can arise simply from the dynamics associated with convective penetration.

Figure 6.25 shows perturbation of the initial height tracer ϕ_h at the time in each simulation where the downward vertical displacement is maximised. We choose to maximise the downward displacement because the largest upward displacements occur within the plume. Note from H10 that jumping cirrus was attributed to co-located upward and downward vertical displacements, representing the bringing together of air from the upper TTL with air in the lower TTL. In our simulations, the location where the maximum in $\phi_h - \phi_h(t = 0)$ is attained – shown with a red dot in each simulation – occurs close to the plume and during collapse of the overshoot, which acts to draw fluid parcels down from higher in the stratified environment. This air may then mix with moist fluid in the plume and, as the environment relaxes and these parcels ascend towards their initial heights, ice could be formed via adiabatic cooling. Note we do not observe this process explicitly because the environment is dry, so the small amounts of vapour mixed into these parcels is not sufficient to bring the parcels close to saturation. However, if the environment had some initial moisture profile then in-situ formation of ice could occur, consistent with H10. Crucially, we find that the maximum downward displacements are of a similar magnitude in all simulations, though upward displacements are stronger at the downstream end of the intrusion in simulation `shear` and above the plume cap in `strong_shear`. In these simulations with $R_{\mathrm{SH}} \gtrsim 1$ the largest downward displacement coincides with regions where the residual circulation shown in figure 6.22 is strongest, whilst in simulations `control` and `weak_shear` with $R_{\mathrm{SH}} < 1$ the largest downward displacement occurs atop the plume cap at the onset of, or during, the collapsing stage of the flow evolution. Although strong downward displacements can be seen in the environment well above the plume in simulation `strong_shear`, the signal is noisy and transient meaning it is difficult to ascertain whether the displacements – which are likely a result of turbulence forced by breaking internal waves – could transport fluid parcels close enough to the plume to pick up moisture. These results suggest that perturbation of the surrounding environment by the penetrating plume plays as much of a role in creating large vertical displacements in the environment as wave breaking in the presence of vertical shear.

6.7 Discussion and conclusions

We have used a minimal moisture model that represents conversion between two forms of moisture, vapour and ice, and sedimentation of ice at a fixed velocity. Using simulations at the lab scale we explored the interaction between turbulent mixing, sedimentation,

convective intensity, and large-scale vertical shear in convective hydration of a stratified layer. Simulation parameters were chosen to be representative of the TTL. This study is analogous to numerical studies of convective overshoots in the literature (Dauhut et al., 2018; Hassim and Lane, 2010; Sang et al., 2018), with the added advantage of using a model that allows exploration of a wide range of regimes, direct control of microphysical processes such as the strength of sedimentation, and reduced sensitivity to the representation of sub-grid-scale turbulence. The use of a minimal model that retains only the essential processes also aids interpretation of the results.

We explored the competition between sedimentation, which acts to remove ice from the plume, and mixing, which acts to convert ice to vapour, by varying the sedimentation velocity. The results are summarised in figure 6.7. When sedimentation is weak, observed vapour concentrations are consistent with the environmental temperature at the equilibrium height $z = z_{\mathrm{n}}$ where plume fluid settles at late times. This means that vapour concentrations can be predicted based on dynamics alone, with no knowledge of the mixing that occurs between the plume and environment, by measuring the equilibrium height. Mixing with buoyant fluid surrounding the plume acts to raise the equilibrium height above the height that would be predicted based on the buoyancy in the plume at penetration. Thus measurement of z_{n} encapsulates the effect of mixing on buoyancy in the plume. However, when the sedimentation velocity is close to or stronger than the typical turbulent vertical velocity in the plume then ice settles out before sublimation can occur in the mixed fluid, decreasing total hydration of the stratified layer. This is linked to the result in chapter 3 that the mixing timescale is longer than the dynamical timescale. In this case, observed vapour concentrations can be predicted by measuring the maximum height that parcel trajectories reach, where the minimum temperature is attained. At this temperature, all moisture in excess of the saturation vapour concentration is in the form of ice which settles out of the plume. Thus the final vapour concentrations are determined at this point of the trajectory, though some further reduction in concentration occurs due to dilution via further mixing with the dry environment.

The D18 hypothesis that increased convective intensity (and hence penetration to a greater maximum height) results in increased hydration of the stratified layer was explored by quadrupling the source integral buoyancy flux in the plume in each simulation with varied sedimentation velocity. Our results confirm the D18 hypothesis; for all values of w_s, the total hydration is increased. The influence of sedimentation is reduced as convective intensity increases (figure 6.12) since velocities in the plume

become stronger and mixing becomes more intense, more effectively counteracting sedimentation. Thus for a wider range of (weak) w_s, the plume remains saturated at late times so vapour concentrations are determined by the equilibrium height z_{n}. Although the plume accesses more buoyant environmental fluid when the convective intensity is greater, the energetic efficiency of the mixing remains the same (figure 6.11). This conclusion is perhaps expected since increasing F_0 does not introduce any mechanisms that could result in more energetically efficient mixing. However, a stronger plume is warmer and results in more energetic turbulence, increasing the direct transport of vapour into the stratified layer and allowing larger concentrations of ice to access the most buoyant environmental fluid, thus enhancing vapour transport.

The influence of large-scale vertical shear on turbulent mixing and hydration of the stratified layer was found to be strong, with significant differences in the spatial distribution and intensity of mixing depending on the shear rate. Overall, transport of water vapour increases with shear rate as a result of enhanced mixing (figure 6.14). This supports the conclusion of Homeyer et al. (2017) that hydration is enhanced when there are strong storm-relative winds, which promote gravity wave breaking, but contrasts with the conclusion of S18. As the shear rate increases, a larger proportion of the internal gravity wave spectrum generated by the plume is susceptible to breaking at heights close to the plume (figure 6.20). In the absence of wave breaking when the shear is weak (or absent), the alternating succession of vortices above the plume enhances wind shear at the edge of the plume, resulting in shear instabilities that enhance mixing (figure 6.22), consistent with Dauhut et al. (2018). When the shear timescale is comparable to or stronger than the dynamical timescale of the plume, the vortical response becomes stationary as internal waves can no longer propagate upstream and the region of intense mixing between the plume and environment that is typically found at the edge of the plume cap extends into the intrusion (figure 6.23). In a critical range of shear rates, a vortex forms downstream of the plume cap (resembling a hydraulic jump) which significantly enhances mixing in that region. This is consistent with O'Neill et al. (2021) where hydraulic jumps were identified as a mechanism for hydration of the extratropical stratosphere – note that our study is relevant to both the tropics and extratropics, since the dynamical setup is similar, though hydration in the tropics is more influential globally due to transport by the Brewer-Dobson circulation. Above this range of shear rates, the large-scale flow lifts over the plume and induces a downward flow on the intrusion, which supports the development of shear instabilities at the top of the intrusion. These instabilities enhance turbulent mixing over a wide

spatial region, though mixing appears to be more efficient in the aforementioned recirculating regime where buoyancy contours are more significantly deformed and intense mixing occurs throughout the intrusion (figure 6.17 and figure 6.19).

Whilst our results are consistent with the analogous studies by H10, S18 and D18 in many respects, there are important differences, particularly with respect to the role of vertical shear and gravity wave breaking. We found that large-scale shear increases net hydration by enhancing mixing, which directly contrasts with S18 who concluded that the role of shear is largely to modulate gravity wave amplitudes rather than influence small-scale mixing. Our conclusions on the role of gravity wave breaking can also be contrasted with S18 and H10; whilst wave breaking can be directly linked with enhanced mixing in the strongest shear simulation, turbulent mixing is still enhanced in weaker shear regimes when gravity wave breaking is less important. Similarly, turbulent mixing plays an important role in convective hydration in the absence of any vertical shear, when gravity wave breaking cannot occur. We therefore conclude that it is misleading to attribute mixing to the effect of gravity wave breaking, since shear instabilities also play a role, and in any case we found in chapter 3 that intense mixing in convective penetration is largely a buoyancy-driven process. Another contrasting viewpoint from our results is the complex interplay between dynamical and microphysical processes even in our idealised setup. The studies by H10, S18, and others in the literature (e.g. Homeyer et al. (2017); O'Neill et al. (2021)), seek to identify a dominant process that controls net hydration. However, we have shown that there are modulating factors that compete with one another in many different regimes, and it is not necessarily that case that all convective overshoots in the TTL sit in a narrow regime where a dominant process can be identified. For instance, as discussed in § 6.1, the range of shear rates found in the TTL is vast and, when translated into the language of our model, covers all of the R_{SH} regimes we consider, where the mechanisms that lead to enhanced mixing between the plume and environment vary significantly.

Chapter 7

Conclusions

7.1 Thesis summary

This thesis has explored turbulent mixing, tracer transport, and internal gravity wave generation in convective penetration of a buoyant plume into a stably stratified layer. This simple flow is interesting both as a fluid dynamical problem in itself and as an idealised representation of a wide range of industrial and geophysical flows. Despite its widespread relevance, the problem remains relatively understudied owing to practical limitations in laboratory experiments and the need to resolve a wide range of scales in numerical simulations. A particular motivation for this work is the relevance to moisture transport by deep convective systems that overshoot the tropical cold point tropopause (CPT), injecting potentially significant amounts of water vapour into the stratosphere. As a gateway to the wider stratosphere, transport across the tropical CPT can have significant impacts on the composition of the middle atmosphere and consequently Earth's climate. Water vapour is an especially powerful greenhouse gas that has been linked to both stratospheric cooling and tropospheric warming on decadal timescales (Forster and Shine, 2002; Solomon et al., 2010) and plays an important role in the destruction of stratospheric ozone that prevents harmful UV radiation from reaching Earth's surface (Brasseur and Jacob, 2017). The contribution of convective overshooting to the stratospheric water vapour budget is regarded as second order relative to dehydration as air slowly ascends through the CPT, though there remains uncertainty in estimates of this contribution. Open questions remain on the mixing, transport and microphysical processes that drive hydration of the stratosphere and the interaction between these processes. Improving our understanding of convective

hydration of the stratosphere is essential for building parameterisations of its effect in global climate models and refining estimates of the stratospheric water vapour budget in a changing climate.

We use numerical simulations and theoretical analysis to understand the key characteristics of mixing between the plume and stratified environment, and its effect on the transport of passive tracers and simple representations of moisture. We also gain insight into the generation of internal waves with a narrow band of frequencies in a turbulent flow with a wide range of temporal and spatial scales, a ubiquitous problem in stratified shear turbulence that holds relevance to the forcing of large-scale atmospheric winds and small-scale ocean mixing. We use reduced order modelling of complex geophysical problems, retaining only the essential aspects needed to understand the fundamental dynamics and properties that influence the flow. Owing to the wide range of scales in convective penetration, we use large-eddy simulations which parameterise the effect of sub-grid-scale turbulence on the resolved flow. We simulate the flow at 'laboratory' scales, which reduces the separation between the lengthscale at which energy is injected by the buoyant plume and the Kolmogorov scale at which energy is dissipated by turbulence, reducing sensitivity to the chosen sub-grid-scale turbulence model. Our lab scale results can be non-dimensionalised using characteristic length and time scales and interpreted in the context of chosen dimensional scalings. The numerical setup is detailed in chapter 2 and validated in § 2.3 using integral plume theory and comparison with direct numerical simulations of buoyant plumes (Craske and van Reeuwijk, 2015; Van Reeuwijk et al., 2016) that resolve the smallest turbulent scales in the flow.

Chapter 3 addressed turbulent mixing in convective penetration. We derived a novel diagnostic framework, the buoyancy-tracer volume distribution, to quantify irreversible diapycnal transport of a passive tracer. This builds on previous joint probability density functions used in studies of mixing in idealised flows (Penney et al., 2020) and the atmosphere (Plumb, 2007). Using this formalism, in § 3.3 we developed a method for objectively partitioning buoyancy-tracer phase space into three regions that correspond with distinct stages of mixing in a quasi-steady state. In this state, undiluted plume fluid penetrates into the stratified layer and remains shielded from the surrounding environment by a radial intrusion. Plume fluid overturns near the maximum penetration height and mixes with the environment. Mixing continues as fluid subsides, accumulates, and homogenises in the intrusion. As the plume cap impinges on the significantly more buoyant environment, intense buoyancy gradients

are established in a thin layer at the top of the plume where the mixing is most energetically efficient. We also found that mixing is slow relative to the time taken for fluid parcels to reach the top of the plume and subside into the intrusion, meaning mixing with the most buoyant environmental fluid occurs only for a limited time. The proportion of the total plume volume in each stage of mixing changes over time and in § 3.4 we found that the statistics that quantify turbulence, mixing, and entrainment vary significantly between each stage. Consequently, parameterisations that seek to represent mixing in convective penetration by prescribing average mixing statistics for the whole plume must account for the time dependence and significant spatial inhomogeneity. The net effect of mixing is to raise the equilibrium height (where mixed fluid settles) above that which would be predicted based on properties of the plume at penetration by increasing the buoyancy of plume fluid. This is strongly dependent on the maximum penetration height, which determines the largest accessible environmental buoyancy, and the length of time that the plume cap spends close to this height.

In chapter 4 we explored the generation mechanism and spectral properties of internal waves in convective penetration. In previous laboratory experiments (Ansong and Sutherland, 2010) it was found that oscillation of the interface between the plume and environment cannot explain the observed spectrum of internal gravity waves that propagate upwards and outwards from the plume cap. Using numerical simulations where the squared buoyancy frequency N_0^2 ranges over two orders of magnitude, we confirmed this observation and showed that the characteristic wave frequency $\omega_c \approx 0.9N_0$ is an approximately constant fraction of N_0 whilst the characteristic horizontal wavenumber scales as $N_0^{1/2}$. To explain the observation of waves with a narrow-banded frequency and wavenumber spectrum in a flow with a broad-banded axisymmetric turbulence spectrum, in § 4.4.2 we modified a linear viscous decay model (Taylor and Sarkar, 2007) for the axisymmetric wave geometry of this flow. Despite the assumption of a slowly-varying background and neglect of any mean flow, the model accurately predicts the decay in spectral power and selection of high frequencies close to N_0 when initialised from a spectrum taken at the top of but within the turbulent plume, assuming a virtual source close to the height of the intrusion. However, the predicted decay of low frequencies is not as strong as observed, which may be a result of neglecting non-propagating modes, non-linear effects, or breakdown of the underlying slowly-varying assumption. In § 4.4.3 we used dynamic mode decomposition and ray theory to trace internal wave beams from the stratified environment into the

plume, thus presenting the first evidence that internal waves may be generated by the turbulent flow inside the plume cap. In § 4.5 we compared the spectral properties of a buoyant plume penetrating into a stratified layer with a structurally similar flow where the stratified layer is replaced by a (more buoyant) uniform layer, such that waves are not generated by penetration of the plume. The same axisymmetric turbulence was observed within the plume and an evanescent wave signal was identified in the weak stratification that forms surrounding the plume cap, supporting our conclusion that waves are generated by turbulence within the plume and modulated as they propagate into the environment. Recent studies have demonstrated this conclusion in the 'scouring' regime where the stratification is sufficiently strong that convective plumes impinge upon and scour the base of the stratified layer but do not penetrate the interface (Couston et al., 2018; Lecoanet et al., 2015). The analytic method applied to the scouring regime is not applicable to the weakly stratified 'penetrative' regime we consider because the turbulence and wave spectrum overlap. However, we found that our most strongly stratified simulations with $N_0^2 = 10^3\,\mathrm{s}^{-2}$ had a vertical wave energy flux consistent with theoretical predictions for the scouring regime, indicating that a transition between the penetrative regime and the scouring regime occurs as the stratification strength increases (with F_0 fixed).

In chapters 5 and 6 we focus attention on convective hydration of the TTL. In § 5.3 we formulate a minimal moisture model that retains only the essential microphysical processes involved in hydration of the TTL. The cold environment means only two moist species need to be considered: vapour and ice. The low humidity in the TTL also means latent heating can be neglected. Three microphysical processes are represented: condensation of vapour into ice, sublimation of ice into vapour, and sedimentation of ice at a fixed velocity. We use simple functional forms inspired by Hernandez-Duenas et al. (2013) to represent these processes and use a Boussinesq representation of temperature derived following Vallis et al. (2019). The regime where most ice condenses during ascent is representative of the hydration mechanism in the TTL (see § 5.4). In § 5.5 we used a moist variation of the buoyancy-tracer volume distribution formalism from chapter 3 to explain this hydration mechanism in convective hydration of a stratified layer. Mixing between the plume and environment transports the significant ice content of the plume to larger buoyancies where the saturation vapour concentration is larger. This allows sublimation of ice, forming pockets of vapour that later accumulate in the intrusion. Plume fluid tends to remain saturated throughout the flow evolution because ice is abundant. Sedimentation has a strong effect on the total hydration. During

ascent, ice remains in suspension owing to the strong updraft velocity and turbulent vertical velocity. Once fluid overturns near $z_{\max}$, turbulent eddies weaken and the flow becomes predominantly horizontal, allowing ice to sediment out of the plume.

In chapter 6 we investigate the interaction between turbulent mixing, transport, microphysics, and large-scale vertical shear in convective hydration of a stably stratified layer. We use the model regime where the plume is loaded with ice at penetration. Unlike previous model studies that use comprehensive microphysical models and complex meteorological setups that are computationally expensive to simulate, we are able to explore a broader parameter space for the sacrifice of some realism using an idealised flow with a minimal moisture model. We consider controlled experiments where the sedimentation velocity, buoyant plume forcing, and large-scale shear rate in the stratified layer are varied to produce regimes where each process is weak, influential, or dominant relative to characteristic quantities in the plume.

The experiment with varied sedimentation velocity in § 6.4 captures the competition between sedimentation and mixing in controlling total hydration; strong sedimentation acts to remove ice from the plume before it can mix with the warm environment and sublimate to form vapour. A key result of this experiment is that hydration largely depends on the relative sizes of the sedimentation velocity and the typical turbulent vertical velocity. This suggests that given a more realistic size distribution of ice crystals, those with strong sedimentation velocities can be disregarded when determining the hydrating effect of a convective overshoot. In § 6.4.2 we show that semi-quantitative models based only on dynamics can predict the distribution of vapour concentrations in the plume at late times given knowledge of the sedimentation regime. When sedimentation dominates, the vapour concentration of a fluid parcel is determined by the minimum temperature reached along its trajectory, since ice is rapidly lost once vapour condenses. On the other hand, when turbulent velocities in the plume dominate sedimentation then ice remains in suspension so the plume remains saturated throughout its evolution. Thus the final vapour concentrations are determined by the environmental temperature at the height $z = z_{\mathrm{n}}$ where mixed fluid settles. Measuring the height z_{n} essentially captures the effect of mixing in making plume fluid more buoyant.

In § 6.5 we found that quadrupling the source buoyancy flux results in a plume that is warmer and penetrates higher, so mixing between the plume and environment is more effective at raising the buoyancy of plume fluid. Thus more ice is sublimated and the total hydration is increased. This confirms the hypothesis by Dauhut et al.

(2018) that maximum penetration height, which is controlled by the convective forcing, directly influences hydration by allowing access to more buoyant environmental fluid. Although increasing the convective intensity results in more energetic turbulence within the plume and more mixing as a result of a larger energy input, the mixing efficiency is unchanged. Semi-quantitative models capture the increase in hydration because mixing with the warmer environment raises z_{n} further. Stronger turbulent velocities in the plume mean that mixing dominates sedimentation over a wider range of sedimentation velocities.

The presence of large-scale vertical shear has a strong influence on the internal wave and vortical response to convective penetration which acts to enhance turbulent mixing and consequently increase the total hydration. The mean flow significantly deforms the plume cap and leads to formation of a downstream intrusion. Shear instabilities generated at the edge of plume intensify mixing with the environment, raising the temperature of mixed fluid further and thus allowing larger vapour concentrations. As the shear rate increases, a larger portion of the internal wave spectrum encounters a critical layer close to the plume, resulting in wave breaking which generates turbulence and further enhances mixing. The vortical response associated with internal waves also enhances mixing by inducing a residual circulation onto the intrusion that promotes shear instabilities. In a critical range of shear rates, the vortical response resembles a hydraulic jump. In this range, turbulent mixing (indicated by increased values of χ) becomes more widespread in the downstream intrusion without a corresponding increase in TKE dissipation, thus enhancing the mixing efficiency. Changes to the mixing efficiency are not monotonically related to changes in the total hydration, suggesting it is not a useful measure in this context and it is instead more valuable to consider the PE dissipation χ which more directly quantifies mixing. The primary mechanism for hydrating the stratified layer in all cases is the mixing of ice-rich plume fluid with warmer environmental fluid, resulting in sublimation of ice. Mixing between the plume and environment can be enhanced via several mechanisms. Importantly, although wave breaking plays a role in generating turbulence, it is not the primary driver of mixing between the plume and environment and does not appear to be directly related to vertical displacements in the environment that can lead to the formation of cirrus clouds well above convective overshoots. Overall this study shows that a systematic exploration of a simplified framework where only the essential physics is retained is a valuable and insightful approach to understanding convective hydration.

7.2 Future directions & outlook

This thesis has contributed to the understanding of turbulent mixing and internal wave generation in convective penetration of a stably stratified layer and the interaction between processes relevant to convective hydration of the lower stratosphere. Here we discuss aspects of this thesis that could be extended in future research and we highlight open questions.

Firstly, the approach to understanding mixing in this thesis has focused on use of the volume distribution formalism introduced in chapter 3 that translates mixing from physical to phase space. It would be interesting to also explore the problem of convective penetration from an energetic perspective. Whilst we have considered mixing efficiency, which quantifies the fraction of dissipated energy that results in mixing, it would be valuable to quantify the energetic effects of turbulent mixing and radiated internal waves directly. One approach is to use the framework presented by Winters et al. (1995) which describes the conversion between APE, BPE, kinetic, internal and external energy using the z^* formalism, which uses an adiabatic redistribution of the buoyancy field to calculate BPE directly.

The results presented in chapter 6, using the minimal moisture model formulated in chapter 5, motivate further extension of the simplified framework used to understand convective hydration of the TTL. Having established the interaction between mixing, transport, and simplified microphysical processes in the model, it would be valuable to explore more complex parameterisations of moisture. This acts both to validate the choices made in formulating our model and may also further elucidate the essential processes involved in hydration of the stratosphere. Examples of more complex parameterisations include modifying the sedimentation velocity w_s to vary based on a representation of the size of ice crystals. The distinction between ice concentration and crystal size is potentially important (Sang et al., 2018) because of different settling rates based on size; a crude model would be to assume that larger concentrations correspond with more large ice crystals which sediment faster, so that w_s is a function of ϕ_c. An important assumption in our model is that condensation and sublimation operate on the same timescale τ_m, whereas other examples of idealised moist parameterisations allow the rate of conversion of ice into vapour to depend on the ice concentration (Hernandez-Duenas et al., 2013). To validate this assumption, and to introduce a potentially interesting new aspect to the microphysics, we could allow condensation and sublimation to have different timescales. This is likely to influence the competition

between sedimentation and mixing in hydrating the TTL as discussed in § 6.4. To link our simplified framework with examples of convective overshooting in the atmosphere more directly, the environmental setup could be modified to use representative profiles of atmospheric soundings used in more complex numerical studies. For example, Sang et al. (2018) use a wind shear profile where vertical shear is present only in a 2 km deep layer near the overshooting top. More complex velocity profiles in the environment are likely to influence gravity wave breaking and modify the vortical response that enhances mixing in the presence of shear. Another simple extension is to prescribe a background humidity profile in the stratified environment. This would allow a more detailed investigation of the link between in-situ formation of cirrus clouds (i.e. jumping cirrus) and vertical displacements caused by the penetrating plume or gravity wave breaking. A more nuanced addition to our model would be a representation of supersaturation. Hassim and Lane (2010) showed that convective penetration can lead to a dehydration of the stratosphere when the environment is supersaturated, an aspect we chose not to address – though an important question is how often these conditions actually occur in the TTL. It may be possible to allow this in our model simply by increasing the condensation timescale, but this would only allow transient cases of supersaturation when the saturation concentration is reduced. Another simple extension to allow supersaturation is to modify the saturation concentration ϕ_{vs} to $\phi_{vs}(1+\gamma)$ in the vapour/ice conversion rate $\mathcal{E}$, where $0 < \gamma \ll 1$, which emulates 'spontaneous nucleation' well above the saturation concentration.

The work in this thesis could be extended to address parameterisations of moisture transport by convective overshoots in the TTL in climate models. At present, climate models rely on bulk parameterisations which may not accurately represent small-scale turbulent mixing and do not account for the significant spatial inhomogeneity of this mixing as well as its time dependence as highlighted in § 3.4. In § 6.4 we showed that semi-quantitative models based on dynamics alone can be used to estimate the distribution of vapour concentrations given knowledge of the strength of sedimentation relative to turbulent velocities in the plume. Given an estimate of the vertical flux of moisture in the plume, these models could be extended to estimate net hydration of the TTL. Such a model would not require detailed knowledge of the mixing that occurs between the plume and environment, providing motivation that simple parameterisations of the influence of convective overshooting are possible. However, these models do rely on estimates of the dynamics, namely the minimum temperature along parcel trajectories and the equilibrium height of the intrusion. Minimum temperatures

could be estimated given knowledge of the maximum penetration height. The problem therefore reduces to estimating $z_{\max}$ and z_{n}. Although experimental studies have shown that these heights scale with the source integral buoyancy flux and stratification strength, it is not clear how this may extend to more complex environmental stability profiles. Energetic principles could be used to estimate $z_{\max}$, since the maximum height is largely determined by the excess kinetic energy at penetration (Debugne and Hunt, 2016). However, a model for z_{n} must encapsulate the effect of mixing in raising the buoyancy of plume fluid parcels and this remains an open problem. The buoyancy-tracer volume distribution introduced in chapter 3 could act as a useful framework for prescribing idealised versions of the source and mixing flux distributions and exploring the evolution of the volume distribution.

In chapter 4 we showed that internal waves generated by convective penetration can be traced from the stratified environment back into the plume, concluding that internal waves are generated by turbulence in the plume cap. A complete theory for this generation mechanism remains an open problem. As noted in § 4.6, studies of a strongly stratified regime where convective plumes do not penetrate into an adjacent stratified layer have shown that turbulent Reynolds' stresses can explain the observed wave spectrum by acting as non-linear forcing to a wave equation. However, the theoretical approach in these studies relies on a separation of scales between the waves and turbulence which is not applicable to the penetrative regime we consider because the wave and turbulence spectra overlap. We briefly considered a two-layer flow that was designed to be structurally similar to the stratified simulations but without internal waves. By exploring differences between the two flows, we aimed to identify any structural differences that arise from the presence of internal waves in one flow but not the other. An evanescent wave pattern was found in a weakly stratified layer surrounding the two-layer plume cap, that suggests the same wave generation processes occur inside the turbulent plume cap and the waves become evanescent as they propagate out of the plume cap. This can be explored further using the viscous model modified from Taylor and Sarkar (2007). Using decaying modes instead of propagating wave modes would lead to a similar equation predicting amplitude decay that could be compared with the observed wave amplitudes to determine if the same processes are at play. Given the analogous setup, analytical theory on internal wave tunnelling may also shed light on decay of the wave signal and energy reflection from the sudden change in stratification from the weakly stratified plume to the uniform environment (Sutherland and Yewchuk, 2004).

Although beyond the scope of this thesis, it is an open question whether the spectral properties of internal waves identified in § 4.4 can be identified in observations of the gravity wave spectrum in the lower stratosphere. There is some evidence that our results should translate; Lane and Reeder (2001) found that numerical simulations of deep tropical convection generated gravity waves with a peak frequency close to the buoyancy frequency of the surrounding environment. As observations of gravity waves in the upper troposphere and lower stratosphere improve, it may become feasible to link observed spectra with idealised model studies such as ours more closely. In a broader sense, this work intersects with the study of stratified turbulence and internal wave dynamics, which are crucial in both atmospheric and oceanic settings. We have identified spectral properties of internal waves over a wide range of stratification strengths. The demonstration that internal waves may be generated by turbulence within the plume, rather than at the interface between the plume and environment, challenges existing assumptions on internal wave theory. This insight has potential applications in improving gravity wave parameterisations in weather and climate models by linking the wave spectrum with the resolved environmental stability profile. Parameterisations of convectively-generated gravity waves tend to identify the momentum flux given environmental conditions – exploring the dependence of results in chapter 4 on the source buoyancy flux F_0 would represent an important step towards improving these parameterisations.

Finally, the influence of internal gravity wave breaking on the generation of turbulence and mixing in convective hydration of the TTL remains an important open question. Practical limitations meant we were not able to explore the spectral properties of internal waves generated by convective penetration in the presence of shear, but this may have a significant impact on the spectrum of gravity waves generated by deep convection that can influence mean atmospheric winds such as the QBO which is not currently represented in parameterisations. Moreover, our results have shown pathways for wave breaking to enhance hydration but importantly we do not consider wave breaking to be the essential underlying mechanism at play, in contrast with several numerical studies of the atmospheric problem (Hassim and Lane, 2010; Homeyer et al., 2017; O'Neill et al., 2021; Wang, 2003; Wang et al., 2016). Similarly, there remains scope for a clearer understanding of the formation and importance of jumping cirrus above deep convection. It remains unclear whether jumping cirrus is a result of the redistribution of moisture within the TTL, or represents an extension of the direct

injection of moisture by convective overshoots as a result of bringing together air in the upper TTL with moistened air lower in the TTL.

References

Abkar, M., Bae, H. J., and Moin, P. (2016). Minimum-dissipation scalar transport model for large-eddy simulation of turbulent flows. *Physical Review Fluids*, 1(4):041701.

Abkar, M. and Moin, P. (2017). Large-Eddy Simulation of Thermally Stratified Atmospheric Boundary-Layer Flow Using a Minimum Dissipation Model. *Boundary-Layer Meteorology*, 165(3):405–419.

Alfonsi, G. (2011). On Direct Numerical Simulation of Turbulent Flows. *Applied Mechanics Reviews*, 64(2):020802.

Ansong, J. K., Kyba, P. J., and Sutherland, B. R. (2008). Fountains impinging on a density interface. *Journal of Fluid Mechanics*, 595:115–139.

Ansong, J. K. and Sutherland, B. R. (2010). Internal gravity waves generated by convective plumes. *Journal of Fluid Mechanics*, 648:405–434.

Baldwin, M. P., Gray, L. J., Dunkerton, T. J., Hamilton, K., Haynes, P. H., Randel, W. J., Holton, J. R., Alexander, M. J., Hirota, I., Horinouchi, T., Jones, D. B. A., Kinnersley, J. S., Marquardt, C., Sato, K., and Takahashi, M. (2001). The quasi-biennial oscillation. *Reviews of Geophysics*, 39(2):179–229.

Batchelor, G. K. (1954). Heat convection and buoyancy effects in fluids. *Quarterly Journal of the Royal Meteorological Society*, 80(345):339–358.

Bewley, T. R. (2019). *Numerical Renaissance: Simulation, Optimization, & Control*. Renaissance Press.

Billant, P. and Chomaz, J.-M. (2001). Self-similarity of strongly stratified inviscid flows. *Physics of Fluids*, 13(6):1645–1651.

Bloomfield, L. J. and Kerr, R. C. (1998). Turbulent fountains in a stratified fluid. *Journal of Fluid Mechanics*, 358:335–356.

Brasseur, G. P. and Jacob, D. J. (2017). *Modeling of Atmospheric Chemistry*. Cambridge University Press, Cambridge.

Brewer, A. W. (1949). Evidence for a world circulation provided by the measurements of helium and water vapour distribution in the stratosphere. *Quarterly Journal of the Royal Meteorological Society*, 75(326):351–363.

Briggs, G. A. (1965). A Plume Rise Model Compared with Observations. *Journal of the Air Pollution Control Association*, 15(9):433–438.

Butchart, N. (2014). The Brewer-Dobson circulation. *Reviews of Geophysics*, 52(2):157–184.

Carazzo, G., Kaminski, E., and Tait, S. (2006). The route to self-similarity in turbulent jets and plumes. *Journal of Fluid Mechanics*, 547:137.

Carazzo, G., Kaminski, E., and Tait, S. (2008). On the rise of turbulent plumes: Quantitative effects of variable entrainment for submarine hydrothermal vents, terrestrial and extra terrestrial explosive volcanism. *Journal of Geophysical Research: Solid Earth*, 113(B9):2007JB005458.

Carazzo, G., Kaminski, E., and Tait, S. (2010). The rise and fall of turbulent fountains: A new model for improved quantitative predictions. *Journal of Fluid Mechanics*, 657:265–284.

Chemel, C. and Staquet, C. (2007). A formulation of convective entrainment in terms of mixing efficiency. *Journal of Fluid Mechanics*, 580:169–178.

Clark, T. L., Hauf, T., and Kuettner, J. P. (1986). Convectively forced internal gravity waves: Results from two-dimensional numerical experiments. *Quarterly Journal of the Royal Meteorological Society*, 112(474):899–925.

Couston, L.-A., Lecoanet, D., Favier, B., and Le Bars, M. (2018). The energy flux spectrum of internal waves generated by turbulent convection. *Journal of Fluid Mechanics*, 854:R3.

Craske, J. (2016). *Unsteady Turbulent Jets and Plumes*. PhD thesis, Imperial College London.

Craske, J. and van Reeuwijk, M. (2015). Energy dispersion in turbulent jets. Part 1. Direct simulation of steady and unsteady jets. *Journal of Fluid Mechanics*, 763:500–537.

Dauhut, T., Chaboureau, J.-P., Escobar, J., and Mascart, P. (2015). Large-eddy simulations of Hector the convector making the stratosphere wetter. *Atmospheric Science Letters*, 16(2):135–140.

Dauhut, T., Chaboureau, J.-P., Haynes, P., and Lane, T. (2018). The Mechanisms Leading to a Stratospheric Hydration by Overshooting Convection. *Journal of the Atmospheric Sciences*, 75:4383–4398.

Dauhut, T. and Hohenegger, C. (2022). The Contribution of Convection to the Stratospheric Water Vapor: The First Budget Using a Global Storm-Resolving Model. *Journal of Geophysical Research: Atmospheres*, 127(5):e2021JD036295.

Davies Wykes, M. S. and Dalziel, S. B. (2014). Efficient mixing in stratified flows: Experimental study of a Rayleigh–Taylor unstable interface within an otherwise stable stratification. *Journal of Fluid Mechanics*, 756:1027–1057.

Davies Wykes, M. S., Hughes, G. O., and Dalziel, S. B. (2015). On the meaning of mixing efficiency for buoyancy-driven mixing in stratified turbulent flows. *Journal of Fluid Mechanics*, 781:261–275.

Davis, S. M., Rosenlof, K. H., Hassler, B., Hurst, D. F., Read, W. G., Vömel, H., Selkirk, H., Fujiwara, M., and Damadeo, R. (2016). The Stratospheric Water and Ozone Satellite Homogenized (SWOOSH) database: A long-term database for climate studies. *Earth System Science Data*, 8(2):461–490.

De Rooy, W. C., Bechtold, P., Fröhlich, K., Hohenegger, C., Jonker, H., Mironov, D., Pier Siebesma, A., Teixeira, J., and Yano, J.-I. (2013). Entrainment and detrainment in cumulus convection: An overview. *Quarterly Journal of the Royal Meteorological Society*, 139(670):1–19.

DeBonis, J. R. (2019). WRLES: Wave Resolving Large-Eddy Simulation Code, Theory and Usage. Technical Report 2019-220192, Glenn Research Center, Cleveland, Ohio.

Debugne, A. L. R. and Hunt, G. R. (2016). A phenomenological model for fountain-top entrainment. *Journal of Fluid Mechanics*, 796:195–210.

Dessler, A. E. (1998). A reexamination of the "stratospheric fountain" hypothesis. *Geophysical Research Letters*, 25(22):4165–4168.

Devenish, B. J., Rooney, G. G., and Thomson, D. J. (2010). Large-eddy simulation of a buoyant plume in uniform and stably stratified environments. *Journal of Fluid Mechanics*, 652:75–103.

Dhamankar, N. S., Blaisdell, G. A., and Lyrintzis, A. S. (2018). Overview of Turbulent Inflow Boundary Conditions for Large-Eddy Simulations. *AIAA Journal*, 56(4):1317–1334.

Dunkerton, T. J. (1997). The role of gravity waves in the quasi-biennial oscillation. *Journal of Geophysical Research: Atmospheres*, 102(D22):26053–26076.

Durran, D. R. (1986). Another Look at Downslope Windstorms. Part I: The Development of Analogs to Supercritical Flow in an Infinitely Deep, Continuously Stratified Fluid. *Journal of the Atmospheric Sciences*, 43:2527–2543.

Eliassen, A. and Palm, E. E. (1961). On the Transfer of Energy in Stationary Mountain Waves. 12(3):1–23.

Feist, M. M., Westbrook, C. D., Clark, P. A., Stein, T. H., Lean, H. W., and Stirling, A. J. (2019). Statistics of convective cloud turbulence from a comprehensive turbulence retrieval method for radar observations. *Quarterly Journal of the Royal Meteorological Society*, 145(719):727–744.

Flynn, M. R., Onu, K., and Sutherland, B. R. (2003). Internal wave excitation by a vertically oscillating sphere. *Journal of Fluid Mechanics*, 494:65–93.

Flynn, M. R. and Sutherland, B. R. (2004). Intrusive gravity currents and internal gravity wave generation in stratified fluid. *Journal of Fluid Mechanics*, 514:355–383.

Forster, P. M. D. F. and Shine, K. P. (2002). Assessing the climate impact of trends in stratospheric water vapor. *Geophysical Research Letters*, 29(6):10–1–10–4.

Frey, W., Schofield, R., Hoor, P., Kunkel, D., Ravegnani, F., Ulanovsky, A., Viciani, S., D'Amato, F., and Lane, T. P. (2015). The impact of overshooting deep convection on local transport and mixing in the tropical upper troposphere/lower stratosphere (UTLS). *Atmospheric Chemistry and Physics*, 15(11):6467–6486.

Fritts, D. C. and Alexander, M. J. (2003). Gravity wave dynamics and effects in the middle atmosphere. *Reviews of Geophysics*, 41(1):2001RG000106.

Fritts, D. C. and Nastrom, G. D. (1992). Sources of Mesoscale Variability of Gravity Waves. Part II: Frontal, Convective, and Jet Stream Excitation. *Journal of the Atmospheric Sciences*, 49(2):111–127.

Fueglistaler, S., Dessler, A. E., Dunkerton, T. J., Folkins, I., Fu, Q., and Mote, P. W. (2009). Tropical tropopause layer. *Reviews of Geophysics*, 47(1):RG1004.

Fueglistaler, S. and Haynes, P. H. (2005). Control of interannual and longer-term variability of stratospheric water vapor. *Journal of Geophysical Research: Atmospheres*, 110(24):1–14.

García-Franco, J. L., Gray, L. J., Osprey, S., Chadwick, R., and Martin, Z. (2022). The tropical route of quasi-biennial oscillation (QBO) teleconnections in a climate model. *Weather and Climate Dynamics*, 3(3):825–844.

García-Villalba, M. and Del Álamo, J. C. (2011). Turbulence modification by stable stratification in channel flow. *Physics of Fluids*, 23(4):045104.

Grabowski, W. W. (1998). Toward Cloud Resolving Modeling of Large-Scale Tropical Circulations: A Simple Cloud Microphysics Parameterization. *Journal of the Atmospheric Sciences*, 55(21):3283–3298.

Gregg, M., D'Asaro, E., Riley, J., and Kunze, E. (2018). Mixing Efficiency in the Ocean. *Annual Review of Marine Science*, 10(1):443–473.

Hassim, M. E. E. and Lane, T. P. (2010). A model study on the influence of overshooting convection on TTL water vapour. *Atmospheric Chemistry and Physics*, 10(20):9833–9849.

Hernandez-Duenas, G., Majda, A. J., Smith, L. M., and Stechmann, S. N. (2013). Minimal models for precipitating turbulent convection. *Journal of Fluid Mechanics*, 717:576–611.

Herrmann, M., Somot, S., Sevault, F., Estournel, C., and Déqué, M. (2008). Modeling the deep convection in the northwestern Mediterranean Sea using an eddy-permitting and an eddy-resolving model: Case study of winter 1986–1987. *Journal of Geophysical Research*, 113(C4):C04011.

Holliday, D. and Mcintyre, M. E. (1981). On potential energy density in an incompressible, stratified fluid. *Journal of Fluid Mechanics*, 107:221–225.

Holton, J. R. and Tan, H.-C. (1980). The Influence of the Equatorial Quasi-Biennial Oscillation on the Global Circulation at 50 mb. *Journal of the Atmospheric Sciences*, 37(10):2200–2208.

Homeyer, C. R. (2014). Formation of the Enhanced-V Infrared Cloud-Top Feature from High-Resolution Three-Dimensional Radar Observations. *Journal of the Atmospheric Sciences*, 71(1):332–348.

Homeyer, C. R., McAuliffe, J. D., and Bedka, K. M. (2017). On the Development of Above-Anvil Cirrus Plumes in Extratropical Convection. *Journal of the Atmospheric Sciences*, 74(5):1617–1633.

Hosking, J. S., Russo, M. R., Braesicke, P., and Pyle, J. A. (2010). Modelling deep convection and its impacts on the tropical tropopause layer. *Atmospheric Chemistry and Physics*, 10(22):11175–11188.

Howland, C. J., Taylor, J. R., and Caulfield, C. (2021). Shear-induced breaking of internal gravity waves. *Journal of Fluid Mechanics*, 921:A24.

Howland, C. J., Taylor, J. R., and Caulfield, C. P. (2020). Mixing in forced stratified turbulence and its dependence on large-scale forcing. *Journal of Fluid Mechanics*, 898:A7.

Hunt, G. R. and Burridge, H. C. (2015). Fountains in Industry and Nature. *Annual Review of Fluid Mechanics*, 47(1):195–220.

Hunt, G. R. and Debugne, A. L. R. (2016). Forced fountains. *Journal of Fluid Mechanics*, 802:437–463.

Hunt, G. R. and Kaye, N. B. (2005). Lazy plumes. *Journal of Fluid Mechanics*, 533:329–338.

Ivey, G., Winters, K., and Koseff, J. (2008). Density Stratification, Turbulence, but How Much Mixing? *Annual Review of Fluid Mechanics*, 40(1):169–184.

Iwasaki, S. and Yamaguchi, T. (2022). Characteristics of a Jumping Cirrus Retrieved From Rapid Scans by Himawari-8. *Journal of Geophysical Research: Atmospheres*, 127(22):e2022JD037539.

Jensen, E. J., Ackerman, A. S., and Smith, J. A. (2007). Can overshooting convection dehydrate the tropical tropopause layer? *Journal of Geophysical Research: Atmospheres*, 112(D11):2006JD007943.

Jensen, E. J., Pan, L. L., Honomichl, S., Diskin, G. S., Krämer, M., Spelten, N., Günther, G., Hurst, D. F., Fujiwara, M., Vömel, H., Selkirk, H. B., Suzuki, J., Schwartz, M. J., and Smith, J. B. (2020). Assessment of Observational Evidence for Direct Convective Hydration of the Lower Stratosphere. *Journal of Geophysical Research: Atmospheres*, 125(15):e2020JD032793.

Jensen, E. J. and Pfister, L. (2004). Transport and freeze-drying in the tropical tropopause layer. *Journal of Geophysical Research: Atmospheres*, 109(D2):2003JD004022.

Kataoka, T., Ghaemsaidi, S. J., Holzenberger, N., Peacock, T., and Akylas, T. R. (2017). Tilting at wave beams: A new perspective on the St. Andrew's Cross. *Journal of Fluid Mechanics*, 830:660–680.

Kaye, N. B. and Hunt, G. R. (2006). Weak fountains. *Journal of Fluid Mechanics*, 558:319–328.

Keeble, J., Hassler, B., Banerjee, A., Checa-Garcia, R., Chiodo, G., Davis, S., Eyring, V., Griffiths, P. T., Morgenstern, O., Nowack, P., Zeng, G., Zhang, J., Bodeker, G., Burrows, S., Cameron-Smith, P., Cugnet, D., Danek, C., Deushi, M., Horowitz, L. W., Kubin, A., Li, L., Lohmann, G., Michou, M., Mills, M. J., Nabat, P., Olivié, D., Park, S., Seland, Ø., Stoll, J., Wieners, K.-H., and Wu, T. (2021). Evaluating stratospheric ozone and water vapour changes in CMIP6 models from 1850 to 2100. *Atmospheric Chemistry and Physics*, 21(6):5015–5061.

Khaykin, S. M., Moyer, E., Krämer, M., Clouser, B., Bucci, S., Legras, B., Lykov, A., Afchine, A., Cairo, F., Formanyuk, I., Mitev, V., Matthey, R., Rolf, C., Singer, C. E., Spelten, N., Volkov, V., Yushkov, V., and Stroh, F. (2022). Persistence of moist plumes from overshooting convection in the Asian monsoon anticyclone. *Atmospheric Chemistry and Physics*, 22(5):3169–3189.

Kolmogorov, A. (1941). The Local Structure of Turbulence in Incompressible Viscous Fluid for Very Large Reynolds' Numbers. *Akademiia Nauk SSSR Doklady*, 30:301–305.

Kunz, A., Sprenger, M., and Wernli, H. (2015). Climatology of potential vorticity streamers and associated isentropic transport pathways across PV gradient barriers. *Journal of Geophysical Research: Atmospheres*, 120(9):3802–3821.

Kurbatskii, A. F. (2001). Computational Modeling of the Turbulent Penetrative Convection above the Urban Heat Island in a Stably Stratified Environment. *Journal of Applied Meteorology*, 40(10):1748–1761.

Lane, T. P. (2008). The vortical response to penetrative convection and the associated gravity-wave generation. *Atmospheric Science Letters*, 9(3):103–110.

Lane, T. P. and Reeder, M. J. (2001). Convectively Generated Gravity Waves and Their Effect on the Cloud Environment. *Journal of the Atmospheric Sciences*, 58(16):2427–2440.

Lane, T. P. and Sharman, R. D. (2006). Gravity wave breaking, secondary wave generation, and mixing above deep convection in a three-dimensional cloud model. *Geophysical Research Letters*, 33(23):L23813.

Lane, T. P., Sharman, R. D., Clark, T. L., and Hsu, H.-M. (2003). An Investigation of Turbulence Generation Mechanisms above Deep Convection. *Journal of the Atmospheric Sciences*, 60(10):1297–1321.

Lecoanet, D., Le Bars, M., Burns, K. J., Vasil, G. M., Brown, B. P., Quataert, E., and Oishi, J. S. (2015). Numerical simulations of internal wave generation by convection in water. *Physical Review E*, 91(6):063016.

Lecoanet, D. and Quataert, E. (2013). Internal gravity wave excitation by turbulent convection. *Monthly Notices of the Royal Astronomical Society*, 430(3):2363–2376.

Lee, K.-O., Dauhut, T., Chaboureau, J.-P., Khaykin, S., Krämer, M., and Rolf, C. (2019). Convective hydration in the tropical tropopause layer during the StratoClim aircraft campaign: Pathway of an observed hydration patch. *Atmospheric Chemistry and Physics*, 19(18):11803–11820.

Lighthill, M. J. (1952). On sound generated aerodynamically I. General theory. *Proceedings of the Royal Society of London. Series A. Mathematical and Physical Sciences*, 211:564–587.

Linden, P. F. (1975). The deepening of a mixed layer in a stratified fluid. *Journal of Fluid Mechanics*, 71(2):385–405.

List, E. J. (1982). Turbulent Jets and Plumes. *Annual Review of Fluid Mechanics*, 14(1):189–212.

Liu, H.-L. (2017). Large Wind Shears and Their Implications for Diffusion in Regions With Enhanced Static Stability: The Mesopause and the Tropopause. *Journal of Geophysical Research: Atmospheres*, 122(18):9579–9590.

Lorenz, E. N. (1955). Available Potential Energy and the Maintenance of the General Circulation. *Tellus*, 7(2):157–167.

Luderer, G., Trentmann, J., Hungershofer, K., Herzog, M., Fromm, M., and Andreae, M. O. (2007). Small-scale mixing processes enhancing troposphere-to-stratosphere transport by pyro-cumulonimbus storms. *Atmospheric Chemistry and Physics*, 7:5945–5957.

Lumley, J. L. and Newman, G. R. (1977). The return to isotropy of homogeneous turbulence. *Journal of Fluid Mechanics*, 82(1):161–178.

Majda, A. J., Xing, Y., and Mohammadian, M. (2010). Moist multi-scale models for the hurricane embryo. *Journal of Fluid Mechanics*, 657:478–501.

Marshall, J. and Schott, F. (1999). Open-ocean convection: Observations, theory, and models. *Reviews of Geophysics*, 37(1):1–64.

Mercier, M. J., Garnier, N. B., and Dauxois, T. (2008). Reflection and diffraction of internal waves analyzed with the Hilbert transform. *Physics of Fluids*, 20(8):086601.

Millán, L., Santee, M. L., Lambert, A., Livesey, N. J., Werner, F., Schwartz, M. J., Pumphrey, H. C., Manney, G. L., Wang, Y., Su, H., Wu, L., Read, W. G., and Froidevaux, L. (2022). The Hunga Tonga-Hunga Ha'apai Hydration of the Stratosphere. *Geophysical Research Letters*, 49(13):e2022GL099381.

Morton, B. R. (1959). Forced plumes. *Journal of Fluid Mechanics*, 5(1):151–163.

Morton, B. R., Taylor, G. I., and Turner, J. S. (1956). Turbulent gravitational convection from maintained and instantaneous sources. *Proceedings of the Royal Society of London. Series A. Mathematical and Physical Sciences*, 234(1196):1–23.

Mote, P. W., Rosenlof, K. H., McIntyre, M. E., Carr, E. S., Gille, J. C., Holton, J. R., Kinnersley, J. S., Pumphrey, H. C., Russell, J. M., and Waters, J. W. (1996). An atmospheric tape recorder: The imprint of tropical tropopause temperatures on stratospheric water vapor. *Journal of Geophysical Research: Atmospheres*, 101(D2):3989–4006.

Nidhan, S., Schmidt, O. T., and Sarkar, S. (2022). Analysis of coherence in turbulent stratified wakes using spectral proper orthogonal decomposition. *Journal of Fluid Mechanics*, 934:A12.

Noël, S., Weigel, K., Bramstedt, K., Rozanov, A., Weber, M., Bovensmann, H., and Burrows, J. P. (2018). Water vapour and methane coupling in the stratosphere observed using SCIAMACHY solar occultation measurements. *Atmospheric Chemistry and Physics*, 18(7):4463–4476.

O'Neill, M. E., Orf, L., Heymsfield, G. M., and Halbert, K. (2021). Hydraulic jump dynamics above supercell thunderstorms. *Science*, 373(6560):1248–1251.

Osprey, S. M., Butchart, N., Knight, J. R., Scaife, A. A., Hamilton, K., Anstey, J. A., Schenzinger, V., and Zhang, C. (2016). An unexpected disruption of the atmospheric quasi-biennial oscillation. *Science*, 353(6306):1424–1427.

Pan, L. L., Honomichl, S. B., Thornberry, T., Rollins, A., Bui, T. P., Pfister, L., and Jensen, E. E. (2019). Observational Evidence of Horizontal Transport-Driven Dehydration in the TTL. *Geophysical Research Letters*, 46(13):7848–7856.

Pandya, R. E. and Alexander, M. J. (1999). Linear Stratospheric Gravity Waves above Convective Thermal Forcing. *Journal of the Atmospheric Sciences*, 56(14):2434–2446.

Papanicolaou, P. N. and List, E. J. (1988). Investigations of round vertical turbulent buoyant jets. *Journal of Fluid Mechanics*, 195:341–391.

Peltier, W. R. and Caulfield, C. P. (2003). Mixing Efficiency in Stratified Shear Flows. *Annual Review of Fluid Mechanics*, 35(1):135–167.

Penney, J., Morel, Y., Haynes, P., Auclair, F., and Nguyen, C. (2020). Diapycnal mixing of passive tracers by Kelvin–Helmholtz instabilities. *Journal of Fluid Mechanics*, 900:A26.

Pham, M. V., Plourde, F., and Doan, K. S. (2007). Direct and large-eddy simulations of a pure thermal plume. *Physics of Fluids*, 19(12):125103.

Pierce, A. D. and Coroniti, S. C. (1966). A Mechanism for the Generation of Acoustic-Gravity Waves During Thunderstorm Formation. *Nature*, 210(5042):1209–1210.

Pinçon, C., Belkacem, K., and Goupil, M. J. (2016). Generation of internal gravity waves by penetrative convection. *Astronomy & Astrophysics*, 588:A122.

Plumb, R. A. (2007). Tracer Interrelationships in the Stratosphere. *Reviews of Geophysics*, 45(4):RG4005.

Powell, C. W., Haynes, P. H., and Taylor, J. R. (2024). Diagnosing tracer transport in convective penetration of a stably stratified layer. *Journal of Fluid Mechanics*, 997:A48.

Priestley, C. H. B. and Ball, F. K. (1955). Continuous convection from an isolated source of heat. *Quarterly Journal of the Royal Meteorological Society*, 81(348):144–157.

Randel, W. J. and Jensen, E. J. (2013). Physical processes in the tropical tropopause layer and their roles in a changing climate. *Nature Geoscience*, 6(3):169–176.

Ricou, F. P. and Spalding, D. B. (1961). Measurements of entrainment by axisymmetrical turbulent jets. *Journal of Fluid Mechanics*, 11(1):21–32.

Robinson, F. J. and Sherwood, S. C. (2006). Modeling the Impact of Convective Entrainment on the Tropical Tropopause. *Journal of the Atmospheric Sciences*, 63(3):1013–1027.

Rozema, W., Bae, H. J., Moin, P., and Verstappen, R. (2015). Minimum-dissipation models for large-eddy simulation. *Physics of Fluids*, 27(8):085107.

Sang, W., Huang, Q., Tian, W., Wright, J. S., Zhang, J., Tian, H., Luo, J., Hu, D., and Han, Y. (2018). A Large Eddy Model Study on the Effect of Overshooting Convection on Lower Stratospheric Water Vapor. *Journal of Geophysical Research: Atmospheres*, 123(18):10023–10036.

Schiller, C. (2009). Hydration and dehydration at the tropical tropopause. *Atmospheric Chemistry and Physics*, 9(24):9647–9660.

Schmid, P. J. (2010). Dynamic mode decomposition of numerical and experimental data. *Journal of Fluid Mechanics*, 656:5–28.

Schoeberl, M. R., Dessler, A. E., Wang, T., Avery, M. A., and Jensen, E. J. (2014). Cloud formation, convection, and stratospheric dehydration. *Earth and Space Science*, 1(1):1–17.

Schoeberl, M. R., Jensen, E. J., Pfister, L., Ueyama, R., Avery, M., and Dessler, A. E. (2018). Convective Hydration of the Upper Troposphere and Lower Stratosphere. *Journal of Geophysical Research: Atmospheres*, 123(9):4583–4593.

Shabbir, A. and George, W. K. (1994). Experiments on a round turbulent buoyant plume. *Journal of Fluid Mechanics*, 275:1–32.

Sherwood, S. C. and Dessler, A. E. (2001). A Model for Transport across the Tropical Tropopause. *Journal of the Atmospheric Sciences*, 58(7):765–779.

Shrinivas, A. B. and Hunt, G. R. (2014). Unconfined turbulent entrainment across density interfaces. *Journal of Fluid Mechanics*, 757:573–598.

Smagorinsky, J. (1963). General Circulation Experiments with the Primitve Equations: I. The Basic Experiment. *Monthly Weather Review*, 91(3):99–164.

Solomon, S., Rosenlof, K. H., Portmann, R. W., Daniel, J. S., Davis, S. M., Sanford, T. J., and Plattner, G.-K. (2010). Contributions of Stratospheric Water Vapor to Decadal Changes in the Rate of Global Warming. *Science*, 327(5970):1219–1223.

Son, S.-W., Lim, Y., Yoo, C., Hendon, H. H., and Kim, J. (2017). Stratospheric Control of the Madden–Julian Oscillation. *Journal of Climate*, 30(6):1909–1922.

Stull, R. (1976). Internal Waves Generated by Penetrative Convection. *Journal of the Atmospheric Sciences*, 33:1279–1286.

Sunilkumar, S., Muhsin, M., Parameswaran, K., Venkat Ratnam, M., Ramkumar, G., Rajeev, K., Krishna Murthy, B., Sambhu Namboodiri, K., Subrahmanyam, K., Kishore Kumar, K., and Shankar Das, S. (2015). Characteristics of turbulence in the troposphere and lower stratosphere over the Indian Peninsula. *Journal of Atmospheric and Solar-Terrestrial Physics*, 133:36–53.

Sutherland, B. R. (2010). *Internal Gravity Waves*. Cambridge University Press, 1 edition.

Sutherland, B. R. and Linden, P. F. (1998). Internal wave excitation from stratified flow over a thin barrier. *Journal of Fluid Mechanics*, 377:223–252.

Sutherland, B. R. and Yewchuk, K. (2004). Internal wave tunnelling. *Journal of Fluid Mechanics*, 511:125–134.

Talluru, K., Williamson, N., and Armfield, S. (2022). Entrainment and dilution in a fountain top. *Journal of Fluid Mechanics*, 941:A24.

Taylor, G. I. (1945). Dynamics of a mass of hot gas rising in air. Technical Report 236, U.S. Atomic Energy Commission, Los Alamos National Laboratory Research Library.

Taylor, J. (2008). *Numerical Simulations of the Stratified Oceanic Bottom Boundary Layer*. PhD thesis, University of California, San Diego.

Taylor, J. R. and Sarkar, S. (2007). Internal gravity waves generated by a turbulent bottom Ekman layer. *Journal of Fluid Mechanics*, 590:331–354.

Textor, C., Graf, H.-F., Herzog, M., and Oberhuber, J. M. (2003). Injection of gases into the stratosphere by explosive volcanic eruptions. *Journal of Geophysical Research: Atmospheres*, 108(D19):2002JD002987.

Tissier, A.-S. and Legras, B. (2016). Convective sources of trajectories traversing the tropical tropopause layer. *Atmospheric Chemistry and Physics*, 16(5):3383–3398.

Turner, J. S. (1966). Jets and plumes with negative or reversing buoyancy. *Journal of Fluid Mechanics*, 26(4):779–792.

Ueyama, R., Jensen, E. J., and Pfister, L. (2018). Convective Influence on the Humidity and Clouds in the Tropical Tropopause Layer During Boreal Summer. *Journal of Geophysical Research: Atmospheres*, 123(14):7576–7593.

Ueyama, R., Jensen, E. J., Pfister, L., and Kim, J. E. (2015). Dynamical, convective, and microphysical control on wintertime distributions of water vapor and clouds in the tropical tropopause layer. *Journal of Geophysical Research*, 120(19):10483–10500.

Ulses, C., Estournel, C., Fourrier, M., Coppola, L., Kessouri, F., Lefèvre, D., and Marsaleix, P. (2021). Oxygen budget of the north-western Mediterranean deep-convection region. *Biogeosciences*, 18(3):937–960.

Vallis, G. K., Parker, D. J., and Tobias, S. M. (2019). A simple system for moist convection: The Rainy–Bénard model. *Journal of Fluid Mechanics*, 862:162–199.

Van Reeuwijk, M. and Craske, J. (2015). Energy-consistent entrainment relations for jets and plumes. *Journal of Fluid Mechanics*, 782:333–355.

Van Reeuwijk, M., Salizzoni, P., Hunt, G. R., and Craske, J. (2016). Turbulent transport and entrainment in jets and plumes: A DNS study. *Physical Review Fluids*, 1(7):074301.

VanDine, A., Pham, H. T., and Sarkar, S. (2021). Turbulent shear layers in a uniformly stratified background: DNS at high Reynolds number. *Journal of Fluid Mechanics*, 916:A42.

Verstappen, R. (2018). How much eddy dissipation is needed to counterbalance the nonlinear production of small, unresolved scales in a large-eddy simulation of turbulence? *Computers & Fluids*, 176:276–284.

Vogel, B., Günther, G., Müller, R., Grooß, J.-U., Afchine, A., Bozem, H., Hoor, P., Krämer, M., Müller, S., Riese, M., Rolf, C., Spelten, N., Stiller, G. P., Ungermann, J., and Zahn, A. (2016). Long-range transport pathways of tropospheric source gases originating in Asia into the northern lower stratosphere during the Asian monsoon season 2012. *Atmospheric Chemistry and Physics*, 16(23):15301–15325.

Vreugdenhil, C. A. and Taylor, J. R. (2018). Large-eddy simulations of stratified plane Couette flow using the anisotropic minimum-dissipation model. *Physics of Fluids*, 30(8):085104.

Wang, P. K. (2003). Moisture plumes above thunderstorm anvils and their contributions to cross-tropopause transport of water vapor in midlatitudes. *Journal of Geophysical Research: Atmospheres*, 108(D6):1–15.

Wang, P. K. (2004). A cloud model interpretation of jumping cirrus above storm top. *Geophysical Research Letters*, 31(18):2004GL020787.

Wang, P. K., Cheng, K.-Y., Setvak, M., and Wang, C.-K. (2016). The origin of the gullwing-shaped cirrus above an Argentinian thunderstorm as seen in CALIPSO images. *Journal of Geophysical Research: Atmospheres*, 121(7):3729–3738.

Winters, K. B., Lombard, P. N., Riley, J. J., and D'Asaro, E. A. (1995). Available potential energy and mixing in density-stratified fluids. *Journal of Fluid Mechanics*, 289:115–128.

Wright, J. S., Fu, R., Fueglistaler, S., Liu, Y. S., and Zhang, Y. (2011). The influence of summertime convection over Southeast Asia on water vapor in the tropical stratosphere. *Journal of Geophysical Research*, 116(D12):D12302.